Global Properties of Core-Collapse Supernovae in Numerical Simulations

Inauguraldissertation

zur
Erlangung der Würde eines Doktors der Philosophie
vorgelegt der
Philosophisch-Naturwissenschaftlichen Fakultät
der Universität Basel

von

Kevin Nicolas Ebinger

aus Basel, BS

Basel, 2019

Genehmigt von der Philosophisch-Naturwissenschaftlichen Fakultät
auf Antrag von

Fakultätsverantwortlicher: Prof. Dr. Friedrich-Karl Thielemann

Dissertationsleiter: Dr. habil. Matthias Hempel

Korreferentin: Assoc. Prof. Dr. Carla Fröhlich

Basel, den 21.02.2017

Prof. Dr. Martin Spiess
(Dekan)

Dedicated to my family

Abstract

The exact progenitor-remnant connection of CCSNe, i.e. if a star explodes, and if it leaves behind a neutron star or a black hole (BH), is not well understood yet. The understanding of CCSNe and their explosion mechanism(s) is a long standing problem that many astrophysicists tried to illuminate. The uncertainty of the explosion mechanism and the explodability also affect the prediction of the nucleosynthesis yields in the ejecta of CCSNe that contribute to the galactic chemical enrichment. In this thesis we study the explodability, explosion properties, and the ejecta of neutrino-driven core-collapse supernovae (CCSNe) with numerical simulations. This includes the study of the dynamics and trends of CCSNe in dependence of progenitor properties. To investigate the explodability and the progenitor-remnant connection quantitatively one has to study large samples of CCSN progenitors. Even though multi-dimensional simulations provide a promising and necessary tool to study the exact nature of the possible explosion mechanisms, sophisticated three-dimensional models are computationally too expensive to be used in the analysis of large samples of progenitors. With some exceptions for the lightest progenitors of CCSNe, self-consistent numerically affordable one-dimensional simulations that incorporate detailed microphysics, general relativity and sophisticated neutrino-transport fail to explode.

The main focus of this thesis lies on the PUSH method, a parametrized framework to efficiently investigate CCSNe for large samples of progenitors in spherically symmetric simulations. By investigations of CCSNe we can determine the explodability and the nucleosynthesis yields in the ejecta of the explosions obtained for the progenitors, as well as dependencies of explosion properties on the progenitor properties. Main strengths of the presented PUSH method in comparison with other artificial methods are obtaining the mass cut directly from the simulations and the PNS as well as the electron flavor neutrino luminosities are computed self-consistent at all simulation times. No changes of the involved electron neutrino and anti-neutrino cross sections are made. To achieve successful explosions in otherwise non-exploding models in spherical symmetry, we rely on the neutrino-driven mechanism. In this mechanism of CCSNe electron neutrinos and antineutrinos are able to heat matter behind the stalled shock front in the gain region

sufficiently to induce a shock revival that ultimately leads to an explosion. It has been found, that for efficient heating by neutrinos behind the shock multi-dimensional effects as convection are crucial. In our simulations we tap the energy of the $\mu-$ and $\tau-$neutrino luminosities that otherwise stream out of the system and increase the effective heating by neutrinos in regions where electron flavor neutrinos heat the matter. This enables us to successfully induce physically motivated parametrized neutrino-driven CCSNe in spherically symmetric simulations with a realistic SN equation of state (EOS).

After calibrating the PUSH method to SN 1987A for a suitable progenitor model, we proceed to explore large progenitor samples with solar metallicity. This is done by using observational properties of other CCSNe. By extending the calibration of the PUSH method with a dependency on compactness we can investigate CCSN simulations for progenitor models across the ZAMS mass range. We study large samples of progenitors with solar metallicity and discuss trends of the obtained results for explosion energy, nucleosynthesis yields and explodability. The resulting progenitor-remnant connection, the resulting prediction of the neutron star and black hole birth mass distributions that can be compared to observations are presented. In the final part of this thesis we discuss work done with the three-dimensional magnetohydrodynamics code with neutrino transport ELEPHANT and compare our parametrized spherically symmetric CCSN simulations to three-dimensional simulations.

Acknowledgements

I would like to express my gratitude to a couple of people that supported me and contributed to this thesis. My thanks go to:

F.-K. Thielemann for giving me the opportunity to work in his group, encouraging me to go to many interesting conferences and workshops, his advice based on his profound knowledge of physics, and his steady support.

Matthias Hempel for always having time for me, great and fruitful discussions, his invaluable advice, and for motivating and pushing me.

Albino Perego, Carla Fröhlich, Matthias Hempel, Sanjana Sinha, Marius Eichler, F.-K. Thielemann and Matthias Liebendörfer for an interesting and fruitful PUSH collaboration and for valuable work related advice.

Carla Fröhlich and Sanjana Sinha for a smooth extension of the PUSH collaboration, and the great communication, exchange of data, and discussions.

Matthias Liebendörfer and Roger Käppeli for giving me the opportunity to work with the ELEPHANT and the FISH code, and for their guidance and advice.

Rubén Cabezón, Kuo-Chuan Pan, Takami Kuroda, and Raphael Hirschi for interesting discussions and their work related advice.

Maik Frensel for very interesting and enjoyable discussions about various aspects of physics and Marius Eichler for beeing a great roommate at many conferences.

Julia Reichert, Marius Eichler, Maik Frensel, Rubén Cabezón, Andreas Lohs, Matthias Hempel, Oliver Heinimann, Oliver Müller, Francesco Cefala for proofreading parts of this thesis.

My office mates (present and former): Marius Eichler, Maik Frensel, Julia Reichert, Benjamin Wehmeyer, Albino Perego, Francesco Cefala, Eros Cazzato, and Roberto Scalera for nice discussions related to work and otherwise, coffee breaks, and company during extended working sessions.

All the other present and former Basel PhD students Oliver Heinimann, David Gobrecht, Umberto Battino, Chiara Biscaro, Sofie Fehlmann, Arkaprabha Sarangi.

The former members of the Basel group Andreas Lohs, Nobuya Nishimura, Marco Pignatari, Almudena Arcones, Lecturer Thomas Rauscher as well as visiting scientists Igor Panov and Nils Paar for a good atmosphere in the group.

Last but not least my family and friends for their invaluable support during my PhD studies.

Contents

1 Introduction

> *Home is behind, the world ahead,*
> *and there are many paths to tread*
> *through shadows to the edge of night,*
> *until the stars are all alight.*
>
> — **J.R.R. Tolkien, The Fellowship of the Ring**

1.1 Introductory Notes on Supernovae

Supernovae (SNe) are explosive events which mark the end of the life of some stars. During these violent phenomena the dying stars typically eject some of their material with a kinetic energy of the order of 10^{51} erg (1 Bethe, abbreviated as 1 B, is equivalent to 10^{51} erg) into the interstellar space [1–3]. The ejecta contains elements that have been created during the stages of the life of the star and in its explosion. In this way, dying stars contribute to the galactic chemical enrichment of their host galaxies and, therefore, are important for the future generations of stars, planets, and life. Besides the contribution to the chemical enrichment of the universe with their ejecta, some SNe produce a compact remnant, a neutron star (NS) or a black hole (BH), which are amongst the most physically extreme objects that can possibly be observed. SNe are astrophysical scenarios and astronomical objects that are among nature's most energetic and spectacular events and are much brighter and rarer than novae[1]. Their high luminosities, which enable them to outshine even their host galaxy, are mainly powered by the decays $^{56}\mathrm{Ni} \longrightarrow {}^{56}\mathrm{Co}$, and subsequently $^{56}\mathrm{Co} \longrightarrow {}^{56}\mathrm{Fe}$ [2]. Some SNe that took place in our galaxy have been observed by the naked eye. Chinese astronomers observed and recorded "guest stars", at least as early as the second century A.D.[1]. These stars have been named "guest stars" due to their sudden appearance in the sky. They were visible for a certain time and then

[1] A classical nova is a reoccurring explosive event in a stellar binary system fueled by mass accretion onto a white dwarf. Contrary to type Ia SN (see below), the white dwarf is not disrupted [3].

faded away. These “guest stars” are nowadays referred to as novae and SNe. The observed “guest stars” that were visible for a year or longer probably were supernovae, and the shorter visible “guest stars”, common novae. The remnant of one of the most famous SNe, which occurred in 1054 and was observed by Chinese astronomers, is the Crab Nebula which contains a well known pulsar: a rotating neutron star which emits electromagnetic radiation of all frequencies at regular intervals (~30 pulses per second) [1]. Furthermore, two of the observed galactic SNe where discovered by naked eye observations by Tycho Brahe and Johannes Kepler (SN 1572 and SN 1604). In 1572, Tycho Brahe, a Danish nobleman and astronomer, discovered a SN in Cassiopeia. He found that the position of this newly observed star did not change relative to the fixed stars. This observation convinced him that its origin was beyond the moon. His conclusion was against the idea of Aristotle, that everything beyond the moon is fixed. Tycho Brahe's student and assistant, Johannes Kepler, observed another SN in 1604 that remained visible for a year. In the last few centuries, many SNe have been observed in other galaxies with telescopes, but modern astrophysicists still wait for a galactic SN (i.e. in our Milky Way). One of the most extensively observed objects in the history of astronomy is SN 1987A (see [2] and references therein). In table 1.1 we show an overview of the afore mentioned famous historical SNe that occurred in the Milky Way and the Large Magellanic Cloud. SN 1987A started to be observable in 1987, after a blue supergiant star (Sanduleak -69° 202) underwent core collapse and exploded in the Large Magellanic Cloud, a satellite galaxy of the Milky Way [4]. It was the brightest and the first naked eye SN since Kepler's SN, and the first time that neutrinos were detected from the collapse of a stellar core (e.g., with the water Cherenkov detectors Kamiokande II and IMB (Irvine–Michigan–Brookhaven detector) [5–7]). This well-documented event was observed in all wavelengths from gamma rays to radio. Until nowadays SN 1987A is often taken as a reference point in discussions regarding SNe. The second brightest SN since Kepler's SN appeared in 1993 (SN 1993J) in the nearby spiral galaxy M81 [2]. SN 1993J was the brightest SN seen in the Northern Hemisphere since the invention of the telescope. The term Supernova was established by the two astronomers Walter Baade and Fritz Zwicky, who began a systematic study of SNe in the 1930s [9, 10]. They already suggested that the source of the huge amount of energy that is released in a SN could be generated by the gravitational collapse that takes place in the transition of a star to a neutron star. An important statement taking into account that the neutron was discovered by James Chadwick only two years prior to this suggestion [11, 12]. The currently adopted naming scheme of SNe was suggested by Zwicky and collaborators in the early 1960s [13]. In this scheme, the name of each event is initiated with the prefix SN followed by the year of discovery, after which, for years with more than one SN, an upper case letter from A to Z is added for the first 26 SNe in a given year. If there are more than 26 SNe in a year the lower-case letters aa, ab and so forth are used. SNe can be divided into different types that are distinguished by their spectroscopic charac-

Supernova	Year [AD]	Distance [kpc]	Visual Peak [mag]
SN 1054 (Crab)	1054	2.2	-4.0
Tycho	1572	7.0	-4.0
Kepler	1604	10.0	-3.0
SN 1987A	1987	50±5	3.0

Tab. 1.1.: This compilation of 'historical' SNe in the Milky Way and the Large Magellanic Cloud (SN 1987A) represents only a fraction of the total. A few more galactic SNe have been observed (see also [2, 8]) but the majority of SNe in the Milky Way are blocked from view by dust. Note that the values for distances and peak visual magnitude, with the exception of SN 1987A, are guesses at best. The formula for astronomical magnitudes (apparent magnitude) is given by $M = -2.5\log_{10}(\text{brigthness}) + \text{const.}$ (see e.g. [2] chapter 14.2). The limit for naked-eye observations is approximately at a magnitude of 6.0 . This table is adapted from [8].

teristics around maximum luminosity and by the properties of their light curves, which leads to the classification scheme shown in figure 1.1. These characteristics depend on the composition of the envelope of the SN progenitor. The distinction between the two types of SNe, type I and type II, is done based on the presence (type II) or absence (type I) of hydrogen lines. Each type can then be further subdivided based on the presence or absence of absorption lines or other features of the light curve. However, the most important physical characteristic of a SN is the underlying explosion mechanism. Type Ia SNe are thermonuclear explosions, while SNe of types Ib, Ic and II are due to core collapse. Depending on their initial masses at birth, called zero age main sequence (ZAMS)[1] masses, stars live through certain stellar burning stages and can evolve into progenitors of these different SN types [3]. In the following the main characteristics of the two different explosion mechanisms are briefly discussed. Core-collapse SNe (CCSNe) will be discussed in more detail in chapter 2, as they are the focus of this doctoral thesis.

Thermonuclear SNe are thought to be the outcome of a detonation or deflagration of a carbon-oxygen white dwarf that has a close companion star from which it can accrete matter [3, 14]. White dwarfs are the evolutionary products of stars with ZAMS masses $M \lesssim 8M_\odot$ which ended thermonuclear burning after He-burning. When the mass of a white dwarf approaches the Chandrasekhar limit ($M_{CH} \approx 1.4M_\odot$), the star becomes unstable against collapse, because the pressure of the degenerate electron gas inside the star can no longer sustain it against the gravitational force [1, 2]. The collapse of the white dwarf triggers the nuclear fusion of carbon and oxygen into heavy nuclei. Carbon ignites under degenerate conditions and a thermonuclear runaway occurs. This liberates

[1] A star starts its life on the ZAMS when hydrogen burning is initiated.

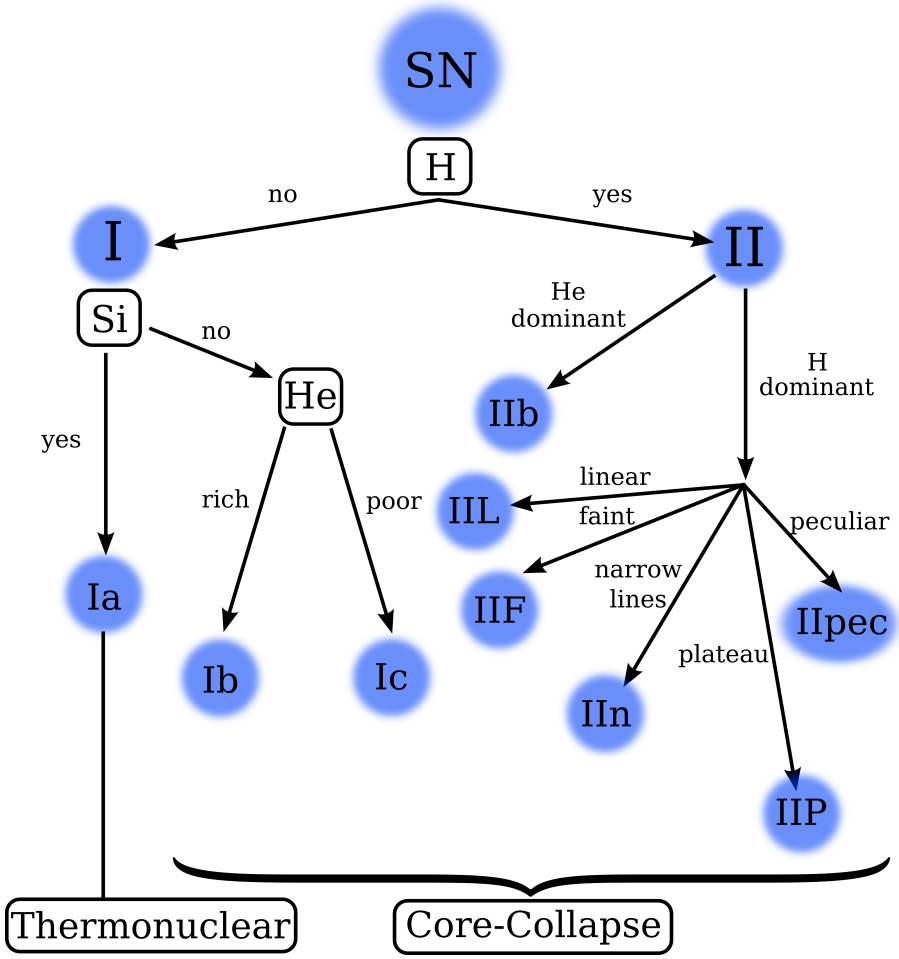

Fig. 1.1.: Classification of supernovae according to their observed spectra (adapted from [13, 14]). The two main types are distinguished by the absence (type I) or presence (type II) of hydrogen Balmer lines. The Type I SNe can be further divided into subtypes depending on the presence or absence of silicon and helium absorption lines. Type Ia SN spectra show an absorption feature attributed to Si. Type Ib and Ic both have weak or absent Si lines. They are distinguished by the presence or absence of He lines. A complimentary classification can be done based on their explosion mechanism: thermonuclear SNe (SN Ia) and core-collapse SNe (SN II,Ib/c). Type Ia SNe originate from the deflagration or detonation of an accreting white dwarf. Type Ib and Ic SNe originate from core collapse where either the H-envelope has been removed (Ib), or the H- and He-envelope have been removed (Ic). Type IIb is a 'cross-over' type, where H-lines are present initially, but then disappear over time. Eventually this type resembles the light curve of a Ib type. Normal type II SNe are either IIL or IIP where the L and P stand for linear decay and plateau of the luminosity after the initial peak, respectively. These types represent core-collapse SNe of massive progenitors with plenty of hydrogen in their shell. Other subtypes of type II SNe include type IIF (faint SNe), IIn (spectrum also has narrow emission lines), and TTpec (spectrum has peculiar features).

a large amount of nuclear binding energy, ultimately causing the thermonuclear explosion of the white dwarf. In this explosion scenario, the white dwarf is disrupted, leaving behind an expanding nebula without a central compact object remnant. The fact that type Ia SNe are all generated under similar physical circumstances, with almost identical characteristics (i.e. the amount of liberated energy and their light curve), makes it possible to use them as standard candles for the measurement of cosmological distance scales [3, 13, 15]. The observation of the variation in the brightness of these SNe with redshift allows to study the expansion of the universe and led to the discovery that the expansion of the universe is accelerating ([16, 17], Nobel Prize in Physics 2011).

CCSNe are the outcome of a series of events that are initiated by the collapse of the iron core of a massive star, $M \gtrsim 8M_{\odot}$, and leave behind a compact remnant, i.e. a neutron star or a black hole. The details of this phenomenon are explained in chapter 2. During the first few hundreds of ms following the collapse, the formed proto neutron star (PNS), is extremely hot and as a result neutrinos of all types are produced in vast numbers ($\sim 10^{58}$). During the collapse, a large amount of gravitational binding energy is liberated ($\sim 3 \times 10^{53}$erg) and about ~99% is carried away by neutrinos, since the PNS and its surrounding envelope are optically thick to photons. Type II SNe are initiated by collapsing cores of massive stars with masses between 8 and about ~60-120 $M_{\odot}$ (the range of explodability can have a metallicity dependence[1] [18]). Moreover, the hydrogen shell of these stars can have various sizes and masses, even if they have the same initial mass. This leads to a wide range of variability in type II SNe (see figure 1.1). To date, SN 1987A remains the best observed CCSN. It is still used as a standard event for this SN type. Table 1.2 gives the basic observational data of SN 1987A. In figure 1.2 we show the visual (V-band) magnitude of SN 1987A (compare the peak magnitude in figure 1.2 to the value given in table 1.1 for the peak visual magnitude of SN 1987A). Besides SN 1987A, there are also other astronomical observations of CCSN events. In chapter 5 in table 5.2, we give an overview of observational properties of a collection of CCSNe that are used in the studies presented in this work.

[1] The resulting remnant of a CCSN depends on the dominating explosion mechanism, ZAMS mass and metallicity, see also figure 2.1 in chapter 2.

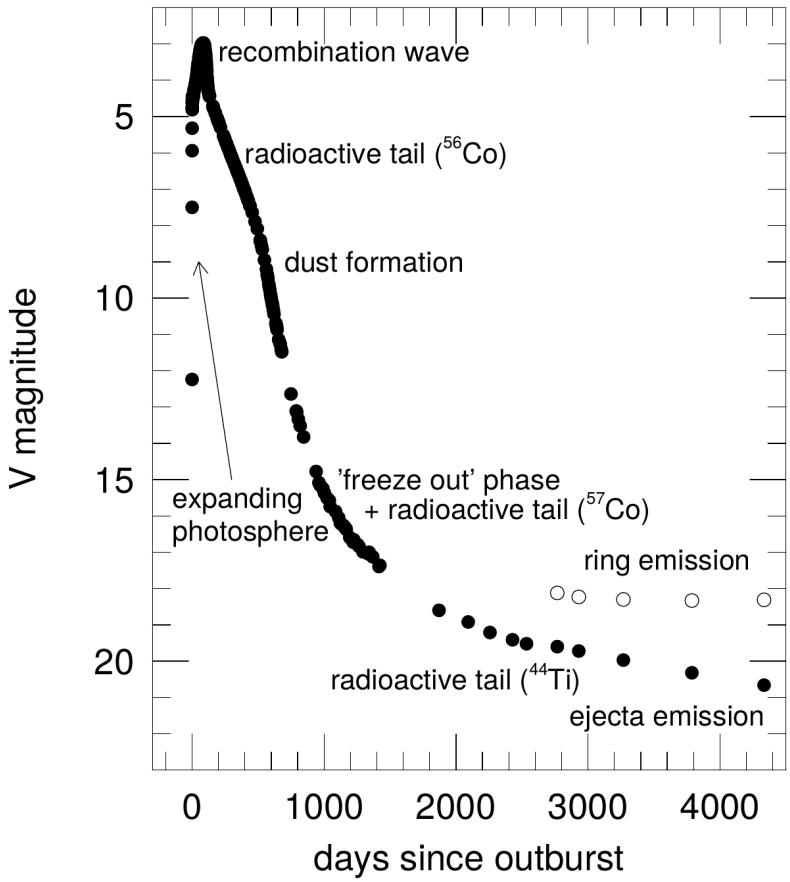

Fig. 1.2.: Apparent V light curve of SN 1987A (figure taken from [19], see also references therein). The different phases in the light curve are labeled. The most important power contribution to the light curve comes in almost all cases from the radioactive decay of material that has been synthesized during the explosion. The major contribution comes from ^{56}Ni, which is the main product of burning to nuclear statistical equilibrium at the temperatures and densities encountered in CCSNe. The half life of ^{56}Ni with respect to decay to ^{56}Co is 6.1 days. Subsequently, ^{56}Co decays with a half life of 77.2 days to ^{56}Fe. The plateau of the light curve after the initial peak is powered by the recombination of the hydrogen that has previously been ionized by the supernova shock [19, 20]. It should be noted that very few objects have been followed beyond about 200 days, a remarkable exception being SN 1987A. Dust formation increased the decline rate of the light curve after about 450 days. After 800 days the light curve flattened due to energy release of recombining ionized matter ("freeze-out"). At later times, the flattening of the light curve is caused by the radioactive decay of long lived ^{57}Co and ^{44}Ti, with a half life of 270 days and 60 year, respectively. Also shown in the figure is the emission of the circumstellar inner ring, which has been ionized by the shock. After about 1500 days the contribution from the ring emission is stronger than the contribution form the SN ejecta itself.

Supernova	SN 1987A (Sanduleak -69° 202)
Progenitor mass [$M_\odot$]	~18-21
Explosion energy [10^{51}erg]	(1.1 ± 0.3)
Ejected mass of ^{56}Ni [$M_\odot$]	(0.071 ± 0.003)
Ejected mass of ^{57}Ni [$M_\odot$]	(0.0041 ± 0.0018)
Ejected mass of ^{58}Ni [$M_\odot$]	0.006
Ejected mass of ^{44}Ti [$M_\odot$]	$(1.5 \pm 0.3) \times 10^{-4}$

Tab. 1.2.: Observational properties of SN 1987A. Even though this SN is often used as a standard case, it is possible that it is in fact a special case. With respect to its light curve, SN 1987A is an extreme case of IIP, the luminosity increased for around 3 months after the collapse and the SN was relatively faint. This is the reason why SN 1987A sometimes also is referred to as type IIF or IIpec [2, 13, 21–24]. The explosion energy is adapted from [21]. The nucleosynthesis yields for SN 1987A are taken from [22] except for ^{58}Ni which is taken from [25] and for ^{44}Ti which is taken from [26]. For ^{58}Ni no error estimates were given.

Another important aspect that is necessary to estimate the observability and the overall impact of SNe on the evolution of galaxies, is SN rates. Figure 1.3 shows the estimated SN rates for different galaxy types given in [27]. The rates depend rather strongly on the galaxy type. For example, in elliptical galaxies, which have a small star formation rate for short-lived massive stars that end their lives with a CCSN, no SN type Ib, Ic, and II have been observed. We show some estimates for the CCSN rate in the Milky Way in table 1.3. The lack of neutrino observations from CCSNe in the Milky Way implies an upper bound of 10 CCSNe per century in our galaxy (at a confidence level of 90%) [28].

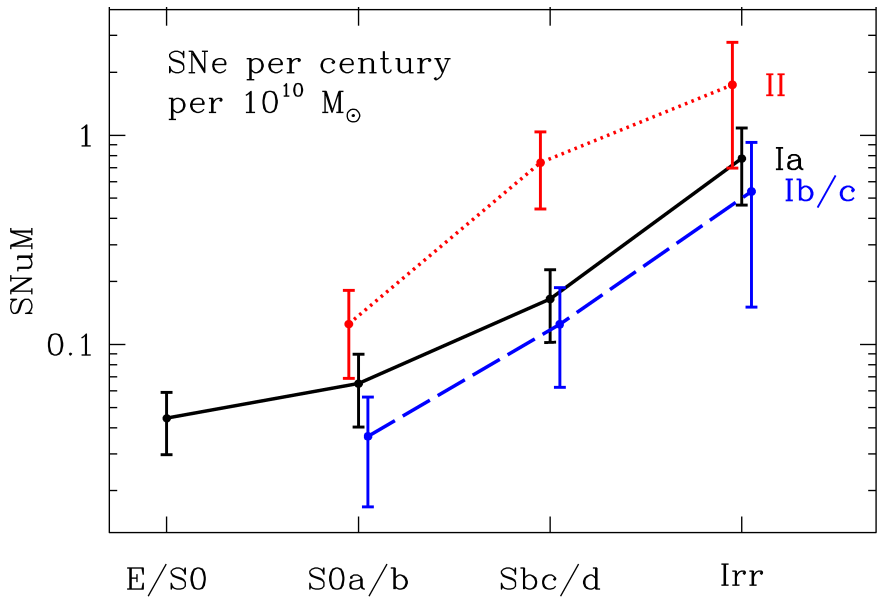

Fig. 1.3.: SN rate normalized to the stellar mass and expressed in SNuM (number of SNe per century per 10^{10} $M_\odot$) as a function of the morphological index (Figure taken from [27]). The lines correspond to type Ia (solid), type II and Ib/c (dotted and dashed), with 1σ error bars. A clear increase of the SN rates from E/S0 (elliptical) to S0a/b (lenticular) to Sbc/d (spiral) to Irr (irregular) can be seen for all the SN types.

SN rate [$10^{-2}y^{-1}$]	Reference (Year)
5.8 ± 2.4	Tammann (1982), [29]
$1.2^{+1.7}_{-0.7}$	Ratnatunga & van den Bergh (1989), [30]
4.0 ± 2.0	Muller et al. (1992), [31]
2.0 ± 1.1	Cappellero et al. (1993), [32]
$2.5^{+0.8}_{-0.5}$	Tammann et al. (1994), [33]
5.7 ± 1.7	Strom (1994), [34]
1.3 ± 0.9	Cappellero et al. (1997), [35]
3.4 ± 2.8	Timmes et al. (1997), [36]
8.4 ± 2.8	Dragicevich et al. (1999), [37]
1.5 ± 1.0	Cappellaro & Turatto (2000), [38]
1-2	Reed (2005), [39]

Tab. 1.3.: Estimated rates of CCSNe in the Milky Way over time [29–39], adapted from [13].

1.2 This Work

The aim of this work is to gain insight on global properties of neutrino-driven CCSNe from numerical simulations. These properties include explosion energy and the amount of ejected matter of certain elements (e.g. ^{56}Ni). In astrophysics, a numerical simulation is an important tool to probe the laws of nature and gain further insight into the physics of the investigated event or scenario. For more than 50 years, physicists tried to understand CCSNe and their possible explosion mechanisms and until today no final answer has been found. These highly complex systems incorporate many branches of physics, such as mechanics, electromagnetism, fluid mechanics, quantum mechanics, nuclear physics and general relativity, which makes them an extremely fascinating subject. We want to find dependencies between CCSN and progenitor properties. We use the parametrized PUSH framework to study the neutrino-driven explosion mechanism in one-dimensional simulations. We introduce the numerical setup of our spherically symmetric simulations in chapter 3. Even though multi-dimensional simulations are the tool of choice to investigate the explosion mechanism of CCSNe, they are not well suited to explore large progenitor samples due to their high computational cost. PUSH on the other hand is well suited to perform such investigations due to its computational efficiency. The two approaches should be used in a complementary way to gain as much insight as possible.

By calibrating the free parameters of the PUSH method to the observational properties of SN 1987A (for a progenitor star in the mass range of 18-21 $M_\odot$) and extending the method with a dependency of one of its free parameters on compactness, we achieve a calibration of PUSH over a wide range of ZAMS masses. We apply the PUSH method to the progenitor sets of Woosley, Heger and Weaver (2002) and Woosley and Heger (2007) [40, 41]. The main focus is directed to the CCSN progenitors with solar metallicity. We also extend the samples to the low metallicity progenitors of [40] to obtain some preliminary results. We discuss the trend of the explosion energy depending on compactness and degeneracies and calibration possibilities for the free parameters of PUSH. In the main part of this thesis, the focus lies on explodability and the investigation of explosion properties of neutrino-driven CCSNe (see chapter 5). We present the results obtained for this study, including the resulting explodability and explosion properties of the investigated progenitors as a function of ZAMS mass or compactness, respectively. Furthermore, the resulting neutron star and black hole birth mass distributions that are obtained from our predicted progenitor-remnant connection are presented. In the last part, we compare three-dimensional ELEPHANT simulations with a similar numerical setup with PUSH. Such a comparison can be used to improve the parametrized method (see chapter 6).

A systematic study with PUSH can be used to learn more about the progenitor-remnant connection of CCSNe and the ejected nucleosynthesis yields that contribute to the chemical evolution of galaxies.

2 Core-Collapse Supernovae

> *Problems worthy of attack prove their worth by fighting back.*
>
> **— Piet Hein**

Core-collapse SNe (CCSNe) have been studied for many years and the exact mechanism behind the explosion is still not fully understood. This chapter is an overview of this phenomenon and the physics that play a role in these extremely energetic and fascinating events.

CCSN explosions are among the most energetic events in the universe. They mark the end of the life of massive stars and at the same moment, depending on the exact cause and series of events during the explosion, also give birth to either a neutron star or a black hole. Stars are essentially gas clouds that, through nuclear burning, fuse lighter elements into heavier ones as they evolve. In the short moments leading up to their death and, thereafter, the extreme conditions that are reached in terms of density, temperature and entropy, enable the fusion of nuclei up to the iron peak, the group of elements with the highest binding energy. Depending on the exact conditions that are reached in the ejected material, also several heavier elements can be created. By means of the matter that the stars eject back into the interstellar medium, they eventually contribute to the chemical evolution of the universe. This synthesis of elements in stars was first proposed in the historical paper by Burbidge, Burbidge, Fowler and Hoyle [42]. Stars come in many sizes and, depending on their initial mass at the beginning of hydrogen burning (the ZAMS mass) they will live different amounts of time and end their lives in different ways.

Relatively light stars, with initial masses $\lesssim 8M_{\odot}$, end their life as carbon-oxygen white dwarfs, compact objects that support themselves against gravitational collapse by means of the pressure of degenerate electrons. These stars formed stable carbon-oxygen cores

during stellar nuclear hydrogen and helium burning. When a white dwarf exceeds its Chandrasekhar mass limit its life ends with a type Ia SN. In the mass range of $8-10M_{\odot}$, the final fate of stars is less certain since this mass region marks a transition region between thermonuclear and CCSN explosions. Stars in this mass range form an oxygen-neon-magnesium core. The core of such a star either undergoes a collapse or it becomes an oxygen-neon-magnesium white dwarf

Stars with masses $\gtrsim 10M_{\odot}$ are massive enough to evolve past the H- and He-burning stages and proceed further with nuclear burning processes, eventually forming a central iron core. By the end of their hydrostatic burning phase, they have formed an onion-like structure where the different layers of elements are roughly sorted by their mass number due to gravitation (see also figure 2.3). Once the central core consists of iron where the binding energy per nucleon has its maximum, further burning would not release but consume energy. CCSNe occur at the end of the evolution of such massive stars. The process of core collapse begins when the central iron core of the star, which is still growing during silicon shell burning, approaches the Chandrasekhar mass limit. At this point in the evolution of the star its core can no longer withstand gravity and starts to collapse. The available gravitational binding energy being released when the core collapses and forms a compact object is given by [43]

$$\Delta \mathrm{E_B} \sim \frac{GM_{\mathrm{core}}^2}{R} = 3\times 10^{53}\left(\frac{M_{\mathrm{core}}}{M_{\odot}}\right)^2\left(\frac{R}{10\mathrm{km}}\right)^{-1}\mathrm{erg}. \tag{2.1}$$

Most of the energy is radiated away by the emission of neutrinos and only $\sim 1\%$ of the gravitational binding energy contributes to the kinetic energy of the ejecta of the explosion ($\sim 10^{51}$ erg). The exact nature of the mechanism that converts a small amount of gravitational energy to enable a successful CCSN is not yet fully resolved and several mechanisms like the neutrino-driven, the magneto-rotational, and quark phase transition are subject of ongoing research (see e.g. [44–46] and references therein). In the following chapters we will cover the contemporary understanding of the so called neutrino-driven mechanism, where neutrinos emitted from the newly born PNS deposit energy behind the shock and enable successful explosions.

Figure 2.1 gives a first qualitative overview of the possible fates of massive stars at the end of their lives [18]. Note that this figure does not contain the newest insights on the topic and is intended as an example. We can see that the fate and remnant of a star also can depend on its metallicity, e.g. a star with higher metallicity loses more material during its life due to wind loss, and can then be less likely to form a BH (or forms a less massive BH in the case of a failed SN or collapse).

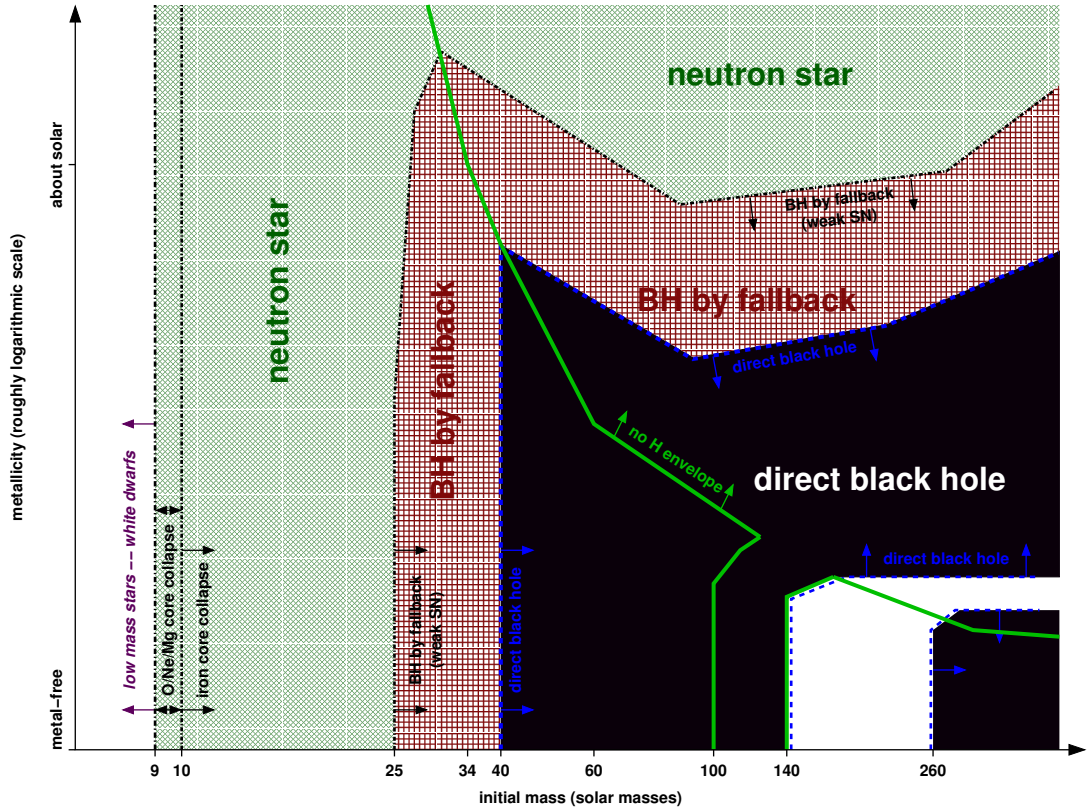

Fig. 2.1.: Qualitative SN remnants of non-rotating massive single stars as a function of initial stellar mass (ZAMS mass) and metallicity (figure taken from [18]). The line marked with "no H envelope" differentiates stars that keep their hydrogen envelope during their hydrostatic burning lives from stars that lose their hydrogen envelope (see also section 2.1 for an overview of the different shell and core masses for progenitors from [40, 41]). The line marked with "direct black hole" indicates the border of the direct black hole forming regime. The direct black hole regime (black) has a gap where pair-instability SNe, which leave behind no remnant, take place (white). Outside of the direct black hole regime are the black hole by fallback (red) and the neutron star regimes (green), where black holes and neutron stars are the possible remnants, respectively. In the low mass regime it is shown that there is a transition between iron core collapse and oxygen-neon-magnesium core collapse. At even lower masses no CCSN takes place (dashed lines, lower left). In this regime a white dwarf is the compact remnant of the star.

2.1 Progenitors of Core Collapse Supernovae: Stellar Evolution of Massive Stars

> *He not busy being born is busy dying*
>
> **— Bob Dylan**
> It's Alright, Ma (I'm Only Bleeding)

This section gives a short overview on the possible progenitors of CCSNe. The lives of massive stars with initial masses bigger than $\sim 8 M_\odot$ are terminated in an explosive event that is called a CCSN, which leaves behind a neutron star or a black hole as a remnant. Before this final stage of a massive star's live takes place, it evolves through the different thermonuclear burning phases that are initiated at its birth on the zero age main sequence (ZAMS). Thermonuclear burning is the main source of energy that provides the internal pressure to oppose the gravitational force on the stellar matter. To be precise, radiation pressure and thermal pressure determine a star's stability during the majority of its life. In the later stages of stellar evolution, when the central density increases, electron degeneracy pressure starts to dominate. Stable burning conditions are attained when the energy generation rate is equal to the energy loss of the star due to emission of photons and neutrinos. The main exothermic nuclear reactions, which produce the energy in the different burning stages, are the fusion of ^{4}He, ^{12}C, ^{20}Ne, ^{16}O and ^{28}Si [1, 47]. Stellar burning starts with hydrogen burning, where hydrogen is fused to helium. Typical temperatures and densities of this burning phase are $T = (0.1 - 0.2)$GK and $\rho = 3 \times 10^2 - 10^4 \mathrm{g\,cm^{-3}}$ [47]. Once a hydrostatic burning phase has exhausted it's primary fuel, the star contracts and heats up, eventually igniting the next burning stage. Thus, the following nuclear burning stages proceed at successively higher temperatures and, as a result of the contraction, higher densities. In each burning stage the Coulomb barriers of the contributing nuclei have to be overcome. The only exception is neon burning, as the photodisintegration of neon, $^{20}\mathrm{Ne}(\gamma,\alpha)^{16}\mathrm{O}$, is triggered before oxygen burning can be established. The ashes of silicon burning are the iron group elements and they form the iron core of the star. Silicon burning marks the last possible hydrostatic burning phase of a massive star because the exothermic fusion of elements in stars stops with the formation of iron group nuclei, the nuclei with the highest binding energies per nucleon (see figure 2.2). At this point the stellar core has no further sources of nuclear energy left and grows in mass as it accumulates the ashes of the surrounding burning shells. Figure 2.3 illustrates this "onion shell" structure of a massive star at the end of its life.

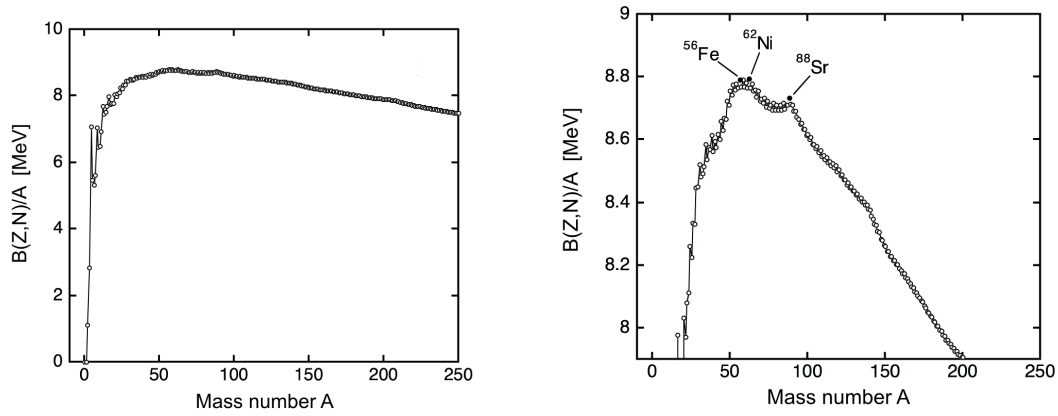

(a) Experimental binding energies per nucleon of the most stable nuclei for each mass number

(b) Zoom showing the binding energies per nucleon in the region of the iron peak nuclei. The strongest bound nuclei are ^{56}Fe, ^{58}Fe and ^{62}Ni

Fig. 2.2.: Binding energy B plotted against atomic mass number [3, 48, 49]. Figures taken from [3].

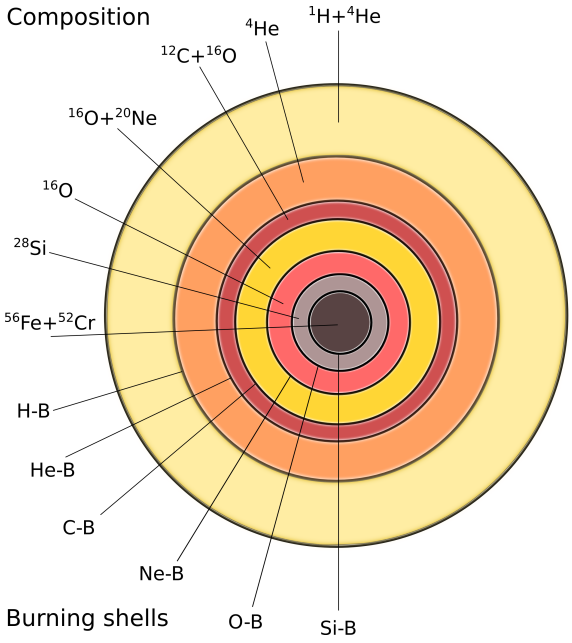

Fig. 2.3.: Onion structure of a massive presupernova star (not to scale). The labels on the upper half show the one or two most abundant nuclear species (also other species are present) that are present in each region (according to [50] see also [3]). The lower half labels show the nuclear burning shells. For example, "H-B" stands for hydrogen burning. Nuclear reactions are very temperature dependent and nuclear burning takes place in relatively thin shells at the interfaces between different compositions. Figure adapted from [3].

Massive stars spend about 90% of their life in the hydrogen and helium burning stages, which correspond to several millions of years [3]. During these burning phases convection and radiation transport dominate the cooling of the star and therefore set the timescales on which energy is transported. The advanced burning stages beyond helium burning have a significant smaller timescale. Silicon burning for instance has a timescale of the order of weeks. When the central temperature of the star exceeds ~ 0.5GK neutrino losses from pair annihilation set the timescale of the energy evolution in the system [40]. The reason for this difference in timescales is due to neutrinos leaving the star immediately as soon as they are created, which leads to a highly increased neutrino luminosity. Thus, in the later burning stages the energy generated by nuclear reactions and gravitational contraction equal the neutrino losses. In table 2.1 we give an overview of the evolutionary burning phases and their characteristic quantities for a $20M_{\odot}$ star. The progenitor structure of stars with different metallicities and ZAMS mass at the onset of collapse is shown in figure 2.4 (data from [40, 41])[1]. These figures illustrate the uncertainties in wind losses and the dependence of the progenitor structure on metallicity.

Burning Stage	ρ_c [g cm^{-3}]	T_c [GK]	τ [yr]	L_γ [erg/s]	L_ν [erg/s]	Primary Reactions
Hydrogen	5.6	0.040	1×10^7	2.7×10^{38}	-	CNO cycle
Helium	9.4×10^2	0.19	9.5×10^5	5.3×10^{38}	$< 10^{36}$	triple α
Carbon	2.7×10^5	0.81	3.0×10^2	4.3×10^{38}	7.4×10^{39}	$^{12}C+^{12}C \rightarrow ^{20}Ne + \alpha$
Neon	4×10^6	1.7	0.4	4.4×10^{38}	1.2×10^{43}	$^{20}Ne+\gamma \rightarrow ^{16}O+\alpha$
Oxygen	6×10^6	2.1	0.5	4.4×10^{38}	7.4×10^{43}	$^{16}O+^{16}O \rightarrow ^{28}Si + \alpha$
Silicon	4.9×10^7	3.7	0.01	4.4×10^{38}	3.1×10^{45}	$^{28}Si+7\alpha \rightarrow ^{56}Ni$

Tab. 2.1.: Stellar Burning Stages for a 20 $M_{\odot}$ star (Table adapted from [7, 51]), where ρ_c and T_c denote the core density and core temperature. The quantities τ, L_γ and L_ν denote the time scale of the process and the corresponding photon and neutrino energy luminosities. The last column gives the primary burning reaction of the corresponding burning stage. Note that the duration of the different burning stages ranges from millions of years to days.

[1] The iron core mass is defined as the layers with an electron fraction $Y_e < 0.495$, the carbon-oxygen core mass is given by the enclosed mass with a helium mass fraction $X_{He} < 0.2$ (i.e., up to the beginning of the helium shell), and the helium core mass is given by the mass regions with a hydrogen mass fraction $X_H < 0.2$ (i.e. up to the beginning of the hydrogen shell).

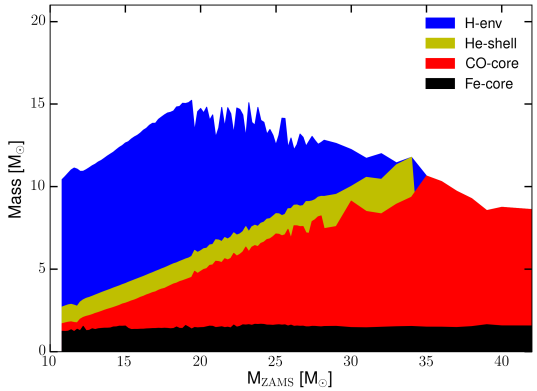

(a) Progenitor structure of stars with solar metallicity. Progenitors from [40]

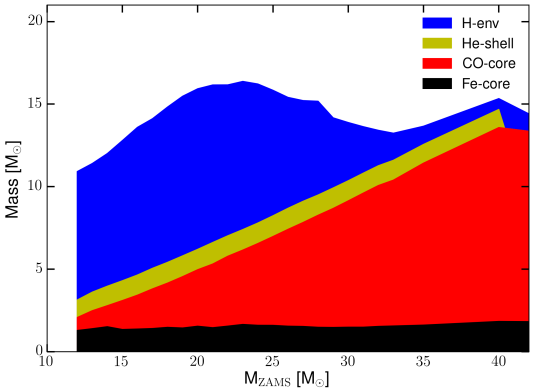

(b) Progenitor structure of stars with solar metallicity. Progenitors from [41]

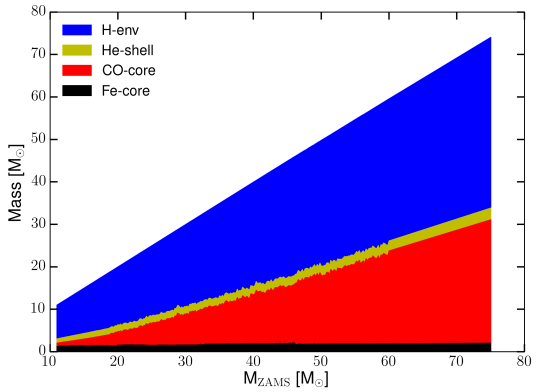

(c) Progenitor structure of stars with metallicity $Z = 10^{-4} \times Z_{\odot}$. Progenitors from [40]

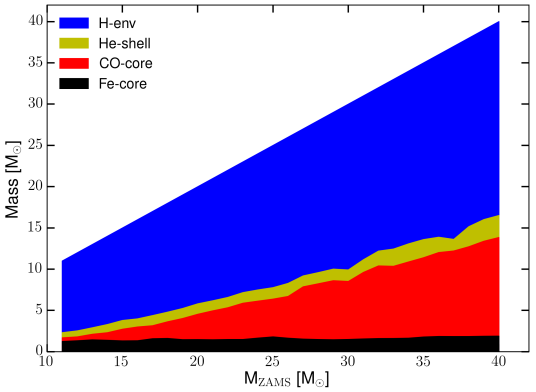

(d) Progenitor structure of stars with metallicity $Z = 0$. Progenitors from [40]

Fig. 2.4.: A comparison of different progenitor sets of non-rotating single massive stars with respect to metallicity (a,c and d) and between different sets with the same metallicity (see a and b) [40, 41]. The low metallicity progenitors experience almost no mass loss during their lives and as a result keep most of their H- and He-envelopes. The plots show the Fe-core, the CO-core as well as the He-envelope, H-envelope and the total mass of the star. The different contributions to the total mass are denoted by $M_{\mathrm{Fe-core}}$, $M_{\mathrm{CO-core}}$, $M_{\mathrm{He-env}}$ and $M_{\mathrm{H-env}}$.

2.2 Core-Collapse

A CCSN begins when the iron core of the star starts to collapse. During the silicon burning phase, at the end of the hydrostatic stellar life, the iron core constantly grows in mass. Consequently, the gravitationally induced contraction becomes stronger and increases the compression of the stellar core. At this stage the pressure that keeps the star from collapsing is provided by degenerate electrons. At first, these electrons are non-relativistic but, due to compression, the central density of the core becomes so high that the relativistic regime is reached. The degeneracy pressure of relativistic electrons is given by [43]

$$P_e \sim \left(Y_e \rho\right)^{4/3}, \tag{2.2}$$

where $Y_e = n_e/\rho N_A$ is the electron fraction per baryon, n_e is the electron number density, and ρ denotes the density. With increasing core density, the resulting Fermi energy $E_F \sim n_e^{\frac{1}{3}} \sim \left(Y_e \rho\right)^{\frac{1}{3}}$ of the electrons grows and drives electron captures on free protons and nuclei [47]

$$\begin{aligned} e^- + p &\rightarrow n + \nu_e, \\ e^- + (Z, A) &\rightarrow (Z-1, A) + \nu_e, \end{aligned} \tag{2.3}$$

where A is the nucleon number and Z the proton number of the corresponding nucleus. Since neutrinos can escape freely in this stage these reactions cause a reduction of the electron fraction Y_e and a decrease of the degeneracy pressure provided by the electrons. Eventually, the mass of the Fe-core exceeds the Chandrasekhar mass limit, which is given traditionally in the form [1, 52][1]

$$M_{CH} \approx M_{CH,0} = 5.83\, Y_e^2 \mathrm{M}_\odot. \tag{2.4}$$

A gas of relativistic electrons and nuclei, with a mass that exceeds M_{CH}, has no stable configuration. The degeneracy pressure can no longer withstand the inward gravitational force and the stellar core starts to collapse. This collapse can only be stopped when the nuclear interaction becomes repulsive, which happens only when matter gets compressed to a degree that densities reach and exceed nuclear densities. Any further compression is resisted by the repulsive component of the strong interaction. Thus, the collapse can only be stopped once the nuclei of the core form nuclear matter [1, 2]. A more precise expression for the Chandrasekhar mass limit that takes into account the

[1] As an example, for an electron fraction of $Y_e = 0.5$ this equation yields $M_{CH} \approx 1.458 \mathrm{M}_\odot$.

thermal structure of the core, in particular that the entropy of the core is non-zero, is given by ([40] and references therein)[1]

$$M_{CH} = M_{CH,0} \times \left[1 + \left(\frac{s_e}{\pi Y_e}\right)^2\right]. \tag{2.5}$$

The variable s_e denotes the electronic entropy per baryon in units of the Boltzmann constant k_B, and its values typically vary between 0.4 in the center and 1 at the edge of the iron core of a 15 $M_\odot$ star at the time of collapse. The collapse of the core is accelerated by two processes. First, the contraction of the iron core increases the density further, this leads to higher electron Fermi energies and as a result more electron captures occur. This is also called "neutronization" of the core. The neutronization is mainly driven by electron captures on protons and on iron group nuclei. See table 2.2 for the neutronization thresholds (Fermi energies of the electron: $E_F \equiv m_e c^2 + \text{threshold}$) for protons and $^{56}_{26}$Fe. Due to the electron loss the electron pressure decreases and the collapse accelerates. Second, at sufficiently high temperatures thermal radiation becomes energetic and

Reaction	Neutronization Threshold [MeV]
$e^- + {}^1_1\mathrm{H} \rightarrow \mathrm{n} + \nu_e$	0.782
$e^- + {}^{56}_{26}\mathrm{Fe} \rightarrow {}^{56}_{25}\mathrm{Mn} + \nu_e$	3.695

Tab. 2.2.: Neutronization thresholds from [43, 53]. The electron rest mass energy, $m_e c^2 \simeq 0.511$MeV, has been subtracted. The reactions listed here correspond to the reactions of equation (2.3).

intense enough that the iron peak nuclei are photodisintegrated [43]:

$$\gamma + {}^{56}\mathrm{Fe} \rightarrow 13\alpha + 4n, \tag{2.6}$$

$$Q = (13m_\alpha + 4m_n - m_{Fe})\, c^2 = 124.4\text{MeV},$$

where Q is the energy required for this process (Q-value of the reaction). These reactions remove thermal energy, in the form of binding energy, from the core that could have provided thermal pressure against the collapse. When the reaction given in equation (2.6) is in equilibrium, the resulting composition of the core can be obtained from the condition for nuclear statistical equilibrium (NSE)[2]. As the stellar core collapses on the free-fall timescale, $t_{\mathrm{ff}}(r) \sim 1/\sqrt{G\langle\rho(r)\rangle}$ (where $\langle\rho(r)\rangle$ is the average density of the enclosed mass

[1] As an example, with rough estimates for the electron fraction and the electronic entropy at the onset of collapse of $Y_e \simeq 0.45$ and $s_e \simeq 0.7$ one gets an effective Chandrasekhar mass of the iron core of $M_{CH} \simeq 1.47 M_\odot$.

[2] See section 2.5

at radius r), the density of the core steadily increases and the mean free path of the neutrinos becomes progressively smaller [43]. The proportionality of the infall velocity to the free-fall timescale indicates that the core collapses while the outer layers remain approximately unmoved since the average density decreases with the radius. Each neutrino emission process (see equation (2.3)) has a corresponding inverse process, an absorption process. At a certain point absorption and scattering of neutrinos make it impossible for them to escape freely from the collapsing core at the speed of light and they start to diffuse out on a longer (diffusion) timescale. The most important processes that contribute to the coupling between neutrinos and matter are ([14, 43] and references therein):

(1) Free nucleon scattering: $\nu + n \rightarrow \nu + n, \quad \nu + p \rightarrow \nu + p$

(2) Coherent scattering by heavy nuclei: $\nu + (Z, A) \rightarrow \nu + (Z, A)$

(3) Nucleon absorption: $\nu_e + n \rightarrow p + e^-$

(4) Electron neutrino scattering: $\nu_e + e^- \rightarrow \nu_e + e^-$.

The first two reactions take place by the exchange of a Z boson and are thus neutral current reactions. Furthermore, coherent scattering by heavy nuclei scales as A^2 rather than as A (A being the atomic mass), which would have been the case for incoherent scattering. Nucleon absorption is a charged reaction and is mediated by the W bosons. Neutrino electron scattering has charged and neutral current contributions. This scattering process can lead to appreciable neutrino-energy loss and is thus believed to be quite important in thermalizing the neutrinos. Once the mean free path of the neutrinos gets significantly smaller than the radius of the iron core and the diffusion timescale of the neutrinos is bigger than the collapse timescale, the neutrinos are considered to be trapped [1]. The trapping of the neutrinos in the core occurs when the densities reach $\sim 10^{11} - 10^{12}\text{gcm}^{-3}$. This causes most of the neutrinos produced from electron captures to remain inside of the core. They establish thermal- and β-equilibrium with matter and the lepton fraction stays constant $Y_L = Y_e + Y_{\nu_e}$, so that the collapse proceeds adiabatically[1] [43]. In this stage, the chemical potentials of protons, neutrons, electrons and neutrinos fulfill the relation,

$$\mu_p + \mu_e = \mu_n + \mu_{\nu_e}, \tag{2.7}$$

where μ stands for the chemical potential of the particles (e^-, p, n, ν) [43, 47] and the neutrino distribution approaches an equilibrium Fermi-Dirac form. The radius inside of

[1] Due to trapping, neutrinos cannot stream out of the core immediately. Thus, the huge amount of liberated gravitational binding energy must therefore be converted into other forms of internal energy (e.g., thermal energy, energy of excited nuclear states, kinetic bounce energy, and neutrinos) and can not be immediately released in the form of neutrinos

the star, from where the neutrinos can stream freely to infinity is called neutrino sphere. It is located where the optical depth of the neutrinos

$$\tau(R, E_\nu) = \int_R^\infty \frac{dr}{\lambda_\nu} \tag{2.8}$$

is equal to $\tau(R_\nu, E_\nu) = 2/3$ (see [1] and references therein). Here, λ_ν is the mean free path of the neutrinos, R_ν the radius of the neutrino sphere and E_ν denotes the energy of the neutrinos. Note that neutrinos with different energies have different neutrino spheres. In between the region of trapped neutrinos and the neutrino sphere the neutrinos do not escape freely but diffuse out on a longer timescale.

At this point the collapse can be divided in two parts. The collapse of the inner part of the core will be homologous [1, 43, 54], where the velocity of the infalling matter is proportional to the radius, $v_r \propto r$, and smaller than the local speed of sound[1]. Homologous means similar to itself, hence the distribution of density and temperature remains similar to the initial profile (at the onset of collapse) during the collapse, and only the scale changes in time [1, 43]. In the outer part, matter is falling in supersonically with velocities that are proportional to the free fall velocity ($v_r \propto 1/\sqrt{r}$). The inner and the outer part of the core are connected by the sonic point, where the speed of sound is equal to the speed of the infalling matter. A sound signal from the inner core can not get past the sonic point because beyond the sonic point the matter in which the sound wave propagates falls in faster than the wave is transmitted.

2.3 Bounce and Prompt Shock

When the center of the core exceeds nuclear densities, $\rho_{\text{nuc}} \sim 10^{14}\text{g cm}^{-3}$, nuclear forces cause the equation of state to stiffen, ultimately stopping the collapse and leading to a bounce of the core. The information of the halt of the collapse and the bounce of the collapsing core initially can not get outside the sonic point, which separates the inner and the outer core (see above), and the outer regions of the star keep falling in. In the center the abrupt end of the collapse forms a pressure wave that propagates to the sonic point where it eventually turns into a shock. The core bounce and the formation of the prompt shock initialize the disruptive event known as a CCSN explosion. After bounce, the inner core of the star settles into hydrostatic equilibrium, forming a proto neutron star (PNS), while the shock propagates outward through the outer iron core, which is still

[1] The homologous inner core has an estimated size of about $M_{\text{hc}} \sim (0.6 - 0.8)M_\odot$ and is roughly proportional to Y_e^2 [43, 54]

collapsing. As the infalling unshocked matter (with velocities proportional to the free fall velocity) reaches the shock front, it is abruptly decelerated. In the shock, the entropy increases[1]. Below the shock, the matter falls much more slowly onto the PNS, which accretes the infalling matter. Consequently, the PNS develops a structure that consists of an unshocked core, with a radius of the order of 10 km, and a shocked mantle, with a radius of about 100 km. Thereby, the PNS has a density of the order of $\rho_{\mathrm{nuc}} \sim 10^{14}\,\mathrm{g\,cm^{-3}}$ in the unshocked core. At entropy values of $s \sim 3k_{\mathrm{B}}$/baryon behind the shock, nuclei dissociate into protons and neutrons. The dissociation of heavy nuclei is an endoenergetic process and it costs about 8.8 MeV per nucleon and drains the shock's energy ([1] and references therein). As a result, the material behind the shock wave mainly consists of free nucleons. This change in composition leads to a high electron neutrino production via electron capture on free protons, which are then transformed into neutrons, behind the shock. These neutrinos cannot escape freely because the matter is still dense and opaque to them, until the shock reaches the neutrino sphere (at densities of $\sim 10^{11}\,\mathrm{g\,cm^{-3}}$). As the shock wave moves through the electron neutrino sphere a neutrino burst is emitted (see figure 2.5). The peak luminosities of this neutrino burst are of the order of $10^{53}\,\mathrm{erg\,s^{-1}}$ and remain for several ms. As the neutrinos escape fast, the now free phase space is refilled and the present matter deleptonizes quickly. The combined energy loss of the shock wave due to photodissociation of heavy nuclei and neutrino emission weakens the shock considerably (about 1.5×10^{51} erg are drained from the shock for each $0.1\mathrm{M}_{\odot}$ of photodissociated material). In the standard CCSN scenario today, this prompt shock is not energetic enough to disrupt the star and it eventually stalls[2]. The stalled shock turns into a standing accretion shock (SAS) at a radius of a few 100 km [44, 55]. Thus, a different mechanism is needed to replenish the energy of the shock, revive it, and eventually form a successful CCSN.

[1] For weak shocks the entropy increase is $\Delta s \simeq \frac{\gamma(\gamma+1)}{12}\left(\frac{v_r}{c_s}\right)^3$, where the adiabatic index is roughly $\gamma = 4/3$ when the shock is formed (see also above) [1].

[2] For some time it was believed that the bounce shock has enough energy to go through the entire star and directly disrupt it (prompt shock explosion [40]). Today it appears that the energy available to the prompt shock is not sufficient, ruling out the prompt shock mechanism.

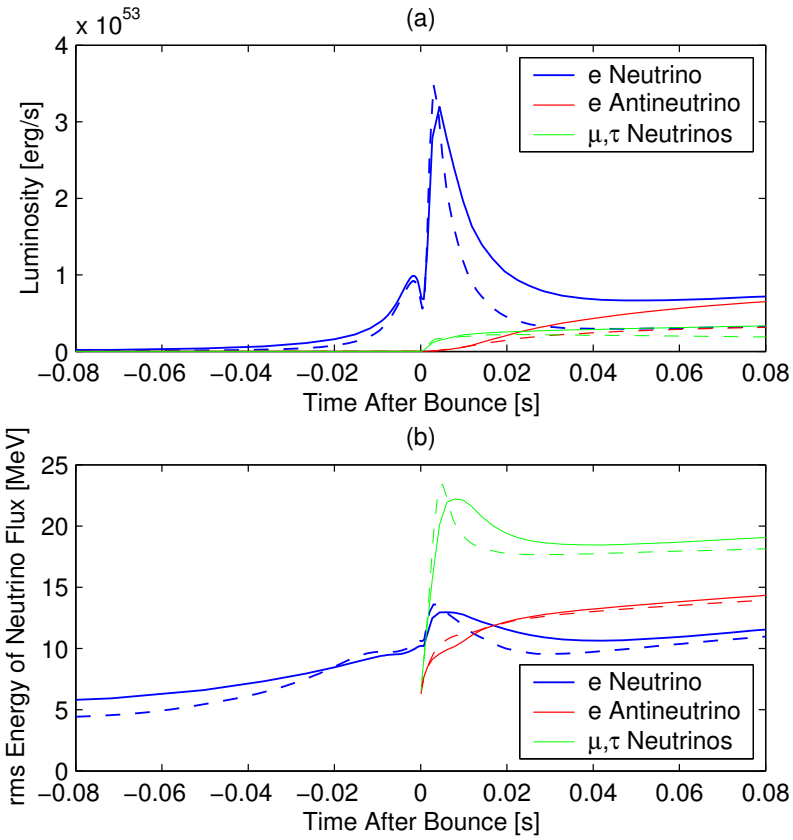

Fig. 2.5.: Temporal evolution of the neutrino luminosities and rms energies obtained from numerical simulations with AGILE-Boltztran (figure taken from [56]). The dashed lines represent the results of a 13 $M_\odot$ model and the solid lines represent the results of a 40 $M_\odot$ model. The blue line belongs to the electron neutrino, the red line to the electron antineutrino, and a green line to the μ- and τ-neutrinos. The luminosities are sampled at a radius of 500 km. The rms energy of the neutrino flux was calculated at the same radius. Both progenitors show a comparable neutrino burst with a peak height of 3.5×10^{53}ergs s^{-1}. Note that significant differences appear in later phases. The accretion-dominated electron flavor luminosities are determined by the variations in the density profiles in the outer layers of the two models. When the bounce shock propagates outward (a period of ~4 ms after bounce), the neutrino luminosity decays to a 30% lower level due to a decrease in the free proton fraction when the shock is formed and the fact that the shock condenses previously still neutrino emitting material to more neutrino opaque densities as it is running out.

2.4 Core-Collapse Supernova Explosion Mechanism

> *These violent delights have violent ends*
> *and in their triumph die, like fire and powder,...*
>
> — **William Shakespeare**
> Romeo and Juliet

The exact physical mechanism behind a CCSN explosion is still not known with certainty. The CCSN mechanism that is currently thought to be able to revive the shock after it has stalled, is the energy deposition by neutrinos that are thermally produced by the PNS and by accretion of matter onto the PNS. Convection below the shock enables more efficient heating by neutrinos, which eventually leads to a successful delayed ν-driven explosion. Note that several possible supernova mechanisms are discussed by astrophysicists. Among them are the neutrino-driven explosion mechanism [44, 45, 57, 58], energy release due to a QCD phase transition in the core from baryonic to quark matter [44, 45, 59, 60], the magneto-rotational mechanism [44, 45, 61, 62], the acoustic mechanism, and the standing accretion shock instability (SASI) [44, 45, 63, 64].

In this work we focus on the neutrino-driven mechanism. The "neutrino-heating mechanism" was first discussed by Colgate and White (1966) [57] and numerically tested by Bethe and Wilson (1985) [58]. In this scenario, the stalled shock can be revived by the neutrino flux coming from the PNS, that deposites some of its energy in the matter behind the shock, on a timescale of ~100 ms after bounce. The revival of the shock by heating of neutrinos ultimately leads to a supernova explosion, leaving behind a neutron star or a black hole as a final remnant. In the following we outline how the stalled shock can be revived in this mechanism. Neutrinos of all flavors are produced in the hot PNS through electron-positron pair annihilation, electron bremsstrahlung, nucleon-nucleon bremsstrahlung, plasmon decay, and photoannihilation. Electron neutrinos and electron antineutrinos are also produced by electron capture and positron capture. In the outer layers of the PNS there is also accretion driven production and emission of neutrinos, until an explosion sets in and the mayor part of the mass shells above the PNS start to move out. The neutrinos that diffuse out of the PNS carry most of the released gravitational energy of the collapsed stellar iron core. Neutrinos can stream out freely once they reach the neutrino sphere (see equation (2.8)), which is inside the mantle of the PNS. There are different energy dependent neutrino spheres for different flavor neu-

trinos[1]. Each neutrinosphere produces a thermal flux of neutrinos of the corresponding flavor and energy. Due to the neutronization of the PNS mantle by the prompt shock, the opacity of electron neutrinos is higher than the opacity of anti-electron neutrinos. Therefore, the ν_e neutrino sphere is further outside than the $\bar{\nu}_e$ neutrino sphere, although they get closer to each other as the PNS contracts.

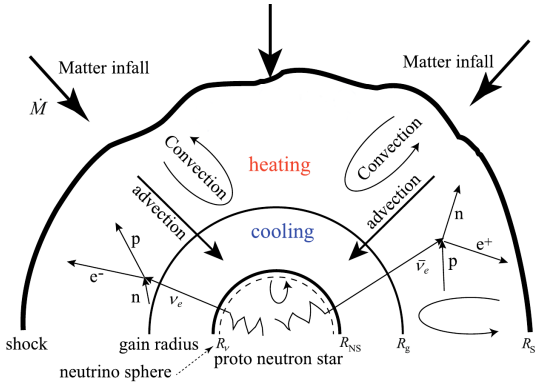

Fig. 2.6.: Schematic that illustrates the situation just before shock revival and supernova explosion in the delayed neutrino driven mechanism. Neutrinos emitted from the PNS heat the matter in the gain region as the outer layers of the star keep falling onto the shock. Convection is increasing the net heating efficiency that on the timescale of $\sim 0.1 - 1$s can lead to a neutrino driven explosion. Figure taken from [65].

In the neutrino-driven mechanism, the deposition of energy is caused by captures of electron neutrinos and electron antineutrinos on nucleons (charged-current reactions)

$$\nu_e + n \rightarrow p + e^-, \tag{2.9}$$

$$\bar{\nu}_e + p \rightarrow n + e^+. \tag{2.10}$$

Figure 2.6 illustrates the stage of the neutrino heating in the gain region where the thermal pressure behind the shock eventually can overcome the ram pressure of the infalling material and revive the shock which can lead to an explosion (delayed neutrino-driven mechanism). The heating of matter by neutrinos behind the shock is occurring in the gain region. At the gain radius R_g which is between the neutrino sphere R_ν and the shock R_s, the temperature gets low enough that the charged-current captures of high energy electron neutrinos and antineutrinos [58, 66] exceed the cooling by neutrino emission. The gain radius is defined as the radius where neutrino cooling equals neutrino heating, which is the case for the radial position where the temperature profile $T(r)$ of the star crosses the temperature values roughly given by $T_g \equiv T_{\text{heating=cooling}}(r) \sim T_\nu (R_\nu / r)^{1/3}$ for

[1]The electron flavor neutrinos can interact with the medium through charged- and neutral-current weak interactions, and the heavy lepton flavor neutrinos can interact only through neutral-current processes.

which heating by neutrinos equals cooling by neutrinos [58, 66–68]. The temperature T_ν denotes the temperature of the neutrino sphere, and R_ν denotes the neutrino sphere radius. This relation follows from the formula for the heating rate by neutrinos evaluated for the case of zero heating (see [58]). Deeper inside the star the neutrino-cooling rate per nucleon (by captures of e^- and e^+ on protons and neutrons) dominates the neutrino heating (mainly caused by absorption of ν_e and $\bar{\nu}_e$ on free neutrons and protons). Furthermore, the gain radius fulfills the relation $T_g^3 R_g \sim \sqrt{L_\nu} \sim \sqrt{4\pi R_\nu^2 T_\nu^4}$ (this also follows from the evaluation of the net heating rate, see [44, 58]). The heating of a mass element in the gain region is dependent on the heating efficiency as well as on the residence time inside the gain region. In multi-dimensional simulations low-entropy bubbles can be accreted from the shock onto the PNS while neutrino-heated matter expands upward. Thus, convection potentially increases the residence time of matter inside the gain region, and, as a result, this matter can be heated for a longer time. In one-dimensional simulations, the residence time of matter inside the gain region is given simply by the time matter needs to be advected from R_s to R_g. Furthermore, when the shock expands in one-dimensional models the neutrino luminosity due to accretion is reduced, which limits possible heating even more. In three-dimensions there are more possibilities for the shock to expand and for matter to be accreted onto the PNS at the same time. Numerical simulations demonstrated that multidimensionality is crucial for the understanding of CCSNe. Hydrodynamic instabilities like convection and standing accretion shock instabilities grow on timescales relevant for the supernova mechanism, and it has been shown that nonradial flows can increase the heating efficiency, and are crucial for a successful explosion (see, e.g., [44, 45] and references therein). Furthermore, with the presently known and accepted standard input physics, energy deposition of neutrinos behind the stalled shock has not proven to be efficient enough in state-of-the-art one-dimensional supernova simulations and therefore does not lead to explosions (e.g., [56]). Thus, the breaking of spherical symmetry due to e.g. convective motion, is seen as crucial and decisive for the success of the neutrino-driven mechanism. Today, the delayed neutrino-driven explosion scenario is believed to be a viable mechanism that enables CCSN explosions.

Next, other explosion mechanisms are briefly discussed. The magneto-rotational mechanism is powered by rotational energy that is converted into pressure via the magnetic field which then leads to an explosion (see, e.g., [44, 45, 61, 62, 69–71]). Crucial for this mechanism is the enhancement of the magnetic field strength during the collapse and in the early post bounce phase due to flux-freezing, the winding up of magnetic field lines, and also the magneto-rotational instability (MRI). The growth of the magnetic field strength in this scenario leads to magnetic pressures ($p_\mathrm{B} = B^2/(8\pi)$) that are comparable to matter pressures. A magneto-rotational mechanism ultimately triggers jet-like explo-

sions along the rotational axis that can reach high explosion energies, reaching even Hypernova levels in the order of ~10 Bethe (1 Bethe is equivalent to 10^{51} erg and can be abbreviated as 1 B). This mechanism, if it reaches the conditions that are necessary for r-process, is believed to be rare and could help to explain the abundance of r-process elements in the early universe [72].

The acoustic mechanism was proposed in the works of Burrows et al. [73, 74] as a new mechanism to trigger CCSN explosions. In the simulations that were performed, which did not explode by neutrino-energy deposition, large dipole (l=1) g-mode oscillations of the PNS core were excited at late times ($\gtrsim$1 s). These excitations are caused by SASI sloshing motions of the post shock layer and by anisotropic accretion downdrafts. PNS vibrations create sound waves that turn into secondary shocks which help to heat the region behind the main shock front. In this mechanism, the vibrating PNS acts as transducer by transforming accretion energy of the infalling material into sound waves. The acoustic mechanism remains controversial as it has not yet been confirmed by other groups. Furthermore, a counterargument to the proposed mechanism has been made in [75].

The QCD phase transition of the PNS from baryonic matter to quark matter, leads to an additional release of (gravitational) binding energy and triggers a second shock wave produced in a bounce. This second shock eventually catches up with the stalled primary shock and leads to an explosion [60, 76]. This mechanism needs an equation of state that also incorporates quarks, which still is not well known.

Until now it is not clearly decided which mechanism (or a combination of them) is the standard case in CCSN explosions. Among other reasons for a lack of convergence, there are still many uncertainties in the input physics, maybe too low resolutions of contemporary state of the art simulations, and effects from the usage of one-dimensional progenitor models as the starting point for multi-dimensional models, which need to be further investigated. Furthermore, recent three-dimensional simulations have revealed new effects such as spiral modes of SASI [77, 78] and a dipolar lepton-number emission self-sustained asymmetry (LESA) [79]. The understanding of these phenomena and their consequences still need further investigations. In the future, three-dimensional simulations that incorporate general relativistic radiation hydrodynamics, sophisticated input physics and are performed at high resolution, might be able to give further insight and help to fully understand the mechanism behind CCSNe. Nevertheless, due to the complexity of the problem, these simulations likely belong to the upcoming sustained exascale era.

2.5 Thermonuclear Reactions: Nucleosynthesis in Core-Collapse Supernovae

The abundance distribution of nuclei that we observe today in the solar system (shown in figure 2.7) consists of products of different physical scenarios and conditions. To understand the origin of the elements one also has to understand the solar abundance distribution. In 1957, Burbidge, Burbidge, Fowler and Hoyle [42] and Cameron [82, 83] proposed

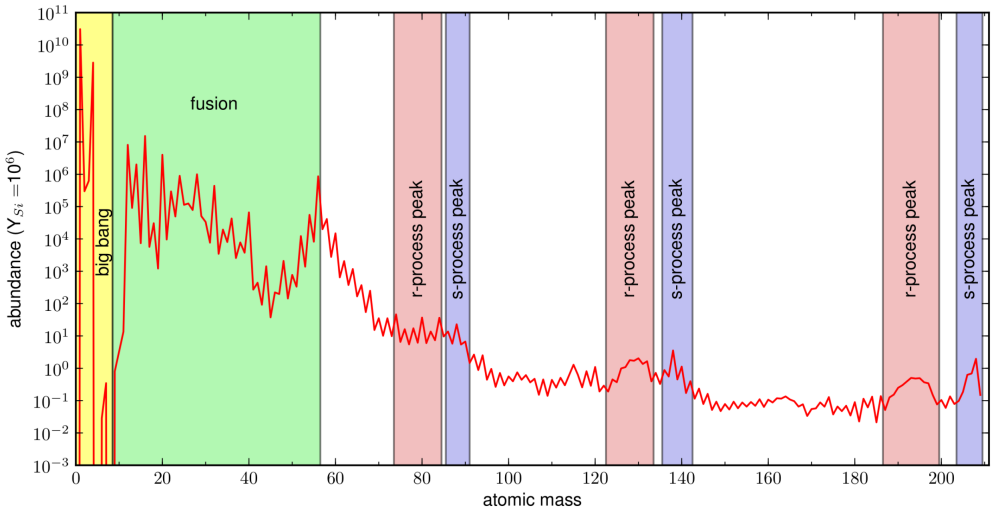

Fig. 2.7.: Solar system abundances with silicon normalized to 10^6 (abundances from [80]). This figure is taken from [81].

how the solar isotopic abundances could be explained. The fusion of elements in stars during their hydrostatic burning processes only explains the nuclear fusion up to the iron group. The heavier nuclei ($A > 60$) are, for the major part, formed by processes involving neutron captures on seed nuclei. The reason for this is that the required temperatures to overcome the Coulomb barriers of heavier nuclei by means of charged-particle reactions are so high that the nuclei would be destroyed by photodissociation instead. Thus, elements heavier than iron must be formed in other scenarios and environments[1].

In this thesis we discuss CCSNe and thus I give a short overview of thermonuclear reactions, explosive burning, and NSE. The intention is to give a basic idea of the involved processes as well as the approximate timescales on which they take place. The timescales

[1] There are two types of neutron-capture processes that are generally believed to occur: the s- and the r-process (slow and rapid neutron capture). These processes are not the topic of this thesis.

of explosive burning are used in the approximative α-network implemented in the PUSH setup (see chapter 3). We first want to introduce expressions and useful concepts that are used in the following descriptions. Matter consisting of a mixture of nuclei of different species i, e.g. in an astrophysical plasma, has a mass density given by $\rho_m = \sum_i n_i m_i$, where n_i is the number density and m_i the mass of a nucleus of species i. The number density of species i, i.e. the number of nuclei i per unit volume, changes due to nuclear reactions but also due to expansion or contraction. A mole of particles of species i has a mass of $M_i = N_A m_i$ grams, where N_A is Avogadro's number. In terms of the atomic mass unit m_u (or u) M_i indicates the relative atomic mass of species i [2, 3, 47][1]. The relative atomic mass is given by [2]

$$M_i = m_i / m_u = (Z_i m_H + (A_i - Z_i) m_n - B_i / c^2) / m_u, \tag{2.11}$$

where A_i denotes the number of nucleons in a nucleus of species i, Z_i the number of protons in a nucleus, m_H is the mass of a hydrogen atom, m_n the mass of a neutron, and B_i the nuclear binding energy of the nucleus i. The mass density is

$$\rho_m = \sum_i n_i m_i = \frac{\sum_i n_i M_i}{N_A}, \tag{2.12}$$

which changes with composition and is not relativistically invariant. Since the number of nucleons is conserved one can use the related quantity,

$$\rho = \frac{\sum_i n_i A_i}{N_A} \tag{2.13}$$

to avoid these difficulties. The fraction of matter of an astrophysical plasma that is represented by nuclei of species i is called the mass fraction $X_i = n_i M_i / (\rho_m N_A)$. These quantities sum up to one, $\sum_i X_i = 1$ (mass conservation). In the same way one can introduce the nucleon fraction, i.e. the fraction of nucleons that are bound in species i,

$$X_i = \frac{n_i A_i}{\rho N_A}. \tag{2.14}$$

If only the changes due to nuclear transmutations are of interest, it is useful to introduce the so called mole fraction (or abundance) of the different species i [2, 3, 47]

$$Y_i = \frac{X_i}{A_i} = \frac{n_i}{\rho N_A} \tag{2.15}$$

a quantity that gives the fraction of species i that is present in a mole of particles of the astrophysical plasma. The equation for charge conservation is $Y_e = \sum_i Z_i Y_i$ (assuming

[1] The atomic mass unit is defined as $m_u = m(^{12}C)/12 = 1/N_A$.

charge neutrality), where Z_i is the number of protons per nucleus of species i and $Y_e = n_e/(\rho N_A)$ the electron fraction. One has to be careful with the usage of the mass fraction since the mass density is strictly speaking not a conserved quantity even if no changes in volume occur. This is due to the fact that nuclear reactions can transform mass in energy and back again. Thus, in order to avoid this difficulty we use the baryon density per mole ρ, as introduced above, since the number of baryons is always conserved in nuclear transmutations.

Particle-Induced Reactions

The nuclear cross section for a reaction of a projectile i with a target nucleus j is defined as [47]

$$\sigma = \frac{\text{number of reactions per target per second}}{\text{flux of projectile particles}} = \frac{\frac{r}{n_j}}{n_i v}, \tag{2.16}$$

with r being the number of reactions per cm^3 and per second, n_i the number density of projectile particles, and n_j the number density of target particles, respectively. The interaction rate between two nuclei of species i and j of the form $i + j \rightarrow n + m$ with number densities n_i and n_j is (in units of reactions per cm^3 and per second) given by

$$r_{ij} = \frac{n_i n_j}{1+\delta_{ij}} \langle \sigma v \rangle_{ij}, \tag{2.17}$$

where δ_{ij} is the Kronecker delta which prevents double counting of reactions between identical particles [3, 47]. The velocity-averaged cross section is given by

$$\langle \sigma v \rangle_{ij} = \int_0^\infty P(v) v \sigma_{ij}(v) dv,$$

where $P(v)$ is the normalized probability distribution function of relative velocities between two reacting particles and σ_{ij} is the cross section for the respective reaction. The probability that the relative velocity of interacting nuclei is in the range of v and $v + dv$ is given by $P(v)dv$. The energy available to nuclei in a stellar plasma is that of their thermal motion. Thus, the reactions triggered by this energy are called thermonuclear reactions. Nuclei in a stellar plasma (with a few exceptions) are non-relativistic and non-degenerate. Therefore, the velocities of nuclei in stellar plasma can be described by a Maxwell-Boltzmann distribution

$$P(v)dv = \left(\frac{m_{ij}}{2\pi kT}\right)^{3/2} \exp\left(-\frac{m_{ij}v^2}{2kT}\right) 4\pi v^2 dv, \tag{2.18}$$

where $m_{ij} = m_i m_j/(m_i+m_j)$ is the reduced mass of the interacting particles [3, 51]. With the relations $E_{ij} = m_{ij}v^2/2$ and $dE_{ij}/dv = m_{ij}v$ we can write the velocity distribution as an energy distribution $P(E_{ij})dE_{ij}$. For the velocity-averaged cross section at given stellar temperature T we get [84, 85]

$$\langle \sigma v \rangle_{ij} = \left(\frac{8}{\pi m_{ij}}\right)^{1/2} \left(\frac{1}{kT}\right)^{3/2} \int_0^\infty E_{ij}\sigma(E_{ij}) \exp\left(-\frac{E_{ij}}{kT}\right) dE_{ij}. \tag{2.19}$$

The number of reactions per nucleus per second (for the reaction $i(j,n)m$) can be written as [47, 84, 85]

$$\lambda_{ij} = -\frac{1}{n_i}\left(\frac{dn_i}{dt}\right)_j \equiv \frac{r_{ij}}{n_i} = \frac{\rho Y_j}{1+\delta_{ij}} N_A \langle \sigma v \rangle_{ij}, \tag{2.20}$$

where λ_{ij} is the interaction rate.

Reactions with Photons, Leptons and Decays

This section will illustrate the way one can assign a decay constant to a reaction rate, $r_{ij} = \lambda_{ij} n_i$, for reactions of nuclei with lighter particles and decays based on the example of reactions with photons. In the case that one of the participating particles is massless or much lighter than the other particle, the relative velocity between the two particles can be approximated by the velocity of the lighter particle which for massless particles as photons or neutrinos is the speed of light c. The reaction $\gamma + j \rightarrow n + m$ is called a photodisintegration for which the number of reactions per cm^3 and second is given by [3]

$$r_{\gamma j} = n_j \int_0^\infty n_\gamma(E_\gamma) c\sigma(E_\gamma) dE_\gamma, \tag{2.21}$$

where the number density of photons in a stellar plasma depends on the temperature and the energy of the photons. We find for the decay constant (probability of decay per nucleus per second) of nucleus j [3, 84]

$$\lambda_{\gamma j} = \frac{1}{\tau_{\gamma j}} = -\frac{1}{n_j}\left(\frac{dn_j}{dt}\right) = \frac{r_{\gamma j}}{n_j} = \int_0^\infty n_\gamma(E_\gamma) c\sigma(E_\gamma) dE_\gamma \tag{2.22}$$

with

$$r_{\gamma j} = \lambda_{\gamma j} n_j, \tag{2.23}$$

where $\tau_{\gamma j}$ is the mean lifetime of the nucleus j with respect to photodisintegration. According to Planck's radiation law the energy density of electromagnetic waves with frequencies in the interval $[\nu, \nu + d\nu]$ at a given temperature T is given by [3, 47]

$$u(\nu)d\nu = \frac{8\pi h\nu^3}{c^3} \frac{1}{\exp\left(\frac{h\nu}{kT}\right) - 1} d\nu. \tag{2.24}$$

Inserting $E_\gamma = h\nu$ for the photon energy we get the following expression for the number of photons per unit volume in the energy interval $[E_\gamma, E_\gamma + dE_\gamma]$ at temperature T

$$n_\gamma(E_\gamma)dE_\gamma = \frac{u(E_\gamma)}{E_\gamma} dE_\gamma = \frac{8\pi}{(hc)^3} \frac{E_\gamma^2}{\exp\left(\frac{E_\gamma}{kT}\right) - 1} dE_\gamma. \tag{2.25}$$

Eventually we get for the decay constant of the photodisintegration at a given temperature, using equations (2.22) and (2.25)

$$\lambda_{\gamma j}(T) = \frac{8\pi}{h^3 c^2} \int_0^\infty \frac{E_\gamma^2}{\exp\left(\frac{E_\gamma}{kT}\right) - 1} \sigma(E_\gamma) dE_\gamma. \tag{2.26}$$

The reaction rates r_i of processes that deplete species i involving leptons and decays have a similar dependence on a decay constant. Thus, the number of reactions involving decays or leptons (per cm^3 per second) can also be given by an expression of the form $r_i = \lambda_i n_i$ (to derive these expressions as well goes beyond the scope of this short introductory section, see e.g., [47, 51]).

Reverse Reactions

Not all thermonuclear reactions have to be determined experimentally. The cross sections of a forward reaction $i + j \rightarrow o + m$ and the corresponding reverse reaction over a compound nucleus state J are related to each other by the reciprocity theorem [86]. From this one obtains [3, 47, 84, 86]

$$\frac{\sigma_i(j,o)_J}{\sigma_m(o,j)_J} = \frac{(1+\delta_{ij}) g_o g_m k_o^2}{(1+\delta_{om}) g_i g_j k_j^2}, \tag{2.27}$$

which is also known as detailed balance, where $g_x = 2S_x + 1$ (ground state degeneracy factor), S_x is the spin of the appropriate nucleus ($x = i, j, m, o$), δ_{ij} is the Kronecker delta, and the k_x are the wave numbers. This relation for the cross sections is valid for all individual transitions summed over the compound nucleus states. Using equation (2.19), we

get an expression for the total cross section at energies E_{ij} and E_{om}, with $E_{ij} = E_{om} + Q_{o,j}$, where $Q_{o,j}$ is the Q-value of the reaction $m(o,j)i$, [3, 47, 84]

$$\langle \sigma v \rangle_{ij,o} = \frac{(1+\delta_{ij})}{(1+\delta_{om})} \frac{g_o g_m}{g_i g_j} \left(\frac{m_{om}}{m_{ij}} \right)^{3/2} \exp\left(\frac{-Q_{o,j}}{kT} \right) \langle \sigma v \rangle_{mo,j}. \tag{2.28}$$

Typically, photodisintegration rates are computed from the inverse capture reaction via detailed balance. Using $p_\gamma^2 = E_\gamma^2/c^2$, $g_\gamma = 2$, $E_\gamma = E_{om} + Q_{o,\gamma}$ and with equations (2.28) and (2.26) we obtain

$$\lambda_{i\gamma}(T) = \frac{g_o g_m}{(1+\delta_{om}) g_i} \left(\frac{m_{om} kT}{2\pi\hbar^2} \right)^{3/2} \exp\left(-\frac{Q_{o,\gamma}}{kT} \right) \langle \sigma v \rangle_{m,o,\gamma}. \tag{2.29}$$

These relations between forward and reverse reaction rates assume that the interacting particles are in their ground states. In an astrophysical plasma also excited states are thermally populated. To take this into account we have to replace the g_x with the partition functions [84]

$$G_x(T) = \sum_i g_{x,i} \exp\left(-E_i/kT\right). \tag{2.30}$$

Explosive Burning Timescales

The burning timescales in stellar evolution depend on the energy loss timescales of the stellar environment. During hydrostatic hydrogen and helium burning the energy loss is dominated by the photon luminosity. The stellar matter is in a condition such that the energy generation rates are equal to the radiation losses. In the later burning stages neutrino losses play the dominant role in the cooling process. Thus the burning timescales are determined by temperatures where the energy generation rate is equal to the neutrino losses. Explosive events are determined by hydrodynamic equations and states which provide different temperatures, densities or timescales for the nuclear burning of the present nuclei. The fuels for explosive nucleosynthesis consist mainly of $N = Z$ nuclei (α-particle nuclei) like ^{12}C, ^{16}O, ^{20}Ne, ^{24}Mg, or ^{28}Si (which are the ashes of prior hydrostatic burning), resulting in heavier nuclei (with $N \approx Z$) [47][1]. The burning timescales for the destruction of species i in the corresponding burning phase can be defined as [47] (corresponding to $\tau = 1/\lambda$, see also equations (2.20), (2.29), and (2.26))

$$\tau_i = \left| \frac{Y_i}{\dot{Y}_i} \right|. \tag{2.31}$$

[1] There are two different scenarios of explosive burning that are not discussed in this thesis which are the following. When a large supply of neutrons or protons is available the r- or rp- process takes place and nuclei close to the neutron or proton drip line can be produced.

Where the timescales of explosive burning for the fuels i (which are H, ^{4}He,^{12}C, ^{20}Ne, ^{16}O, and ^{28}Si) are determined by the major destruction reaction. All of these timescales are temperature dependent. In addition, the timescales of fusion reactions also depend on the density. The Ne- and Si-burning stages are dominated by (γ,α) destructions of ^{20}Ne and ^{28}Si. Thus, these burning stages have timescales determined only by the burning temperatures. We get for the timescale of a two-body interaction (see equation 2.20)

$$\tau_i = \left| \frac{Y_i}{(1+\delta_{ij})^{-1}\rho N_A \langle \sigma v \rangle_{ij} Y_i Y_j} \right| = \left(\frac{\rho Y_j}{1+\delta_{ij}} N_A \langle \sigma v \rangle_{ij} \right)^{-1}. \tag{2.32}$$

The timescale of a three-body reaction is given by [51, 85]

$$\tau_i = \left(\frac{N_i}{N_i! N_j! N_k!} \rho^2 N_A^2 \langle \sigma v \rangle_{ijk} Y_j Y_k \right)^{-1}, \tag{2.33}$$

where N_a equals the number of particles of type $a = i, j, k$ involved in the reaction. For a photodisintegration dominated process we obtain the timescale of the reaction with the reverse reaction rate (see equation (2.29))

$$\tau_i = \frac{1}{\lambda_{i\gamma}} = \left(\frac{g_o g_m}{(1+\delta_{om}) g_i} \left(\frac{m_{om} kT}{2\pi\hbar^2} \right)^{3/2} \exp\left(-\frac{Q_{o,\gamma}}{kT} \right) \langle \sigma v \rangle_{m,o,\gamma} \right)^{-1}, \tag{2.34}$$

where the definitions are the same as given above.

Energy Generation in Thermonuclear Reactions

Nuclear processes are closely coupled to the hydrodynamic behavior of the stellar plasma. The release or the absorption of energy due to thermonuclear processes changes the pressure, temperature and the internal energy of the plasma and causes hydrodynamic motions. The induced hydrodynamic motions may influence the continued supply of thermonuclear fuel. The changes in nuclear composition can also change the equation of state and the opacity of the plasma. Thermonuclear reaction rates (abundance changes) define the rate of thermonuclear energy release, $\dot{\epsilon}_{\rm nuc}$ (with units [MeVg^{-1}s^{-1}]). We consider the forward reaction $i + j \rightarrow n + m$ and assume it to be exothermic. The

nuclear energy released per reaction is defined by the Q-value of the reaction, Q_{ij}. The Q-value of a reaction i(j,n)m is defined as

$$\begin{aligned} Q_{ij} &= m_i c^2 + m_j c^2 - m_n c^2 - m_m c^2 \\ &= \left[m_i c^2 + m_j c^2 - m_n c^2 - m_m c^2\right] + \left[A_n m_u c^2 + A_m m_u c^2 - A_i m_u c^2 - A_j m_u c^2\right] \\ &= (M.E.)_i + (M.E.)_j - (M.E.)_n - (M.E.)_m, \end{aligned}$$

where m_i denotes the mass (here m_i is the atomic mass), A_i is the mass number and $(M.E.)_i = (m_i - A_i m_u)c^2$ is the atomic mass excess of species i in units of energy [3]. The energy production per unit mass and unit time is then given by [3]

$$\dot{\epsilon}_{\mathrm{nuc},ij} = \frac{Q_{ij}}{\rho} r_{ij} = \frac{Q_{ij}}{\rho} \frac{n_i n_j \langle \sigma v \rangle_{ij}}{(1+\delta_{ij})}.$$

The energy of nuclei, photons, electrons and positrons produced in the reaction is retained in the plasma. Since neutrinos interact weakly with the bulk medium, they escape from the site of thermonuclear burning. Thus, the neutrinos carry their energy away due to their small cross section and this energy has to be subtracted from the Q-value when calculating the nuclear energy generation. The thermonuclear energy generation rate summed over all reactions can be calculated with [3, 51]

$$\dot{\epsilon}_{\mathrm{nuc}} = \frac{1}{\rho} \sum_{i,j} r_{ij} Q_{ij}. \tag{2.35}$$

Since the thermonuclear energy release is determined only by the abundance changes we ultimately use a different way to express the total rate of thermonuclear energy release (see section 3.1.3).

Nuclear Statistical Equilibrium

For temperatures that exceed $T \geq 3 - 4 \times 10^9$K (≃0.26-0.35 MeV) capture reactions that form heavier nuclei are in competition with the corresponding inverse photodissociation reactions. At such high temperatures eventually the reactions and inverse reactions are sufficiently rapid that an equilibrium is established. Such a situation ultimately leads to a complete chemical equilibrium. For such an equilibrium, also called nuclear statistical equilibrium (NSE) [3, 47], the following relations are valid for each nuclear species

$$(Z_i, A_i) \rightleftharpoons Z_i \,\text{protons} + (A_i - Z_i)\,\text{neutrons}, \tag{2.36}$$

$$\mu_i = \mu_{(Z_i,A_i)} = Z_i\mu_p + (A_i - Z_i)\mu_n, \tag{2.37}$$

where A_i is the number of nucleons in the nucleus, Z_i the number of protons, and μ_i the chemical potential of the nucleus (Z_i, A_i) of species i. Such conditions are achieved during SNe explosions and also in other scenarios where the timescales on which nuclear reactions occur is shorter than the timescale on which the system evolves. For the temperatures and densities involved all nucleons and nuclei are nondegenerate. As a consequence Maxwell-Boltzmann statistics apply and the nucleons and nuclei are described by Maxwell-Boltzmann distributions. Thus, the chemical potentials are given by [47]

$$\mu_i = m_i c^2 + kT\ln\left(\frac{\rho N_A Y_i}{G_i}\left(\frac{2\pi\hbar^2}{m_i kT}\right)^{3/2}\right), \tag{2.38}$$

Inserted in equation (2.37) this yields

$$\begin{aligned}
\mu_i &= kT\ln\left(\frac{\rho N_A Y_i}{G_i}\left(\frac{2\pi\hbar^2}{m_i kT}\right)^{3/2}\right) + m_i c^2 \\
&= Z_i\left[kT\ln\left(\frac{\rho N_A Y_p}{g_p}\left(\frac{2\pi\hbar^2}{m_p kT}\right)^{3/2}\right) + m_p c^2\right] \\
&+ (A_i - Z_i)\left[kT\ln\left(\frac{\rho N_A Y_n}{g_n}\left(\frac{2\pi\hbar^2}{m_n kT}\right)^{3/2}\right) + m_n c^2\right] \\
&= Z_i\mu_p + (A_i - Z_i)\mu_n.
\end{aligned} \tag{2.39}$$

The binding energy of species i is given by

$$B_i = \Delta m_i c^2 = \left[Z_i m_p + (A_i - Z_i)m_n - m_i\right]c^2. \tag{2.40}$$

Together with 2.39 and also using

$$m_p \approx m_n \approx m_u, \quad m_i \approx A_i m_u, \quad g_p = g_n = 2, \tag{2.41}$$

we obtain the following expression for the abundance of species i

$$Y_i = \frac{G_i A_i^{3/2}}{2^{A_i}}\left(\frac{\rho}{m_u}\right)^{A_i-1}\left(\frac{2\pi\hbar^2}{m_u kT}\right)^{3(A_i-1)/2} Y_p^{Z_i} Y_n^{A_i-Z_i}\exp\left(\frac{B_i}{kT}\right). \tag{2.42}$$

In NSE the nuclear abundances can be determined uniquely for a given temperature T, density ρ and electron fraction Y_e with the constraints of mass conservation and charge conservation[1]

$$\sum_i A_i Y_i = \sum_i X_i = 1 \tag{2.43}$$

$$\sum_i Z_i Y_i = Y_e. \tag{2.44}$$

[1]The weak interaction is not necessarily in equilibrium and the change of Y_e due to weak interactions has to be taken into account as well.

3 Numerical Implementation of Parametrized One-Dimensional Core-Collapse Supernova Simulations: The PUSH Method

This chapter gives an introduction to the numerical setup of the PUSH method and the runs that were performed [87, 88]. The aim of PUSH is to provide an efficient parametrized framework that makes it possible to investigate CCSNe in spherically symmetric simulations. Even though multi-dimensional simulations are needed for an accurate investigation of the explosion mechanism they are computationally too expensive for systematic studies that have to be based on a large set of progenitors.

PUSH and other artificial explosion methods are necessary because simulations in spherical symmetry which include detailed neutrino transport and general relativity fail to explode self-consistently, except for the core-collapse progenitors with the lowest masses [89, 90]. One-dimensional simulations show a smaller heating efficiency of electron flavor neutrinos behind the shock due to an absence of convective motion and the inability of an exploding system to further accrete matter onto the central object which would result in additional accretion luminosity. The PUSH method provides extra energy deposition in the heating region by tapping the energy of μ- and τ- (anti)-neutrinos in otherwise consistent spherically symmetric simulations to mimic multi-dimensional effects (e.g., convection, SASI) that enhance neutrino heating (see section 3.2). This enables a consistent evolution of the PNS and treatment of the electron fraction of the ejecta. Also, after the onset of explosion the method also prevents a too strong decrease in ν-heating behind the shock caused by a drop in electron (anti)neutrino luminosity that occurs in spherically symmetric simulations due to drastic reduction of the mass accre-

tion rate onto the PNS. PUSH is well suited to investigate the dependence of explosive nucleosynthesis, the progenitor-remnant connection, and the explosion dynamics and energetics as a function of progenitor properties. Spherically symmetric models of CCSN explosions are still a pragmatic and feasible method to study large numbers of progenitor stars, from the onset of the SN explosion up to several seconds post bounce.

In this chapter we also introduce the tools that have been created in order to analyze these parametrized one-dimensional simulations and e.g. evaluate their explosion energy and create tracer particles for network post-processing analysis (see section 3.3). Furthermore, a description of the launching and managing of hundredths to thousands of runs of different progenitor sets, parametrizations, resolutions and the tools that are involved is given as well (see section 3.4).

The simulations are performed with the general relativistic hydrodynamics code AGILE [91, 92], the neutrino transport scheme IDSA for electron neutrinos [93], and with an implementation of the advanced spectral leakage (ASL) scheme to treat the μ- and $\tau-$neutrinos [94] (see sections 3.1.1 and 3.1.2). The equation of state (EOS) that we use for matter in NSE is the HS(DD2) EOS [95, 96]. This EOS and its extension to non-NSE conditions is treated in section 3.1.3. With this numerical setup we model the collapse, the bounce, and the subsequent onset of explosion due to neutrino heating and the post-explosion phase. The major part of the simulations have been performed with 180 radial zones for a total time of 5 s which corresponds to a post bounce time of ~ 4.6 s. AGILE has an adaptive grid which distributes its grid points according to the gradients of variables inside the computational domain. In regions where hydrodynamic and thermodynamic variables are steeper the resolution is higher. The surface of the PNS and the shock front are better resolved than other regions in the post bounce phase and the explosion phase.

3.1 AGILE-IDSA-Leakage: Numerical Setup

3.1.1 General Relativistic Hydrodynamics

CCSNe are complex events which include a variety of physics. A realistic treatment of the collapse and the post bounce evolution of a massive star requires a relativistic description of the system. In this chapter we give a short introduction to general relativistic

hydrodynamics and the equations that are implemented in the AGILE code. We adapt the notations and conventions used in Liebendörfer et al. [56, 91]. The Greek letters denote the space time coordinates. Furthermore, we use relativistic units, with c=G=1 [97, 98]. The Einstein field equations of general relativity are given by (with the cosmological constant Λ set to zero)

$$G_{\mu\nu} = R_{\mu\nu} - \frac{1}{2} g_{\mu\nu} R = 8\pi T_{\mu\nu}, \tag{3.1}$$

where $G_{\mu\nu}$ is the Einstein tensor, $R_{\mu\nu}$ is the Ricci tensor, $g_{\mu\nu}$ is the metric tensor, R is the curvature scalar (or Ricci scalar) and $T_{\mu\nu}$ is the stress-energy tensor. This is a covariant tensor equation where all tensors are symmetric and therefore correspond to a set of ten field equations. The Einstein equation shows the coupling between space-time curvature and energy-matter distribution and gives the relation between the metric tensor $g_{\mu\nu}$ and the stress-energy tensor $T_{\mu\nu}$. This relation can be seen by looking at the left hand side of the Einstein field equations. The Ricci scalar is a contraction of the Ricci tensor

$$R = R^{\mu}_{\mu} = g^{\mu\nu} R_{\mu\nu}, \tag{3.2}$$

and the Ricci tensor itself is a contraction of the Riemann tensor

$$R_{\mu\nu} = R^{\lambda}_{\mu\lambda\nu}. \tag{3.3}$$

The Riemann tensor is given by

$$R^{\alpha}_{\beta\gamma\delta} = \Gamma^{\alpha}_{\beta\delta,\gamma} - \Gamma^{\alpha}_{\beta\gamma,\delta} + \Gamma^{\epsilon}_{\beta\delta}\Gamma^{\alpha}_{\epsilon\gamma} - \Gamma^{\epsilon}_{\beta\gamma}\Gamma^{\alpha}_{\epsilon\delta}, \tag{3.4}$$

where $\Gamma^{\alpha}_{\beta\gamma}$ is the metric connection (also called Christoffel symbol), which is given as

$$\Gamma^{\alpha}_{\beta\gamma} = \frac{1}{2} g^{\alpha\delta} \left(g_{\delta\gamma,\beta} + g_{\delta\beta,\gamma} - g_{\beta\gamma,\delta} \right). \tag{3.5}$$

We make use of the comma notation where a comma denotes a partial differentiation with respect to the component which follows the comma, e.g. $\phi_{,\mu} = \partial\phi/\partial x^{\mu}$. The stress-energy tensor is given by the energy and matter distribution of the described system, in vacuum it is equal to zero, $T^{\mu\nu} = 0$. In a closed system the stress-energy tensor has to fulfill the conservation equations

$$T^{\mu\nu}{}_{;\nu} = 0, \tag{3.6}$$

thus the covariant divergence of $T^{\mu\nu}$ must be zero (the semicolon denotes the covariant differentiation, see e.g. [99])[1]. This equation describes the conservation of energy and momentum. The covariant divergence of the Einstein tensor represents the contracted Bianchi identity and is zero as well

$$G^{\mu\nu}{}_{;\nu} = 0. \tag{3.7}$$

In order to describe a SN we have to find equations that describe the interior of a star. The interior of a star can be described approximately with the stress-energy tensor of a perfect fluid given by [97]

$$T^{\mu\nu} = \left(\varepsilon + p\right) u^{\mu} u^{\nu} + p g^{\mu\nu}, \tag{3.8}$$

where the total energy-density of the system is described by $\varepsilon = \rho(1+e)$ (here ρ is the rest mass density and e is the specific internal energy), p represents the isotropic pressure and $u^{\mu} = dx^{\mu}/d\tau$ is the 4-velocity. In the rest frame of matter the stress-energy tensor of a perfect fluid has the non-vanishing components (in the coordinate system (t, r, θ, ϕ))

$$T^{tt} = \rho(1+e),$$

$$T^{rr} = T^{\theta\theta} = T^{\phi\phi} = p. \tag{3.9}$$

In addition p and ρ are related by an equation of state of the form $p = p(\rho, T)$ (also other dependencies are possible). The invariant line element ds between a point x^{μ} and a neighboring point $x^{\mu} + dx^{\mu}$ is given by

$$ds^2 = g_{\mu\nu} dx^{\mu} dx^{\nu}. \tag{3.10}$$

For a spherically symmetric distribution of matter around the origin of the coordinate system, e.g. an idealization of a massive star, we follow [91, 100] and make the spherically symmetric ansatz for the metric

$$ds^2 = -e^{2\phi} dt^2 + e^{2\Lambda} da^2 + r^2 \left(d\theta^2 + \sin^2\theta d\phi^2\right), \tag{3.11}$$

where the angles θ and ϕ describe a 2-sphere ($d\Omega^2 = d\theta^2 + \sin^2\theta d\phi^2$). Here ϕ, Λ and r are functions of the coordinate time t and the radial coordinate a. The function $r(t, a)$

[1] We show an example for a mixed tensor of type (1,1): $T^i_{k;l} = T^i_{k,l} + \Gamma^i_{ml} T^m_k - \Gamma^m_{kl} T^i_m$. Each upper index results in similar positive term and each lower index in a negative term.

denotes the areal radius $r = \sqrt{A_s/4\pi}$, where A_s is the surface of the corresponding 2-sphere. Following Liebendörfer et al. (2001), we choose a metric of the form [91]

$$ds^2 = -\alpha^2 dt^2 + \left(\frac{r'}{\Gamma}\right)^2 da^2 + r^2\left(d\theta^2 + \sin^2\theta d\phi^2\right), \tag{3.12}$$

where the exponentials in the metric 3.11 are substituted with the lapse function α for e^{ϕ} and the function r'/Γ for e^{Λ}. The prime indicates a partial derivation of r with respect to a and $\Gamma = \sqrt{1 + u^2 - 2m/r}$. We choose a Lagrangian system of coordinates comoving with matter. In the frame comoving with the rest mass the proper time lapse is related to the coordinate time dt by the lapse function α, $d\tau = \alpha dt$ (see also [101]). The radial coordinate a is related to the enclosed rest mass. A mass shell with the rest mass A between coordinates a_1 and a_2 at a fixed time t is given in this metric by [91]

$$A(a_1, a_2) = \int_0^{2\pi}\int_0^{\pi}\int_{a_1}^{a_2} \rho_0\left(\frac{r'}{\Gamma}\right) da\, r d\theta\, r\sin\theta d\phi = \int_{a_1}^{a_2} \frac{4\pi r^2 r' \rho_0}{\Gamma} da.$$

We require that

$$A(a_1, a_2) \stackrel{!}{=} \int_{a_1}^{a_2} da,$$

correlating the spatial coordinate to the enclosed rest mass. This requirement is equivalent to the relation

$$r' = \frac{\Gamma}{4\pi r^2 \rho}. \tag{3.13}$$

We also define the velocity u which describes the change of areal radius with the proper time of an observer comoving with a fluid element $u = \partial r/\alpha\partial t = \dot{r}/\alpha$ [91, 102]. Furthermore, we introduce the notation for conserved quantities according to [92, 103]. In analogy to Newtonian hydrodynamics the specific volume, specific energy and specific momentum are defined as

$$\frac{1}{D} = \frac{\Gamma}{\rho}, \tag{3.14}$$

$$\tau = \Gamma e + \frac{2}{\Gamma + 1}\left(\frac{u^2}{2} - \frac{m}{r}\right), \tag{3.15}$$

$$S = u(1 + e). \tag{3.16}$$

In the non-relativistic limit ($\alpha = \Gamma = 1$) these equations become the well known specific volume $1/D = 1/\rho$, the specific energy as a sum of specific internal, kinetic and gravitational energy $\tau = e + u^2/2 - m/r$ and the specific radial momentum $S = u$. The equations that describe the system for a given metric and stress-energy tensor are given by the Einstein field equations. Using the definitions above, the complete system of general

relativistic hydrodynamics equations can be written in a conservative from [91, 92, 98]

$$\frac{\partial}{\partial t}\left(\frac{1}{D}\right) = \frac{\partial}{\partial a}\left(4\pi r^2 \alpha u\right), \tag{3.17}$$

$$\frac{\partial \tau}{\partial t} = -\frac{\partial}{\partial a}\left(4\pi r^2 \alpha u p\right), \tag{3.18}$$

$$\frac{\partial S}{\partial t} = -\frac{\partial}{\partial a}\left(4\pi r^2 \alpha \Gamma p\right) - \frac{\alpha}{r}\left(\left[1+e+\frac{3p}{\rho_0}\right]\frac{m}{r} + 8\pi r^2 (1+e)p - \frac{2p}{\rho_0}\right), \tag{3.19}$$

$$\frac{\partial V}{\partial a} = \frac{1}{D}, \tag{3.20}$$

$$\frac{\partial m}{\partial a} = 1+\tau, \tag{3.21}$$

$$(1+e)\frac{\partial \alpha}{\partial a} + \frac{1}{\rho_0}\frac{\partial}{\partial a}\left(\alpha p\right) = 0, \tag{3.22}$$

where the enclosed volume $V = 4\pi r^3/3$ is defined by the areal radius. The equations (3.17)-(3.19) represent volume conservation, total energy conservation, and radial momentum conservation. The equations (3.20)-(3.22) represent constraints for the rest mass density ρ, the gravitational mass m, and the lapse function α [91, 92]. In AGILE, the nonlinear differential equations (3.17)-(3.19) together with the constraints (3.20)-(3.22) (and one additional constraint for the adaptive grid) are finite differenced in the spatial dimension to build a set of coupled ordinary differential equations. These equations which are fulfilled for a state vector y are solved implicitly with the Newton-Raphson method for the corrections [92, 104]

$$\Delta y = -\left[\frac{\partial F(y^n, \tilde{y}^{n+1}, dt)}{\partial y^{n+1}}\right]^{-1} F(y^n, \tilde{y}^{n+1}, dt), \tag{3.23}$$

where F denotes the set of implicit equations (with $F = 0$), the upper indices n denote the time step ($dt = t^{n+1} - t^n$), and $\tilde{y}^{n+1}$ is a guess for the future solution of F. The term $\left[\partial F/\partial y\right]^{-1}$ denotes the inverted Jacobian of the Taylor expansion around a guessed solution vector. For a detailed description of AGILE we refer to [91, 92].

3.1.2 Neutrino Transport

In this section we introduce the implementation of the neutrino transport used in the presented PUSH simulations [87, 88]. We use the Isotropic Diffusion Source Approximation (IDSA) for the electron neutrinos and electron antineutrinos [93]. For the heavy-lepton flavor neutrinos ($\nu_x = \nu_\mu, \overline{\nu}_\mu, \nu_\tau, \overline{\nu}_\tau$) we use an an Advanced Spectral Leakage scheme (ASL) [105]. During the stellar collapse phase, we use a parametrized deleptonization scheme [106] to take neutrino-electron scattering effectively into account. In the post bounce phase we neglect electron-neutrino scattering. The neutrino energy is discretized using 20 geometrically increasing energy bins, in the energy range $3\,\mathrm{MeV} \leq E_\nu \leq 300\,\mathrm{MeV}$ [87]. In table 3.1 we summarize the neutrino reactions which are included in the IDSA and ASL scheme. These reactions represent the minimal set of the most relevant weak processes in the post-bounce phase, especially up to the onset of an explosion. Electron captures on heavy nuclei and neutrino scattering on electrons, which are relevant in the collapse phase (see, e.g., [107, 108]), are included as part of the parameterized deleptonization scheme and not explicitly in the form of reaction rates. Furthermore, we omit nucleon-nucleon bremsstrahlung, $N + N \leftrightarrow N + N + \nu_x + \bar{\nu}_x$ in the ASL scheme (see, e.g., [109, 110]). The inclusion of nucleon-nucleon bremsstrahlung would overestimate μ and τ neutrino luminosities during the cooling phase of the PNS in our simulations [87, 88]. The reason is the missing neutrino thermalization provided by inelastic scattering on electrons and positrons at the PNS surface. It has been tested that the omission of this process does not significantly alter the μ and τ neutrino luminosities predicted by the ASL scheme before the onset of explosion [87]. Therefore, not including nucleon-nucleon bremsstrahlung is only relevant for the cooling phase, where it improves the overall behavior when compared to simulations performed with detailed Boltzmann neutrino transport (see, e.g., [89]). The EOS HS(DD2) which we are using includes various light nuclei, such as alphas, deuterons or tritons (see also section 3.1.3). Note that the inclusion of all neutrino reactions for such a detailed nuclear composition would go beyond the standard approach implemented in contemporary supernova simulations, where only scattering on alpha particles is usually included. However, in order to not completely neglect the contributions of the other light nuclei, we have added their mass fractions to the unbound nucleons. This treatment is motivated by their very weak binding energies and, therefore, by the idea that they behave similarly as the unbound nucleons.

Reactions	Treatment	Reference
$e^- + p \leftrightarrow n + \nu_e$	IDSA	[111]
$e^+ + n \leftrightarrow p + \overline{\nu}_e$	IDSA	[111]
$N + \nu \leftrightarrow N + \nu$	IDSA & ASL	[111]
$(A, Z) + \nu \leftrightarrow (A, Z) + \nu$	IDSA & ASL	[111]
$e^- + e^+ \leftrightarrow \nu_{\mu,\tau} + \overline{\nu}_{\mu,\tau}$	ASL	[111], [112]

Tab. 3.1.: An overview of the relevant neutrino reactions, where nucleons are denoted by N. The nucleon charged current rates are based on [111], but we take into account the effects of mean-field interactions [113–116]. This table is adapted from [87].

3.1.3 Equation of State: Treatment of the Nuclei and the Transition Between Non-NSE and NSE

During a CCSN the thermodynamical quantities vary over many orders of magnitude. Hot and dense matter is described by NSE. The outer layers, where the shock eventually passes through, consist of a mixture of fully ionized nuclei. These nuclei are described as an ideal gas. In the simulations presented in this thesis we use the tabulated microphysical equation of state (EOS) HS(DD2) [95, 96] for the high-density plasma in NSE, unless stated otherwise. The used supernova EOS is based on the model by Hempel and Schaffner-Bielich (2010) [95]. It uses the DD2 parametrization for the nucleon interactions by Typel et al. (2010) [96], the nuclear masses from Audi et al. (2003) [48, 49], and the Finite Range Droplet Model (Möller et al. [117]). The electrons are assumed to be distributed uniformly and are described by a general Fermi-Dirac gas (including positron contributions). The photon gas contribution is also taken into account (Stefan-Boltzmann law). In total, there are 8140 nuclei included (up to Z=136 and to the neutron drip line). The supernova EOS HS(DD2) was first introduced in Fischer et al. (2014) [118]. It has been demonstrated that the HS(DD2) gives better agreement with the constraints from nuclear experiments and astrophysical observations than the commonly used EOSs of Lattimer and Swesty (1991) [119] and Shen et al. (1998) [120]. Furthermore, the maximum mass of a cold neutron star for the HS(DDS) EOS is $2.42 M_\odot$ [118], which is above the limits from Demorest et al. (2010) [121] and Antoniadis et al. (2013) [122].

The EOS employed in the PUSH framework includes an extension to non-NSE conditions. This enables the inclusion of a larger computational domain, since also layers that are not in NSE conditions, with lower temperature and density, can be included. With a larger domain it is possible to follow the outgoing shock and investigate the temporal

evolution of the total energy of the system, and all its contributions, for a longer time. In order to follow the shock of the supernova explosion that is propagating outwards in the computational domain with a velocity of the order of $\langle v_{\rm shock} \rangle \sim 10^9$ cm s^{-1} for a time $t_{\rm sim}$ of the simulation that is long enough to observe a saturation of the explosion energy ($t_{\rm sim} \sim 1 - 10$s), one should include a computational domain that ranges up to $t_{\rm sim} \times \langle v_{\rm shock} \rangle$ on the order of $10^9 - 10^{10}$ cm. In the non-NSE regime, the nuclear composition of the stellar material is described by 25 representative nuclei, covering the range form neutrons and protons up to iron-group nuclei. The choice of nuclei that have been included in this representative nuclear composition was guided by the goal to give a realistic approximation of the nuclear composition of the stellar material, include explosive burning in the simulations, use the information that was provided in the available progenitor models, and to achieve a mapping of abundances from the progenitor calculations into the PUSH framework which is consistent with the provided electron fraction (maintaining charge neutrality). These guidelines led to the inclusion of the set of nuclei in the PUSH simulations given in table 3.2. The set of nuclei that we include consists of neutrons, protons, the alpha nuclei ^{4}He, ^{12}C, ^{16}O, ^{20}Ne, ^{24}Mg, ^{28}Si, ^{32}S, ^{36}Ar, ^{40}Ca, ^{44}Ti, ^{48}Cr, ^{52}Fe, ^{56}Ni complemented by ^{14}N and the asymmetric isotopes ^{3}He, ^{36}S, ^{50}Ti, ^{54}Fe, ^{56}Fe, ^{58}Fe, ^{60}Fe, ^{62}Fe, to be able to get a consistent distribution of nuclei also for situations with $Y_e \neq 0.5$. The nuclear masses M_i of the nuclei are taken from Audi et al. (2009) [48, 49].

In the following we explain the temporal evolution of the nuclei which we implemented into the general relativistic spherically symmetric hydrodynamics code AGILE [56, 92]. We follow the solution for the temporal evolution of the electron abundance that is evolved as a part of the state vector of AGILE

$$\mathbf{y} = (a, r, v, m, \rho, T, Y_e, \alpha), \tag{3.24}$$

where a is the enclosed baryon mass, r the radius, v the velocity, m the gravitational mass, ρ the baryon density, T the temperature, Y_e the electron fraction, and α the lapse function. The adaptive grid used in AGILE consists of grid points (i.e. N mass shells in the star) that continuously move through the computational domain with respect to the enclosed rest mass label $a_i(t)$, a_i being the enclosed mass of the ith shell [92]. The enclosed rest mass between two shells, e.g. between shells $i+1$ and i, at the nth time step t^n is denoted by $da^n_{i+\frac{1}{2}}$, where zone edges are addressed with indices i and zone centers with $i+\frac{1}{2}$. The enclosed rest mass label of each zone j at time t^n is then given by [89]

$$a^n_j = \sum_i^{j-1} da^n_{i+\frac{1}{2}}. \tag{3.25}$$

Non-NSE Nuclei (PUSH simulations)	Z	A	Progenitor values [40, 41]
n	0	1	×
p	1	1	×
^{3}He	2	3	×
^{4}He	2	4	×
^{12}C	6	12	×
^{14}N	7	14	×
^{16}O	8	16	×
^{20}Ne	10	20	×
^{24}Mg	12	24	×
^{28}Si	14	28	×
^{32}S	16	32	×
^{36}S	16	36	-
^{36}Ar	18	36	×
^{40}Ca	20	40	×
^{44}Ti	22	44	×
^{50}Ti	22	50	-
^{48}Cr	24	48	×
^{52}Fe	26	52	×
^{54}Fe	26	54	×
^{56}Fe	26	56	×
^{62}Fe	26	62	-
^{58}Fe	26	58	-
^{60}Fe	26	60	-
^{56}Ni	28	56	×
^{62}Ni	28	62	-

Tab. 3.2.: List of nuclei included in the nuclear composition in the non-NSE regime of the simulations performed in the PUSH framework. Also listed are the nuclei included in the progenitors of Woosley, Heger and Weaver (2002) [40], which are directly mapped onto the simulations, with the exception of the given iron-group abundance, which is not further specified in the progenitor data. We map it onto the available iron nuclei in our EOS treatment. The amount of nuclei implemented in the progenitor calculations of Woosley and Heger (2007) [41] is vast and not listed. For these progenitors the abundances of the symmetric alpha nuclei are renormalized and then mapped onto the simulation.

Now we have a look at the temporal changes of the zone-integrated values of observable quantities in the comoving frame of the fluid given in the framework of the adaptive grid [92]. In addition to changes inside a zone due to physical processes we also have to consider the motion of the zone boundaries, which leads to fluxes entering and leaving the zones. The resulting total change in time of a conserved quantity ϕ (e.g. the number

of electrons) can be finite differenced in the form of the generic time evolution equation [92]

$$\frac{\phi^{n+1}_{i+\frac{1}{2}} da^{n+1}_{i+\frac{1}{2}} - \phi^{n}_{i+\frac{1}{2}} da^{n}_{i+\frac{1}{2}}}{dt} + F^{\mathrm{adv}}_{i+1} - F^{\mathrm{adv}}_{i} - S^{\mathrm{ext}}_{i+\frac{1}{2}} = 0, \tag{3.26}$$

where the temporal change of the quantity $\phi_{i+\frac{1}{2}} da_{i+\frac{1}{2}}$ in a zone with the enclosed baryon mass $da_{i+\frac{1}{2}}$ is given by the changes due to advection at the boundaries F^{adv} and a source term S^{ext}. The advection terms F^{adv}_{i+1} and F^{adv}_{i}, denote the changes due to advection at the upper and lower boundary, respectively [92]. The variable S^{ext} describes the changes of ϕ due to a source term, which is correspondent to the changes in abundances due to explosive nuclear burning in the case of the advected nuclei. By introducing $\delta_i = a^{n+1}_i - a^n_i$, the difference of enclosed masses between the times t^n and t^{n+1}, and using $da^{n+1}_{i+\frac{1}{2}} = da^{n}_{i+\frac{1}{2}} + \delta_{i+1} - \delta_i$ to denote the new values for the individual zone masses (which leads to convergence of the Newton-Raphson scheme in AGILE even in the presence of huge density gradients between neighboring zones [89]), we get

$$\frac{\phi^{n+1}_{i+\frac{1}{2}} \left(da^{n}_{i+\frac{1}{2}} + \delta_{i+1} - \delta_i \right) - \phi^{n}_{i+\frac{1}{2}} da^{n}_{i+\frac{1}{2}}}{dt} + F^{\mathrm{adv}}_{i+1} - F^{\mathrm{adv}}_{i} - S^{\mathrm{ext}}_{i+\frac{1}{2}} = 0. \tag{3.27}$$

The relative velocity between the fluid and the adaptive grid used in the computation of the advection terms F^{adv} is given by [56, 89, 92]

$$u^{\mathrm{rel}}_i = -\frac{a^{n+1}_i - a^n_i}{dt} = -\frac{\delta_i}{dt}. \tag{3.28}$$

The nuclear abundances of the advected composition in the numerical implementation of the PUSH setup are not included in the state vector $\mathbf{y}$ as in [89]. Instead, the generic time evolution equations (3.26) and (3.27) are used to describe the evolution of the abundances explicitly. Following the expression for the solution of the temporal change of the electron fraction Y_e [92], we get the following equation for the abundances $Y^n_{m,i+\frac{1}{2}}$ (m denotes the nuclear species)

$$\frac{Y^{n+1}_{m,i+\frac{1}{2}} da^{n+1}_{i+\frac{1}{2}} - Y^{n}_{m,i+\frac{1}{2}} da^{n}_{i+\frac{1}{2}}}{dt} + F^{\mathrm{adv}}_{m,i+1} - F^{\mathrm{adv}}_{m,i} - \alpha^{n+1}_{i+\frac{1}{2}} Y^{\mathrm{ext}}_{m,i+\frac{1}{2}} = 0, \tag{3.29}$$

where we adapted the form of the source term given in [92] (for the treatment of electrons) for our description of the nuclei, α denotes the lapse function, and Y^{ext} denotes

the change of the abundances due to reaction rates. This leads to the explicit expression of the temporal change of the abundances,

$$Y^{n+1}_{m,i+\frac{1}{2}} = \left[\alpha^{n+1}_{i+\frac{1}{2}} Y^{\mathrm{ext}}_{m,i+\frac{1}{2}} - A_m\right]\left(\frac{dt}{da^{n+1}_{i+\frac{1}{2}}}\right) + Y^{n}_{m,i+\frac{1}{2}}\left(\frac{da^{n}_{i+\frac{1}{2}}}{da^{n+1}_{i+\frac{1}{2}}}\right), \tag{3.30}$$

where the advection terms have been replaced by $A_m = F^{\mathrm{adv}}_{m,i+1} - F^{\mathrm{adv}}_{m,i}$. The quantities $\alpha^{n+1}_{i+\frac{1}{2}}$ and $da^{n+1}_{i+\frac{1}{2}}$ are computed with the Newton-Raphson scheme of AGILE and the quantities $Y^{n}_{m,i+\frac{1}{2}}$ and $Y^{\mathrm{ext}}_{m,i+\frac{1}{2}}$ are stored and computed within the approximative α-network in the non-NSE region. To advect the nuclear composition inside the adaptive grid, we implement the consistent multi-fluid advection method introduced by Plewa and Müller (1999) [123]. This scheme is based on a correction of the partial mass fluxes of the different species of nuclei in such a way, that they consistently add up to the total mass flux across zone boundaries. Two conditions have to be fulfilled in order to achieve consistent multi-fluid advection. For an abundance distribution consisting of N different nuclei (fluid phases) the following relation must hold for all times and zones

$$\sum_{m}^{N} X_m = 1, \tag{3.31}$$

where X_m denotes the mass fraction of the mth species. Furthermore, AGILE is a conservative hydrodynamics code and thus, the total mass of one species across the domain of the simulation can not change due to advection which is the second condition. The total mass flux across boundaries due to the adaptive grid u^{rel} is given in equation (3.28). The consistent multi-fluid advection fluxes of the mth species in the nth zone $F_{n,m}$ are then computed with

$$F_{n,m} = \theta_n f_{n,m}, \tag{3.32}$$

where

$$\theta_n = \frac{u^{\mathrm{rel}}_n}{\sum_m f_{n,m}} \tag{3.33}$$

is the scaling correction to the original partial mass fluxes $f_{n,m}$. Like this the sum of all modified mass fluxes adds up to the total mass flux across the boundaries due to the movement of the adaptive grid. We compute the partial mass fluxes across the boundaries according to [92] with the extension of conditional switching to a donor cell advection scheme to guaranty consistent evolution of the composition, the fluxes, and numerical stability. In the case that one of these criteria does not hold the advection terms of

species m in the ith zone is computed with the stable but diffusive donor cell advection scheme

$$F^{\mathrm{adv}}_{m,i} = \begin{cases} Y_{m,i-\frac{1}{2}}\, u^{\mathrm{rel}}_i & u^{\mathrm{rel}}_i \geq 0 \quad (3.34a) \\ Y_{m,i+\frac{1}{2}}\, u^{\mathrm{rel}}_i & \text{otherwise.} \quad (3.34b) \end{cases}$$

Non-NSE EOS of the Nuclei

The approximate α-network is used to follow the changes in composition due to explosive burning outside of NSE. Explosive Helium, Carbon, Neon, and Oxygen burning are currently implemented in the simulation. Thereby the burning converts the main fuel of the corresponding burning phase to heavier elements on the typical burning timescale $\tau_i = \left|\frac{Y_i}{\dot{Y}_i}\right|$ (see also chapter 2 section 2.5). The energetics of the nuclear reactions are fully incorporated via the detailed non-NSE treatment. The non-NSE EOS is calculated with the same underlying physical model of [95] that is used for the EOS in the NSE regime. Such a consistent description of the NSE and the non-NSE regimes prevents spurious effects in the transition region between the two phases. We will shortly explain the EOS of the non-NSE region in the following. For a homogeneous medium the grand-canonical thermodynamic potential is given by the expression $\Omega = -PV$ [47], where P is the pressure of the medium and V is the volume of the system[1]. Outside of NSE, the EOS of nuclei can be described by an ideal Maxwell-Boltzmann gas. First, we give the expressions for pressure and energy without Coulomb corrections which are discussed in a second step below. In the following the entropy density $\tilde{s}$, the energy density $\tilde{e}$, and the particle number density $\tilde{n}$ are related to the entropy, energy and particle number in the way $\tilde{s} = S/V$, $\tilde{e} = E/V$, and $\tilde{n} = N/V$. For a non-relativistic Maxwell-Boltzmann gas of a mixture of nuclei the internal energy density, the pressure, and the entropy density are given by

$$\tilde{e} = \sum_i \tilde{e}_i, \quad (3.35)$$

$$\tilde{s} = \sum_i \tilde{s}_i, \quad (3.36)$$

[1] For a homogeneous gas with constant temperature T and pressure P in a volume one gets the expression $G = \sum_i \bar{\mu}_i N_i$ for the free enthalpy. Inserted in equation $G = U - TS + PV$ and solved for $\Omega = U - TS - \sum_i \bar{\mu}_i N_i$ this gives the presented equation ($\bar{\mu}_i = \mu_i + m_i c^2$) [47].

$$P = \sum_i P_i. \tag{3.37}$$

The single components are given by

$$\tilde{e}_i = \frac{3}{2}\tilde{n}_i kT, \tag{3.38}$$

and

$$P_i = \tilde{n}_i kT, \tag{3.39}$$

where k denotes the Boltzmann constant. The entropy is computed from $\Omega = -\tilde{n}VkT$ with [47]

$$S = -\left(\frac{\partial\Omega}{\partial T}\right)_{V,\mu}, \tag{3.40}$$

which yields[1]

$$\tilde{s}_i = \tilde{n}_i k\left(\frac{5}{2} + \ln\left[\frac{g_i}{\tilde{n}_i h^3}(2\pi m_i kT)^{3/2}\right]\right). \tag{3.41}$$

We show in the following lines how we describe and treat the EOS of the nuclei in the non-NSE region in an equivalent way to the relativistic treatment in the NSE region. First, we introduce the energy density of a single species of nuclei (also including the rest mass)

$$\tilde{\epsilon}_i = \tilde{n}_i\left(m_i c^2 + \frac{3}{2}kT\right), \tag{3.42}$$

where m_i is the total nuclear mass of the corresponding nucleus. The total internal energy per baryon is then given by (without electrons)

$$e_{\text{int}} = \frac{\sum_i \tilde{\epsilon}_i}{n_b}, \tag{3.43}$$

where $n_b = N_b/V$ is the baryon number density. With

$$\tilde{n}_i/n_b = X_i/A_i = Y_i, \tag{3.44}$$

we see that the total internal energy per baryon is given by (where A_i is the nuclear mass number of species i)

$$e_{\text{int}} = \sum_i Y_i\left(m_i c^2 + \frac{3}{2}kT\right), \tag{3.45}$$

and that the rest mass energy per baryon is given by

$$e_{\text{mass}} = \sum_i Y_i m_i c^2. \tag{3.46}$$

[1] The number density of particles is given by $\tilde{n} = e^{\mu/kT}\frac{g}{h^3}(2\pi mkT)^{3/2}$, where g is the degeneracy factor of the considered particles [47].

The thermal energy per baryon is given by

$$e_{\text{th}} = e_{\text{int}} - e_{\text{mass}} = \sum_i \frac{3}{2} Y_i k T. \tag{3.47}$$

In this case, since e_{int} is conserved in the relativistic treatment of the EOS, the nuclear reactions will decrease the rest mass energy by increasing the binding energy and as a consequence will increase the thermal energy, i.e. heat up matter. Note that by dividing the equations (3.45), (3.46), and (3.47) by the baryon mass m_B we get the specific total energy, specific rest mass energy, and the specific thermal energy.

Next we show how a change in the composition of the nuclei changes the temperature. We consider a change in the composition $\vec{X} \rightarrow \vec{X}'$ and we know that e_{int}=e'_{int}. This gives us the temperature of the new composition as a

$$T' = \frac{\sum_i \frac{m_i c^2}{A_i} \left(X_i - X'_i\right) + \frac{3}{2} k T \sum_i \frac{X_i}{A_i}}{\frac{3}{2} k \sum_i \frac{X'_i}{A_i}}. \tag{3.48}$$

This temperature change corresponds to a change in thermal energy due to released energy ΔQ by nuclear burning. The obtained energy release rate due to nuclear burning is equivalent to $\dot{e}_{\text{nuc}} = -\sum_i \dot{Y}_i m_i c^2$ (-$\Delta e_{\text{mass}} = \Delta e_{\text{nuc}}$). If we compare the thermal energy at two different times we find that ΔQ has the form

$$\Delta Q = e'_{\text{th}} - e_{\text{th}} = -\sum_i \Delta Y_i m_i c^2, \tag{3.49}$$

with $\Delta Y_i = Y'_i - Y_i$. Divided by the time step Δt we get the energy release rate due to nuclear burning (see also section 2.5)

$$\dot{e}_{\text{nuc}} = -\sum_i \dot{Y}_i m_i c^2. \tag{3.50}$$

Now we also introduce the Coulomb corrections that account for the interaction of the nuclei with the electron background in the total specific energy and the total pressure of nuclei according to [43]. With the assumption that n_e is in first approximation uniform we give an approximation of the Coulomb corrections. For small temperatures, i.e. T approaching zero, the ions are positioned in a lattice. For simplicity the derivation is done for one species of nuclei. For a given density of nuclei with charge Z (number of protons of the nucleus) the lattice energy is minimized for a body-centered lattice. The energy of the lattice is calculated by considering the Wigner-Seitz approximation, where

the nuclei are in the centers of the cells. If we consider a "spherical" cell of the lattice to be of the volume $4\pi R^3/3 = 1/\tilde{n}$, where $\tilde{n}$ denotes the number density of nuclei, the gas can be divided into neutral spheres of radius R with a nucleus in the center (each cell contains the Z electrons that are closest to the corresponding nucleus). The total Coulomb energy of each cell is the sum of the potential energies due to electron-electron and ion-electron interactions[1]

$$E_C = E_{ee} + E_{ie} = \int_0^R \frac{Q_r\, dQ_r}{r} + Ze\int_0^R \frac{dQ_r}{r} = -\frac{9}{10}\frac{Z^2e^2}{R}, \tag{3.51}$$

where E_{ee} represents the energy necessary to assemble a sphere of electrons with radius R and charge $Q_R = -Ze$, and E_{ie} represents the energy to assemble the electron sphere around a nucleus with charge Ze. The electrostatic energy per electron is given by

$$\frac{E_C}{Z} = -\frac{9}{10}\left(\frac{4\pi}{3}\right)^{1/3} Z^{2/3}e^2\tilde{n}_e^{1/3}, \tag{3.52}$$

with $\tilde{n}_e = Z/(4\pi/3R^3)$. The numerical coefficient in equation 3.52, given by $(9/10)\,(4\pi/3)^{1/3} = 1.450793$, is very close to the exact value for a body-centered cubic lattice: 1.44423 [43, 124]. The negative pressure corresponding to the Coulomb correction is given by [43]

$$P_C = \tilde{n}_e^2\frac{d(E_C/Z)}{d\tilde{n}_e} = -\frac{3}{10}\left(\frac{4\pi}{3}\right)^{1/3} Z^{2/3}e^2\tilde{n}_e^{4/3}. \tag{3.53}$$

With this we have given the description of the EOS of composition of nuclei in non-NSE. The description of the Coulomb corrections for the pressure was derived for small temperatures $T \to 0$ and overestimates this aspect for finite temperatures. Note that contributions of electrons and photons to the specific internal energy are also considered. In the non-NSE region the electrons contribute like an ideal gas and photons with the internal energy of a black body photon gas.

Transition Between NSE and Non-NSE

In the following, we describe how the transition between NSE and non-NSE is implemented. We define a transition region in temperature where this is done. First, we give the boundary temperatures that describe the transition region of the EOS. Above the temperature $T_2 = T_{\mathrm{NSE}} = 0.44$MeV the matter is assumed to be in NSE and the EOS is described by the supernova EOS HS(DD2). Below $T_1 = T_{\mathrm{non-NSE}} = 0.4$MeV the EOS is given

[1] With $Q_r = \rho_R\frac{4\pi}{3}r^3 = -Ze\frac{r^3}{R^3}$ being the charge of the electrons inside one cell ($\rho_R = -en_e$ is the charge density of the electrons inside the cell)

by the ideal gas description presented above. For the exception that the entropy per baryon and the internal energy per baryon of the non-NSE EOS evaluated for T_1 are bigger than the same quantities of HS(DD2) evaluated for T_2 the temperature limit for NSE can be increased up to a maximum value of $T_2(\rho, Y_e, T) = T_{2,\max} = 1.4$ MeV. This is done to maintain stability of the hydrodynamics code by ensuring a unique solution for a given temperature and to fulfill the condition of thermodynamical consistency, $(\partial S/\partial T) > 0$. Thus, we have four regions (often this reduces to three) of the EOS, the non-NSE EOS region below T_1, a transition region between non-NSE to NSE between T_1 and T_2, either an extended transition region or NSE region between T_2 and $T_{2,\max}$, and the NSE region above a temperature of $T_{2,\max}$. In the transition region, between the temperatures T_1 and T_2, the EOS is linearly interpolated with respect to temperature. A thermodynamic quantity, Λ (e.g. pressure), is then given by the interpolation with the parameter

$$\chi(T) = \frac{T - T_1}{T_2 - T_1}, \tag{3.54}$$

by the expressions

$$\Lambda(\rho, Y_e, T) = \big(1 - \chi(T)\big)\, \Lambda_{\text{non-NSE}}(\rho, Y_e, T_1) + \chi(T) \Lambda_{\text{NSE}}(\rho, Y_e, T_2). \tag{3.55}$$

This description is not thermodynamic consistent but works well in this framework since the differences between the two phases are small. We valued stability and simplicity higher than thermodynamic consistency that would have a very high computational cost and would be extremely complex to implement.

Furthermore, a mapping from the abundances of the NSE to the non-NSE distribution of the nuclei in the approximative α-network has been implemented. This is done to ensure a smooth transition between the two regimes. The possible effects of nuclear reactions in the transition to NSE and in the freeze-out of NSE that are not included in the approximative α-network because the relevant reaction rates are not implemented. Thus, the mapping of the nuclei mimics such possible reactions in an effective way. Between the temperatures $T_0 = 0.3$ MeV and $T_1 = 0.4$ MeV the distribution of nuclei is mapped from the NSE distribution of HS(DD2) to the network distribution on a characteristic burning timescale that is computed during the mapping (see below). If the temperature is above T_1 this transition happens instantly. In the case of a transition from non-NSE to NSE the approximative α-network prevents the distribution of nuclei to go beyond ^{28}Si. Thus, the mapping approximates the explosive burning that would happen in a network that includes more reactions. For a freeze-out from NSE to non-NSE, the mapping in the transition region ensures that the distribution of nuclei in the α-network still follows the NSE ground state of the distribution of nuclei given in HS(DD2). Like this, the still pos-

sible changes of the distribution of the nuclei after freeze-out due to nuclear reactions is mimicked. This mapping is rather complicated and it would be a good step of future works to implement a more complete network that is able to compute a NSE distribution of nuclei for its reduced set of nuclei at all given times (see, e.g., [125]). In the transition region the nuclei of the NSE distribution are mapped to the network nuclei as follows. First the distribution of nuclei obtained from HS(DD2), which consists out of neutrons, protons, alphas, and a representative heavy nucleus, given by X_n^{NSE}, X_p^{NSE}, X_α^{NSE}, and X_h^{NSE}, $\langle A_h \rangle$, $\langle Z_h \rangle$, is mapped to a representative distribution in the framework of the nuclei implemented inside of the network: $X_i^{\mathrm{non-NSE}}$. Then, the nuclei are burned from the current distribution inside the approximative network to the representative distribution of HS(DD2) on a computed burning timescale dt_α. During the mapping it is always ensured and used that mass and charge are conserved

$$\sum_i X_i = 1, \tag{3.56}$$

$$Y_e = \sum_i \frac{Z_i}{A_i} X_i. \tag{3.57}$$

For a NSE distribution of nuclei that contains no heavy elements $X_h = 0$ the mapping is simply done by

$$X_\alpha^{\mathrm{non-NSE}} = X_\alpha^{\mathrm{NSE}} \tag{3.58}$$

$$X_p^{\mathrm{non-NSE}} = Y_e^{\mathrm{NSE}} - \frac{1}{2} X_\alpha^{\mathrm{NSE}} \tag{3.59}$$

$$X_n^{\mathrm{non-NSE}} = 1 - X_p^{\mathrm{NSE}} - X_\alpha^{\mathrm{NSE}}. \tag{3.60}$$

If heavy nuclei are present, $X_h \neq 0$, then the representative heavy nucleus of the NSE is mapped onto the nucleus or the nuclei contained inside the network that are closest to its charge and mass and the remaining neutrons or protons are added to $X_n^{\mathrm{non-NSE}}$ or $X_p^{\mathrm{non-NSE}}$, respectively. We illustrate the mapping of the mass fraction X_n^{NSE}, X_p^{NSE}, X_α^{NSE}, and X_h^{NSE}, to the representative non-NSE mass fraction $X_n^{\mathrm{non-NSE}}$, $X_p^{\mathrm{non-NSE}}$, $X_\alpha^{\mathrm{non-NSE}}$, and $X_h^{\mathrm{non-NSE}}$, in figure 3.1 for two different situations. For both cases the neutrons, protons and α's are directly mapped onto the respective abundances in the network. In case 1, the heavy NSE nucleus is surrounded by nuclei of the network and distributed among them. In case 2 the nucleus is strongly asymmetric and thus mapped on the nucleus that is most similar to it, and the remaining neutrons or protons are added to the others. Once the $X_i^{\mathrm{non-NSE}}$ are defined, the burning timescale for the burning from the current mass fractions to the new defined ones is computed and the nuclei are "burned" to the new distribution within the range of the time step of the hydrodynamics. This timescale

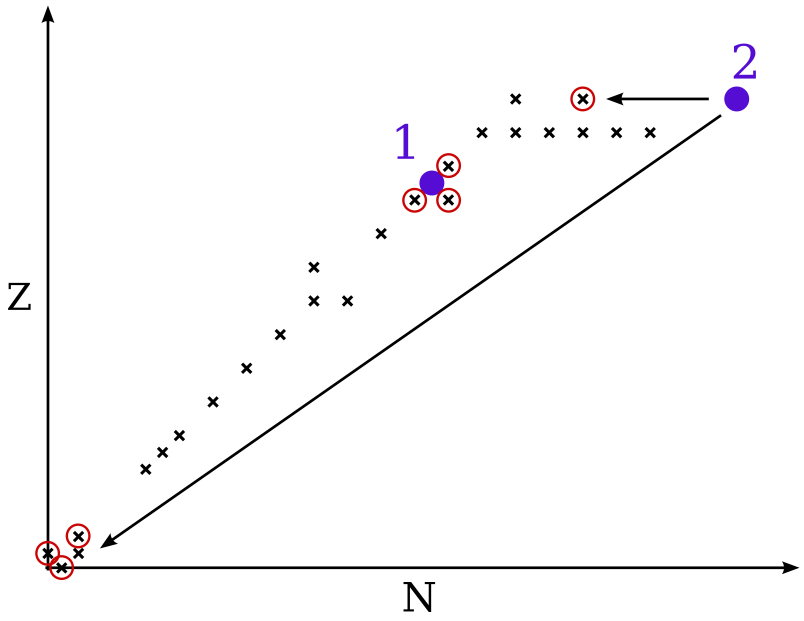

Fig. 3.1.: Illustration of the mapping to the network. Crosses are nuclei that are implemented in the network. The red circles indicate the nuclei that are used to map the NSE distribution onto. Neutrons, protons and alphas are directly translated. The blue dots indicate two cases of a representative heavy NSE nucleus that has to be mapped onto the network nuclei. If the nucleus is surrounded by network nuclei as in case 1 it is mapped onto the neighboring nuclei. A nucleus that is far from stability as in case 2 is mapped onto the best fitting nucleus nearby and the remaining protons or neutrons are added to the other protons and neutrons. This is how the $X_i^{\text{non-NSE}}$ are defined.

$dt_\alpha(T)$ is defined by a set of fixed parameters and the temperature. The rate of change with which the old distribution is "burned" to the new one is defined by

$$R(dt, dt_\alpha(T)) = 1 - \exp\left(-\frac{dt}{dt_\alpha(T)}\right), \tag{3.61}$$

where dt is the hydro time step of the simulation. The new distribution of nuclei that is obtained by the mapping and the subsequent evolution of the abundances is given by

$$X_{\text{new}}^{\text{non-NSE}} = R(dt, dt_\alpha(T)) X^{\text{non-NSE}} + (1 - R(dt, dt_\alpha(T)))\, X_{\text{old}}^{\text{non-NSE}}. \tag{3.62}$$

3.2 The PUSH Method: Parametrized Spherically Symmetric Core-Collapse Supernova Simulations

In this chapter we describe the numerical implementation of the PUSH method that was introduced and published in Perego et al. (2015) [87]. Results that were obtained with this version of PUSH are presented in chapter 4. The content of this section is partially part of the publication Perego et al. [87]. Improvements and extensions to the PUSH method, e.g., in the form of a dependence on compactness is presented in chapter 5. The aim of the PUSH method is to provide a computationally efficient framework to investigate neutrino-driven CCSNe in spherically symmetric simulations to study multiple aspects of CCSNe. Multi-dimensional simulations of CCSNe have shown that convection, turbulence and SASI in the shocked layers of the star increase the heating efficiency of electron- and anti-electron-neutrinos inside of the gain region in comparison with spherically symmetric simulations (see, e.g., [126–132]). This effect, in addition to the simultaneous increase in time that a fluid element spends inside the gain region due to convective motion (e.g., [133, 134]), provides better conditions for the development of a successful explosion. Furthermore, in multi-dimensional explosion models, the shock revival is followed by a phase of continued mass accretion onto the PNS and shock expansion on a time scale of $\tau \gtrsim 1\,\mathrm{s}$ (see e.g., [132, 135–137]). After the onset of explosion, this mass accretion through low-entropy down flows continues to power an accretion luminosity. Also, re-ejection (due to neutrino heating) of a fraction of this down flow matter accelerates the shock and increases the explosion energy. The exact length of this phase and the amount of energy that is injected into the explosion are still uncertain.

Self-consistent spherically symmetric simulations show a smaller heating efficiency of electron neutrinos and antineutrinos behind the shock due to an absence of convective motion. Therefore, such one-dimensional simulations of CCSNe, including general relativity and detailed neutrino transport, do not lead to explosions, with the exception of the lowest-mass CCSN progenitors [89, 90]. In the case of an explosion, one-dimensional simulations would additionally suffer from a too strong decrease of ν-heating behind the shock due to a drop in electron (anti)neutrino luminosity that occurs in these models due to a drastic reduction of the mass accretion rate on the PNS (lack of dimensionality prohibits infalling matter after the onset of explosion). PUSH aims to capture and reproduce in spherically symmetric models the increased net neutrino heating on fluid elements in the gain region observed in multi-dimensional simulations due to convection

and other multidimensional effects. This is done by providing extra energy deposition in the gain region by tapping the energy of the $\mu-$ and $\tau-$(anti)-neutrinos in otherwise consistent spherically symmetric simulations to mimic multi-dimensional effects that enhance neutrino heating. We deposit a fraction of the luminosity of the heavy flavor neutrinos (ν_x's) behind the shock to ultimately provide successful explosion conditions. The presented approach of PUSH is different to other artificial methods that try to mimic the delayed neutrino-driven mechanism using electron flavor neutrinos to trigger explosions in 1D models. The additional energy deposition in PUSH is calibrated by comparing the explosion energies and nucleosynthesis yields obtained from our progenitor sample with observations of SN 1987A (see chapters 4 and 5). This fitting ensures that our artificially increased heating efficiency has an empirical foundation. Even though in later chapters the originally presented PUSH method (this chapter and chapter 4) is extended to reproduce the observed explodability and the explosion energies of a large variety of progenitors (chapter 5), the fitting of PUSH to SN 1987A remains a core aspect.

The usage of heavy lepton flavor neutrinos presents a number of advantages for the parametrization of artificially triggered CCSN simulations, even though their contribution in self-consistent models is insignificant (see, e.g., [58]) and these neutrinos only show a weak dependence on the temporal variation of the accretion rate (see,e.g., [56]). The $\mu-$ and $\tau-$(anti)neutrinos that stream out of the PNS provide a large energy reservoir that can be easily tapped. Hence, it is possible to trigger an explosion in spherically symmetric models without either a modification of the ν_e and $\bar{\nu}_e$ luminosities or a change of charged current reactions. The $\mu-$ and $\tau-$neutrino luminosities are calculated consistently within our model. Thus, they include dynamical feedback from the accretion history, progenitor properties, and the cooling of the newly born PNS. O'Connor and Ott showed in broad progenitor studies that properties of the ν_x spectral fluxes correlate significantly with the properties of ν_e's and $\bar{\nu}_e$'s during the accretion phase that precedes the shock revival [138]. Furthermore, as mentioned above, ν_x luminosities are only marginally affected by the onset of an explosion and can be used to mimic enhanced neutrino heating in the gain region due to continued accretion onto the PNS. The main feature of PUSH is the deposition of additional energy in the gain region. This is done by introducing a local heating term, $Q^{+}_{\mathrm{PUSH}}(t,r)$ (energy per mass and time). Its dependencies are chosen to ensure a behavior of the parametrization that mimics and corresponds to the multi-dimensional effects that it is aimed to reproduce. In the following, we introduce the heating provided by PUSH according to [87]. The local heating term is given by

$$Q^{+}_{\mathrm{PUSH}}(t,r) = 4\mathcal{G}(t)\int_0^\infty q^{+}_{\mathrm{PUSH}}(r,E)\,dE, \tag{3.63}$$

with

$$q^{+}_{\mathrm{PUSH}}(r,E) \equiv \sigma_0 \, \frac{1}{4\,m_B} \left(\frac{E}{m_e c^2}\right)^2 \frac{1}{4\pi r^2} \left(\frac{dL_{\nu_x}}{dE}\right) \mathscr{F}(r,E), \tag{3.64}$$

where

$$\sigma_0 \equiv \frac{4}{\pi} \left(\frac{\hbar}{m_e c}\right)^{-4} \left(\frac{G_F}{m_e c^2}\right)^2 \approx 1.76 \times 10^{-44} \mathrm{cm}^2, \tag{3.65}$$

is the typical neutrino cross-section[1], $m_B \approx 1.674 \times 10^{-24}$g the average baryon mass, and $(dL_{\nu_x}/dE)/(4\pi r^2)$ the spectral energy flux for a single ν_x neutrino species with the energy E. All four heavy neutrino flavors are treated identically within the ASL scheme. This is reflected in the factor 4 appearing in the expression for Q^{+}_{PUSH}. The spatial dependencies of $Q^{+}(t,r)$ (i.e. where PUSH is active) are captured in the term $\mathscr{F}(r,E)$ which is introduced in equation (3.64) and given by

$$\mathscr{F}(r,E) = \begin{cases} 0 & \text{if} \quad ds/dr > 0 \quad , \quad \dot{e}_{\nu_e,\bar{\nu}_e} < 0 \quad \text{or} \quad r > r_s \\ \exp(-\tau_{\nu_e}(r,E)) & \text{otherwise} \end{cases} , \tag{3.66}$$

where τ_{ν_e} is the optical depth of the electron neutrinos, s the matter entropy, $\dot{e}_{\nu_e,\bar{\nu}_e}$ the net specific energy rate due to electron neutrinos and antineutrinos , and r_s the shock radius. Note that the term $\mathscr{F}(r,E)$ has this form in Perego et al. (2015) (see also chapter 4), in the new analysis and investigation of large progenitor sets presented in chapter 5 it will be restated in a slightly changed form (the entropy-gradient criterion is omitted). The two criteria in equation (3.66) capture the essential idea for the description of CCSN explosions with PUSH: the version of PUSH used in chapter 4 is only active where electron-neutrinos are heating and where neutrino-driven convection can occur[2]. The free parameters of the PUSH method are introduced in the term $\mathscr{G}(t)$ which determines the temporal behavior of $Q^{+}_{\mathrm{PUSH}}(t,r)$ (see equation (3.63)) and is given by

$$\mathscr{G}(t) = k_{\mathrm{PUSH}} \times \begin{cases} 0 & t \le t_{\mathrm{on}} \\ (t - t_{\mathrm{on}}) \,/\, t_{\mathrm{rise}} & t_{\mathrm{on}} < t \le t_{\mathrm{on}} + t_{\mathrm{rise}} \\ 1 & t_{\mathrm{on}} + t_{\mathrm{rise}} < t \le t_{\mathrm{off}} \\ (t_{\mathrm{off}} + t_{\mathrm{rise}} - t) \,/\, t_{\mathrm{rise}} & t_{\mathrm{off}} < t \le t_{\mathrm{off}} + t_{\mathrm{rise}} \\ 0 & t > t_{\mathrm{off}} + t_{\mathrm{rise}} \end{cases} , \tag{3.67}$$

and it is illustrated in figure 3.2. The definition of the function $\mathscr{G}(t)$ introduces a set of parameters. Two of them remain free parameters that can be used to calibrate the method (see later chapters), k_{PUSH} and t_{rise}. In the following we summarize the different parameters of the PUSH method [87, 88].

[1] See also section A.1 in the appendix.

[2] In the appendix in section A.2 a short derivation of this criterion is given.

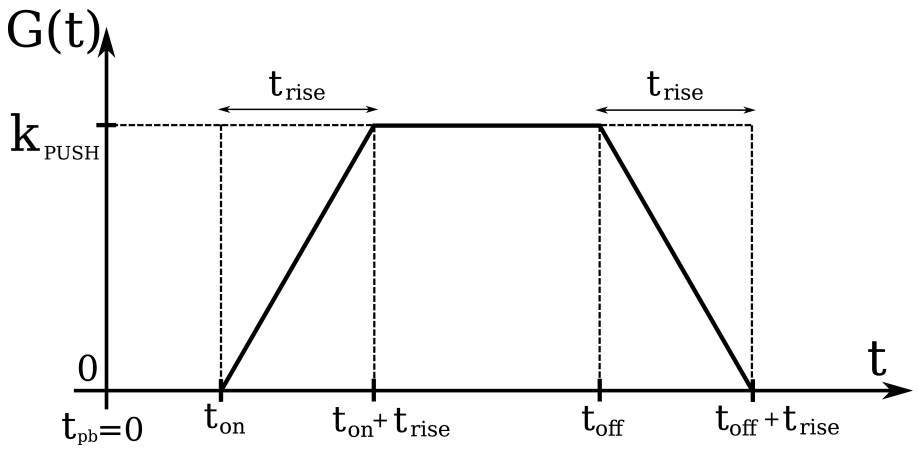

Fig. 3.2.: The function $\mathcal{G}(t)$ defines the temporal behavior of the heating due to the PUSH method. The time PUSH heating begins, $t_{\rm on}$, is fixed by comparisons with multi-dimensional models (it is set to 80 ms in our computations). The free parameters of PUSH, $t_{\rm rise}$ and $k_{\rm PUSH}$, are set by our calibration procedure(s), spanning a wide range from 50 ms to 600 ms, and from 0 (no PUSH heating) to ~5, respectively. We assume that the explosion due to the delayed neutrino-driven mechanism takes place within the first second after core bounce. The time PUSH is switched of is set to $t_{\rm off}$ = 1s.

$k_{\rm PUSH}$ is a factor that controls the amount of extra heating provided by the PUSH method (see figure 3.2). We make use of the μ and τ neutrino luminosity as energy reservoir and σ_0 as reference cross-section. Overall, this suggests a PUSH parameter $k_{\rm PUSH} \gtrsim 1$.

$t_{\rm on}$ sets the time at which the PUSH method is initiated. We connect $t_{\rm on}$ to the time when deviations from spherically symmetric behavior appear in multi-dimensional simulations. The onset of aspherical behavior is related to the advection and convective growth time scale denoted by $\tau_{\rm adv}$ and $\tau_{\rm conv}$. The time scales are given by $\tau_{\rm adv} = \dot{M}_{\rm shock}/M_{\rm gain}$, where $\dot{M}_{\rm shock}$ is the accretion rate at the shock and $M_{\rm gain}$ the mass in the gain region, and $\tau_{\rm conv} = f_{B-V}^{-1}$, where f_{B-V} is the Brunt-Väisäla frequency. Matter convection in the gain region sets in once the relation $\tau_{\rm adv}/\tau_{\rm conv} \gtrsim 3$ is fulfilled [139]. For all the models explored in [87], this relation starts to be fulfilled $t = 0.06 - 0.08$ s. For the studies presented in this thesis, $t_{\rm on}$ is ultimately set to 80 ms.

$t_{\rm rise}$ sets the time scale over which $\mathcal{G}(t)$ increases from zero to the calibrated magnitude of the PUSH heating, $k_{\rm PUSH}$. We connect the parameter $t_{\rm rise}$ with the time scale that characterizes the growth of multi-dimensional perturbations between the the gain radius, $R_{\rm gain}$, and shock radius, $R_{\rm shock}$ (see, e.g., [126]). A lower limit to the parameter $t_{\rm rise}$ is given by the overturn time scale, $\tau_{\rm overturn}$, defined as

$$\tau_{\rm overturn} \sim \frac{\pi(R_{\rm shock} - R_{\rm gain})}{\langle v \rangle_{\rm gain}}, \tag{3.68}$$

where $\langle v \rangle_{\text{gain}}$ denotes the average velocity of matter inside the gain region. In [87] we have found $\tau_{\text{overturn}} \approx 0.05\,\text{s}$ at times $\sim t_{\text{on}}$ and after. For a contracting shock, SASIs are expected to develop around $0.2 - 0.3\,\text{s}$ post bounce [129]. We adapt values of the parameter t_{rise} that have a similar order of magnitude. In the presented studies we used t_{rise} values in the range $0.05\,\text{s} \lesssim t_{\text{rise}} \lesssim 0.6\,\text{s}$.

t_{off} sets the time at which the heating provided by PUSH starts to decrease. Neutrino-driven CCSN explosions are expected to develop for times $t \lesssim 1$ s. This expectation is based on the fast decrease of the neutrino luminosities during the first seconds after core bounce [87]. In the simulations performed with the PUSH method we set the parameter t_{off} to $t_{\text{off}} = 1$ s. Note that heating by PUSH starts decreasing naturally even before 1 s after core bounce due to the decreasing neutrino luminosities. The decrease of the PUSH heating on a time scale of a few hundreds of milliseconds after an explosion has been launched successfully makes results obtained with PUSH largely independent of the choice of t_{off} (for explosions that are not initiated too close to t_{off}).

We see that the quantities t_{on} (it is ultimately set to 80 ms) and t_{off} (set to 1 s) are not free parameters of the PUSH method. Still, PUSH has two remaining free parameters, t_{rise} and k_{PUSH} in particular. The choices for k_{PUSH} and t_{rise} and their effect on the model and on the explosion properties are discussed in the chapters 4 and 5.

With this implementation of PUSH, defined through the equations (3.63), (3.64), (3.66), and (3.67), we have a framework to parametrize spherically symmetric CCSN simulations. The energy deposited by PUSH, E_{push}, can be calculated from the energy deposition rate of PUSH $\mathrm{d}E_{\text{push}}/\mathrm{d}t$ as

$$E_{\text{push}}(t) = \int_{t_{\text{on}}}^{t} \left(\frac{\mathrm{d}E_{\text{push}}}{\mathrm{d}t} \right) \mathrm{d}t' = \int_{t_{\text{on}}}^{t} \left(\int_V Q^{+}_{\text{PUSH}}\, \rho\, \mathrm{d}V \right) \mathrm{d}t'. \tag{3.69}$$

The energy deposited by PUSH and the corresponding energy rate have to be distinguished from the corresponding energy and energy rate obtained by IDSA,

$$E_{\text{idsa}}(t) = \int_{0}^{t} \left(\frac{\mathrm{d}E_{\text{idsa}}}{\mathrm{d}t} \right) \mathrm{d}t' = \int_{0}^{t} \left(\int_{V_{\text{gain}}} \dot{e}_{\nu_e,\bar{\nu}_e}\, \rho\, \mathrm{d}V \right) \mathrm{d}t'. \tag{3.70}$$

Note that PUSH heating only can take place in the gain region due to its definition above (thus, with $V = V_{\text{gain}}$ in equation 3.69 the result is the same). In figure 3.3 we give the energy deposition rates of IDSA and of PUSH (see equations (3.69) and (3.70)), as well as the total energy deposited by neutrinos in the first 800 ms of our simulation for a 15 $\text{M}_\odot$ progenitor (with k_{PUSH} =3.5 and t_{rise} =200 ms). To give an example of a Parametrized

CCSN simulation with the PUSH method we show a first comparison of a model with and without PUSH in the figures 3.4, and 3.5. The presented PUSH runs were done for the progenitor with 15 $M_\odot$ and solar metallicity from Woosley and Heger (2007) [41] and a setting of the PUSH parameters k_{PUSH} =3.5 and t_{rise} =200 ms. In figure 3.4 we show how the shock, PNS, and gain radii as well as the mass accretion onto the PNS and on the shock evolve in time (with and without PUSH). The accretion rate at the shock front is given by $\dot{M}_{\mathrm{shock}} = \mathrm{d}M(R_{\mathrm{shock}})/\mathrm{d}t$, and the accretion rate on the PNS is given by $\dot{M}_{\mathrm{PNS}} = \mathrm{d}M(R_{\mathrm{PNS}})/\mathrm{d}t$. In both expressions, $M(R)$ is the baryonic mass enclosed inside of the sphere of radius R, R_{shock} is the shock radius, and R_{PNS} is the PNS radius ($\rho(R_{\mathrm{PNS}}) = 10^{11}\mathrm{g\,cm^{-3}}$). Figures 3.5 show the corresponding neutrino luminosities and mean energies. These plots illustrate the mentioned problems of one-dimensional CCSN simulations. The neutrino heating behind the shock front is not efficient enough and no explosion is formed in the model without PUSH. PUSH enables a successful explosion. Once an explosion forms successfully, the electron (anti)neutrino luminosities dip because of the reduction of the accretion rate. Also, the mean electron neutrino energy is clearly affected by the onset of explosion. The heating due to infalling matter at the surface of the PNS is reduced and the electron neutrinos, for which the ν sphere radius is largest, immediately reflect this. The heavy lepton neutrino luminosities and mean energies are robust in this phase and well suited to model the energy deposition of the accretion luminosity of electron neutrinos that is present in multi-dimensional simulations.

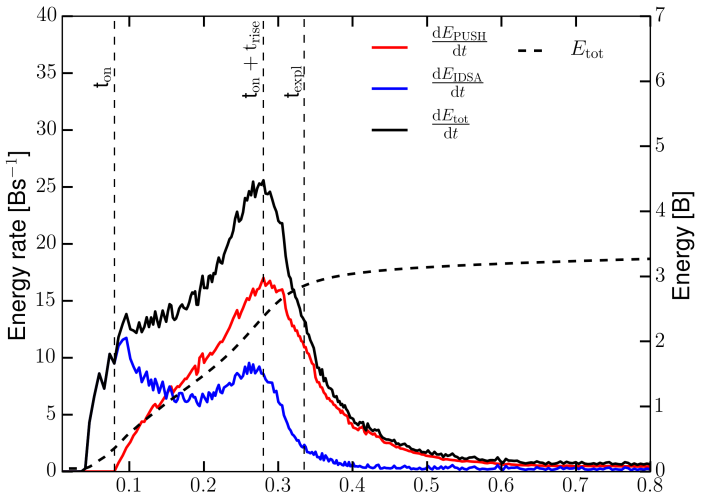

Fig. 3.3.: Energy deposition rates of IDSA and PUSH for the model presented in figures 3.4 and 3.5. Also the total energy deposition is shown. The times when PUSH is switched on, its heating reaches maximum, and the explosion time (defined as the time when the shock reaches and exceeds 500 km) are indicated by dashed lines.

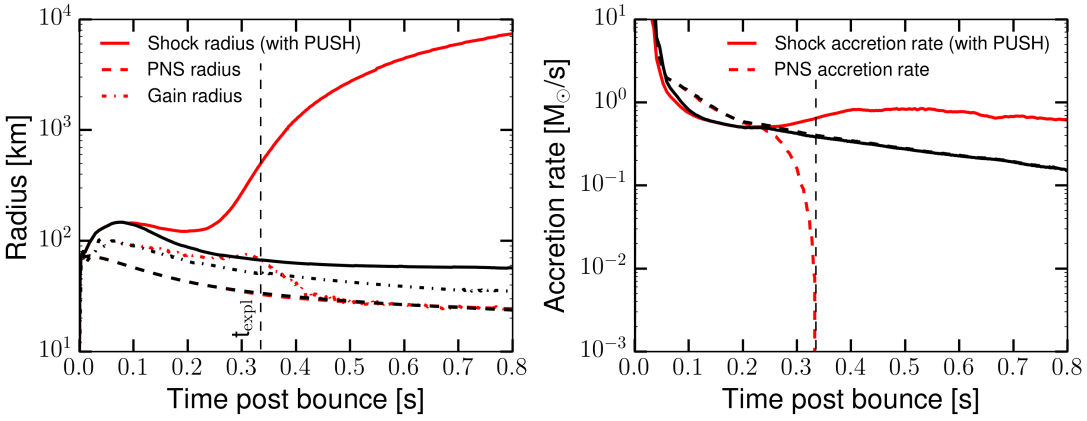

Fig. 3.4.: Temporal evolution of the shock radius, the PNS radius, the gain radius, and the mass accretion rate at the PNS and the shock surface of a 15 $M_\odot$ progenitor with solar metallicity from Woosley and Heger (2007) [41]. We show the results with (red) and without (black) PUSH. The PUSH parameters of the presented run are: k_{PUSH} =3.5, t_{rise} =200 ms. The vertical dashed line indicates the explosion time.

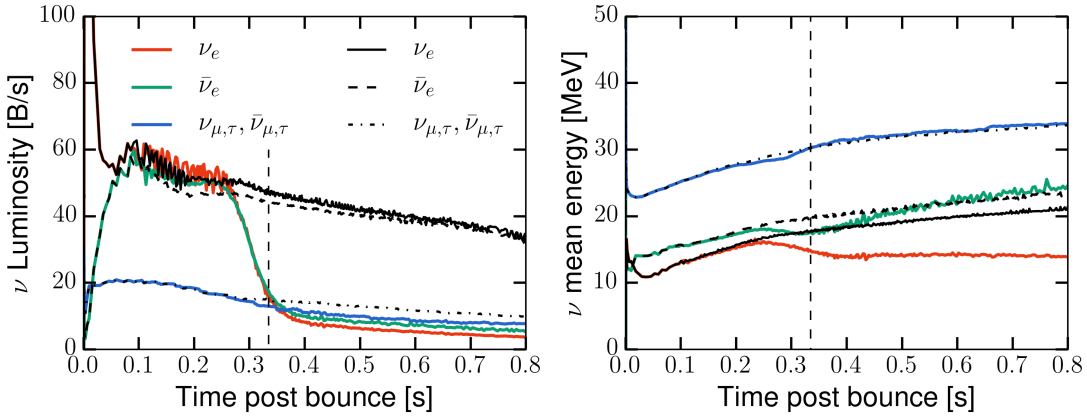

Fig. 3.5.: Temporal evolution of the neutrino luminosities as well as the mean energies for a run with (colored lines) and without (black lines) PUSH for a 15 $M_\odot$ progenitor with solar metallicity from Woosley and Heger (2007) [41]. The PUSH parameters of the presented run are: k_{PUSH} =3.5, t_{rise} =200 ms. The vertical dashed line indicates the explosion time.

3.3 Analysis of PUSH Runs: Post-processing Analysis

An important part of the analysis of PUSH simulations is done with a post-processing approach [87, 88, 140]. This means that quantities that are used to classify and evaluate the whole model are computed after the simulation is finished. We distinguish between the explosion properties (explosion energy, mass cut, and explosion time), and the nucleosynthesis yields. The explosion properties are computed from the simulation profiles. To evaluate the nucleosynthesis yields we create tracer trajectories for detailed nuclear reaction network calculations. To efficiently investigate large samples of CCSN progenitor models we furthermore define a set of criteria to quickly distinguish between different outcomes of simulations, from explosions to black hole formation.

3.3.1 Explosion Properties

Throughout this thesis, we consider the time when the shock reaches and exceeds 500 km as the explosion time t_{expl} (with respect to core bounce) [141]. There are several definitions of t_{expl} in the literature and some other studies (see, e.g., [126, 134]) use different definitions, e.g., the time when the explosion energy increases above 10^{48} erg. We do not expect that the different definitions of t_{expl} result in qualitatively different explosion times. In the following we introduce how the explosion energy and the mass cut is evaluated in our models. An important quantity for the further discussion and analysis of the models is the total energy of matter between an inner boundary at the mass shell m_0 and the upper boundary, the surface of the star, given by

$$E_{\mathrm{total}}(m_0, t) = -\int_M^{m_0} e_{\mathrm{total}}(m, t)\,\mathrm{d}m\,, \tag{3.71}$$

where M is the enclosed baryonic mass at the surface of the star and m_0 is the enclosed baryonic mass of the mass sphere at the inner considered boundary $0 \leq m_0 \leq M$, where m_0 corresponds to a value of the enclosed mass coordinate given in section 3.1.1). The specific total energy is given by

$$e_{\mathrm{total}} = e_{\mathrm{int}} + e_{\mathrm{kin}} + e_{\mathrm{grav}}\,. \tag{3.72}$$

This expression represents the sum of the internal, kinetic, and gravitational specific energies. We use the general-relativistic expressions in the laboratory frame for all these

quantities [89]. The integral of the total energy enclosed in the mass shell includes both the part of the star evolved inside the computational domain of the hydrodynamical simulation, and the outer layers, which are considered as stationary profiles from the progenitor model. In section 3.4 we give a set of criteria to automatically define the portion of the star that is read into the computational domain. The explosion energy of a CCSN simulation is used to compare different models among each other and with observations. For our analysis of the explosion energy we evaluate:

(1) the total energy of the neutrino-heated matter that initiates the shock revival which leads to an explosion,
(2) the nuclear energy released by the recombination of nucleons and alpha-particles into heavy nuclei during the transition to non-NSE conditions,
(3) the energy released by explosive nuclear burning in the shock heated ejected matter,
(4) the total energy associated with the neutrino-driven wind developing after the onset of explosion up to the end of our simulations,
(5) the total (negative) energy of the outer stellar layers (also called the "overburden", see below).

We are not taking into account the variation of the ejecta energy due to the appearance of late-time fallback (i.e., for the results obtained in chapters 4 and 5). This approach is justified as long as the fallback represents only a small fraction of the total ejected mass. We assume that the total energy of the ejected matter (with rest-masses subtracted) converts into kinetic energy of the expanding supernova remnant at times $t \gg t_{\mathrm{expl}}$. Thus, to get the explosion energy we have to consider the thermal energy e_{th} instead of the internal energy e_{int} during the evaluation of the energy of the ejected material. This is done by subtracting the rest mass contribution from e_{total} which is included in the form of e_{int} (see equation 3.47). With this, we define the specific explosion energy

$$e_{\mathrm{expl}} = e_{\mathrm{th}} + e_{\mathrm{kin}} + e_{\mathrm{grav}} \,. \tag{3.73}$$

This leads to the definition of the time- and mass-dependent explosion energy for the fixed mass domain between m_0 and M (see also equation 3.71)

$$H_{\mathrm{expl}}(m_0, t) = -\int_M^{m_0} e_{\mathrm{expl}}(m, t)\, \mathrm{d}m \,. \tag{3.74}$$

This expression can be interpreted as the total energy of this region in a non-relativistic EOS approach, where the rest masses are not included. The time-dependent explosion energy is given by

$$E_{\mathrm{expl}}(t) = H_{\mathrm{expl}}(m_{\mathrm{cut}}(t), t)\,. \tag{3.75}$$

which denotes the energy of the ejected matter above the mass cut $m_{\mathrm{cut}}(t)$. The mass cut is identified with an expression suggested by Bruenn [89]

$$m_{\mathrm{cut}}(t) = m\left(\max(H_{\mathrm{expl}}(m, t)\right)\,. \tag{3.76}$$

Note that the maximum of $H_{\mathrm{expl}}(m, t)$ is evaluated outside the homologous core. Inside the homologous core the specific explosion energy e_{expl} has large positive values once the PNS has formed due to the high compression. Figure 3.6 shows the radial behavior of e_{expl}, illustrating why the mass cut can be found this way.

The specific explosion energy of the outer stellar envelope is dominated by the negative gravitational contribution. In the neutrino-heated region and in the shocked region above it the specific explosion energy is positive. In deeper layers it becomes negative again, as these layers are gravitationally bound. Therefore, the definition given in equation (3.76) for m_{cut} essentially locates the transition from gravitationally unbound to bound layers. We evaluate the final mass cut for $t = t_{\mathrm{final}}$.

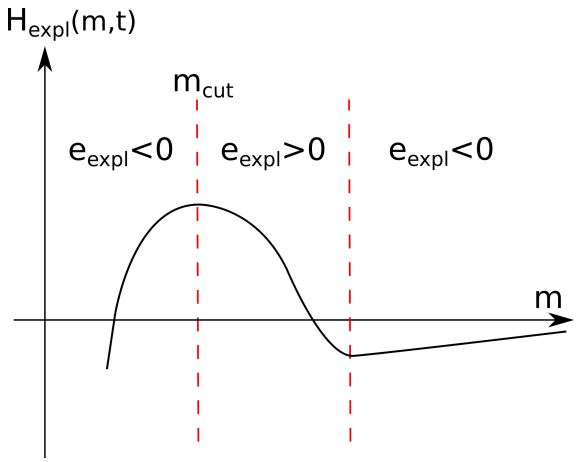

Fig. 3.6.: Illustration of the dependence of the Integral $H_{\mathrm{expl}}(m, t)$ (defined in equation (3.74)) on the ("radial") enclosed mass coordinate m, and the definition of the mass cut. The outer layers are gravitationally bound. In the gain region and the region behind the shock e_{expl} becomes positive. For the gravitationally bound layers of the forming neutron star or black hole we have $e_{\mathrm{expl}} < 0$ again.

If not mentioned otherwise, our final simulation time is of the order of $t_{\mathrm{final}} \gtrsim 4.6$ s, which is always much larger than the explosion time and allows $E_{\mathrm{expl}}(t)$ to saturate (and fulfills $t \gg \tau_{\mathrm{heating}}$, where τ_{heating} denotes the timescale on which neutrinos deposit a substan-

tial amount of energy behind the shock). We consider $E_{\rm expl}(t = t_{\rm final})$ as the explosion energy of our models. In this work, if we use $E_{\rm expl}$ without the time as an argument, the value represents this final explosion energy.

We also want to introduce the diagnostic energy $E^+(t)$, and the overburden energy $E_{\rm ov}(t)$ which was mentioned above (see e.g., [142]). The diagnostic energy is an alternative measure of the explosion energy used in the literature for reasons of comparison (see chapter 4). This quantity is given by the integral of $e_{\rm expl}$ over regions where it is positive. This means it is similar to $E_{\rm expl}(t)$ with the exception that it does not include the gravitationally bound outer layers. The contribution of the gravitationally bound outer layers in the integral given in equation (3.75) is also called "overburden"[142]. If we add the overburden, $E_{\rm ov}(t)$ to the diagnostic energy $E^+(t)$ we obtain the explosion energy defined above (in equation (3.75))

$$E_{\rm expl}(t) \equiv E^+_{\rm ov}(t) = E^+(t) + E_{\rm ov}(t). \tag{3.77}$$

The diagnostic energy is often used in multidimensional simulations as an estimate of the explosion energy at early simulation times, see e.g., [143–147]. It should approach the explosion energy for long enough simulation times, since all matter above the mass cut eventually gets positive specific explosion energies ($E_{\rm ov} \to 0$). An upper limit for the explosion energy is obtained by taking into account the residual recombination energy $E_{\rm rec}(t)$ (not liberated in our simulations) [87, 142]

$$E^+_{\rm ov,r}(t) = E^+_{\rm ov}(t) + E_{\rm rec}(t)\,, \tag{3.78}$$

where $E_{\rm rec}(t)$ represents the energy that would be released if all neutron-proton pairs and all ^{4}He recombined to ^{56}Ni in the regions of positive specific explosion energy.

3.3.2 The Tracer Tool

To evaluate the explosion properties of a large amount of runs at the same time we use the tracer tool, the abtool (abundance tool) and various bash scripts to quickly gather the data. In this section an overview of the mentioned tools that are used to perform a progenitor scan evaluation with PUSH is given. Furthermore, explicit expressions are given for several important quantities such as the specific explosion energy $e_{\rm expl}$. Also, the total and the explosion energy are described in more detail (it is also mentioned how the progenitor profiles enters the expressions). These quantities were introduced in section 3.3.1. The tracer tool uses the hydrodynamics and neutrino data profiles that are computed during a PUSH run and evaluates them to compute tracer data, e.g., $r(t)$, $v(t)$, $\rho(t)$, $T(t)$, $Y_e(t)$ $L_\nu(t)$, $\langle E_\nu(t)\rangle$ (for all neutrino flavors) and computes among others the

total energy and the explosion energy of the simulation. The tracer mass of the presented data is 10^{-3} $M_\odot$. These tracers are used for the computations of the composition of the ejecta (section 3.3.3).

First the progenitor profile and the last time step of the simulation t_{final} are evaluated to determine the enclosed baryon mass in the computational domain m_{sim}, the total mass of the progenitor model m_{prog}, and whether or not the shock left the outer boundary (i.e. if no energy is lost due to the fact that the shock left the domain). This is done by checking the radial velocity of the outer boundary of the computational domain.

The explosion energy defined in equation (3.74) is given by

$$H_{\text{expl}}(m_0, t) = -\int_{m_{\text{sim}}}^{m_0} e_{\text{expl}}(m, t)\,\mathrm{d}m - \int_{m_{\text{prog}}}^{m_{\text{sim}}} e_{\text{expl,prog}}(m, t=0)\,\mathrm{d}m\,, \tag{3.79}$$

where the contribution of the progenitor shells are considered as a static boundary. Here, m_{sim} is the mass enclosed in the computational domain, and m_{prog} is the total progenitor mass (m_0 is the inner boundary for which the expression is evaluated). The specific explosion energy is given by [89]

$$e_{\text{expl}}(m, t) = \Gamma e + \frac{2}{\Gamma + 1}\left(\frac{v^2}{2} - \frac{Gm}{r}\right), \tag{3.80}$$

where e is the specific thermal energy (the internal energy without the contribution of the rest masses, see sections 3.1.3 and 3.3.1), v is the radial velocity of the fluid, m is the enclosed baryon mass, r the radius, and Γ is given by [89, 91]

$$\Gamma(m, t) = \sqrt{1 + \left(\frac{v}{c}\right)^2 - \frac{2Gm}{c^2 r}}. \tag{3.81}$$

In the special relativistic limit the function Γ becomes the Lorentz factor which takes the boost between the inertial and the comoving observers into account [92]. The progenitor mass shells that are not included in the computational domain are evaluated by calculating the specific thermal energy (either with the supernova EOS HS(DD2) or the ideal gas approach as in section 3.1.3), the gravitational energy, and the specific kinetic energy (see equations (3.80) and (3.81)). These quantities are then integrated over the progenitor domain by taking the sum over all zones with masses $\mathrm{d}m$ that are not included inside of the computational domain of the simulation.

The domain included inside the simulation is evaluated in a similar way. The difference in the evaluation is that some quantities have to be interpolated from the grid that is de-

fined on the zone edges to the grid that is defined on the zone centers with zone masses that correspond to the mass differences of neighboring mass shells $dm_{i+\frac{1}{2}}$. The total enclosed masses of the mass shells in the simulation are given by $m_j = \sum_i^{j-1} dm_{i+\frac{1}{2}}$ (see also section 3.1.3 and [89]). With all the quantities of the last time step prepared, the integral given in equation (3.79) is computed by summing over the contributions of the zones in the computational domain from the outer boundary to the inner boundary. The contribution of the outer progenitor zones is computed first (outer boundary of the computational domain at $m_{\mathrm{i,max}}$),

$$H_{\mathrm{expl}}(m_{\mathrm{i,max}}, t_{\mathrm{final}}) = H_{\mathrm{expl}}(m_{\mathrm{sim}}, t_{\mathrm{final}}) = -\int_{m_{\mathrm{prog}}}^{m_{\mathrm{sim}}} e_{\mathrm{expl,prog}}(m, t=0)\,\mathrm{d}m\,, \tag{3.82}$$

and added at the beginning of the iteration described below. The explosion energy at the enclosed mass of the computational domain m_i can then be successively calculated with

$$H_{\mathrm{expl}}(m_i, t_{\mathrm{final}}) = H_{\mathrm{expl}}(m_{i+1}, t_{\mathrm{final}}) + e_{\mathrm{expl}}(m_i, t_{\mathrm{final}}) dm_{i+\frac{1}{2}}. \tag{3.83}$$

This evaluation of $H_{\mathrm{expl}}(m, t_{\mathrm{final}})$ is then used to find the final mass cut of the simulation, which corresponds to the remnant mass (see also section 3.3.1)

$$m_{\mathrm{cut}}(t_{\mathrm{final}}) = m\left(\max(H_{\mathrm{expl}}(m, t_{\mathrm{final}})\right). \tag{3.84}$$

The explosion energy of the run E_{expl} that is used for further analysis or comparisons is given by

$$E_{\mathrm{expl}}(t_{\mathrm{final}}) = H_{\mathrm{expl}}(m_{\mathrm{cut}}(t_{\mathrm{final}}), t_{\mathrm{final}})\,. \tag{3.85}$$

which denotes the energy of the ejected matter above the final mass cut $m_{\mathrm{cut}}(t_{\mathrm{final}})$. Once the final explosion energy and the final mass cut are determined, the time dependent explosion energy for the determined final mass cut is computed for all times.

Based on this analysis of the explosion energy the tracer tool assigns a label to the run that gives the information about the outcome. Thus, the tracer tool uses a set of criteria to decide if the model exploded, formed a black hole, or did not yet form a black hole but failed to explode. These criteria are used to quickly evaluate a large number of PUSH runs (used in chapter 5). We distinguish between successful explosions, black hole formation, and failed explosions. To do this we check the related quantities of the simulation (the explosion time, the explosion energy $E_{\mathrm{expl}}(t_{\mathrm{final}})$, the time of the end of simulation, the evolution of the central density). The simulation outcomes can be defined as follows:

(1) A simulation corresponds to an explosion if it completes the set final simulation time of t_{final} = 5 s (which corresponds approximately to a time of 4.6 s – 4.8 s post bounce) and/or has a saturated positive explosion energy.

(2) A simulation corresponds to a non-exploding model (black hole formation) if a black hole is formed in the 5 s run time.

(3) A simulation corresponds to a failed explosion and hence a non-exploding model which eventually will form a black hole, if it has a negative explosion energy at times when PUSH is no longer active (or at t_{final}).

Summarizing information about the basic explosion properties like the explosion energy or the mass cut are written out in a summary file. Thus, the described criteria allow us to quickly evaluate large samples of PUSH runs. In addition to the explosion energy we also compute the diagnostic energy, the diagnostic energy with overburden and the diagnostic energy with overburden and the recombination energy (as introduced in section 3.3.1) and their rate of change, respectively. Furthermore, also the neutrino quantities are evaluated. In the tracers which are computed for the network post-processing the mean average energies of the neutrinos are computed by dividing the energy luminosity by the number luminosity.

The tracer with a resolution of 10^{-3} $M_{\odot}$ that are computed and written out for the whole simulation represent the 0.34 $M_{\odot}$ above the mass cut (additional ten tracer inside the mass cut are written out but they do not contribute to the ejecta). Note that the resolution of the tracers as well as the evaluated range can be adjusted. The tracer masses that are defined by the mass cut, the resolution and the range, are used to evaluate the respective masses in the simulation output. This is done with the bisection method. The zones that are closest to a tracer mass are used to assign the tracer its properties based on the conditions of the hydro zone neighbors with either a linear, or a logarithmic interpolation (the density, the temperature and the radius are interpolated logarithmically). The tracers are written out for all time steps. One point that might be changed is the way the program accesses files. At the moment each time step involves various I/O actions which makes the tool rather slow, especially when several simulations are evaluated at the same time. The optimal way to evaluate large amounts of tracers as fast as possible is to limit the amount of executed tools with a "qsub" script to about 20 at each given time. An example for the tracer output is given in figure 3.7.

The abundance tool is another tool that has been created to analyze the PUSH runs. This tool has the ability to evaluate a certain mass range of the simulations that can be cho-

sen at the beginning of the evaluation. It is constructed to investigate the different energy components and their temporal evolution inside a given mass range. A meaningful range to investigate the different energies is given by the mass cut and the outer boundary of the hydro simulation. We use the specific energies that are computed for a given time step (these are the same routines that are used by the tracer tool) and evaluate them over the chosen mass range. The integral over the selected range is done by only evaluating the zones of interest and therefore a simple sum of the specific quantity times the zone masses over the respective zones is calculated. Furthermore, this tool is well suited to read-out the abundance distributions off the different time steps for further analysis. With this evaluation of the different energy components we can investigate how they evolve in time.

3.3.3 Nucleosynthesis Yields

We describe how we compute the nucleosynthesis yields that are presented in chapters 4 and 5. The obtained yields are an important part of the fitting process and the analysis of PUSH and can be used in GCE simulations in the future. Note that two different networks, which we both mention here, have been used in chapter 4 and 5. The tracer particles that are used by the networks are computed in the same way.

In chapter 4 we perform nucleosynthesis calculations using the full nuclear network WINNET [61] to predict the composition of the ejecta. These computations include isotopes up to ^{211}Eu covering the neutron-deficient as well as the neutron-rich side of the valley of β-stability. The same reaction rates as in [61] are used. These reaction rates are based on experimentally known rates where available and predictions otherwise. The n-, p-, and alpha-captures are taken from [148]. In [148], known nuclear masses were used where available and the *Finite Range Droplet Model* [117] was used for unstable nuclei far from stability. The used β-decay rates are from the nuclear database *NuDat2*[1].

In chapter 5 we perform the nucleosynthesis calculations using the full nuclear network CFNET. The nuclear reaction network, CFNET [149], follows the abundances of ~2000 isotopes from free neutrons and protons to element Dysprosium to compute the composition of the SN ejecta. The included isotopes cover the neutron-deficient as well as the neutron-rich side of the valley of β-stability. The reaction rates are the same as in [150] and include charged-particle and neutron-capture reactions, electron and positron capture reactions, β-decays, and neutrino and antineutrino capture reactions on free nucle-

[1] http://www.nndc.bnl.gov/nudat2/

ons. These reaction rates are based on the same measurements and descriptions as the ones of WINNET.

The mass tracers used for the nucleosynthesis have the following properties (they are created with the stand alone "tr_network.f90"). To create them we divide the ejecta into different mass elements of 10^{-3} $M_\odot$ each and follow the trajectory of each individual mass element. The tracers contain the time post bounce, the radius, the density, the temperature, the electron fraction, the electron neutrino and electron antineutrino number luminosity, the electron neutrino and antineutrino mean energy, as well as the μ- and τ neutrino number luminosity and the mean energy. The neutrino luminosities are evaluated at the radius of the tracer and the mean energies of the neutrinos are computed by dividing the number luminosity by the energy luminosity of the neutrinos. We are mainly interested in the amounts of ^{56}Ni, ^{57}Ni, ^{58}Ni, and ^{44}Ti. Thus, we only consider the 340 innermost mass elements above the mass cut, corresponding to a total mass of 0.34 $M_\odot$. This can be done because the contribution of the outer mass elements to the production of those nuclei is negligible.

The post-processing for the nucleosynthesis yields is split into two phases. For the times $t < t_{\text{final}}$, we use the temperature and density evolution from the hydrodynamical simulations as inputs for our network. Furthermore, the way the tracers are evaluated is depending on their peak temperature. For each mass element of the ejecta we start the nucleosynthesis post-processing when the temperature drops below 10 GK ($\sim$ 0.86 MeV), using the NSE abundances (determined by the current electron fraction Y_e) as the initial composition. For the tracer particles that never reach 10 GK we start at the moment of bounce and use the abundances from the approximate α-network at this point as the initial composition. For all tracers the further evolution of Y_e in the nucleosynthesis post-processing is determined inside the WINNET and CFNET networks themselves.

At the end of the performed PUSH simulations ($t = t_{\text{final}}$), the temperature and density of the inner zones of the ejecta are still high enough for nuclear reactions to occur ($T \approx 1$ GK and $\rho \approx 2.5 \times 10^3$ g cm^{-3}). We extrapolate the radius, density and temperature of the tracers up to $t_{\text{end}} = 100$ s for an expansion with constant velocity using:

$$r(t) = r(t_{\text{final}}) + t\,v(t_{\text{final}}) \tag{3.86}$$

$$\rho(t) = \rho(t_{\text{final}}) \left(\frac{r(t_{\text{final}})}{r(t)} \right)^2 \tag{3.87}$$

$$T(t) = T[s(t_{\text{final}}), \rho(t), Y_e(t)], \tag{3.88}$$

where r denotes the radial position, v the radial velocity, ρ the density, T the temperature, s the entropy per baryon, and Y_e the electron fraction of the tracer. Furthermore, the temperature is computed at each time step with the EOS of [151]. The expansion described in the equations (3.86)–(3.88) corresponds to an expansion with constant velocity. To illustrate the tracers and how they are distributed we show the radial evolution of the tracer trajectories and their peak temperature for tracers of a PUSH simulation in figure 3.7 (progenitor: 15 $M_\odot$ [41], k_{PUSH} =3.5, t_{rise} =200). The dashed black line indicates the shock front.

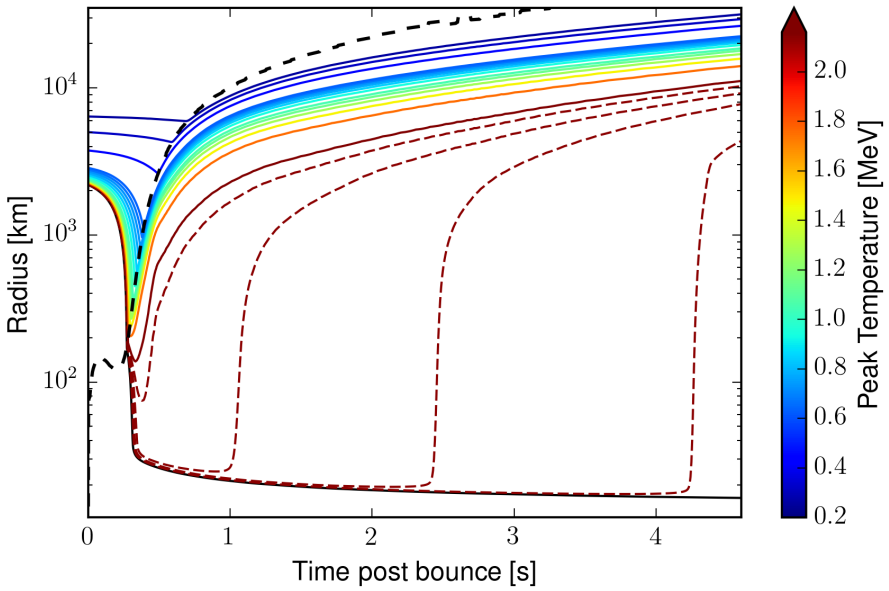

Fig. 3.7.: We show the mass tracers for a PUSH model (progenitor: 15 $M_\odot$ [41], k_{PUSH} =3.5, t_{rise} =200). The black line denotes the PNS surface, the dashed tracer lines (increasing in mass with steps of 10^{-3} $M_\odot$) are delayed ejecta (wind) that reach temperatures around 4 MeV before they are ejected. The colors of the remaining tracers denote their peak temperatures (the first six colored lines are separated by 5×10^{-3} $M_\odot$, then the next six by 10^{-2} $M_\odot$, and the last three tracers are separated by 0.1 $M_\odot$. The black dashed line denotes the shock front.

3.4 Launching and Managing of a Large Number of Runs

The investigation of the explodability and various other aspects of CCSNe with parametrized spherically symmetric simulations using many different progenitors, heating criteria, and parameter sets involves the running and the evaluation of hundredths to thousands of models. To make this task more manageable a collection of tools and scripts written in Fortran, Python, and Bash has been created.

First, we introduce a simple aspect that makes the data management considerably easier, a naming system (also given and used in chapter 5). We introduce the naming system by giving an example and then explain the meaning of the different components. The run name

$$\text{s20.0\_t200\_k3.5} \equiv [\text{Progenitor set and metallicity}][\text{Model mass}]\_[\text{t}_{\text{rise}}]\_[\text{k}_{\text{PUSH}}], \quad (3.89)$$

corresponds to a model using the $20\,\text{M}_\odot$ progenitor with the setting t_{rise}=200 ms and k_{PUSH}=3.5. Thus, the PUSH parameters are directly included in the name of the run (this also corresponds to the folder name of the corresponding data of the simulation). The first letter or letters of the name indicate the progenitor sample that is used. This letter is followed by the ZAMS mass of the used progenitor, a t and the used t_{rise} parameter, and a k and the used k_{PUSH} parameter (separated by an underscore). We use the progenitor sets of Woosley, Heger and Weaver (2002) and Woosley and Heger (2007) [40, 41]. The naming system evolved historically and therefore the choice of the first letters does not follow a consistent intrinsic logic. The set of the non-rotating progenitors of Woosley Heger and Weaver (2002) with the metallicities $Z = Z_\odot$, $Z = Z_\odot \times 10^{-4}$, and $Z = 0$ correspond to the letters s, u, and z. The set of non-rotating progenitors of Woosley and Heger (2007) with solar metallicity $Z = Z_\odot$ corresponds to the letter w. Thus, the example given in Relation (3.89) corresponds to a progenitor from the set of Woosley, Heger and Weaver (2002) with solar metallicity. This naming scheme has proved useful in the context of the presented work.

The runs are initialized with a Python script that copies the programs source folder with the correct progenitor (we do not include all the progenitors in the source folder because they partially have sizes of ~ 40 MB) and creates the desired sample of run folders. This process involves the adjustment of Bash scripts that are adjusted to launch the different runs (with qsub we submit jobs to the scheduler by the sun grid engine). Before this Bash scripts are initiating the runs, the Python script changes command lines in the Bash scripts which alter parameter entries of the input files that are read in by the CCSN simulation at the moment of launch. With this chain of scripts we can launch several hundreds of runs within a few minutes by only adjusting the Python script which automatically takes care of the other scripts.

The initial choice of domain size has been set by hand in the input files for earlier versions but is automatized in the newest version of the numerical setup of PUSH (used for the runs presented in chapter 5). In order to follow the shock of the supernova explosion that is propagating outwards with a velocity of the order of $\langle v_{\text{shock}} \rangle \sim 10^9$ cm s^{-1} for a time t_{sim} of the simulation that is long enough to observe a saturation of the explosion

energy ($t_{\rm sim} \sim 1 - 10$s), one should include a computational domain that ranges up to $t_{\rm sim} \times \langle v_{\rm shock} \rangle$. In the automatic read-in, the progenitor is mapped onto the computational domain up to an upper limit that is set by one of the following criteria (the criteria that is fulfilled first is the one which is applied):

(1) The density drops below $\rho(r) < 10\ \mathrm{gcm}^{-3}$,

(2) The radius exceeds the value $r > 10^{10}$ cm,

(3) The read-in stellar mass exceeds $M(r) > 10\ \mathrm{M}_{\odot}$.

These criteria are useful to quickly set up large simulation samples when a large progenitor set is investigated (see chapter 5).

4

Results 1: Dependencies and the First Calibration of the PUSH Method[1]

In this chapter we present the results obtained with the PUSH method introduced in chapter 3. The here presented material has been published in Perego, Hempel, Fröhlich, Ebinger et al. (2015) [87] and consists of an overview of different methods to artificially trigger explosions in spherical symmetric CCSN simulations, the introduction and calibration of the PUSH method, and the analysis of the obtained results first published in the paper[2]. In chapter 5 we update and improve the PUSH method and eventually apply a recalibrated version to extended progenitor star sets in order to study the explodability, explosion, and remnant properties of neutrino-driven CCSNe across the ZAMS mass range.

In the past, predictions of SN nucleosynthesis relied on artificially triggered explosions, either using a piston (e.g. [152–154]) or a thermal energy bomb (e.g., [155, 156]). For the piston model, the motion of a mass point is specified along a ballistic trajectory. For the thermal energy bomb, explosions are triggered by adding thermal energy to a mass zone. In both cases, additional energy is added to the system to trigger an explosion. In addition, the mass cut (bifurcation between the proto-neutron star (PNS) and the ejecta) and the explosion energy are free parameters which have to be constrained from the mass of the ^{56}Ni ejecta. While these approaches are appropriate for the outer layers, where the nucleosynthesis mainly depends on the strength of the shock wave, they are clearly incorrect for the innermost layers. There, the conditions and the nucleosynthesis are di-

[1] The content of this chapter has been published in Perego et al. (2015), The Astrophysical Journal, Volume 806, Number 2 [87].

[2] With the following exceptions: Figures 4.1 and 4.2 have been added or redone. Table 4.1 only shows the compactness at onset of collapse because of spatial reasons. The definition of the diagnostic energy, the overburden, and the recombination energy is now given in section 3.3.1 and not in section 4.3.7.

rectly related to the physics of collapse and bounce, and to the details of the explosion mechanism. Besides the piston and thermal bomb methods, another widely used way to artificially trigger explosions is the so-called "neutrino light-bulb". In this method, the PNS is excised and replaced with an inner boundary condition which contains an analytical prescription for the neutrino luminosities. The neutrino transport is replaced by neutrino absorption and emission terms in optically thin conditions. Suitable choices of the neutrino luminosities and energies can trigger neutrino-driven explosions (e.g., [157–161]). The light-bulb method has also been used to investigate models with respect to their dimensionality. The transition from spherical symmetry (1D) to axisymmetry (2D) delivers the new degree of freedom to bring cold accreting matter down to the neutrinospheres while matter in other directions can dwell longer in the gain region and efficiently be heated by neutrinos [162]. The standing accretion shock instability (SASI, e.g., [160, 163–167]) strongly contributes to this effect in 2D light-bulb models and leads to strong polar oscillations of expansion during the unfolding of the explosion [133]. It was first expected that the trend toward a smaller critical luminosity for successful explosions will continue as one goes from 2D to three-dimensional (3D) models [127, 134], but other studies pointed toward the contrary [128, 131]. One has to keep in mind, that a light bulb approach might not include the full coupling between the accretion rate and the neutrino luminosity. However, recent models that derive the neutrino luminosity from a consistent evolution of the neutron star support the result that 2D models show faster explosions than 3D models [130, 142, 147, 168]. Most important for this work is a finding that is consistent with all above investigations: In 3D there is no preferred axis. The 3D degrees of freedom lead to a more efficient cascade of fluid instabilities to smaller scales. In spite of vivid fluid instabilities, the 3D models show in their overall evolution a more pronounced sphericity than the 2D models. Hence their average conditions resemble more closely the shock expansion that would be obtained by an exploding 1D model.

In a 1D model with detailed Boltzmann neutrino transport two other methods to trigger explosions using neutrinos have been used [89, 169]. These "absorption methods" aim at increasing the neutrino energy deposition in the heating region by mimicking the expected net effects of multi-dimensional simulations. In one case, the neutral-current scattering opacities on free nucleons are artificially decreased to values between 0.1 and 0.7 times the original values. This leads to increased diffusive neutrino fluxes in regions of very high density. The net results are a faster deleptonization of the PNS and higher neutrino luminosities in the heating region. In the other case, explosions are enforced by multiplying the reaction rates for neutrino absorption on free nucleons by a constant factor. To preserve detailed balance, the emission rates also have to be multiplied by the same factor. This reduces the timescale for neutrino heating and again results in a more

efficient energy deposition in the heating region. However, the energy associated with these explosions were always weak.

Recently, [141] have presented a more sophisticated light-bulb method to explode spherically symmetric models using neutrino energy deposition in post-shock layers. They use an approximate, grey neutrino transport and replace the innermost 1.1 $M_\odot$ of the PNS by an inner boundary. The evolution of the neutrino boundary luminosity is based on an analytic cooling model of the PNS, which depends on a set of free parameters. These parameters are set by fitting observational properties of SN 1987A for progenitor masses around 20 $M_\odot$ (see also [170]).

Artificial supernova explosions have been obtained by other authors using a grey leakage scheme that includes neutrino heating via a parametrized charged-current absorption scheme [171] in spherically symmetric simulations [172].

The PUSH method enables the deposition of a fraction of the luminosity of the heavy flavor neutrinos emitted by the PNS in the gain region in order to increase the neutrino heating efficiency. An accurate treatment of the electron fraction of the ejecta is ensured through a spectral neutrino transport scheme for ν_e and $\bar{\nu}_e$ and a detailed evolution of the PNS. This work covers the observed correlation between explosion dynamics of CCSN progenitors and their compactness as well as the possible fitting of SN1987A with the PUSH method for a set of red giant progenitors with solar metallicity in the mass range between 18 $M_\odot$ and 21 $M_\odot$ from Woosley, Heger and Weaver (2002) [40]. PUSH provides a framework to study many important aspects of CCSNe for large progenitor sets: explosive supernova nucleosynthesis, neutron-star remnant masses, explosion energies, and other aspects where until recently full multi-dimensional simulations were too expensive and traditional piston or thermal bomb models do not capture all the relevant physics.

4.1 Initial Models

For this PUSH study, we use solar-metallicity, non-rotating stellar models from the stellar evolution code KEPLER [40]. Our set includes 16 pre-explosion models with zero-age main sequence (ZAMS) mass between 18.0 $M_\odot$ and 21.0 $M_\odot$ in increments of 0.2 $M_\odot$. These models have been selected to have ZAMS mass around 20 $M_\odot$, similar to the progenitor of SN1987A (e.g., [173]). We label the models by their ZAMS mass. In figure 4.1, the density profiles of the progenitor models are shown. For each of them the compact-

ness parameter ξ_M is defined following [172] by the ratio of a given mass M and the radius $R(M)$ which encloses this mass:

$$\xi_M \equiv \frac{M/M_\odot}{R(M)/1000\text{km}}. \tag{4.1}$$

Typically, either $\xi_{1.75}$ or $\xi_{2.5}$ are used. The compactness can be computed at the onset of collapse or at bounce, as suggested by [172]. For our progenitors, the difference in the compactness parameter between these two moments is not significant for our discussions. Thus, for simplicity, in the following we will use $\xi_{1.75}$ computed at the onset of the collapse. The progenitor models considered here fall into two distinct families of compactness: low compactness ($\xi_{1.75} < 0.45$; LC models) and high compactness ($\xi_{1.75} > 0.45$; HC models), see table 4.1. Figure 4.2 shows the compactness as function of ZAMS mass for the progenitors of this study. The non-monotonous behavior is a result of the evolution before collapse. The mass range between 19 and 21 $M_\odot$ is particularly prone to variations of the compactness. For a detailed discussion of the behavior of the compactness as function of ZAMS mass see [174].

4.2 Fitting and Results

To test the PUSH method, we perform a large number of runs where we vary the free parameters and explore their impact on the explosion properties. We also analyze in detail the basic features of the simulations and of the explosions in connection with the properties of the progenitor star. Finally, we fit the free parameters in the PUSH method to reproduce observed properties of SN1987A for a progenitor star in the range 18-21 $M_\odot$.

4.2.1 General Effects of Free Parameter Variations

k_{PUSH}

The parameter with the most intuitive and strongest impact on the explosion is k_{PUSH}. Its value directly affects the amount of extra heating which is provided by PUSH. As expected, larger values of k_{PUSH} (assuming all other parameters to be fixed) result in the explosion being more energetic and occurring earlier. In addition, a faster explosion implies a lower remnant mass, as there is less time for the accretion to add mass to the forming PNS.

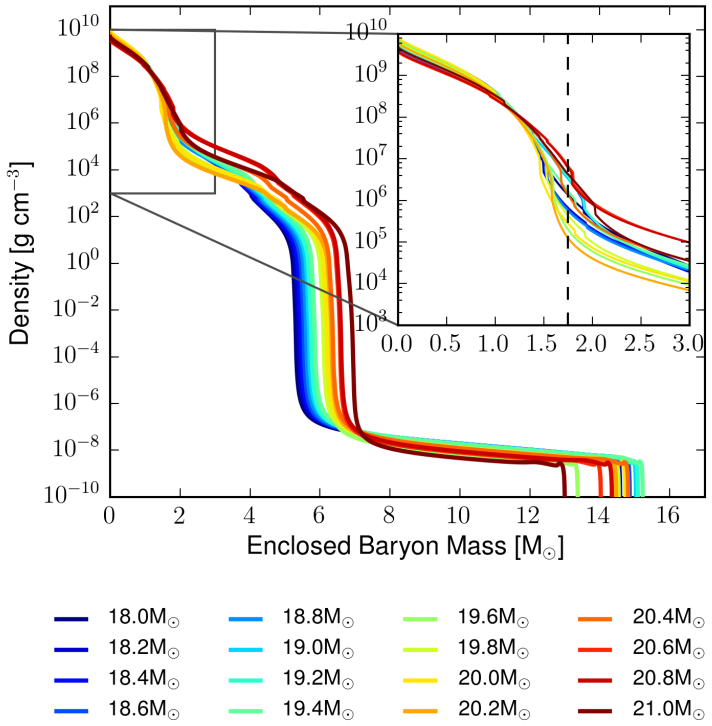

(a) Progenitors between 18 and 21 $M_\odot$.

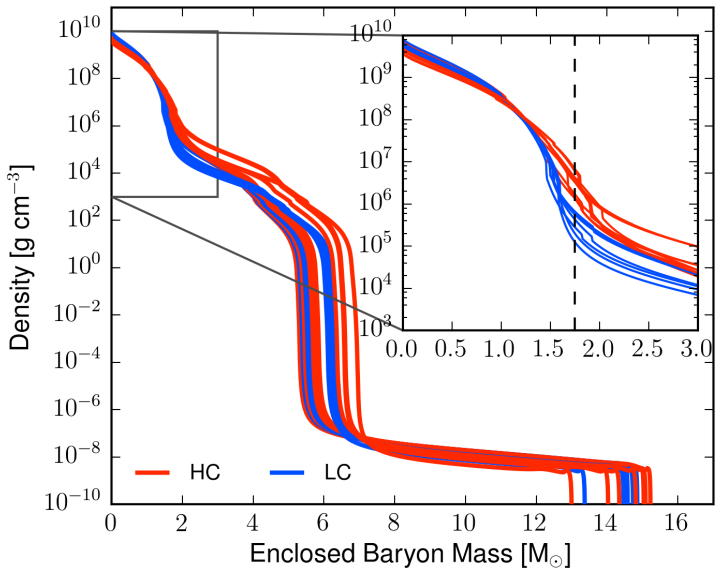

(b) Progenitors sorted into LC and HC.

Fig. 4.1.: Density profiles as function of ZAMS mass for the progenitor models included in this study (18.0 $M_\odot$ to 21.0 $M_\odot$). HC models are shown in red, LC models are shown in blue. The vertical line in the inset is located at 1.75 $M_\odot$ and indicates that mass at which the compactness parameter $\xi_{1.75}$ is determined (see equation (4.1)).

Beyond these general trends with k_{PUSH}, the detailed behavior depends also on the compactness of the progenitor. For all 16 progenitor models in the 18-21 $M_\odot$ ZAMS mass

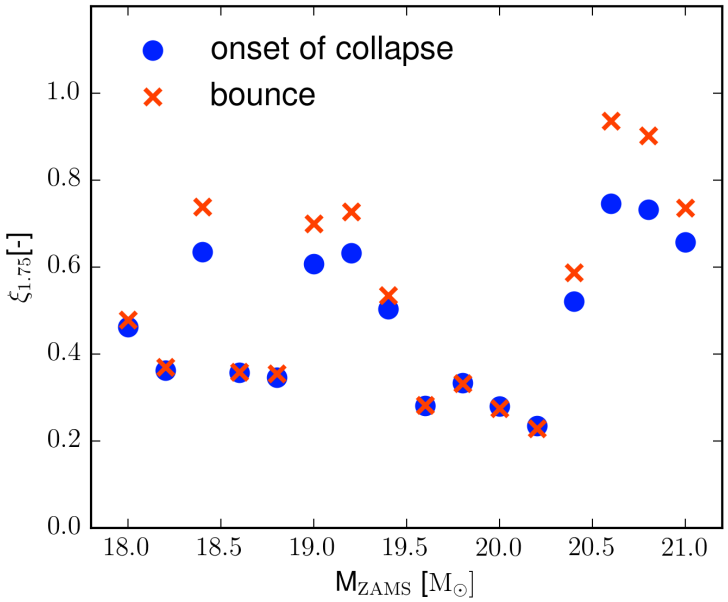

Fig. 4.2.: Compactness $\xi_{1.75}$ as function of ZAMS mass for our pre-explosion models at the onset of collapse (blue dots) and at bounce (red crosses).

range, we have explored several PUSH models, varying k_{PUSH} between 0.0 and 4.0 in increments of 0.5 but fixing t_{on} = 80 ms and t_{rise} = 150 ms. For $k_{\mathrm{PUSH}} \leqslant 1$, none of the models explode and for k_{PUSH} = 1.5 only the lowest compactness models explode. Figure 4.3 shows the explosion energy, the explosion time and the (baryonic) remnant mass as function of the progenitor compactness for $k_{\mathrm{PUSH}} = 1.5, 2.0, 3.0, 4.0$. A distinct behavior between low and high compactness models is seen. The LC models ($\xi_{1.75} < 0.4$) result in slightly weaker and faster explosions, with less variability in the explosion energy and in the explosion time for different values of k_{PUSH}. Even for relatively large values of k_{PUSH}, the explosion energies remain below 1 Bethe. On the other hand, the HC models ($\xi_{1.75} > 0.45$) explode stronger and later, with a larger variation in the explosion properties. In this case, for high enough values of k_{PUSH} ($\gtrsim 3.0$), explosion energies of $\gtrsim 1$ Bethe can be obtained. The HC models also lead to a larger variability of the remnant masses, even though this effect is less pronounced than for the explosion time or energy. For the values of k_{PUSH} used here, we obtain (baryonic) remnant masses from approximately 1.4 to 1.9 $M_\odot$. The differences of LC and HC models will be investigated further in section 4.2.3.

There are three models with $0.37 \lesssim \xi_{1.75} \lesssim 0.50$ (corresponding to ZAMS masses of 18.0 (HC), 18.2 (LC), and 19.4 $M_\odot$ (HC)) which do not follow the general trend. In particular, we find the threshold value of k_{PUSH} for successful explosions to be higher for these mod-

M_{ZAMS} ($M_\odot$)	$\xi_{1.75}$ at collapse	$\xi_{2.5}$ at collapse	M_{prog} ($M_\odot$)	M_{Fe} ($M_\odot$)	M_{CO} ($M_\odot$)	M_{He} ($M_\odot$)	M_{env} ($M_\odot$)
18.2	0.37	0.173	14.58	1.399	4.174	5.395	9.186
18.6	0.365	0.170	14.85	1.407	4.317	5.540	9.313
18.8	0.357	0.166	15.05	1.399	4.390	5.613	9.435
19.6	0.282	0.118	13.37	1.461	4.959	6.243	7.125
19.8	0.334	0.135	14.54	1.438	4.867	6.112	8.428
20.0	0.283	0.125	14.73	1.456	4.960	6.215	8.517
20.2	0.238	0.104	14.47	1.458	5.069	6.342	8.125
18.0	0.463	0.199	14.50	1.384	4.104	5.314	9.187
18.4	0.634	0.185	14.82	1.490	4.238	5.459	9.366
19.0	0.607	0.191	15.03	1.580	4.461	5.693	9.341
19.2	0.633	0.191	15.08	1.481	4.545	5.760	9.325
19.4	0.501	0.185	15.22	1.367	4.626	5.860	9.365
20.4	0.532	0.192	14.81	1.500	5.106	6.376	8.433
20.6	0.742	0.278	14.03	1.540	5.260	6.579	7.450
20.8	0.726	0.271	14.34	1.528	5.296	6.609	7.735
21.0	0.654	0.211	13.00	1.454	5.571	6.969	6.026

Tab. 4.1.: ZAMS mass, compactness $\xi_{1.75}$ and $\xi_{2.5}$ at the onset of collapse and at bounce, total progenitor mass at collapse (M_{prog}), mass of the iron core (M_{Fe}), carbon-oxygen core (M_{CO}), and helium core (M_{He}), and mass of the hydrogen-rich envelope (M_{env}) at collapse, for all the progenitor models included in this study. The top part of the table includes the low-compactness progenitors (LC; $\xi_{1.75} < 0.4$ at collapse), the bottom part includes the high-compactness progenitors (HC; $\xi_{1.75} > 0.45$ at collapse). Table adapted from [87].

els. A common feature of these three models is that they have the lowest Fe-core mass of all the models in our sample and the highest central densities at the onset of collapse.

The choice of t_{rise} does not affect the observed trends with k_{PUSH}: similar behaviors are also seen for $50\,ms \lesssim t_{rise} \lesssim 250\,ms$.

t_{on}

To test the sensitivity of our method to the parameter t_{on}, we compute models with $k_{PUSH} = 2.0$ and $t_{rise} = 0.15\,s$ for a very large onset parameter, $t_{on} = 120\,ms$. We compare the corresponding results with the ones obtained for $t_{on} = 80\,ms$. As expected, the shock revival happens slightly later (with a temporal shift of $\sim 30\,ms$), the explosion energies are smaller (by ~ 0.05 B) and the remnant masses are marginally larger (by $0.08\,M_\odot$). However, all the qualitative behaviors described above, as well as the distinction between

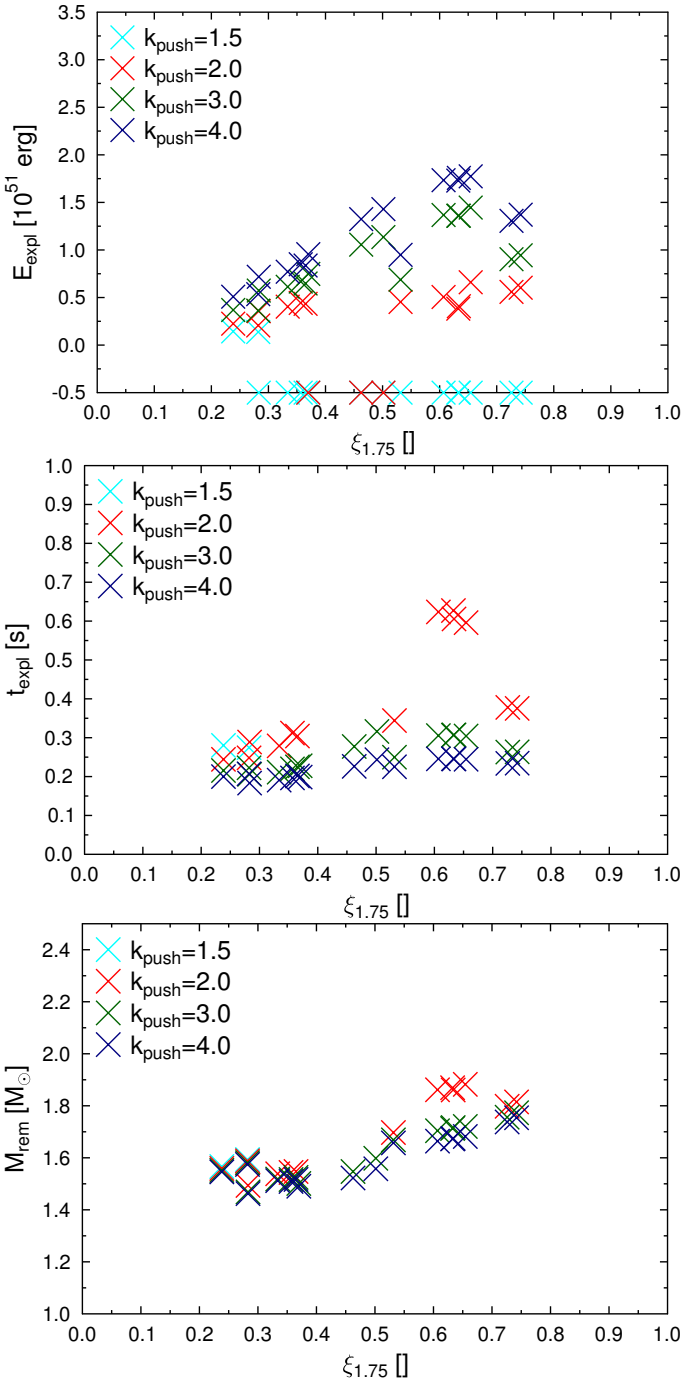

Fig. 4.3.: Explosion energies (top), explosion times (middle), and (baryonic) remnant mass (bottom) as function of compactness for k_{PUSH} 1.5, 2.0, 3.0, and 4.0, and fixed t_{rise} = 0.15 s for all progenitor models included in this study (ZAMS mass between 18.0 and 21.0 $\mathrm{M}_{\odot}$). Non-exploding models are indicated with $E_{\mathrm{expl}} = -0.5$ B in the top panel and are omitted in the other panels. Figures taken from [87].

high and low compactness models, do not show any dependence on t_{on}. In the following, we will always assume $t_{\mathrm{on}} = 80\,\mathrm{ms}$.

k_{PUSH} & t_{rise}

Previously, we have investigated the dependency of the model on the single parameters k_{PUSH} and t_{on}. Now, we explore the role of t_{rise} in combination with k_{PUSH}. For this, we approximately fix the explosion energy to the canonical value of ~ 1 B for the high compactness models (corresponding, for example, to the previously examined models with $k_{\mathrm{PUSH}} = 3.0$ and $t_{\mathrm{rise}} = 150\,\mathrm{ms}$), and investigate which other combinations of k_{PUSH} and t_{rise} result in the desired explosion energy. We restrict our explorations to a sub-set of progenitor models (18.0 $\mathrm{M}_\odot$, 18.6 $\mathrm{M}_\odot$, 19.2 $\mathrm{M}_\odot$, 19.4 $\mathrm{M}_\odot$, 19.8 $\mathrm{M}_\odot$, 20.0 $\mathrm{M}_\odot$, 20.2 $\mathrm{M}_\odot$ and 20.6 $\mathrm{M}_\odot$) that spans the $\xi_{1.75}$-range of all 16 progenitors. Figure 4.4 summarizes the explosion energies, explosion times, and remnant masses for various combinations of k_{PUSH} and t_{rise} for progenitors of different compactness. The required constraint can be obtained by several combinations of parameters, which lie on a curve in the k_{PUSH}-t_{rise} plane. As a general result, a longer t_{rise} requires a larger k_{PUSH} to obtain the same explosion energy. This can be understood from the different roles of the two parameters: while k_{PUSH} sets the maximum efficiency at which PUSH deposits energy from the reservoir represented by the $\nu_{\mu,\tau}$ luminosity, t_{rise} sets the time scale over which the mechanism reaches this maximum. Together, they control the slope of $\mathcal{G}(t)$ in the rising phase (see figure 3.2). A model with a longer rise time reaches its maximum efficiency later, at which time the luminosities have already decreased and a part of the absorbed energy has been advected on the PNS or re-emitted in the form of neutrinos. To compensate for these effects, a larger k_{PUSH} is required for a longer t_{rise}. This is seen in figure 4.5, where we plot the cumulative neutrino contribution ($E_{\mathrm{push}} + E_{\mathrm{idsa}}$) and its time derivative for four runs of the 18.0 $\mathrm{M}_\odot$ progenitor model, but with different combinations of t_{rise} and k_{PUSH}. Runs with larger parameter values require PUSH to deposit more energy (see ($E_{\mathrm{push}} + E_{\mathrm{idsa}}$) at $t \approx t_{\mathrm{expl}}$), and the corresponding deposition rates are shifted towards later times. Moreover, for increasing values of t_{rise}, the explosion time t_{expl} becomes larger, but the interval between ($t_{\mathrm{on}} + t_{\mathrm{rise}}$) and t_{expl} decreases. Despite the significant variation of k_{PUSH} between different runs, the peak values of $\mathrm{d}(E_{\mathrm{push}} + E_{\mathrm{idsa}})/\mathrm{d}t$ at the onset of the shock revival that precedes the explosion are very similar in all cases.

t_{off}

Even though PUSH is active up to $t_{\mathrm{off}} + t_{\mathrm{rise}} \gtrsim 1\,\mathrm{s}$, its energy deposition reduces progressively on a timescale of a few 100 ms after the explosion has set in (see figure 4.5). This shows explicitly that the value of t_{off} does not have important consequences in our sim-

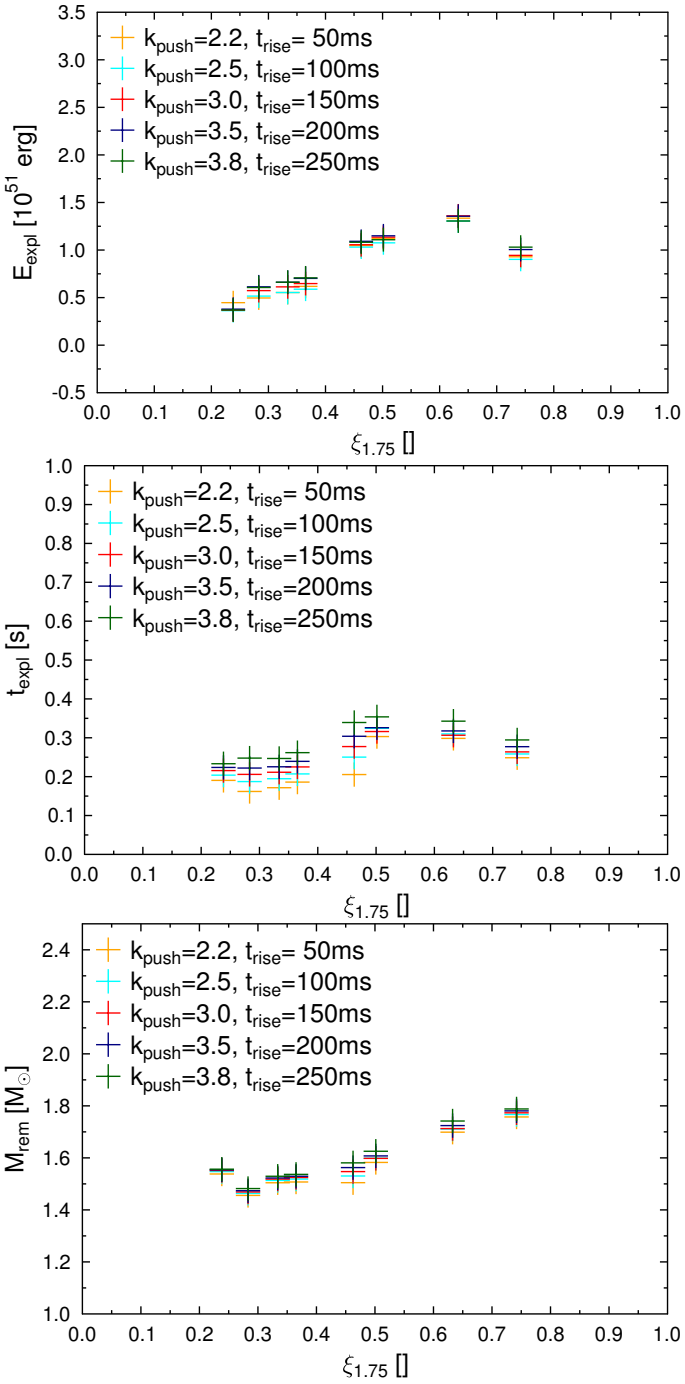

Fig. 4.4.: Explosion energies (top), explosion times (middle), and (baryonic) remnant mass (bottom) as function of compactness for pairs of k_{PUSH} and t_{rise}, and for the progenitor models with ZAMS mass 18.0, 18.6, 19.2, 19.4, 19.8, 20.0, 20.2, and 20.6 $\mathrm{M}_{\odot}$. Figures taken from [87].

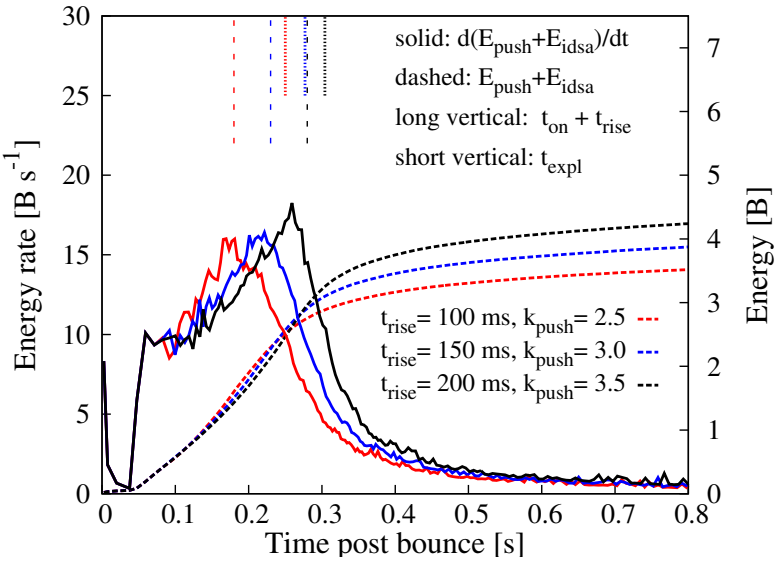

Fig. 4.5.: Temporal evolution of the total neutrino energy contribution inside the gain region ($E_{\rm push} + E_{\rm idsa}$) (solid lines) and of its time derivative (dashed lines), for four runs with the same ZAMS progenitor mass (18.0 $M_\odot$), but different combinations of PUSH parameters $t_{\rm rise}$ and $k_{\rm PUSH}$. For each run, the vertical lines correspond to $t = t_{\rm on} + t_{\rm rise}$ (long, dashed) and to $t_{\rm expl}$ (short, dot-dashed). Figure taken from [87].

ulations, at least as long as we have typical explosion times well below one second. The observed decrease of the PUSH energy deposition rate after the launch of the explosion will be explained in section 4.2.3.

4.2.2 Contributions to the Explosion Energy

In the following, we discuss the contributions to and the sources of the explosion energy, i.e., we investigate how the explosion energy is generated. This is done in several steps: first, we have a closer look at the neutrino energy deposition. Then we show how it relates to the increase of the total energy of the ejected layers, and finally how this increase of the total energy transforms into the explosion energy. For this analysis, we have chosen the 19.2 and 20.0 $M_\odot$ ZAMS mass progenitor models as representatives of the HC and LC samples, respectively. We consider their exploding models obtained with $t_{\rm on} = 80$ ms, $t_{\rm rise} = 150$ ms, and $k_{\rm PUSH} = 3.0$. A summary of the explosion properties can be found in table 4.2.

The table shows that for both models neutrinos are required to deposit a net cumulative energy ($E_{\rm push} + E_{\rm idsa}$) much larger than $E_{\rm expl}$ to revive the shock and to lead to an explosion that matches the expected energetics. For the two reference runs, when the PUSH contribution is switched off ($t = t_{\rm off} + t_{\rm rise}$), the cumulative deposited energy is ~ 4

Quantity		HC	LC
ZAMS	($M_\odot$)	19.2	20.0
$\xi_{1.75}$	(-)	0.637	0.283
$t_{\rm on}$	(ms)	80	
$t_{\rm rise}$	(ms)	150	
$k_{\rm PUSH}$	(-)	3.0	
$t_{\rm expl}$	(ms)	307	206
$M_{\rm remn}$	($M_\odot$)	1.713	1.469
$E_{\rm expl}$ ($t_{\rm final}$)	(B)	1.36	0.57
$E_{\rm push}$ ($t_{\rm off} + t_{\rm rise}$)	(B)	3.51	1.08
$E_{\rm idsa}$ ($t_{\rm off} + t_{\rm rise}$)	(B)	2.76	1.01
$E_{\rm idsa}$ ($t_{\rm final}$)	(B)	4.10	2.11

Tab. 4.2.: Explosion properties for two reference runs. These two runs are used to compare the HC and LC samples. Table taken from [87].

times larger than $E_{\rm expl}$. This can also be inferred from figure 4.5 for other runs. That ratio increases further up to ~ 5.5 at $t = t_{\rm final}$, due to the neutrino energy deposition happening at the surface of the PNS which generates the ν-driven wind. According to equations (3.69) and (3.70), $E_{\rm push}$ and $E_{\rm idsa}$ are the total energies which are deposited in the (time-dependent) gain region. This neutrino energy deposition increases the internal energy of the matter flowing in that region. However, since the advection timescale is much shorter than the explosion timescale, a large fraction of this energy is advected onto the PNS surface by the accreting mass before the explosion sets in, and hence does not contribute to the explosion energy. Only the energy deposited by neutrinos in the region above the final mass cut will eventually contribute to the explosion energy.

To identify this *relevant* neutrino contribution, in figure 4.6 we show the time evolution of the integrated net neutrino energy deposition $E_\nu(m_{\rm cut}^{\rm fin}, t)$ within the domain above the fixed mass $m_{\rm cut}^{\rm fin} = m_{\rm cut}(t_{\rm final})$. We choose $m_{\rm cut}^{\rm fin}$ to include all the relevant energy contributions to the explosion energy, up to the end of our simulations. Despite the significant differences in magnitudes, the two models show overall similar evolutions. If we compare $E_\nu(m_{\rm cut}^{\rm fin}, t)$ at late times with $(E_{\rm push}(t_{\rm off} + t_{\rm rise}) + E_{\rm idsa}(t_{\rm final}))$ from table 4.2, we see that it is significantly smaller. About two thirds of the energy originally deposited in the gain region are advected onto the PNS and hence do not contribute to the explosion energy.

In addition to the neutrino energy deposition, in figure 4.6 we also show the variation of the total energy for the domain above $m_{\rm cut}^{\rm fin}$, i.e.,
$\Delta E_{\rm total}(m_{\rm cut}^{\rm fin}, t) = E_{\rm total}(m_{\rm cut}^{\rm fin}, t) - E_{\rm total}(m_{\rm cut}^{\rm fin}, t_{\rm initial})$, where $t_{\rm initial}$ is the time when we start

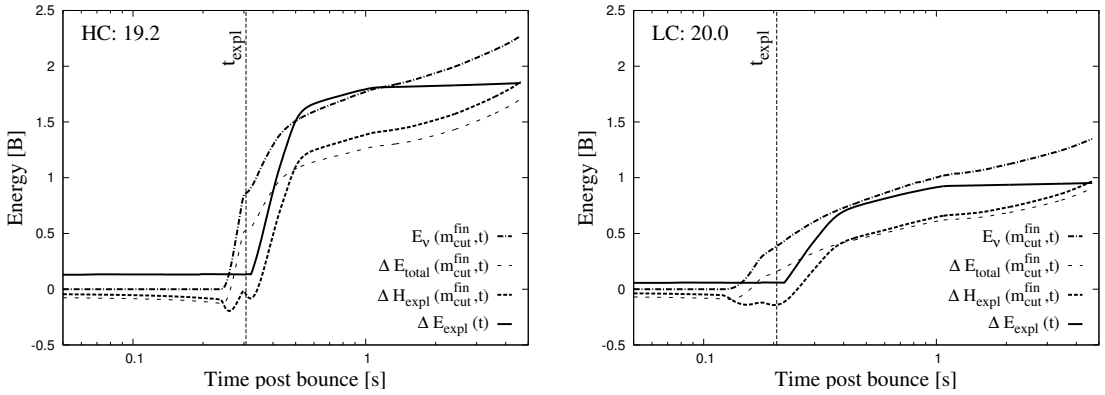

Fig. 4.6.: Time evolution of the time- and mass-integrated variation of the total energy $\Delta E_{\rm total}$ (thin dashed line), of the neutrino net deposition energy E_ν (dot-dashed line) and of the explosion energy for a fixed domain $\Delta H_{\rm expl}$ (thick dashed line), above $m_{\rm cut}^{\rm fin} = m_{\rm cut}(t_{\rm final})$, for the HC (left) and for the LC (right) reference runs reported in table 4.2. The evolution of the time-dependent explosion energy, $\Delta E_{\rm expl}$, is also shown (solid line). Both $\Delta H_{\rm expl}$ and $\Delta E_{\rm expl}$ are computed with respect to $H_{\rm expl}(m_{\rm cut}^{\rm fin}, t_{\rm initial})$. The difference between $\Delta E_{\rm total}(m_{\rm cut}^{\rm fin}, t)$ and E_ν represents the mechanical work, $E_{\rm mech}$; the difference between $\Delta E_{\rm total}(m_{\rm cut}^{\rm fin}, t)$ and $\Delta H_{\rm expl}(m_{\rm cut}^{\rm fin}, t)$ represents the released rest-mass energy, $-\Delta E_{\rm mass}$. Figures taken from [87].

our simulation from the stage of the progenitor star. The variation of the total energy can be separated into the net neutrino contribution and the mechanical work at the inner boundary, $\Delta E_{\rm total} = E_\nu + E_{\rm mech}$. We note that in our general relativistic approach the variation of the gravitational mass due to the intense neutrino emission from the PNS is consistently taken into account. It is visible in figure 4.6, that the net deposition by neutrinos makes up the largest part of the change of the total energy. The transfer of mechanical energy $E_{\rm mech}$ is negative because of the expansion work performed by the inner boundary during the collapse and the PNS shrinking. However it is significantly smaller in magnitude than E_ν.

Next, we investigate the connection between the variation of the total energy and the explosion energy. In figure 4.6, we show the variation of the explosion energy above the fixed mass $m_{\rm cut}^{\rm fin}$, i.e. $\Delta H_{\rm expl}(m_{\rm cut}^{\rm fin}, t) = H_{\rm expl}(m_{\rm cut}^{\rm fin}, t) - H_{\rm expl}(m_{\rm cut}^{\rm fin}, t_{\rm initial})$, together with the relative variation of the time-dependent explosion energy, $\Delta E_{\rm expl}(t) = E_{\rm expl}(t) - H_{\rm expl}(m_{\rm cut}^{\rm fin}, t_{\rm initial})$. It is obvious from equations (3.47), (3.71), and (3.74) that the difference between $\Delta H_{\rm expl}(m_{\rm cut}^{\rm fin}, t)$ and $\Delta E_{\rm total}(m_{\rm cut}^{\rm fin}, t)$ is given by the variation of the integrated rest mass energy, $\Delta H_{\rm expl}(m_{\rm cut}^{\rm fin}, t) = \Delta E_{\rm total}(m_{\rm cut}^{\rm fin}, t) - \Delta E_{\rm mass}(m_{\rm cut}^{\rm fin}, t)$. In figure 4.6, $-\Delta E_{\rm mass}(m_{\rm cut}^{\rm fin}, t)$ can thus be identified as the difference between the long-thin and the short-thick dashed lines. We find that the overall rest mass contribution to the final explosion energy is positive, but much smaller than the neutrino contribution. Figure 4.6 also makes evident the conceptual difference between $H_{\rm expl}$ and $E_{\rm expl}$, and, at the same time,

shows that $H_{\rm expl}(m_{\rm cut}^{\rm fin}, t) \rightarrow E_{\rm expl}(t)$ for $t \rightarrow t_{\rm final}$, since we have chosen $m_{\rm cut}^{\rm fin} = m_{\rm cut}(t_{\rm final})$. It also reveals that the explosion energy $E_{\rm expl}$ has practically saturated for $t \gtrsim 1$ s, while E_ν (and, consequently, $\Delta E_{\rm tot}$ and $\Delta H_{\rm expl}$) increases up to $t_{\rm final}$, when $m_{\rm cut}^{\rm fin}$ is finally ejected. However, this energy provided by neutrinos is mostly spent to unbind matter from the PNS surface. Thus, the late ν-driven wind, which occurs for several seconds after 1 s, still increases $E_{\rm expl}$, but at a relative small, decreasing rate.

To summarize, the variation of the explosion energy above $m_{\rm cut}^{\rm fin}$ can be expressed as

$$\begin{aligned} \Delta H_{\rm expl}(m_{\rm cut}^{\rm fin}, t) &= \Delta E_{\rm total}(m_{\rm cut}^{\rm fin}, t) - \Delta E_{\rm mass}(m_{\rm cut}^{\rm fin}, t) \\ &= E_\nu(m_{\rm cut}^{\rm fin}, t) + E_{\rm mech}(m_{\rm cut}^{\rm fin}, t) - \Delta E_{\rm mass}(m_{\rm cut}^{\rm fin}, t)\,. \end{aligned} \tag{4.2}$$

The quantity $-\Delta E_{\rm mass}$ is positive, but significantly smaller than $E_\nu(m_{\rm cut}^{\rm fin}, t)$. $E_{\rm mech}$ is negative and also smaller than $E_\nu(m_{\rm cut}^{\rm fin}, t)$. Therefore, we conclude that in our models the explosion energy is mostly generated by the energy deposition of neutrinos in the eventually ejected layers, especially within the first second after bounce.

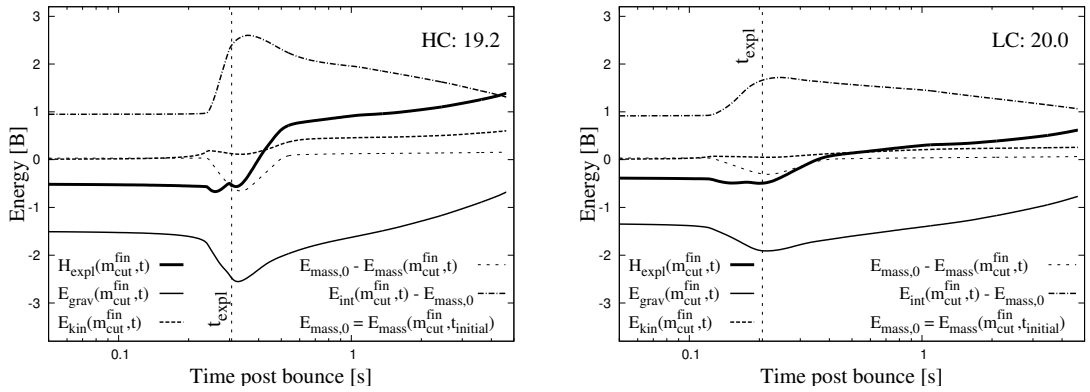

Fig. 4.7.: Temporal evolution of the gravitational (thin solid), kinetic (long dashed), negative rest mass (short dashed), internal (dot-dashed), and explosion (solid thick) energies above $m_{\rm cut}^{\rm fin} = m_{\rm cut}(t_{\rm final})$, for the HC (left) and for the LC (right) reference runs, see table 4.2. The internal and the rest mass energy are given with respect to the initial rest mass, $E_{\rm mass,0} = E_{\rm mass}(m_{\rm cut}^{\rm fin}, t_{\rm initial})$. The difference between the internal energy and the rest mass energy represents the thermal energy. Figures taken from [87].

To give further insight, in figure 4.7 we show the time evolution of all energies which contribute to the explosion energy together with the explosion energy itself, for both the HC (left panel) and the LC model (right panel). We present $E_{\rm int}(m_{\rm cut}^{\rm fin}, t)$, $-E_{\rm mass}(m_{\rm cut}^{\rm fin}, t)$,

$E_{\rm grav}(m^{\rm fin}_{\rm cut}, t)$ and $E_{\rm kin}(m^{\rm fin}_{\rm cut}, t)$, which together give a complete decomposition of the explosion energy, i.e.,

$$\begin{aligned} H_{\rm expl}(m^{\rm fin}_{\rm cut}, t) &= E_{\rm kin}(m^{\rm fin}_{\rm cut}, t) + E_{\rm grav}(m^{\rm fin}_{\rm cut}, t) \\ &\quad + E_{\rm int}(m^{\rm fin}_{\rm cut}, t) - E_{\rm mass}(m^{\rm fin}_{\rm cut}, t)\,. \end{aligned} \tag{4.3}$$

Compared to figure 4.6 we are now not dealing with variations any more but with absolute values. Gravitational energy initially dominates ($H_{\rm expl}(m^{\rm fin}_{\rm cut}, t) < 0$), meaning that the portion of the star above $m^{\rm fin}_{\rm cut}$ is still gravitationally bound. The HC model is initially more bound than the LC model (for example, $H_{\rm expl}(m^{\rm fin}_{\rm cut}, t = 0.1\,{\rm s}) \approx -0.54\,{\rm B}$, versus $H_{\rm expl}(m^{\rm fin}_{\rm cut}, t = 0.1\,{\rm s}) \approx -0.40\,{\rm B}$, respectively). Before providing positive explosion energy, neutrinos have to compensate for this initial negative binding energy as well as for the negative $E_{\rm mech}$. This can be seen explicitly by expressing equation (4.2) as:

$$\begin{aligned} H_{\rm expl}(m^{\rm fin}_{\rm cut}, t_{\rm final}) &\sim H_{\rm expl}(m^{\rm fin}_{\rm cut}, t_{\rm initial}) + E_\nu(m^{\rm fin}_{\rm cut}, t_{\rm final}) \\ &\quad + E_{\rm mech}(t_{\rm final})\,, \end{aligned} \tag{4.4}$$

where we have neglected $\Delta E_{\rm mass}$.

In the following, we discuss the evolution of the relevant energies and, in particular, of the rest mass energy (see section 3.1.3 for the description of the (non-)NSE EOS and of the related definitions of the internal, thermal and rest mass energies). The innermost part of the ejecta (corresponding to $\sim 0.15\ {\rm M}_\odot$ and $\sim 0.07\ {\rm M}_\odot$ above $m^{\rm fin}_{\rm cut}$ for the $19.2\ {\rm M}_\odot$ and $20.0\ {\rm M}_\odot$ model, respectively) is initially composed of intermediate mass nuclei (mainly silicon and magnesium). In the first part of the evolution, during the gravitational collapse, no significant changes of $E_{\rm int}$ and $E_{\rm mass}$ are observed in figure 4.7. However, when this matter enters the shock, it is quickly photodissociated into neutrons, protons, and alpha particles. This process increases the rest mass energy, as is visible in figure 4.7 between roughly 200 and 300 ms for the HC model and between 100 and 200 ms for the LC model. At the same time, the release of gravitational energy of the still infalling matter and the dissipation of kinetic energy happening at the shock, together with the large and intense neutrino absorption on free nucleons, increase $E_{\rm int}$. Later, once neutrino heating has halted the collapse and started the explosion, the expanding shock decreases its temperature and free neutrons and protons inside it recombine first into alpha particles and then into iron group nuclei. At the same time, fresh infalling layers are heated by the shock to temperatures above 0.44 MeV, and silicon and magnesium are converted into heavier nuclei and alpha particles under NSE conditions, leading to an alpha-rich freeze-out from NSE. The production of alpha particles, which are less bound than the heavy nuclei initially present in the same layers, limits the amount

of rest mass energy finally released. Thus, these recombination and burning processes liberate in a few hundred milliseconds after $t_{\rm expl}$ an amount of rest mass energy larger but comparable to the energy spent by the shock to photodissociate the infalling matter during shock revival and early expansion. We have checked in post-processing that the full nucleosynthesis network WINNET confirms these results.

4.2.3 Explosion Dynamics and the Role of Compactness

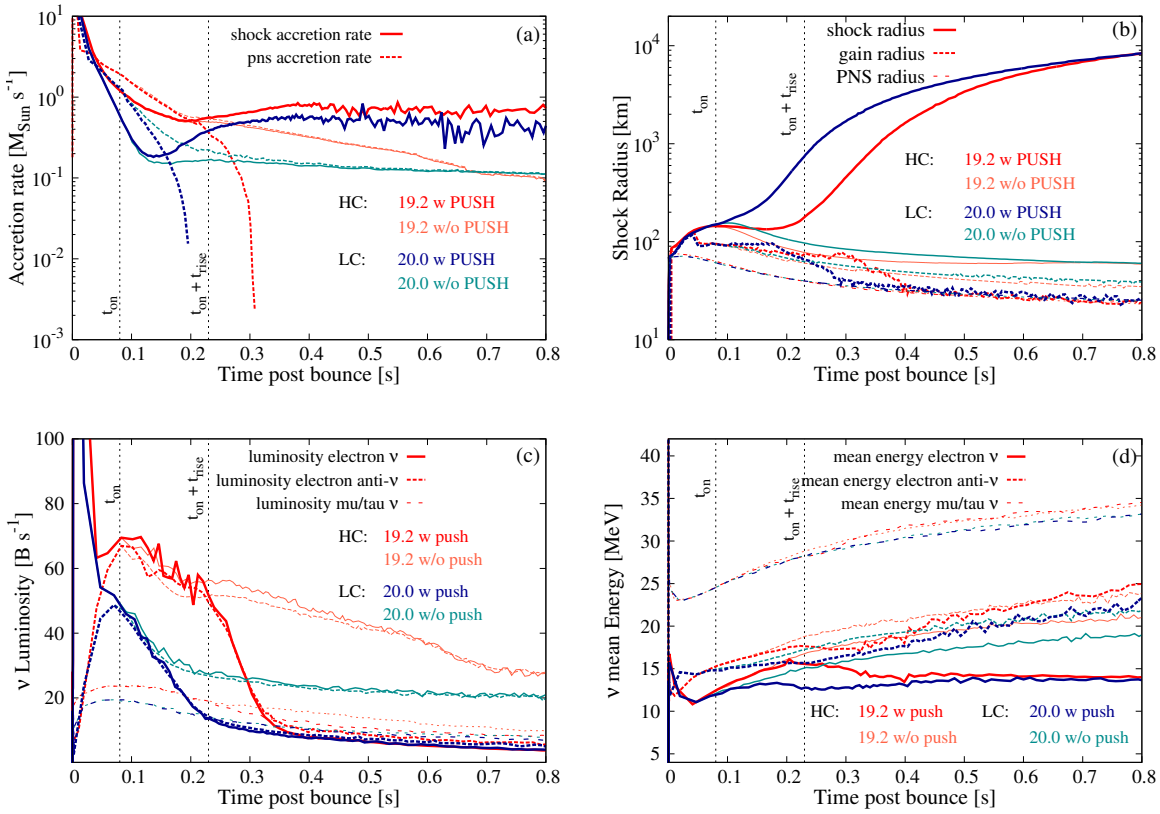

Fig. 4.8.: Temporal evolution of (a) the accretion rate at the PNS and at the shock, (b) the shock, the gain, and the PNS radii, (c) the neutrino luminosities, and (d) the neutrino mean energies, for all modeled neutrino flavors. In all panels, we present exploding runs for the 19.2 $M_\odot$ (red lines) and then 20.0 $M_\odot$ (blue lines) ZAMS mass models obtained with the PUSH parameters reported in table 4.2. We also plot the corresponding non-exploding runs obtained by setting $k_{\rm PUSH} = 0$ for the 19.2 $M_\odot$ (light red) and 20.0 $M_\odot$ (light blue) ZAMS mass progenitor models. Figures taken from [87].

The distributions of the explosion energy and explosion time obtained with PUSH, as well as their variations in response to changes of the model parameters, suggest a possible distinction between high and low compactness progenitors. In the following, we

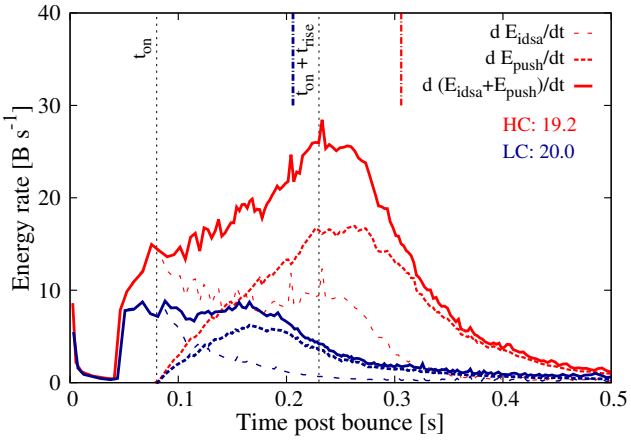

Fig. 4.9.: Temporal evolution of the neutrino energy deposition inside the gain region from ν_e and $\bar{\nu}_e$ ($dE_{\rm idsa}/dt$, long-thin dashed lines), from PUSH ($dE_{\rm push}/dt$, short-thick dashed lines), and their sum (solid lines). The 19.2 $M_\odot$ (HC) ZAMS mass model is represented in red, while the 20.0 $M_\odot$ (LC) ZAMS mass is in blue, with PUSH parameters reported in table 4.2. The short colored vertical lines show the time of explosion. Figure taken from [87].

investigate how basic properties of the models (e.g., the accretion history or the neutrino luminosities), ultimately connected with the compactness, relate to differences in the explosion process and properties. For a similar discussion in self-consistent 1D and 2D SN simulations, see [175]. Again, we choose the 19.2 and 20.0 ZAMS mass progenitor runs with $t_{\rm rise} = 150\,$ms and $k_{\rm PUSH} = 3.0$, as representatives of the HC and LC samples, respectively.

In figure 4.8, we show the temporal evolution of several quantities of interest for both the 19.2 $M_\odot$ and 20.0 $M_\odot$ models, with and without PUSH. The evolution before $t_{\rm on}$ follows the well known early shock dynamics in CCSNe (see, for example, [157]). In both models, a few tens of milliseconds after core bounce, the expanding shock turns into an accretion front, and the mantle between the PNS surface and the shock reaches a quasi-stationary state. In this accretion phase, $\dot{M}_{\rm shock}$ and $\dot{M}_{\rm PNS}$ are firmly related. However, the two different density profiles already affect the evolution of the shock. Since $\rho_{19.2}/\rho_{20.0} \gtrsim 1.2$ outside the shock and up to a radius of 2×10^8 cm (while the infalling velocities of the unshocked matter are initially almost identical), $\dot{M}_{\rm shock}$ (and in turn also $\dot{M}_{\rm PNS}$) starts to differ between the two models around $t_{\rm pb} \approx 30$ ms.

The difference in the accretion rates has a series of immediate consequences. For the HC case, (i) neutrino luminosities are larger (figure 4.8c); (ii) the shock is subject to a larger ram pressure (i.e., a larger momentum transfer provided by the collectively infalling mass flowing through the shock), and, as visible in the case without PUSH, shock stalling hap-

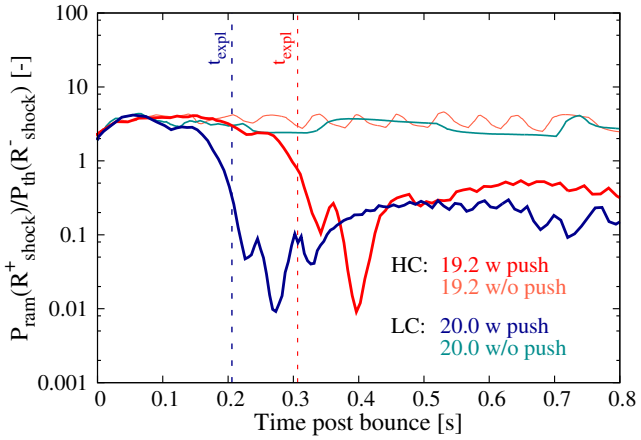

Fig. 4.10.: Temporal evolution of the ratio between the ram pressure above the shock and the thermal pressure below the shock. The 19.2 $M_\odot$ (HC) ZAMS mass model is represented in red, while the 20.0 $M_\odot$ (LC) ZAMS mass model is in blue. The PUSH parameters are reported in table 4.2. Light red and light blue lines represent the corresponding runs without PUSH ($k_{\mathrm{PUSH}} = 0$). Figure taken from [87].

pens earlier and at a smaller radius (figure 4.8b); (iii) the PNS mass grows faster. Since the mass of the PNS at bounce is almost identical for the two models ($M_{\mathrm{PNS}} \approx 0.63\ M_\odot$), the stronger gravitational potential implied by (iii) increases the differences in the accretion rates even further by augmenting the ratio of the radial velocities inside the gain region (larger by 12–15% at $t \approx t_{\mathrm{on}}$ for the 19.2 $M_\odot$ case).

For $t > t_{\mathrm{on}}$, the differences between the two runs amplify as a result of the PUSH action. In the LC case, due to the lower accretion rate, a relatively small energy deposition by PUSH in the gain region (smaller than or comparable to the energy deposition by ν_e and $\bar{\nu}_e$ from IDSA, as visible in figure 4.9) is able to revive the shock expansion a few milliseconds after t_{on}. Later, the increasing $\mathrm{d}E_{\mathrm{push}}/\mathrm{d}t$ triggers an explosion in a few tens of milliseconds, even before $\mathscr{G}(t)$ reaches its maximum (figure 4.8b). In the HC case, the energy deposition by neutrinos is more intense from the beginning due to the larger neutrino luminosities and harder neutrino spectra (figures 4.8c and 4.8d) and due to the higher density inside the gain region. However, because of the larger accretion rate, the extra contribution provided by PUSH is initially only able to prevent the fast shock contraction observed in the model without PUSH. During this shock stalling phase, the accretion rate and the luminosity decrease, but only marginally and very similarly to the non-exploding case. When PUSH reaches its maximum energy deposition rate ($t \approx t_{\mathrm{on}} + t_{\mathrm{rise}}$), the shock revives and the explosion sets in (figure 4.8b).

In figure 4.10, we plot the ratio of the ram pressure just above the shock front ($P_{\mathrm{ram}}(R^+_{\mathrm{shock}}) = \rho v^2$ calculated at $R^+_{\mathrm{shock}} = R_{\mathrm{shock}} + 1\,\mathrm{km}$) to the thermal pressure just in-

side it ($P_{\rm th}(R^-_{\rm shock})$ where $R^-_{\rm shock} = R_{\rm shock} - 1\,{\rm km}$). In the non-exploding runs (i.e., without PUSH), both these pressures decrease with time, but their ratio stays always well above unity. On the other hand, in runs with PUSH, the more efficient energy deposition by neutrinos reduces the decrease of the thermal pressure inside the shock. The corresponding drop in the pressure ratio below unity determines the onset of the explosion.

In both runs, once the explosion has been launched, the density in the gain region decreases and the PUSH energy deposition rate reduces accordingly. The conversion from an accreting to an expanding shock front decouples $\dot{M}_{\rm shock}$ from $\dot{M}_{\rm PNS}$. The latter drops steeply, together with the accretion neutrino luminosities (figures 4.8a and 4.8c), while $\dot{M}_{\rm shock}$ decreases first but then stabilizes around an almost constant (slightly decreasing) value. In the case where the shock expansion velocity is much larger than the infalling matter velocity at $R_{\rm shock}$, $\dot{M}_{\rm shock}$ can be re-expressed as

$$\dot{M}_{\rm shock} \approx 4\pi R^2_{\rm shock}\, \rho(R_{\rm shock})\, v_{\rm shock}, \tag{4.5}$$

where $v_{\rm shock} = {\rm d}R_{\rm shock}/{\rm d}t \propto R^{\delta}_{\rm shock}$. For $R > R_{\rm shock}$ we have in good approximation $\rho(R) \propto R^{-2}$, and thus

$$\dot{M}_{\rm shock} \propto R^{\delta}_{\rm shock}. \tag{4.6}$$

The stationary value of $\dot{M}_{\rm shock}$ implies that $\delta \approx 0$. Thus, after an initial exponential expansion, the shock velocity is almost constant during the first second after the explosion.

Despite the larger difficulties to trigger an explosion, the HC model explodes more energetically than the LC model. According to the analysis performed in section 4.2.2, the difference in the explosion energy between the HC and the LC model depends ultimately on the different amount of energy deposited by neutrinos. Since the high compactness model requires a larger energy deposition to overcome the ram pressure and the gravitational potential, the total energy of the corresponding ejecta (and in turn the explosion energy) will be more substantially increased. In addition, after the explosion has been triggered, the larger neutrino luminosities and densities that characterize the HC model inject more energy in the expanding shock compared with the LC model.

4.2.4 Fitting of SN1987A

The ultimate goal of CCSN simulations is to reproduce the properties observed in real SNe. So far we have only focused on the dependence of dynamical features of the explosion (e.g., the explosion energy) on the parameter choices in the PUSH method. However, the ejected mass of radioactive nuclides (such as ^{56}Ni) is an equally important property of the SN explosion. Here, we describe how we calibrate the PUSH method by reproducing the explosion energy and mass of Ni ejecta of SN 1987A for a progenitor within the expected mass range for this SN.

Observational Constraints from SN 1987A

The analysis and the modeling of the observational properties of SN 1987A just after the luminosity peak have been the topics of a long series of works (e.g., and references therein [7, 21–25, 176–178]). They provide observational estimates for the explosion energy, the progenitor mass, and the ejected masses of ^{56}Ni, ^{57}Ni, ^{58}Ni, and ^{44}Ti, all of which carry rather large uncertainties. In table 4.3, the values used for the calibration of the PUSH method are summarized.

The ZAMS progenitor mass is assumed to be between 18 $M_\odot$ and 21 $M_\odot$, corresponding to typical values reported in the literature for the SN1987A progenitor, see, e.g., [23, 24]. For the explosion energy we consider the estimate reported by [21], $E_{\rm expl} = (1.1 \pm 0.3) \times 10^{51}$ erg (for a detailed list of explosion energy estimates for SN 1987A, see for example table 1 in [134]). This value was obtained assuming ~14.7 $M_\odot$ of ejecta and an hydrogen-rich envelope of ~10.3 $M_\odot$. The uncertainties in the progenitor properties and in the SN distance were taken into account in the error bar. The employed values of the total ejecta and of the hydrogen-rich envelope are compatible (within a 15% tolerance) with a significant fraction of our progenitor candidates, especially for $M_{\rm ZAMS} < 19.6\ M_\odot$ (see table 4.1, where the total ejecta can be estimated subtracting 1.6 $M_\odot$ from the mass of the star at the onset of the collapse). Explosion models with larger ejected mass (i.e., less compatible with our candidate sample) tend to have larger explosion energies (see, for example, [178]). Finally, we consider the element abundances for ^{56,57}Ni and ^{44}Ti provided by [22], which were obtained from a least squares fit of the decay chains to the bolometric lightcurve. For ^{58}Ni we use the value provided by [25].

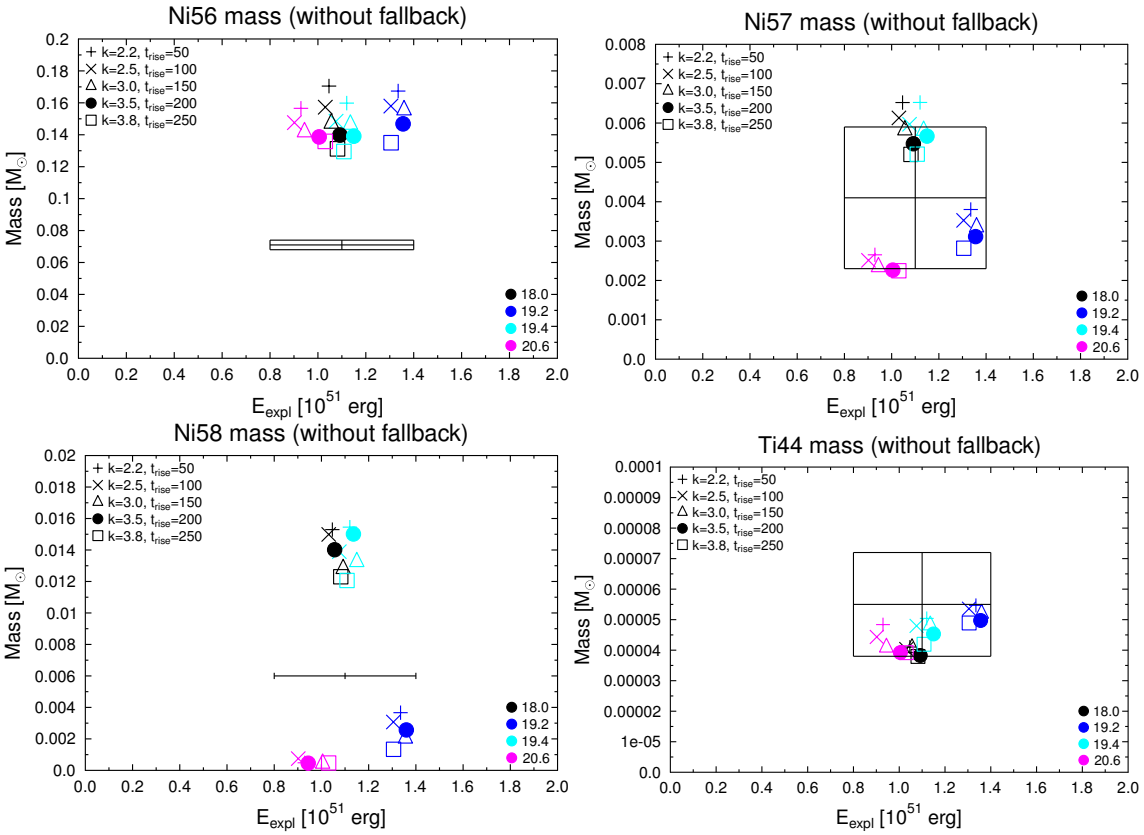

Fig. 4.11.: Ejected mass of ^{56}Ni (top left), ^{57}Ni (top right), ^{58}Ni (bottom left), and ^{44}Ti (bottom right) and explosion energy for four representative HC progenitor models. Five combinations of k_{PUSH} and t_{rise} are shown, each with a different symbol. The error bar box represents the observational values from [22] (for ^{56,57}Ni and ^{44}Ti) and from [25] (for ^{58}Ni). No error bars are reported for ^{58}Ni. Figures taken from [87].

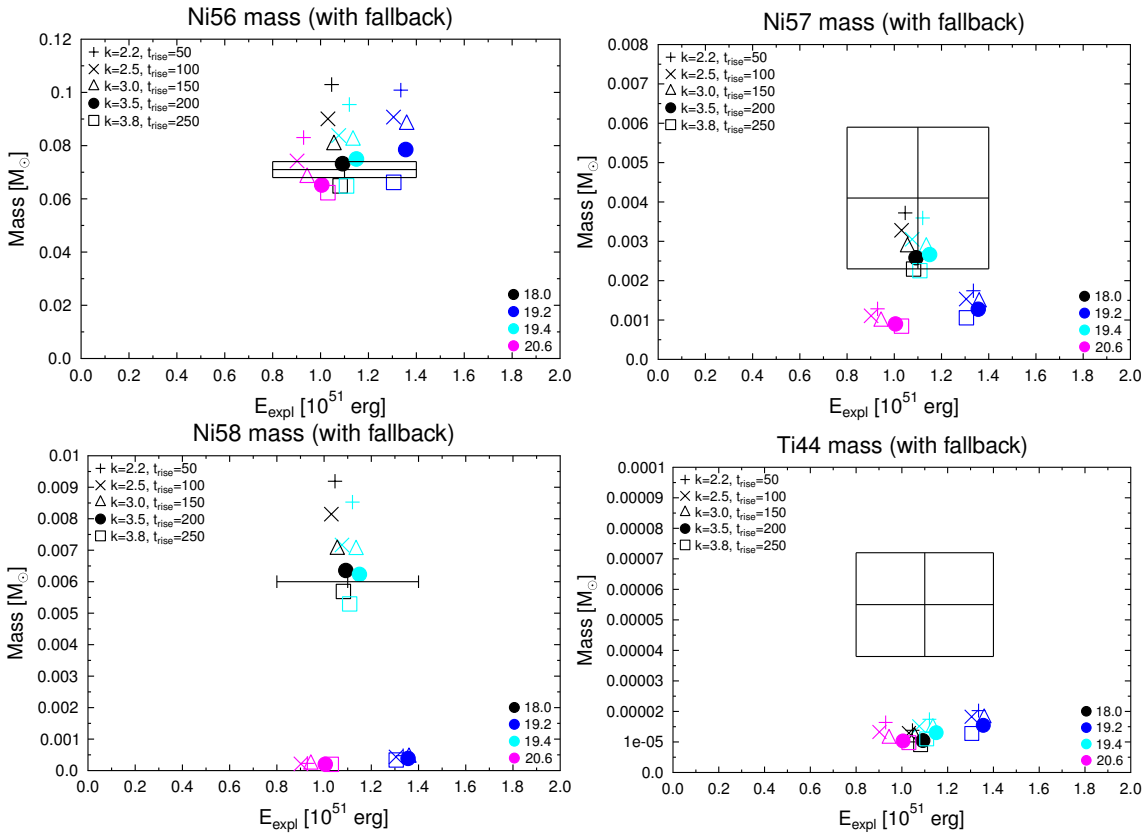

Fig. 4.12.: Same as figure 4.11, but assuming 0.1 $M_\odot$ fallback. Note the different scale for ^{56}Ni and ^{58}Ni compared to figure 4.11. Figures taken from [87].

E_{expl}	$(1.1 \pm 0.3) \times 10^{51}$ erg
m_{prog}	18-21 $M_\odot$
$m(^{56}\mathrm{Ni})$	(0.071 ± 0.003) $M_\odot$
$m(^{57}\mathrm{Ni})$	(0.0041 ± 0.0018) $M_\odot$
$m(^{58}\mathrm{Ni})$	0.006 $M_\odot$
$m(^{44}\mathrm{Ti})$	$(0.55 \pm 0.17) \times 10^{-4}$ $M_\odot$

Tab. 4.3.: Observational properties of SN 1987A. The nucleosynthesis yields are taken from [22] except for ^{58}Ni which is taken from [25]. No error estimates were given for ^{58}Ni. The explosion energy is adapted from [21]. For the progenitor range we chose typical values found in the literature, see e.g. [23, 24]. Table taken from [87].

Fitting Procedure

We calibrate the PUSH method by finding a combination of progenitor mass, k_{PUSH}, and t_{rise} which provides the best fit to the all observational quantities of SN 1987A mentioned above. The weight given to each quantity is related to the uncertainty. For example, due to the large uncertainty in the ^{44}Ti mass, this does not provide a strong constraint on selecting the best fit.

Figure 4.11 shows the explosion energy and ejected mass of ^{56}Ni, ^{57}Ni, ^{58}Ni, and ^{44}Ti for different cases of k_{PUSH} and t_{rise} and for four select HC progenitors used to calibrate the PUSH method. We do not consider the LC progenitors, because of their generally lower explosion energies, see figure 4.3. The different cases of k_{PUSH} and t_{rise} span a wide range of explosion energies around 1 Bethe. For all parameter combinations shown, at least one progenitor in the 18-21 $M_\odot$ range fulfills the requirement of an explosion energy between 0.8 Bethe and 1.4 Bethe. There is a roughly linear correlation between the explosion energy and the synthesized ^{56}Ni-mass. However, this correlation is not directly compatible with the observations, as the ejected ^{56}Ni is systematically larger than expected (up to a factor of ~ 2 for models with an explosion energy around 1 Bethe). There is a weak trend that models with higher t_{rise} tend to give lower nickel masses for given explosion energy. Among the parameter combinations that produce robustly high explosion energies (i.e., $k_{\mathrm{PUSH}} \geq 3$), $k_{\mathrm{PUSH}} = 3.5$ with the high value of t_{rise} of 200 ms gives the lowest ^{56}Ni mass for similar explosion energies, but still much too high.

Our simulations can be reconciled with the observations by taking into account fallback from the initially unbound matter. Since we do not model the explosion long enough to see the development of the reverse shock and the appearance of the related fallback when the shock reaches the hydrogen-rich envelope, we have to impose it, removing

some matter from the innermost ejecta[1]. With a value of ~ 0.1 $M_\odot$ we can match both the expected explosion energy and ^{56}Ni ejecta mass, see figure 4.12. In this way we have fixed the final mass cut by observations. However, we point out that we are able to identify the amount of late-time fallback only because we also have the dynamical mass cut from our hydrodynamical simulations. This is not possible in other methods such as pistons or thermal bombs. Our value of ~ 0.1 $M_\odot$ of fallback in SN 1987A will be further discussed and compared with other works in section 4.3.3.

The observed yield of ^{56}Ni provides a strong constraint on which parameter combination would fit the data. From the observed yields of ^{57}Ni and ^{58}Ni, only the 18.0 and 19.4 progenitors remain viable candidates. Without fallback our predicted ^{44}Ti yields are compatible with the observed yields (see figure 4.11). However, if we include fallback (which is needed to explain the observed Ni yields), ^{44}Ti becomes underproduced compared to the observed value. Since this behavior is true for all our models, we exclude the constraint given by ^{44}Ti from our calibration procedure. From the considered parameter combinations, we obtained the best fit to SN 1987A for the 18.0 $M_\odot$ progenitor model with $k_{\mathrm{PUSH}} = 3.5$, $t_{\mathrm{rise}} = 200$ ms, and a fallback of 0.1 $M_\odot$. These parameters are summarized in table 4.4. In figure 4.13, we show the temporal evolution of the accretion rates, of the relevant radii, and of the neutrino luminosities and mean energies for our best fit model. For comparison purposes, we present also the results obtained for the same model without PUSH. Note that in this non-exploding case the ν_e and $\bar{\nu}_e$ luminosities stay almost constant over several ~ 100 ms after core bounce, despite the decreasing accretion rate. This is due to the relatively slow variation of $\dot{M}_{\mathrm{PNS}}$ (for example, compared with the variation obtained in the 19.2 $M_\odot$ model, figure 4.8) and due to the simultaneous increase of the PNS gravitational potential, proportional to $M_{\mathrm{PNS}}/R_{\mathrm{PNS}}$ (see, for example, [179]). A summary of the most important results of the simulations using this parameter set for the different progenitors in the 18-21 $M_\odot$ window is given in table 4.5. For the remnant mass and for the ^{56}Ni yields of our best-fit model, we provide both the values obtained with and without assuming a fallback of 0.1 $M_\odot$.

4.2.5 Ni and Ti Yields, Progenitor Dependence

Figures 4.11 and 4.12 show that the composition of the ejecta is highly dependent on the progenitor model, especially for the amount of ^{57}Ni and ^{58}Ni ejected. From the four HC progenitors shown, two (18.0 $M_\odot$ and 19.4 $M_\odot$) produce a fairly high amount of those

[1] Note that we did not modify the explosion energy due to the fallback. This is based on the expectation that at the late time when fallback forms, the explosion energy is approximately equally distributed among the total ejected mass, which is about two orders of magnitude higher than our fallback mass.

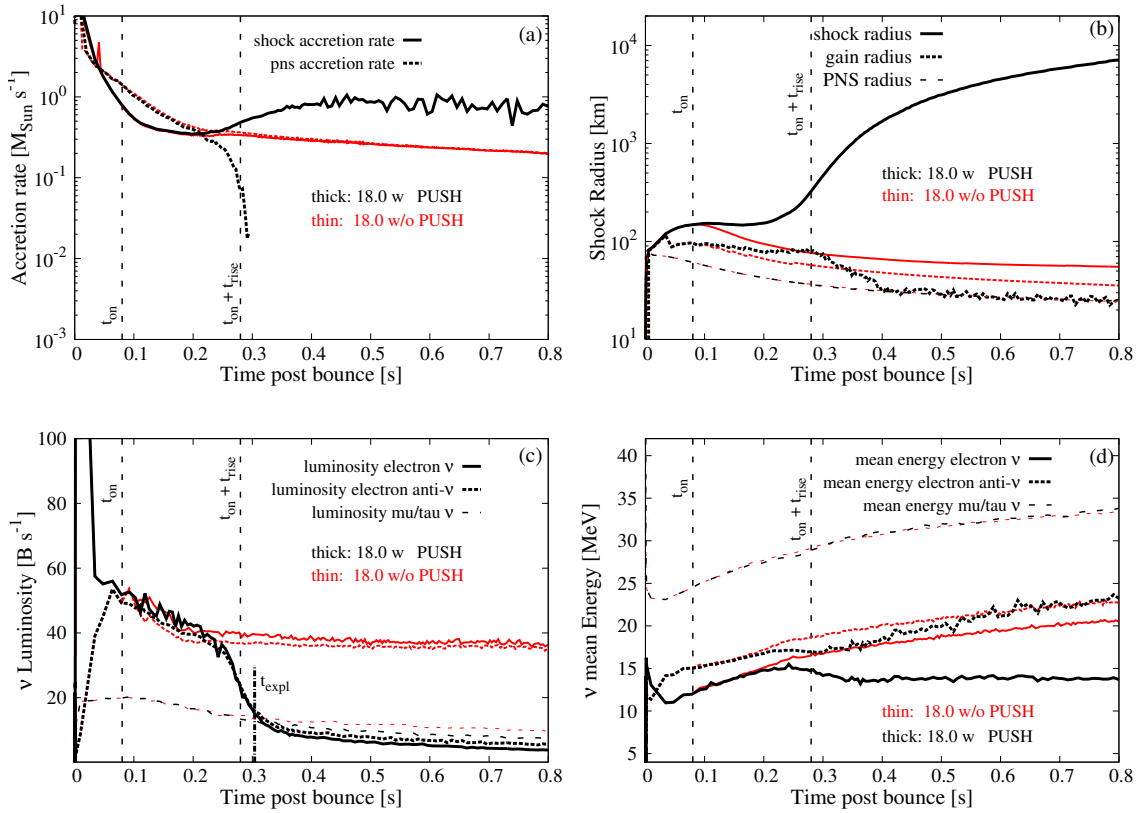

Fig. 4.13.: Same as in figure 4.8, but for the SN 1987A best fit model: 18.0 $M_\odot$ progenitor, with $t_{on} = 80$ ms, $t_{rise} = 200$ ms, and $k_{PUSH} = 3.5$. Figures taken from [87].

k_{PUSH} (-)	t_{rise} (ms)	t_{on} (ms)	t_{off} (s)
3.5	200	80	1

Tab. 4.4.: Parameter values for best fit to SN 1987A. We identified the 18.0 $M_\odot$ model as the progenitor which fits best, whereas we had to impose a late-time fallback of 0.1 $M_\odot$. Table taken from [87].

isotopes, while the other two (19.2 $M_\odot$ and 20.6 $M_\odot$) do not reach the amount observed in SN 1987A. A thorough investigation of the composition profile of the ejecta reveals that ^{57}Ni and ^{58}Ni are mainly produced in the slightly neutron-rich layers ($Y_e < 0.5$), where the alpha-rich freeze-out leads to nuclei only one or two neutron units away from the $N = Z$ line. A comparison of the Y_e and composition profiles for the 18.0 $M_\odot$ and the 20.6 $M_\odot$ progenitors is shown in figure 4.14. For the 18.0 $M_\odot$ model, the cutoff mass is 1.56 $M_\odot$ and a large part of the silicon shell is ejected. In this shell, the initial matter composition is slightly neutron-rich (due to a small contribution from ^{56}Fe) with $Y_e \simeq 0.498$ (dotted line in top left graph) and the conditions for the production of ^{57}Ni and ^{58}Ni are favorable. The increase in Y_e around 1.9 $M_\odot$ marks the transition to the oxygen shell. The same transition for the 20.6 $M_\odot$ model happens around 1.74 $M_\odot$, i.e., inside the mass cut. Therefore, this model ejects less ^{57}Ni and ^{58}Ni (see also [180]). In all our models, ^{44}Ti is produced within the innermost 0.15 $M_\odot$ of the ejecta (see figure 4.14). Since we assume 0.1 $M_\odot$ fallback onto the PNS, most of the synthesized ^{44}Ti is not ejected in our simulations.

4.3 Implications and Discussion

4.3.1 Sensitivities of Nucleosynthesis Yields

While post-processing the ejecta trajectories for nucleosynthesis, Y_e is evolved by the nuclear network independently of the hydrodynamical evolution. This leads to a discrepancy at later times between the electron fraction in the initial trajectory (Y_e^{hydro}) and in the network (Y_e^{nuc}). In order to estimate the possible error in our nucleosynthesis calculations arising from this discrepancy, we have performed reference calculations using $Y_e^{\mathrm{hydro}}(t = t_{\mathrm{final}})$ instead of $Y_e^{\mathrm{hydro}}(T = 10\,\mathrm{GK})$ as a starting value for the network (see section 3.3.3). The results are shown in figure 4.14 for two progenitors: 18.0 $M_\odot$ and 20.6 $M_\odot$. The label "standard" refers to the regular case which uses $Y_e^{\mathrm{hydro}}(T = 10\,\mathrm{GK})$ as input.

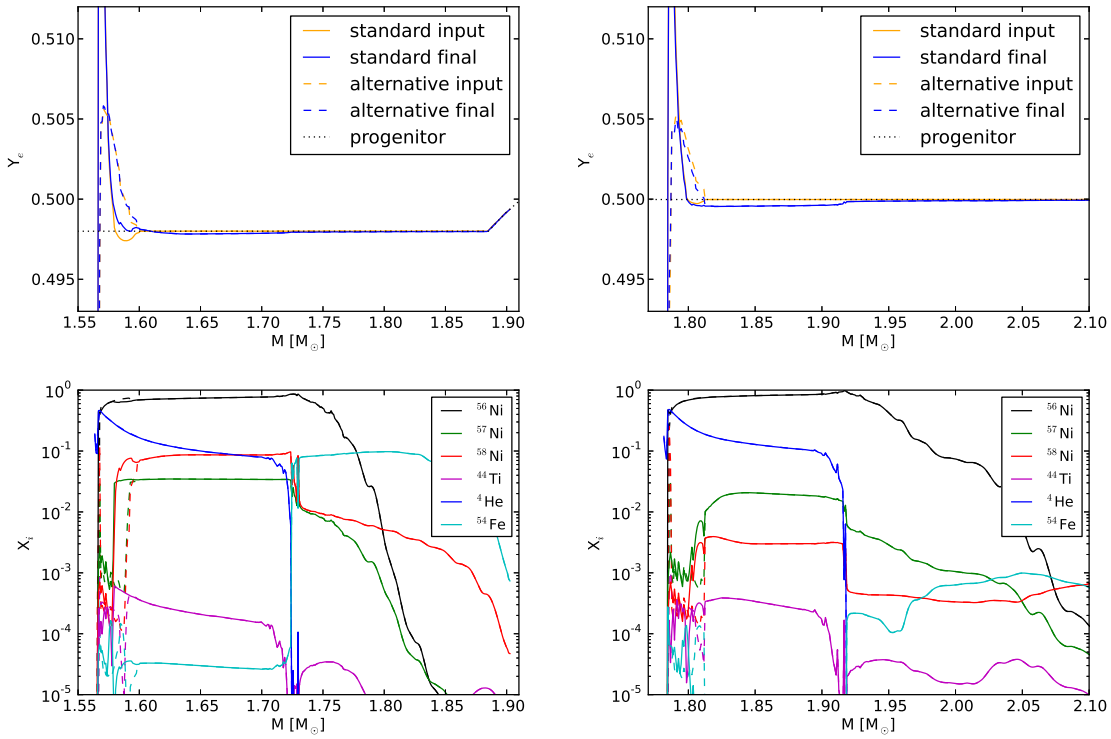

Fig. 4.14.: Electron fraction profiles (top) and nuclear compositions at 100 s (bottom) above the mass cut for the 18.0 $M_\odot$ (left) and the 20.6 $M_\odot$ (right) progenitors with the parameters $k_{\mathrm{PUSH}} = 3.5$ and $t_{\mathrm{rise}} = 200$ ms. The electron fraction is plotted for two different times in the network: the input values for the first time step ("input") and the value after post-processing ("final"). The dashed lines in all panels correspond to the alternative case, where $Y_e^{\mathrm{hydro}}(t = 4.6\ \mathrm{s})$ is taken as the initial electron fraction in the network, whereas the solid lines represent the standard case (using $Y_e^{\mathrm{hydro}}(T = 10\ \mathrm{GK})$). Figures taken from [87].

ZAMS ($M_\odot$)	$E_{\rm expl}$ (Bethe)	$t_{\rm expl}$ (s)	$M^B_{\rm remnant}$ ($M_\odot$)	$M^G_{\rm remnant}$ ($M_\odot$)	$M(^{56}Ni)$ ($M_\odot$)
18.0	1.092	0.304	1.563	1.416	0.158
18.2	0.808	0.249	1.509	1.371	0.110
18.4	1.358	0.318	1.728	1.549	0.144
18.6	0.702	0.239	1.529	1.388	0.090
18.8	0.721	0.236	1.522	1.382	0.093
19.0	1.366	0.317	1.716	1.54	0.161
19.2	1.356	0.318	1.724	1.546	0.152
19.4	1.15	0.326	1.608	1.452	0.158
19.6	0.371	0.230	1.584	1.433	0.04
19.8	0.661	0.225	1.523	1.383	0.088
20.0	0.613	0.222	1.474	1.342	0.085
20.2	0.379	0.224	1.554	1.408	0.039
20.4	0.743	0.263	1.674	1.506	0.094
20.6	1.005	0.277	1.781	1.592	0.141
20.8	0.959	0.277	1.764	1.578	0.135
21.0	1.457	0.316	1.733	1.554	0.198
18.0 (fb)	1.092	0.304	1.663	1.497	0.073

Tab. 4.5.: Summary of simulations for $k_{\rm PUSH} = 3.5$ and $t_{\rm rise} = 200$ ms. For the model 18.0 (fb), which is our best fit to SN 1987A, we have included 0.1 $M_\odot$ of fallback, determined from observational constraints. See the text for more details. Table taken from [87].

The calculation using $Y_e^{\rm hydro}(t = t_{\rm final})$ as input is labeled "alternative" and is represented by the dashed lines. The point in time at which the Y_e profile is shown is indicated by the supplements "input" (before the first time step) and "final" (at $t = 100$ s). The corresponding nuclear compositions of the ejecta, each at the final calculation time of 100 s, are shown in the bottom panels. For the alternative Y_e profile of the 18.0 $M_\odot$ progenitor (top left) the minimum around 1.59 $M_\odot$ disappears, leading to an increase in ^{56}Ni in this region at the expense of ^{57}Ni and ^{58}Ni (bottom left). For the 20.6 $M_\odot$ progenitor the situation is similar, with only a very small region just above 1.8 $M_\odot$ showing significant differences. In general, we observe that the uncertainties in Y_e in our calculations are only present up to 0.05 $M_\odot$ above the mass cut. The resulting uncertainties in the composition of the ejecta are very small or even inexistent in the scenarios where we consider fallback.

The radioactive isotope ^{44}Ti can be detected in SNe and SN remnants. Several groups have used different techniques to estimate the ^{44}Ti yield [22, 25, 181–185]. The inferred values span a broad range, $(0.5-4)\times10^{-4}$ $M_\odot$. Traditional SN nucleosynthesis calculations (e.g. [152, 155]) typically predict too low ^{44}Ti yields. Only very few models predict

high ^{44}Ti yields: Thielemann et al. [180] report ^{44}Ti yields around 10^{-4} $M_\odot$ and above in the best fits of their artificial SN explosions to SN 1987A. Rauscher et al. [186] argue that the yields of ^{56}Ni and ^{44}Ti are very sensitive to the "final mass cut" (as we have shown, too), which is often determined by fallback. Ejecta in a SN may be subject to convective overturn. To account for this, we can assume homogeneous mixing in the inner layers up to the outer boundary of the silicon shell before cutting off the fallback material (see, for example, [187] and references therein). For our best-fit model, the ejected ^{44}Ti mass increases to 2.70×10^{-5} $M_\odot$, if this prescription is applied. Comparing to the previous yield of 1.04×10^{-5} $M_\odot$, we observe that the effect of homogeneous mixing is considerable, but not sufficient to match the observational values. The ejected $^{56-58}$Ni masses also show a slight increase. However, there are also uncertainties in the nuclear physics connected to the production and destruction of ^{44}Ti. The final amount of produced ^{44}Ti depends mainly on two reactions: $^{40}\mathrm{Ca}(\alpha,\gamma)^{44}\mathrm{Ti}$ and $^{44}\mathrm{Ti}(\alpha,p)^{47}\mathrm{V}$. Recent measurements of the $^{44}\mathrm{Ti}(\alpha,p)^{47}\mathrm{V}$ reaction rate within the Gamow window concluded that it may be considerably smaller than previous theoretical predictions [188]. In this study, an upper limit cross section is reported that is a factor of 2.2 smaller than the cross section we have used in our calculations (at a confidence level of 68%). Using this smaller cross section for the $^{44}\mathrm{Ti}(\alpha,p)^{47}\mathrm{V}$ reaction, our yield of ejected ^{44}Ti for our best-fit model (18.0 $M_\odot$ progenitor, $k_{\mathrm{PUSH}} = 3.5$, $t_{\mathrm{rise}} = 200$ ms) rises to 1.49×10^{-5} $M_\odot$ with fallback and 5.65×10^{-5} $M_\odot$ without fallback. This corresponds to a relative increase of 43% with fallback and 48% without fallback. If we include both the new cross section and homogeneous mixing, the amount of ^{44}Ti in the ejecta is 3.99×10^{-5} $M_\odot$ including fallback. This value, however, is still below the expected value derived from observations, but within the error box.

4.3.2 Wind Ejecta

In the analysis of the nucleosynthesis yields above, we have used a mass resolution of 0.001 $M_\odot$ for the tracers. This is too coarse to resolve the ejecta of the late neutrino-driven wind. Note that in our best-fit approach, where no mixing is assumed, none of the neutrino-driven wind is ejected because it is part of the fallback. Nevertheless, in the following we report briefly on the properties of the wind obtained by our detailed neutrino-transport scheme. For our best-fit model, the 18.0 $M_\odot$ progenitor, at t_{final} we find an electron fraction around 0.32, entropies up to 80 k_B per baryon, and fast expansion velocities ($\sim 10^9$ cm/s). Similar conditions are also found for the other progenitors. They are not sufficient for a full r-process (see, for example, [189]). On the other hand, we have found that the entropy is still increasing and the electron fraction still decreasing in the further evolution. The high asymmetries are only obtained if we include the nucleon mean-field interaction potentials in the neutrino charged-current rates [115].

However, they are much higher than found in other long-term simulations which also include these potentials [114, 115, 190]. This could be related to the missing neutrino-electron scattering in our neutrino transport, which is an important source of thermalization and down-scattering, especially for the high energy electron antineutrinos at late times, see [191]. More detailed comparisons are required to identify the origin of the found differences which will be addressed in a future study.

4.3.3 Amount of Fallback

To reconcile our models with the nucleosynthesis observables of SN 1987A we need to invoke 0.1 $M_\odot$ of fallback (see section 4.2.4). The variation in the amount of synthesized Ni isotopes between runs obtained with different PUSH parameters (figure 4.11) suggests that a smaller $t_{\rm rise}$ (and consequently smaller $k_{\rm PUSH}$) could also be compatible with SN 1987A observables, if a larger fallback is assumed. On the one hand, assuming that $t_{\rm rise}$ ranges between 50 ms and 250 ms, fallback for the 18.0 $M_\odot$ model compatible with observations is between 0.14 $M_\odot$ (for $t_{\rm rise}$ = 50 ms) and 0.09 $M_\odot$ (for $t_{\rm rise}$ = 250 ms). On the other hand, if the amount of fallback has been fixed, the observed yields (especially of ^{56}Ni) reduce the uncertainty in $t_{\rm rise}$ to $\lesssim$ 50 ms.

Our choice of 0.1 $M_\odot$ is compatible with the fallback obtained by [141] in exploding spherically symmetric models for progenitor stars in the same ZAMS mass window. Moreover, Chevalier [192] estimated a total fallback around 0.1 $M_\odot$ for SN 1987A, which is supposed to be an unusually high value compared to "normal" type II SNe. Recent multi-dimensional numerical simulations by [193, 194] confirmed this scenario and furthermore showed that such a hypercritical accretion can lead to a submergence of the magnetic field, giving a natural explanation why the neutron star (possibly) born in SN 1987A has not been found yet.

4.3.4 Compact Remnant of SN 1987A

From the observational side, the compact remnant in SN 1987A is still obscure. From the neutrino signal (see, e.g., [7, 195] and [196] for a recent detailed analysis) one can conclude that a PNS star was formed and that it lasted at least for about 12 s. The mass cut in our calibration run is located at an enclosed baryon mass of 1.56 $M_\odot$ without fallback. If we include the 0.1 $M_\odot$ of late-time fallback required to fit the observed nickel yields and the explosion energy, we have a final baryonic mass of 1.66 $M_\odot$. For the employed HS(DD2) EOS this corresponds to a gravitational mass of a cold neutron star of 1.42 $M_\odot$

(without fallback) or 1.50 $M_\odot$ (with fallback). The CCSN simulations with artificial explosions of [180], where a final kinetic energy of 1 Bethe was obtained by hand and where the mass-cut was deduced from a ^{56}Ni yield of (0.07 ± 0.01) $M_\odot$, lead to a similar baryonic mass of (1.6 ± 0.045) $M_\odot$. These authors also wrote that uncertainties in the stellar models could increase this value to 1.7 $M_\odot$ which would also be fully compatible with our result.

The prediction of the neutron star mass has important consequences. From the observations of [121] and [122] it follows that the maximum gravitational mass of neutron stars has to be above two solar masses. The maximum mass of the HS(DD2) EOS is 2.42 $M_\odot$, corresponding to a baryonic mass of 2.92 $M_\odot$. If the compact remnant in SN 1987A was a black hole, and not a neutron star, it means that at least ~ 0.5 $M_\odot$ of additional accreted mass were required, if we just take the two solar mass limit. If we use the maximum baryonic mass of HS(DD2) we even have to accrete $\sim$1.3 $M_\odot$ of additional material. Obviously, if such a huge amount of material would be accreted onto the neutron star, our predictions for the explosion energy and the nucleosynthesis would not apply any more.

Nevertheless, we have the impression that it would be difficult to fit the SN 1987A observables and obtain a black hole as the compact remnant at the same time. For spherical fallback, it is certainly excluded. The only possibility could be a highly anisotropic explosion and aspherical accretion, which we cannot address with our study. To show if such a scenario can be realized remains a task for future multi-dimensional studies. In the 2D simulations of [161] the remnant mass is decreasing with the explosion energy and an explosion energy above 1 Bethe would result in neutron stars below ~ 2 $M_\odot$ baryonic mass. Note that [197] already came to the same conclusion that the formation of a black hole in SN 1987A "is quite unlikely", based on 2D simulations with a 15 $M_\odot$ progenitor.

Another possibility was proposed by [198]. These authors argued that the time delay of ~ 5 s observed for the neutrino signal by the IMB detector could be related to a collapse to a quark star. Due to the proposed faster neutrino cooling of quark stars, this would give a natural explanation why it has not been observed until today. The end of our simulations is also around 5 s, thus we can make statements about the conditions at which the phase transition to quark matter took place in SN 1987A, if the scenario of [198] was true. We have a central mass density of 4.56×10^{14} g/cm^3 corresponding to $n_B^c = 0.272$ fm^{-3} or $n_B^c = 1.83\ n_B^0$, a temperature of 23.2 MeV, and an electron fraction of 0.24. Some simplified models for quark matter predict that the phase transition in symmetric matter is shifted to higher densities compared with SN conditions [76]. Under that hypothesis, a phase transition around 2 ρ_0 and 20 MeV cannot be excluded.

A simpler explanation is given by the possibility that a pulsar in the SN 1987A remnant is simply not (yet) observable. Ögelman and Alpar [199], Graves et al. [200] showed that the non-detection of any compact remnant puts important limits on the magnetic field the NS can have (either unusually low or very high, in the realm of magnetars). Furthermore, for both cases (NS and BH) [200] put severe constraints on currently ongoing accretion scenarios, e.g., spherical accretion is almost ruled out. Graves et al. [200] conclude that "it seems unlikely that the remnant of SN 1987A currently harbors a pulsar". Our simulations would be in line with the option of a neutron star with a very low magnetic field or with a "normal" magnetic field which is still (partly) buried in the crust due to the late time fallback, similar to what is observed for neutron stars in binary systems. In this respect, recent high-resolution radio observations of the remnant indicate the presence of a compact source or a pulsar wind nebula [201, 202]. Future observations will be able to clarify the nature of this emission.

4.3.5 Correlations

As a byproduct of exploring the 18-21 $M_\odot$ window and the fitting procedure to SN 1987A we have found interesting correlations between different quantities, which we will discuss here. In figure 4.15, we plot the explosion energy, the explosion time, and the (baryonic) remnant mass as function of the progenitor compactness. The results obtained with the calibrated runs indicate a general trend with progenitor compactness for $E_{\rm expl}$. The explosion time, $t_{\rm expl}$, is almost constant within each the LC and the HC group, while the difference between the two groups is related to the difference between how LC and HC models explode (discussed in section 4.2.3). The remnant mass increases with compactness, as expected. Nevertheless, we notice significant deviations from the described trends: for $E_{\rm expl}$ and $t_{\rm expl}$ in the HC sample, for $M_{\rm rem}$ mainly in the LC sample.

Figure 4.16 shows explosion times and explosion energies for all the exploding runs in our sample. We can identify a correlation between $t_{\rm expl}$ and $E_{\rm expl}$ for a given progenitor: the larger $t_{\rm expl}$ the higher is $E_{\rm expl}$. This correlation is more pronounced for the HC models than for the LC models.

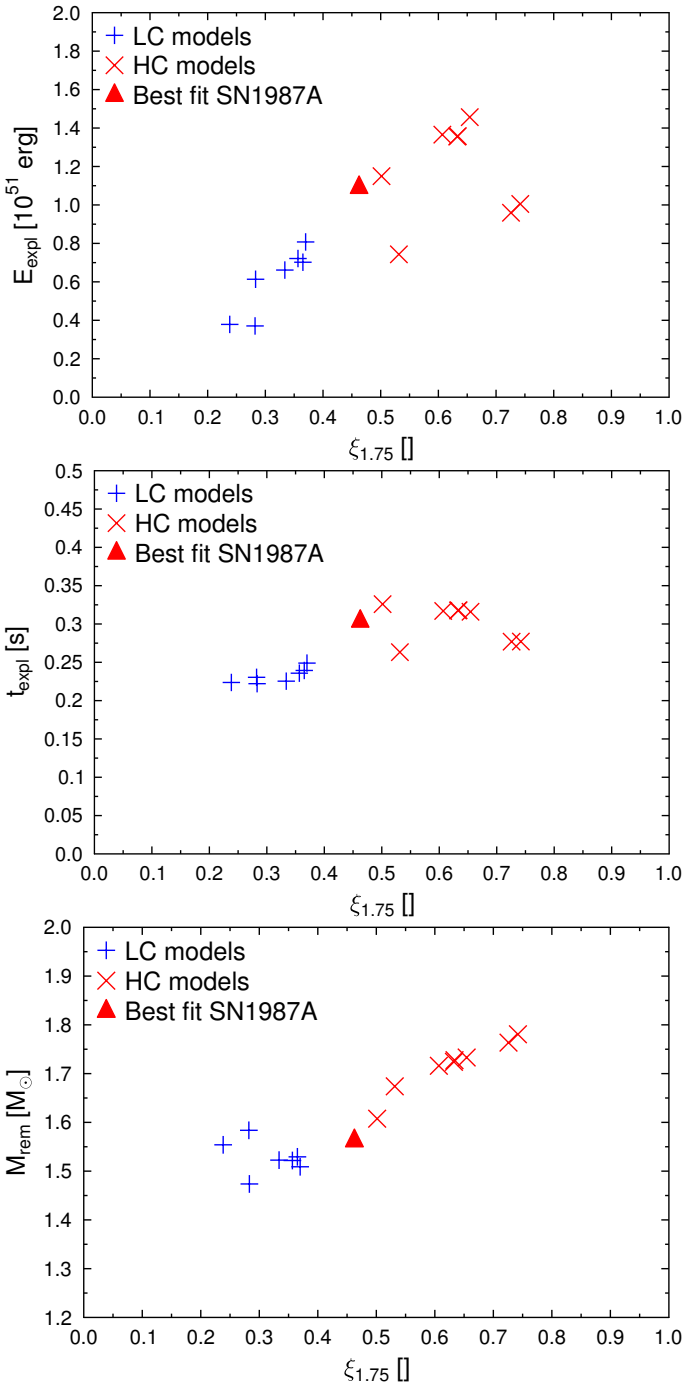

Fig. 4.15.: Explosion energies (top), explosion times (middle), and (baryonic) remnant mass (bottom) as function of compactness for the PUSH parameters of our best-fit model (k_{PUSH} = 3.3 and t_{rise} = 0.15 s) for all progenitors in the 18-21 $M_\odot$ window. HC models are denoted by a red cross, LC models by a blue plus. Our best-fit model for SN 1987A is highlighted by a filled triangle. Figures taken from [87].

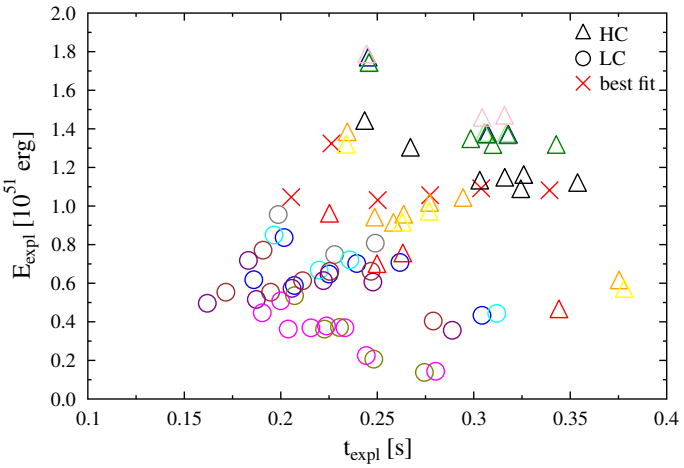

Fig. 4.16.: Explosion energy E_{expl} versus explosion time t_{expl} for all the progenitors in the 18-21 $M_\odot$ range and for different combinations of k_{PUSH} and t_{rise}, however only the exploding models are included. HC models are indicated by a triangle, LC models by a circle. The best fit model is indicated by a cross. The different colors distinguish different progenitors. Figure taken from [87].

4.3.6 Heating Efficiency and Residence Time

In the context of CCSNe, the heating efficiency η is often defined as the ratio between the volume-integrated, net energy deposition inside the gain region and the sum of the ν_e and $\bar{\nu}_e$ luminosities at infinity:

$$\eta = \frac{\int_{V_{\mathrm{gain}}} \rho\, \dot{e}_{\nu_e,\bar{\nu}_e} \mathrm{d}V}{L_{\nu_e} + L_{\bar{\nu}_e}}, \tag{4.7}$$

see, e.g., [133, 136, 146, 168, 203]. In non-exploding, spherically symmetric simulations, η usually rises within a few tens of milliseconds after core bounce and reaches its maximum around $\eta \sim 0.1$ at $t \approx 100\,\mathrm{ms}$, when the shock approaches its maximum radial extension. As soon as the shock starts to recede and the volume of the gain region decreases, η diminishes quickly to a few percents (see, for example, the long-dashed lines in figure 4.17).

In multi-dimensional simulations, where the shock contraction is delayed or even not happening, energy deposition is expected to be slightly more efficient ($\eta \sim 0.10 - 0.15$ at maximum) and to decrease more slowly, within a few hundreds of milliseconds after bounce or at the onset of an explosion (see, for example, [131, 133, 146, 168]). These differences arise not only because the gain region does not contract, but also because neutrino-driven convection efficiently mixes low and high entropy matter between the neutrino cooling and the heating regions below the shock front. Furthermore, convec-

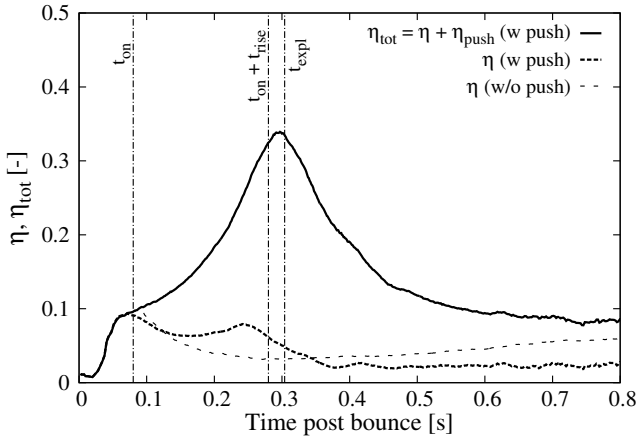

Fig. 4.17.: Neutrino heating efficiency for the SN 1987A best fit model: 18.0 $M_\odot$ model with t_{on} = 80 ms, t_{rise} = 200 ms, and k_{PUSH} = 3.5. The solid lines represent the total efficiency (i.e., due to ν_e and $\bar{\nu}_e$ absorption and due to PUSH), the short-thick dashed lines the efficiency only due to ν_e and $\bar{\nu}_e$ absorption. For comparison, the heating efficiency of the corresponding non-exploding model (k_{PUSH} = 0) is also presented (long-thin dashed lines). Figure taken from [87].

tive motion and SASIs are expected to increase significantly the residence time of fluid particles inside the gain region during which they are subject to intense neutrino heating (see, e.g., [133, 134]). Since the increase of the particle internal energy is given by the time integral of the energy absorption rate over the residence time, this translates to a larger energy variation [134].

In spherically symmetric models, the imposed radial motion does not allow the increase of the residence time. This constraint limits the energy gain of a mass element traveling through the gain region. In models exploded using the light-bulb approximation, a large enough internal energy variation is provided by increasing the neutrino luminosity above a critical value, which depends on the mass accretion rate and on the dimensionality of the model (e.g., [127, 128, 130, 131, 133, 134, 157–160, 175]). Since in our model the neutrino luminosities are univocally defined by the cooling of the PNS and by the accretion rate history, we increase the energy gain by acting on the neutrino heating efficiency. This effect can be made visible by defining a heating efficiency that takes the PUSH contribution into account, η_{tot}:

$$\eta_{tot} = \eta + \eta_{push} = \frac{\int_{V_{gain}} \rho \left(\dot{e}_{\nu_e,\bar{\nu}_e} + \dot{Q}^{+}_{push} \right) dV}{L_{\nu_e} + L_{\bar{\nu}_e}}. \tag{4.8}$$

In figure 4.17, we plot η_{tot} as a function of time for our SN 1987A calibration model, with PUSH (k_{PUSH} = 3.5) and without it (k_{PUSH} = 0). We first notice that the heating

efficiency provided by ν_e and $\bar{\nu}_e$ can differ between exploding (short-thick dashed lines) and non-exploding models (long-thin dashed lines). In the case of the exploding model, PUSH provides an increasing contribution to $\eta_{\rm tot}$. It continues to increase steeply up to $t \approx t_{\rm on} + t_{\rm rise}$, but also later, up to $t \approx t_{\rm expl}$, due to the shock expansion preceding the explosion. Thus, the increasing heating efficiency in our spherically symmetric models can be interpreted as an effective way to include average residence times longer than the advection timescale.

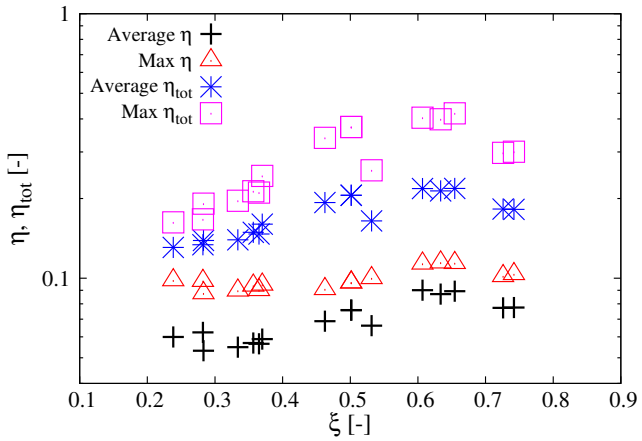

Fig. 4.18.: Average and maximum heating efficiencies, calculated between $t = t_{\rm on}$ and $t = t_{\rm expl}$ for the runs obtained with the fitted parameters, table 4.4, and plotted as a function of the progenitor compactness $\xi_{1.75}$. The black crosses and the red triangles refer to the average and the maximum efficiency due to ν_e and $\bar{\nu}_e$ (η), while the blue stars and the magenta squares to the average and the maximum total efficiency ($\eta_{\rm tot}$), including also the PUSH contribution. Figure taken from [87].

In figure 4.18, we collect the average and the maximum heating efficiencies, for all the models obtained with the set of parameters resulting from the fit procedure (table 4.4). Both the average and the maximum values are computed within the interval $t_{\rm on} \leq t \leq t_{\rm expl}$. We plot them as a function of the compactness and we distinguish between η and $\eta_{\rm tot}$. The maximum of η is usually realized at $t \approx t_{\rm on}$, while the maximum of $\eta_{\rm tot}$ is reached around $t \approx t_{\rm expl}$ (see also figure 4.17). Since the explosion sets in later for HC models, when $t_{\rm expl} \gtrsim t_{\rm on} + t_{\rm rise}$, the PUSH factor $\mathcal{G}(t)$ has time to rise to $k_{\rm PUSH}$ for these models. This increases not only the maximum but also the average $\eta_{\rm tot}$ compared with the LC cases. We notice that all four quantities show a correlation with $\xi_{1.75}$, but much weaker in the case of η than in the case of $\eta_{\rm tot}$. Moreover, in the HC region, we recognise deviations from monotonic behaviors which reproduce the irregularities already observed in the explosion properties.

4.3.7 Alternative Measures of the Explosion Energy

In the following, we discuss alternative measures of the explosion energy (introduced in section 3.3.1) used in the literature for reasons of comparison. We investigate their behaviors at early simulation times and their general rate of convergence. The quantity $E^{+}_{\mathrm{ov}}(t)$ is defined as the sum of the overburden E_{ov} and of the diagnostic energy $E^{+}(t)$. This measure of the explosion energy is equivalent to the one defined in equation (3.75):

$$E_{\mathrm{expl}}(t) \equiv E^{+}_{\mathrm{ov}}(t) = E^{+}(t) + E_{\mathrm{ov}}(t). \tag{4.9}$$

For long enough simulation times, all matter above the mass-cut should get positive specific explosion energies, and thus the overburden should approach zero and the diagnostic energy should become equal to the explosion energy $E_{\mathrm{expl}}(t)$. The "residual recombination energy" $E_{\mathrm{rec}}(t)$ [142] given by

$$E^{+}_{\mathrm{ov,r}}(t) = E^{+}_{\mathrm{ov}}(t) + E_{\mathrm{rec}}(t)\,, \tag{4.10}$$

where $E_{\mathrm{rec}}(t)$ is the energy that would be released if all neutron-proton pairs and all ^{4}He recombined to ^{56}Ni in the regions of positive specific explosion energy, is an upper limit for the explosion energy. We call it *residual* recombination energy to make clear that this is energy which is *not* liberated in our simulations, in contrast to the energy of the recombination processes which we identified in section 4.2.2.

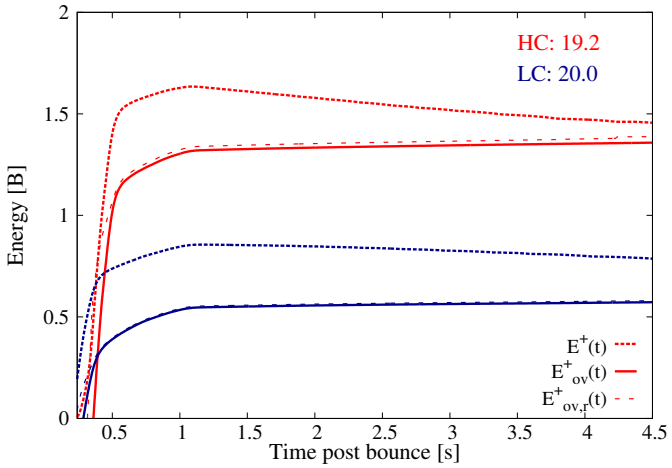

Fig. 4.19.: Temporal evolution of the diagnostic energy E^{+}, the explosion energy E^{+}_{ov}, and the upper limit of the explosion energy also including the recombination energy E_{rec} for a HC (19.2 $M_{\odot}$ progenitor) and a LC case (20.0 $M_{\odot}$ progenitor), for PUSH parameters reported in table 4.2. Figure taken from [87].

In figure 4.19, we investigate the behavior of the diagnostic energy $E^{+}(t)$, and we compare it with our estimate of the explosion energy $E_{\mathrm{expl}}(t) \equiv E^{+}_{\mathrm{ov}}(t)$ and with its upper limit

represented by $E^{+}_{\mathrm{ov,r}}(t)$. We want to emphasize that these quantities are obtained from mass integrals above the time-dependent mass-cut, in contrast to most of the energies investigated in section 4.2.2, where a fixed mass domain was considered.

While $E^{+}_{\mathrm{ov}}(t)$ and $E^{+}_{\mathrm{ov,r}}(t)$ have already saturated to a constant value at $t \approx 1.5$ s, even at $t \approx 4.6$ s the diagnostic energy has not yet converged. $E^{+}_{\mathrm{ov}}(t)$ and $E^{+}_{\mathrm{ov,r}}(t)$ approach their asymptotic values from below, and any late time increase ($t \gtrsim 1.5$ s) is due to the energy carried by the neutrino-driven wind ejected from the PNS surface. On the other hand, $E^{+}(t)$ reaches its maximum around $\lesssim 1$ s after t_{expl}, when the neutrino absorption and the nuclear recombination have released most of their energy in the expanding shock wave, and then it decreases towards $E^{+}_{\mathrm{ov}}(t)$, since matter with negative total specific energy is accreted at the shock. The difference between $E^{+}_{\mathrm{ov}}(t)$ and $E^{+}(t)$ is mainly represented by the gravitational binding energy of the stellar layers above the shock front. Thus, the rate of convergence of the diagnostic energy depends on the amount of gravitational binding energy contained in the outer envelope of the star and on the relative speed at which the shock propagates inside it. Since the gravitational binding energy of the outer layers is similar between the two explored models, the different rate of convergence depends mostly on the different expansion velocity of the shock wave, which is larger for more energetic HC models.

Yamamoto et al. [161] found for a 15 $\mathrm{M}_{\odot}$ progenitor that the diagnostic energy saturates and thus reaches the asymptotic explosion energy already between 1 and 2 s post-bounce. This difference to what we find is related to the different progenitors used and, in particular, to the different binding energy of the outer envelopes, which is expected to be much smaller for a 15 $\mathrm{M}_{\odot}$ progenitor than for a ~ 20 $\mathrm{M}_{\odot}$ progenitor (see, for example, figure 5 of [204]). Nevertheless, we conclude that the diagnostic energy is in general (i.e., without further considerations) not suited to give an accurate estimate of the explosion energy at early times.

4.3.8 Comparison with other Works

A similar fitting to SN 1987A energetics has been done for multi-dimensional simulations (2D and 3D) using a light-bulb scheme for the neutrinos by [134]. As initial conditions they used a post-collapse model based on the 15 $\mathrm{M}_{\odot}$ blue supergiant progenitor model of [24]. Even if they did not provide the corresponding compactness, the values of the accretion rate ($\sim 0.2 - 0.3$ $\mathrm{M}_{\odot}$ s^{-1}) and of the electron neutrino luminosity ($\sim 1.8 - 3.5 \times 10^{51}$ erg s^{-1}) at the onset of the explosion are more compatible with our LC models. In their fitting, only the diagnostic explosion energy E^{+} was used at a time of

$t_{\rm pb}$ = 1.5 s when it is expected to have saturated to $E_{\rm expl}$ (see [161]). But no estimates for the nucleosynthesis yields were given. The time when the shock reaches 500 km (which corresponds for us to $t_{\rm expl}$) is significantly lower in their models (90-140 ms after bounce), mainly due to the different extension and evolution of the shock during the first 100 ms after core bounce. A more detailed quantitative comparison (albeit limited by the different dimensionality of the two models) requires to use a more similar progenitor. However, the advection timescale and the mass in the gain region are larger than the corresponding values we have obtained in all our models, as expected from the larger average residence time resulting from multi-dimensional hydrodynamical effects.

Ugliano et al. [141] also calibrated their spherically symmetric exploding models with the observational constraints from SN 1987A, and used progenitor models identical to the ones we have adopted [40]. They also found that the remnant mass and the properties of the explosion exhibit a large variability inside the narrow 18-21 $M_\odot$ ZAMS mass window (they even found some non-exploding models). However, they did not find any clear trend with progenitor compactness (for example, their calibration model is represented by the 19.8 $M_\odot$ ZAMS mass progenitor which belongs to the LC sample). The explosion timescales for models in the 18-21 $M_\odot$ ZAMS mass interval are much longer in their case ($t_{\rm expl} \sim 0.3 - 1$ s), while their range for the explosion energy (0.6 – 1.6 Bethe) is relatively compatible with ours (0.4 – 1.6 Bethe). Clearly, all these differences are related to the numerous diversities between the two models.

A possible relation between explosion properties and progenitor compactness has been first pointed out by [171], who searched for a minimum enhanced neutrino energy deposition in spherically symmetric models. Similarly to us, they found that more compact progenitors require larger heating efficiency to explode. However, they do not investigate the explosion energy of their models. Moreover, they consider it to be unlikely that a model which requires $\eta \gtrsim 0.23$ ($\xi_{2.5} \gtrsim 0.45$) will explode in nature. In our analysis, we have interpreted a large neutrino heating efficiency in spherically symmetric models as an effective way to take into account longer residence time inside the gain region. We have pointed out that HC models, characterized by larger $\eta_{\rm tot}$, are required to obtain the observed properties of SN 1987A. However, these models still have $\xi_{2.5} < 0.45$ and our average heating efficiency are below the critical value of [171].

A clear correlation between explosion properties and progenitor compactness has been recently discussed by [205]. They performed systematic 2D calculations of exploding CCSNe for a large variety of progenitors, using the IDSA to model ν_e and $\bar{\nu}_e$ transport. Due to computational limitations and due to the usage of only a NSE EOS, their simulations were limited to $\sim$ 1 s after core bounce. Thus, they could not ensure the convergence

of the diagnostic energy and could not directly compare their results with CCSN observables. However, they found trends with compactness similar to the ones we have found in our reduced sample.

Other authors have also compared the predicted explosion energy and Ni yield from their models to the observational constraints. For example, [161], using the neutrino light-bulb method to trigger explosions in spherical symmetry, found a similar trend between explosion energies and nickel masses as we found (see table 4.5). They also compared to a thermal bomb model with similar explosion energies and mass cut, and found that the neutrino heating mechanism leads to systematically larger ^{56}Ni yields. They related it to higher peak temperatures, which appear because a greater thermal energy is required to unbind the accreting envelope. They also concluded that the neutrino-driven mechanism is more similar to piston-driven models by comparing with [206]. The problem of overproducing ^{56}Ni is lessened in the 2D simulations of [161] because of slightly lower peak temperatures and the occurrence of fallback.

The conclusions drawn in section 4.2.2 about the contributions of nuclear reactions to the explosion energy are somewhat opposite to what can be found in other works in the literature. For example, [161] state that the contribution of the nuclear reactions to the explosion energy is comparable to or greater than that of neutrino heating. Furthermore, they identify the recombinations of nucleons into nuclei in NSE as the most important nuclear reactions. However, they also point out that this "recombination energy eventually originates from neutrino heating". We think that this aspect is crucial for understanding the global energetics. Indeed, if we had started the analysis presented in figure 4.7 not at bounce but at $t_{\rm expl}$ we would also have identified a strong contribution from the nuclear reactions, given roughly by the difference between $-(E_{\rm mass} - E_{\rm mass,0})$ at $t_{\rm expl}$ (which is close to the minimum) and the final value. However, as is clear from the figure, roughly the same amount of energy was actually taken from the thermal energy before $t_{\rm expl}$. The dominant net contribution to the explosion energy originates from neutrino heating, as is evident from figure 4.6 and as we have discussed in detail in section 4.2.2.

4.4 Summary and Conclusions

The investigation of the explosion mechanism of CCSNe as well as accurate explorations of all the aspects related with it, is a long lasting, but still fascinating problem. Sophisticated multi-dimensional hydrodynamical simulations, possibly including detailed neutrino transport, microphysical EOS, magnetic fields and aspherical properties of the pro-

genitor structure, are ultimately required to address this problem. The high computational costs of such models and the uncertainties in several necessary ingredients still motivate the usage of effective spherically symmetric models to perform extended progenitor studies.

In this work we have presented a new method, PUSH, for artificially triggering parametrized CCSN explosions of massive stars in spherical symmetry. The method provides a robust and computationally affordable framework to study important aspects of CCSNe that require modeling of the explosion for several seconds after its onset for extended sets of progenitors. For example, the effects of the shock passage through the star, the neutron star mass distribution, the determination of the explosion energy, or explosive SN nucleosynthesis. Here, we have focused on the exploration of basic explosion properties and on the calibration of PUSH by reproducing observables of SN 1987A. We considered progenitors in the ZAMS mass range of 18 – 21 $M_\odot$ which corresponds to typical values for the progenitor mass of SN 1987A [23].

Unlike traditional methods (such as thermal bombs, pistons, or neutrino light-bulbs), our method does not require any external source of energy to trigger the explosion nor a modification of the charged-current neutrino reactions. Instead, the PUSH method taps a fraction of the energy from muon- and tau-neutrinos which are emitted by the PNS. This additional energy is deposited inside the gain region for a limited time after core bounce. The introduction of a local heating term that is only active where electron-neutrinos are heating and where neutrino-driven convection can occur is inspired by qualitative properties of multi-dimensional CCSN simulations. We have two major free parameters, $t_{\rm rise}$, describing the temporal evolution of PUSH, and $k_{\rm PUSH}$, controlling the strength. They are determined by comparing the outcome of our simulations with observations.

Our setup allows us to model the entire relevant domain, including the PNS and the ejecta. In particular, (i) the thermodynamic properties of matter both in NSE and non-NSE conditions are treated accurately; (ii) the neutrino luminosities are directly related to the PNS evolution and to the mass accretion history; (iii) the evolution of the electron fraction is followed by a radiative transport scheme for electron flavor neutrinos, which is important for the nucleosynthesis calculations.

We have studied the evolution of the explosion energy and how it is generated. The energy deposition by neutrinos is the main cause of the increase of the total energy of the ejecta and, thus, the main source of the explosion energy. The net nuclear binding energy released by the ejecta during the whole SN (including both the initial endothermic pho-

todissociation and the final exothermic explosive burning) is positive, but much smaller than the energy provided by neutrinos. Furthermore, we obtain an approximate convergence of the explosion energy typically only after 1 to 2 seconds and only if the full progenitor structure is taken into account. Vice-versa, we find that the so-called "diagnostic energy" is, in general, not suited to give an accurate estimate of the explosion energy at early times.

Our broad parameter exploration has revealed a distinction between high compactness ($\xi_{1.75} > 0.45$) and low compactness ($\xi_{1.75} < 0.45$) progenitor models for the ZAMS mass range of 18 – 21 $M_\odot$. The LC models tend to explode earlier, with lower explosion energy, and with a lower remnant mass. When the HC models explode, they tend to explode later, more energetically, and producing more massive remnants. This is due to different accretion histories of the LC and HC models. The HC models have larger accretion rates, which produce larger neutrino luminosities, (marginally) harder neutrino spectra, and a stronger ram pressure at the shock. In order to overcome this pressure a more intense neutrino energy deposition is required behind the shock. And, once the explosion has been launched, a more intense energy deposition inside the expanding shock is observed. Thus, HC models require more time to explode but the resulting explosions are more energetic.

The fitting of the PUSH parameters to observations of SN 1987A has lead to several interesting conclusions. The requirement of an explosion energy around 1 Bethe has restricted our progenitor search to HC models. At the same time, our parameter space exploration has shown that a constraint on the explosion energy is equivalent to a tight correlation between the two most relevant PUSH parameters, $t_{\rm rise}$ and $k_{\rm PUSH}$: if a certain explosion energy has to be achieved, a longer timescale for PUSH to reach its maximum efficiency ($t_{\rm rise}$) has to be compensated by a larger PUSH strength ($k_{\rm PUSH}$). This degeneracy can be broken by including nucleosynthesis yields in the calibration of the free parameters.

We find an overproduction of ^{56}Ni for runs with an explosion energy around and above 1 Bethe. This problem is observed for all the tested parameter choices and progenitors that provide a sufficiently high explosion energy. Thus, fallback is necessary in our models to reproduce the observed nucleosynthesis yields. This fallback could be associated with the formation of a reverse shock when the forward shock reaches the hydrogen shell. The relatively large amount of fallback that we use (0.1 $M_\odot$) is consistent with observational constraints from SN 1987A and with explicit calculations of the fallback for exploding models of ~ 20 $M_\odot$ ZAMS mass progenitors [141, 192].

The production of $^{57-58}$Ni is sensitive to the electron fraction of the innermost ejecta. A final mass cut initially located inside the silicon shell can provide slightly neutron rich ejecta, corresponding to the conditions required to fit the $^{57-58}$Ni yields of SN 1987A. We found that this is only possible for the 18.0 $M_\odot$ and 19.4 $M_\odot$ ZAMS mass progenitors, whereas for the other HC models, characterized by larger $\xi_{1.75}$, the mass cut is located inside the oxygen shell. The 18.0 $M_\odot$ and 19.4 $M_\odot$ ZAMS mass progenitors can explain the energetics and all nickel yields if fallback is included. For ^{44}Ti, in contrast, we find that it is underproduced. However, we have shown that uncertainties in the relevant nuclear reaction rates, together with mixing of the ejecta, can help reducing this discrepancy.

Our work has demonstrated that the progenitor structure and composition are of great importance for the nucleosynthesis yields. Recently, it has been pointed out that asphericities in the progenitor structure could aid the multi-dimensional neutrino-driven SN mechanism [207–209]. For our work, the compositional changes induced by multi-dimensional effects in the progenitor evolution [210] would be of particular interest and could be the subject of future work. However, at present, databases with large sets of progenitors are only available for calculations that were done in spherical symmetry.

Finally, we have identified a progenitor (18.0 $M_\odot$ ZAMS mass, compactness $\xi_{1.75} = 0.463$ at collapse) that fits the observables of SN 1987A for a suitable choice of the PUSH parameters ($t_{\rm on} = 80$ ms, $t_{\rm rise} = 200$ ms, and $k_{\rm PUSH} = 3.5$) and assuming 0.1 $M_\odot$ of fallback. The associated explosion energy is $E_{\rm expl} = 1.092$ Bethe, while $M(^{56}\mathrm{Ni}) = 0.073$ $M_\odot$. The formation of a BH in SN 1987A seems to be unlikely, since it would require a much larger fallback compared with our analysis and/or an extremely asymmetric explosion. Instead, we predict that in SN 1987A a neutron star with a baryonic mass of 1.66 $M_\odot$ was born, corresponding to a gravitational mass of 1.50 $M_\odot$ for a cold neutron star with our choice of the EOS. This will hopefully be probed by observations soon [202].

For our best model of SN 1987A the explosion happens on a timescale of a few hundreds of milliseconds after core bounce. This timescale is consistent with the overall picture of a neutrino-driven SN, and broadly compatible with the first results obtained in exploding, self-consistent, multi-dimensional simulations.

From exploring the progenitor range of 18 – 21 $M_\odot$ ZAMS mass we found indications of a correlation between explosion properties and the compactness of the progenitor model. However, a more complete analysis will require the exploration of a larger set of progenitors with the PUSH method. This will be the topic of a forthcoming work. An extended study considering all possible progenitors for CCSNe in the mass range of 8 – 100 $M_\odot$ will be relevant for several open questions in nuclear astrophysics, for example for the

comparison of predicted to observed explosion energies, neutron-star remnant masses, and ejected ^{56}Ni (see, e.g., [137]) or for the prediction of complete nucleosynthesis yields of all elements which is a crucial input to galactic chemical evolution. A full progenitor study could also give more insight into the extent to which the compactness parameter affects the SN energetics and nucleosynthesis.

5

Results 2: An Explodability Study of One-Dimensional CCSN Simulations [1]

> *Das Glück des Forschers besteht nicht darin eine Wahrheit zu besitzen, sondern die Wahrheit zu erringen...*
>
> **— M. Planck**

The PUSH method, introduced in chapter 3, is a viable tool to investigate the explodability of progenitors by means of the neutrino-driven CCSN mechanism, the resulting progenitor-remnant connection, and the nucleosynthesis in the ejecta. For the first fitting procedure of PUSH (see chapter 4) the progenitors of Woosley, Heger and Weaver (2002) [40] (abbreviated with WHW02) with solar metallicity in the mass range between 18 and 21 $M_\odot$, corresponding to the progenitor mass range of SN 1987A, were used. In this chapter the PUSH method eventually is applied to a broad range of progenitors, i.e. the whole sets of progenitors with solar metallicity from WHW02 and from Woosley and Heger (2007) [41] (abbreviated with WH07), covering progenitors in the mass range between 10.8 $M_\odot$ and 120 $M_\odot$[2]. This task might initially sound straightforward but experience taught that the application of PUSH to a larger sample of progenitors covering many different compactness values needs a more variable approach, i.e., a calibration of the PUSH method that allows variability of the parameters and not only uses one single fixed set for all models. This complication is not too surprising, since, after all, the full understanding of the nature of the CCSN explosion mechanism has been elusive for decades. Here, I give an outline of the contents of this chapter. The results of which have been published in the two papers Ebinger et al. and Curtis, Ebinger, et al. [88, 140]. As mentioned

[1] The content of this chapter has been published in an abbreviated version in Ebinger et al. (2018), The Astrophysical Journal, Vol 870 Number 1 [88]

[2] The mentioned progenitor models are available online on the webpage, "http://2sn.org/stellarevolution/", see also figures 5.1 and 5.2.

above, the aim of this chapter is to develop a calibration of the PUSH method that can be applied to the extended ZAMS mass range of the progenitor samples WHW02 and WH07. To do this, we formulate constraints based on observed CCSN properties (discussed in section 5.1) and experience resulting from our application of the PUSH framework to large model samples that the calibration needs to fulfill. Ultimately, the PUSH method allows us to gain some insight on the explodability and the nucleosynthesis yields of CCSN explosions and the resulting remnants. This is done step by step, beginning with the description of the improvements made to PUSH since the version in Perego et al. [87]. After the introduction of the updated heating criteria and a discussion of the dependencies, we present a new calibration model for SN 1987A obtained with the updated PUSH method.The best fit parameters obtained from a calibration with the new heating criterion to a star from the samples WHW02 and WH07 in the mass range of the progenitor of SN 1987A are then applied to the whole range of progenitors to study the outcome of this straightforward extension of the previous work on PUSH [87]. This initial approach to investigate the explodability of the whole CCSN progenitor mass range leads to robust explosions for all considered stars if reasonable explosion energies around 10^{51} erg for possible progenitors of SN 1987A are imposed as a constraint. We conclude that the idea of constant PUSH parameters is not able to explain observational data of CCSNe and the the explodability of the whole range of progenitor models and proceed by searching for a new approach, introducing a dependency of k_{PUSH} on compactness. To achieve this, we define a set of constraints that enable us to find a calibration of the PUSH method with the compactness value. In the literature the compactness value $\xi_M = \frac{M/M_\odot}{R(M)/1000km}$ is commonly evaluated for M between 1.5 and 3.0 $M_\odot$, see, e.g., [138, 211–213]. The compactness value used in the previous PUSH investigation [87], where we studied exploding models that were intended to reproduce SN 1987A, was evaluated for $M = 1.75\,M_\odot$. Now we want to investigate a much broader ZAMS mass range range of CCSN progenitor models. This involves the formation of BHs and more massive NSs than in the previous investigation. Thus, to account for the larger possible masses that are included in the layers of the progenitor star that are crucial for the neutrino-driven explosion mechanism as well as the larger possible NS remnant masses and BH formation, we use $M = 2\,M_\odot$ to evaluate the compactness value $\xi_M = \xi_{2.0}$ at bounce, if not otherwise indicated. The calibration of PUSH is applied to the progenitor sets from WHW02 and WH07 [40, 41] with solar metallicity and subsequently the results are presented. We also discuss the remnants of neutrino-driven CCSNe and give their birth-mass distribution. In the last section we give an outlook on the application of the PUSH method.

5.1 Observational Data of CCSNe and the Faint SN Branch

Before we go into the details of the calibration process, we want to discuss what can be expected from the study of CCSNe with the PUSH method and summarize the observational constraints. As stated in the definition of the PUSH method, we rely on the neutrino-driven mechanism to parametrize our one-dimensional SN models. An important aspect that can be investigated with a PUSH calibration applied to the whole progenitor range for solar, and also low metallicity progenitor stars, is the question which stars do explode and which stars ultimately form a black hole (BH). This question and in general the question about the explodability of CCSN progenitors has been also investigated (amongst others) in the works of O'Connor and Ott (2011), Ugliano et al. (2012), Nakamura et al. (2015), Ertl et al. (2016), Sukhbold et al. (2016), and Müller et al. (2016) [141, 170, 211, 212, 214, 215]. In figure 5.1 the progenitor masses, different core and envelop masses, as well as different compactness values as a function of ZAMS mass for the two progenitors samples WHW02 and WH07 with solar metallicity are shown. We see that progenitors of the two solar metallicity sets with the same ZAMS mass can have very different properties. This indicates that already at the level of the progenitors some uncertainties are present which then can be reflected in the outcome of the simulations. The recent observation of gravitational waves of a BH merger event, presented in the work of Abbott et al. (2016) [216], confirmed the physical reality of gravitational waves. What it also showed is that BHs with masses between 25 and 35 $M_\odot$ do exist in the universe. Presumably the simplest way to form a BH of a given mass is the collapse of the corresponding progenitor to a BH. Thus, if the observed merging BHs did form directly in failed SNe, this and future observations also give hints which progenitors will not form successful CCSN explosions but collapse to BHs. In this case, the observation of the BH merger event [216] would suggest that low metallicity stars in the mass range between 25 and 41 $M_\odot$ (see table 5.1) can form BHs as can be seen in figure 5.2, were the green band indicates the mass region of the two observed BHs.

Primary Black Hole Mass	$36^{+5}_{-4}\ M_\odot$
Secondary Black Hole Mass	$29^{+4}_{-4}\ M_\odot$

Tab. 5.1.: Black hole masses observed in Abbott et al (2016) [216]

Even though solar metallicity progenitors are the main subject of this chapter, in section 5.6 we will give some first results on the explodability of CCSN progenitors of the samples

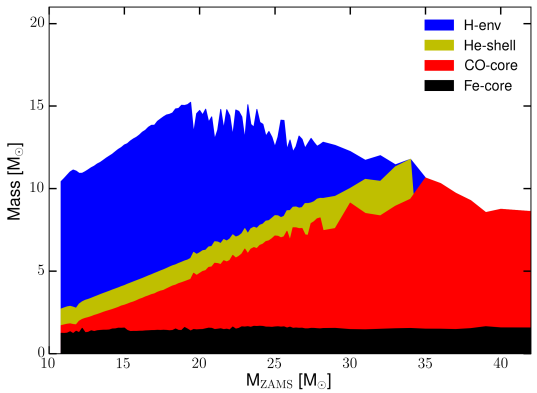

(a) Progenitor structure of stars with solar metallicity from the WHW02 series in the mass range between 10.8 $M_\odot$ and 40 $M_\odot$ [40].

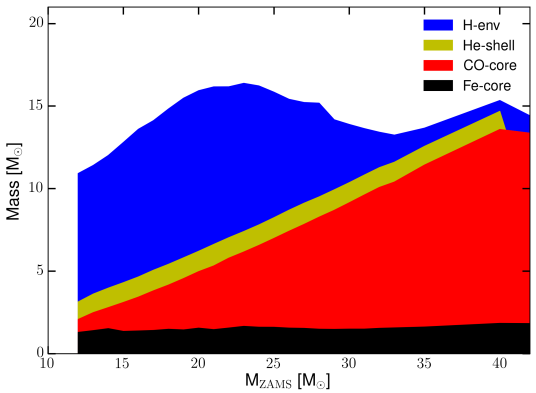

(b) Progenitor structure of stars with solar metallicity from the WH07 series in the mass range between 12 $M_\odot$ and 40 $M_\odot$ [41].

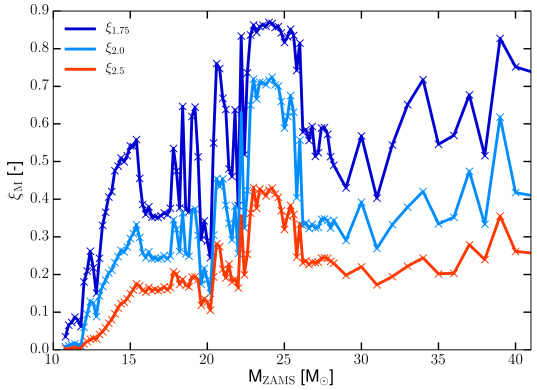

(c) Compactness of progenitors of stars from the WHW02 series in the mass range between 10.8 $M_\odot$ and 40 $M_\odot$ [40].

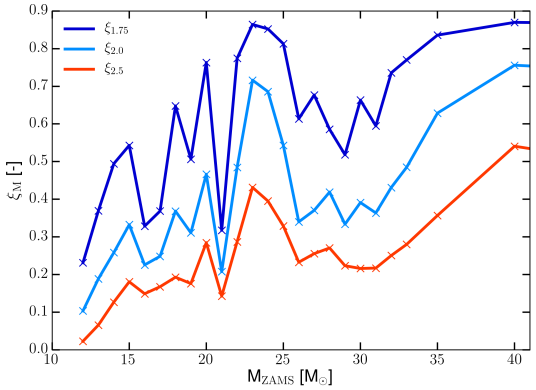

(d) Compactness of progenitors of stars from the WH07 series in the mass range between 12 $M_\odot$ and 40 $M_\odot$ [41].

Fig. 5.1.: The structure and the compactness of the stars contained in the progenitor set of non-rotating single massive stars with solar metallicity of Woosley, Heger and Weaver (2002), WHW02 [40], and Woosley and Heger (2007), WH07 [41], are shown. The plots (a) and (b) show the Fe-core, the CO-core as well as the He-envelope, H-envelope and the total mass of the star. The plots (c) and (d) show the compactness $\xi_M = \frac{M/M_\odot}{R(M)/1000km}$ evaluated at different enclosed masses, M=1.75 $M_\odot$,2.0 $M_\odot$ and , 2.5 $M_\odot$.

from Woosley, Heger, and Weaver (2002) [40] with low metallicities, i.e., $Z = Z_\odot \times 10^{-4}$ and $Z = 0$. Future observations surely will give more insights into the distribution of BH masses and with this also give clues on the explodability of CCSN progenitors.

Furthermore, by looking at the observed explosion energies in figure 5.3 it is possible to define two branches of observed explosion energies of CCSNe above a certain ZAMS mass of the involved star. For massive stars around or below 21 $M_\odot$ a more or less well

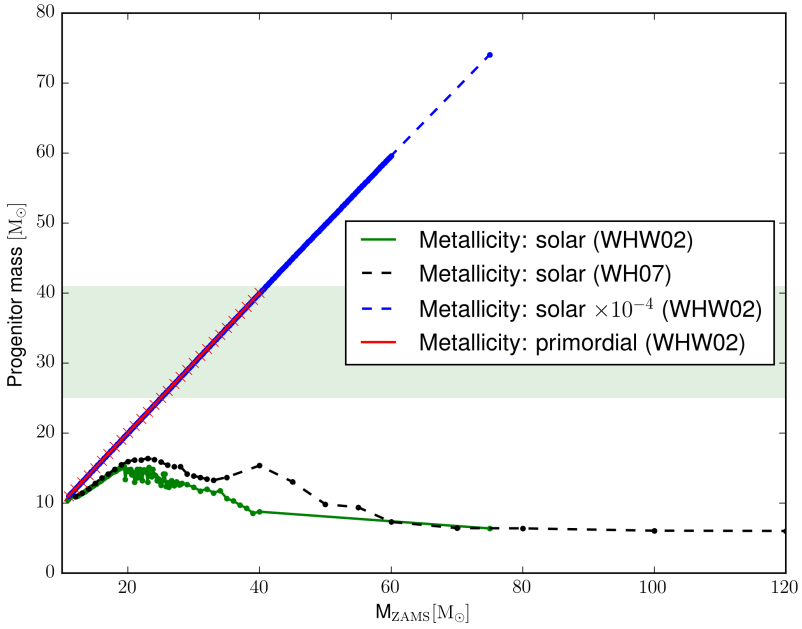

Fig. 5.2.: Progenitor masses as a function of ZAMS mass of the sets from [40, 41]. The green band indicates the mass range of the recently observed merging BHs, Abbott et al. (2016) [216].

connected region of SNe energies is observed which also includes SN 1987A. This suggests that the ZAMS mass region in between ~15-21 $M_\odot$ represents a region where the standard neutrino-driven mechanism is dominating, i.e., which is the driving component responsible for the observed explosions. Towards lower masses the explosion energies slightly decline. This could mark a transition to weaker, "Crab like" SNe. The branching into two observational seemingly distinct branches of possible explosion energy and nickel production takes place for stars in the ZAMS mass region above ~21 $M_\odot$, see also figure 5.3 [46].

One of the branches is given by the observations of very energetic γ-ray burst (GRB) SNe and Hypernovae (HNe) [46, 145, 217]. For these scenarios rapid stellar rotation and strong magnetic fields are thought to be crucial, thus, the PUSH method is not designed to reproduce these observational values. The term HNe originated from the exceptional brightness caused by a large nickel production in hyperenergetic explosions with energies of the order of $\gtrsim 10^{52}$erg [218–220]. A possible central engine of HNe and GRB SNe are rapidly rotating BHs (collapsars), where matter around the central object sets free energy in neutrinos, electromagnetic Poynting flux, and mass outflow. An alternative to this scenario is a rapidly spinning neutron star with a strong magnetic field of the order of $\gtrsim 10^{15}$ G that is formed during stellar collapse, where the HN or GRB is powered by rotational energy, which is converted into explosion energy by the magnetic field. As

briefly mentioned in section 2, in these events the magnetic field strength is increased due to flux freezing in the collapse phase, curling up of field lines due to rotation, and potentially amplified by MRI and can lead to the formation of jets and eventually a HN explosion with an energy of the order of $\sim 10^{52}$erg. Another aspect which separates the neutrino-driven SNe parametrized with PUSH from the HN branch is the limited explosion energy and production of Ni which results from the PUSH method even in the most energetic explosions. Thus we conclude that the HN branch likely is caused by a different mechanism than the neutrino-driven SNe, presumably the magnetorotational one. Of course one could imagine transitions and couplings between the two mechanisms for models with certain degrees of rotation.

The second branch represents faint SNe, thus, CCSNe with low explosion energies that are arguably not supported by a strong magnetorotational central engine. These SNe mark a transition to failed SNe. This indicates a mechanism that can no longer efficiently power explosions for progenitor models with ZAMS masses above ~21-25 $M_\odot$ and therefore directly leads to BH formation without an explosion or an explosion that fails because most of the eventually ejected material falls into the BH. This branch of presumably neutrino-driven CCSNe can be reproduced with PUSH for a fit of the method to observational values. The change of typical explosion energies could indicate that a transition from efficiently neutrino-driven SNe to inefficiently neutrino-driven SNe takes place. We argue that a possible explanation for this faint branch of CCSNe for more massive progenitors with higher compactness values marks a transition from efficiently convective neutrino-driven CCSNe of lighter non-rotating stars to less efficiently neutrino-driven CCSNe of heavier more compact non-rotating stars. Thus, we conclude that the observation of the faint and the Hypernova branch together with the constraint that Hypernovae are likely to be caused by a different somewhat rarer mechanism, suggests that the neutrino-driven mechanism "powers" the Faint Supernova branch. Note that the number of observed Faint and Hypernovae is biased towards Hypernovae since Faint SNe are weaker and represent the transition to failed SNe that are not well, if at all, observable. However, definitive consensus on the existence of such a faint branch has, as of now, not been reached by observers.

In this chapter we develop PUSH into a method that aims to reproduce observed CCSN properties ranging from the mass region between ~10-21 $M_\odot$ of the region of presumably standard convective neutrino-driven SNe to the faint branch of SNe in the high mass region above ~21-25 $M_\odot$ with a calibration of its parameters in compactness. To do this, we compare and fit the PUSH method to observational data that are available and also compare our spherically symmetric simulations with multi-dimensional simulations. Besides SN 1987A, which we use to gauge PUSH for standard neutrino-driven

SNe, we also use a collection of other observational data of CCSN events presented in table 5.2. The presented data are mainly taken from [46, 137] and references therein.

Event	M_{ZAMS} ($\mathrm{M}_\odot$)	E_{expl} (10^{51} erg)	$m(^{56}\mathrm{Ni})$ ($\mathrm{M}_\odot$) BL ; S ; L ; O/V**		References
SN 1987A	18-21	1.1 ± 0.3	0.071 ± 0.003	L	1, 2
SN 1993J	12-17	1-2	0.06-0.09	L	3, 4, 5, 6, 7
			0.07-0.11*	L	8
SN 2004A	12.0 ± 2.1	0.76-1.3	$0.046^{+0.031}_{-0.017}$	O/V	3, 9, 10, 11, 12
SN 2004dj	12-15	0.7-0.9	0.020 ± 0.002	O/V	3, 9, 10, 13, 14, 15, 16, 17
SN 2004et	12-15	1.1-1.8	0.062 ± 0.02	S	3, 9, 10, 18, 19
	25-29*	2.0-2.6*			20
			0.062 ± 0.02*	BL	18
	8^{+5}_{-1}*				21
SN 2005cs	9^{+3}_{-2}	0.27-0.39	0.009 ± 0.003	BL	3, 9, 10, 22, 23
	17.2-19.2*	0.41±0.03*			24
SN 2009kr	11-20	1.6-3			3, 9, 10, 25
SN 2012aw	14-18	1.0-1.7	0.06 ± 0.01	O/V	3, 9, 10, 18, 26, 27
		1-2*	0.06±0.01*		27
		1.5*	0.05±0.06*		28
SN 2012ec	14-22	0.6-1.9	-		3, 9, 10, 29
SN 1994I	~13-15	~1.0	~0.07	O/V	30, 31
SN 2005bf	$\sim 25-30$	$\sim 1.0-1-5$	~0.32	O/V	30, 32, 33
	8.3*	~2*			34

Tab. 5.2.: Compilation of observational properties of CCSNe. Except for the values for SN 1987A, this table mainly consists of values presented in Bruenn et al. [137] and Nomoto et al. [46], and references therein. * Values in rows following a given SN name represent alternative ZAMS masses, explosion energies and the amounts of ejected nickel. ** The abbreviations given in the column of the listed nickel values denote: values obtained with the BL-method (BL), values obtained with the S-method (S), values obtained with modeling of the lightcurve (L), and values obtained by means of other methods or with a combination of various methods (O/V). The values for the event SN 1994I given here are taken from Nomoto et al. [46, 221]. See also Bruenn et al. [137] for a discussion on the selection procedure. The used references are:(1) Blinnikov et al. [21]; (2) Seitenzahl et al. [22]; (3) Bruenn et al. [137]; (4) Shigeyama et al. [222]; (5) Woosley et al. [223]; (6) Young et al. [224]; (7) Bartunov et al. [225]; (8) Freedman et al. [226]; (9) Poznanski [227];(10) Dessart et al. [228]; (11) Hendry et al. [229]; (12) Maund et al. [230]; (13) Chugai et al. [231]; (14) Zhang et al. [232]; (15) Maíz-Apellániz et al. [233]; (16) Wang et al. [234]; (17) Vinkó et al. [235]; (18) Jerkstrand et al. [236]; (19) Sahu et al. [237]; (20) Utrobin and Chugai [238]; (21) Crockett et al. [239]; (22) Maund et al. [240]; (23) Takáts and Vinkó [241]; (24) Utrobin and Chugai [242]; (25) Fraser et al. [243]; (26) Jerkstrand et al. [244]; (27) Bose et al. [245]; (28) Dall'Ora et al. [246]; (29) Maund et al. [247]; (30) Nomoto et al. [46]; (31) Nomoto et al. [221]; (32) Janka [44]; (33) Tominaga et al. [248];(34) Folatelli et al. [249]. Table taken and adapted from Ebinger et al. [88].

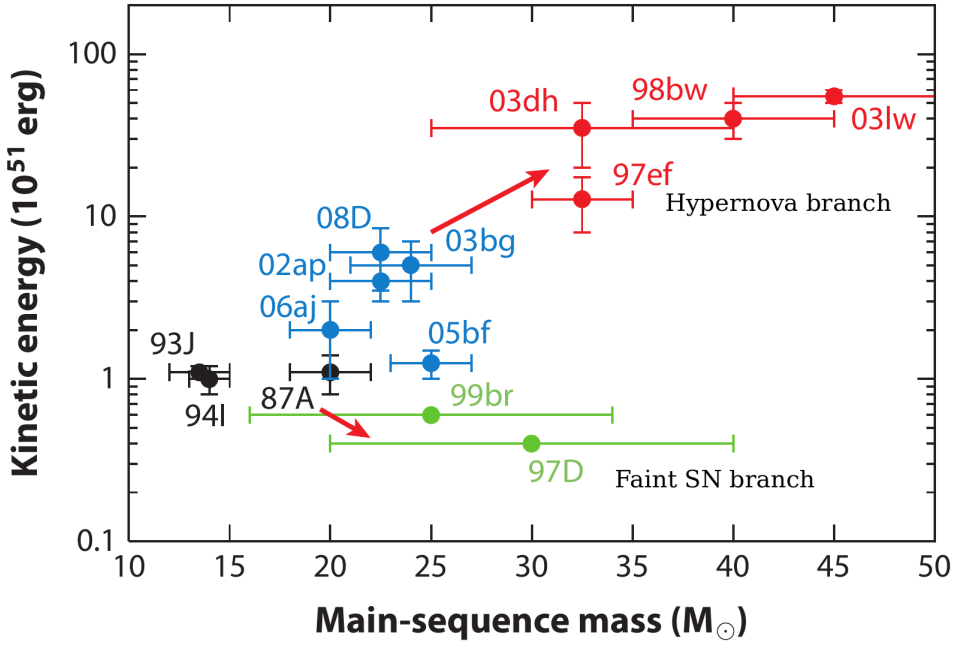

(a) Explosion energy as a function of the ZAMS mass of the progenitors for several SN and HNe reported by different authors.

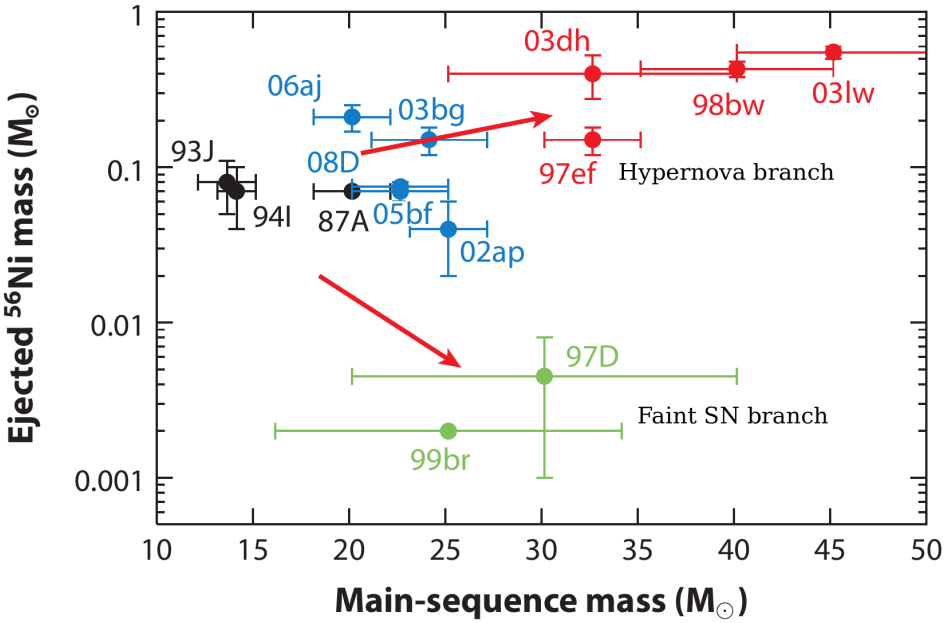

(b) Ejected ^{56}Ni masses as a function of the ZAMS mass of the progenitors for several SN and HNe reported by different authors.

Fig. 5.3.: Explosion energy (a) and ejected ^{56}Ni masses (b) as a function of the ZAMS mass of the progenitors for several SN and HNe reported by different authors, see Nomoto et al. (2013) [46] and references therein. The values for explosions below 25 $M_\odot$ seem to lie in the region of standard SNe, whereas for explosions for stars between 25-40 $M_\odot$ a large variety from faint SNe to HNe (indicated in the figures). These figures are taken and modified from [46]. Note, the shown figures are intended as an illustration of the two possible SN branches. The observational properties we use in our study mainly consists of observational data presented in [46, 137], and references therein, given in table 5.2.

5.2 The Entropy-gradient Criterion and SN 1987A

In this section we will summarize the settings, dependences and degeneracies of parameters of the PUSH setup which we will use for new investigations throughout this chapter. The various constraints that can be applied to a parametrized method and are ultimately necessary to find a good solution are found in the course of many different tests and investigations of different aspects. In the following we want to give an overview of the criteria that eventually are used and the progenitor models that are investigated.

After various explorations it became clear that the PUSH method presented in [87] is not directly applicable to a larger progenitor set (i.e. exceeding the mass range between 18 and 21 $M_\odot$ progenitors with solar metallicity). The main problem being the apparent possibility of a dependence on compactness that should be taken into account. The compactness dependence of the calibration of PUSH will be discussed in the sections 5.3 and 5.4. In this section we focus on changes of the setup of PUSH. In table 5.3 we show the different models that are used in the presented investigations and list the different progenitor sets, their resolutions in ZAMS mass, and assign a progenitor name to them to quickly reference to the different models. Below we give an easy set of rules that generates the names for the models. Note that the naming system developed historically and does not follow a consistent intrinsic logic. We investigate the progenitor sets of solar metallicity by Woosley, Heger and Weaver (2002) [40] and Woosley and Heger (2007) [41].The different sets and model names are indicated by a letter: "s" denotes the progenitors with solar metallicity from [40], and "w" denotes the progenitors with solar metallicity from [41].The indication letter combined with the progenitor ZAMS mass for "s" and "w" together with the two free PUSH fitting parameters k_{PUSH} and t_{rise} defines the name of a specific run. Here, we use model names that include the indication letter and the ZAMS mass to refer to a specific model. As an example, s20.0 corresponds to a model using the 20 $M_\odot$ progenitor from the WHW02 series [40] with solar metallicity.

After some initial analysis of PUSH results and a comparison to multi-dimensional results a change in the PUSH heating criteria was made. The additional energy deposition

Series	Label	Min Mass ($M_\odot$)	Max Mass ($M_\odot$)	Δm ($M_\odot$)	Ref.
WHW02	s	10.8	28.2	0.2	1
		29.0	40.0	1.0	1
		75.0			1
WH07	w	12.0	33.0	1.0	2
		35.0	60.0	5.0	2
		70.0			2
		80.0	120.0	20.0	2

Tab. 5.3.: The table shows the letters used in the PUSH run names and the available progenitor masses for the pre-explosion models with solar metallicity ($Z = Z_\odot$) mainly used in this chapter [40, 41]. The Δm denotes the mass spacings of available CCSN progenitor models for each mass interval (Min Mass to Max Mass). The references for the models are (1) Woosley et al. [40] and (2) Woosley and Heger [41]. This table is taken and adapted from Ebinger et al. [88].

of PUSH is given by the local heating term, $Q^+_{\rm PUSH}(t,r)$ (introduced in chapter 3, equations (3.63) and (3.64))[1],

$$Q^+_{\rm PUSH}(t,r) = 4\mathscr{G}(t)\int_0^\infty q^+_{\rm PUSH}(r,E)\,dE,$$

with

$$q^+_{\rm PUSH}(r,E) \equiv \sigma_0\,\frac{1}{4\,m_b}\left(\frac{E}{m_e c^2}\right)^2\frac{1}{4\pi r^2}\left(\frac{dL_{\nu_x}}{dE}\right)\mathscr{F}(r,E),$$

where $(dL_{\nu_x}/dE)/(4\pi r^2)$ is the spectral energy flux for any single ν_x neutrino species with energy E. From here on, we use the spatial term

$$\mathscr{F}(r,E) = \begin{cases} 0 & \text{if} \quad r > R_s \quad \text{or} \quad \dot{e}_{\nu_e,\bar{\nu}_e} < 0 \\ \exp(-\tau_{\nu_e}(r,E)) & \text{otherwise} \end{cases}, \tag{5.1}$$

contained in equations (3.63) and (3.64). In equation 5.1, τ_{ν_e} denotes the optical depth of the electron neutrinos, s is the matter entropy, $\dot{e}_{\nu_e,\bar{\nu}_e}$ the net specific energy rate due to electron neutrinos and anti-neutrinos, and $R_{\rm s}$ the shock radius. The PUSH method is only active where electron-neutrinos are heating ($\dot{e}_{\nu_e,\bar{\nu}_e} > 0$) behind the shock. The temporal dependence of PUSH, defined by $\mathscr{G}(t)$ in equation (3.63) remains unaltered (see also figure 3.2). The implemented shock finder that is used to find the shock radius has been updated. A gradient based shock search proofed to be problematic for a sub-

[1] with σ_0 being the typical neutrino cross-section $\sigma_0 \approx 1.76\times10^{-44}\mathrm{cm}^2$ and $m_b \approx 1.674\times10^{-24}$g an average baryon mass.

set of runs and captures different gradients if certain conditions are fulfilled. Thus, we enhance the performance of this shock finder by using a similar method as in the implementation of the shock finder used for ELEPHANT in chapter 6, by going from outside to the inside of the domain and locating the shock where a critical entropy value is reached (when the entropy exceeds ~6.5 k_B per baryon). Note that the entropy-gradient criterion, which stated that PUSH could only provide extra heating in regions for which the relation $ds/dr < 0$ held true (criterion for possible convection), is no longer included in the spatial heating term.[1] Even though the entropy-gradient criterion used previously as one of the heating criteria in PUSH is physical, it proved to be too restrictive in spherically symmetric simulations. Unlike spherically symmetric simulations, multi-dimensional simulations exhibit simultaneous outflow and downflow of matter. These regions of different matter flows and entropies can be at similar distances from the PNS making it a difficult task for one-dimensional simulations to match their multi-dimensional counterparts. In our simulations the entropy-gradient criterion tends to flatten the entropy profile, resulting in a self-canceling effect of the parametrized method from the inside to the outside on a relatively short timescale. Ultimately, it only allowed parameter values which lead to relatively early explosion times for simulations reaching explosion energies around $\sim 10^{51}$ erg. Furthermore, in order to reproduce SN 1987A (in the context here with a focus on explosion energy), the entropy-gradient criteria made PUSH parameters necessary which were too robust in producing explosions over the investigated progenitor range and in general confines the allowed parameter space. In figure 5.4 we have a look at the entropy profiles for both settings around their respective time of explosion with PUSH parameters that lead to the same explosion energy and compare them to an entropy profile of a two-dimensional FLASH simulation (see [250] and references therein). See also chapter 6 for further comparisons to multi-dimensional simulations done with the ELEPHANT code [251]). The entropy profiles of the two PUSH runs at their respective explosion times are similar. The main difference is the time of explosion itself and the evolution of the profiles in later stages. The entropy-gradient criterion is good in the sense that it keeps the entropy at lower values that seem closer to the temporal evolution available from multi-dimensional simulations after the explosion sets in. As mentioned above, when combined with the constraint that PUSH needs to allow for explosion properties compatible with SN 1987A, the implementation of the entropy-gradient criterion for convective enhanced heating limits the range of possible choices of t_{rise} to relatively small values which leads to rather quickly exploding models and rapid evolutions of the entropy profile if one wants to match observed explosion energies. In chapter 6 we will also show that if we compare the shock radii of the two PUSH implementations to an ELEPHANT model which is performed for the same progenitor model, the larger t_{rise} lead to a better agreement with the shock radii. Thus, the switch to the new implementa-

[1] See section A.2 in the appendix for a short derivation.

tion of $\mathscr{F}(r, E)$ allows for more flexibility in the fitting of the PUSH parameters which also includes runs that match explosion energies of one Bethe with explosion times that are later and therefore in better agreement with the presented multi-dimensional results.

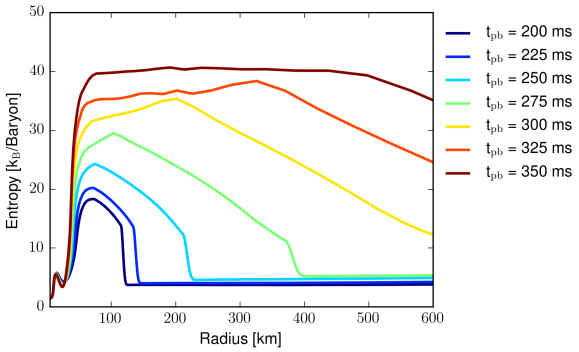

(a) The entropy per baryon as a function of radius is shown for a PUSH setup corresponding to the best fit presented in [87] ($k_{\mathrm{PUSH}} = 3.5$, $t_{\mathrm{rise}} = 200$ms and with the entropy-gradient criterion).

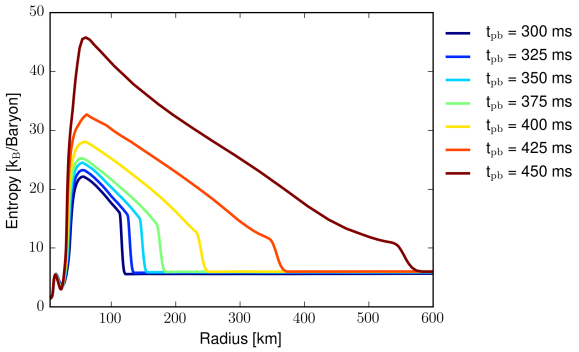

(b) The entropy per baryon as a function of radius is shown for a PUSH setup with no entropy-gradient criterion and the free parameters set to $k_{\mathrm{PUSH}} = 4.0$ and $t_{\mathrm{rise}} = 500$ms.

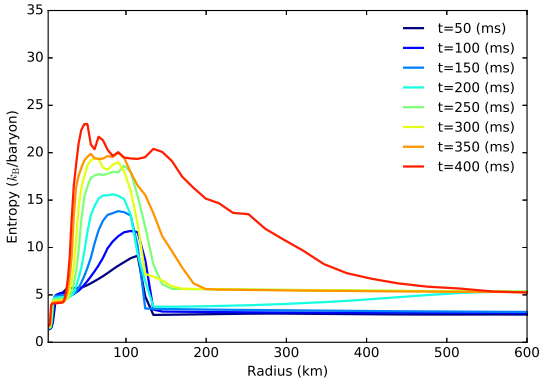

(c) The spherically averaged entropy per baryon as a function of radius is shown for a 2D FLASH setup which uses the same electron (anti)neutrino transport [93] (figure courtesy of K.-C. Pan).

Fig. 5.4.: All three simulations done for the 20 $M_\odot$ progenitor (w20.0). Such comparisons can be used as a further fit requirement (in addition to explosion energy and nucleosynthesis yields) for the free parameters of the PUSH method. The PUSH runs have almost the same explosion energy but different explosion times: (a) E_{expl}= 1.12 B, t_{expl}= 285 ms, (b) E_{expl}= 1.14 B, t_{expl}=443 ms.

To illustrate the effect of the inclusion or exclusion of the entropy-gradient criterion we show the outcome of different parameter sets (variations of the two free parameters t_{rise} and k_{PUSH}) with respect to resulting explosion energy, remnant mass and explosion time for one progenitor model. In figure 5.5 we show the resulting explosion energies for the s18.8 progenitor (a star with solar metallicity and a ZAMS mass of $18.8\,\mathrm{M}_{\odot}$). The area of degeneracy in which the PUSH parameters result in similar explosion energies represents a degree of freedom with respect to the parameter choice for this quantity.

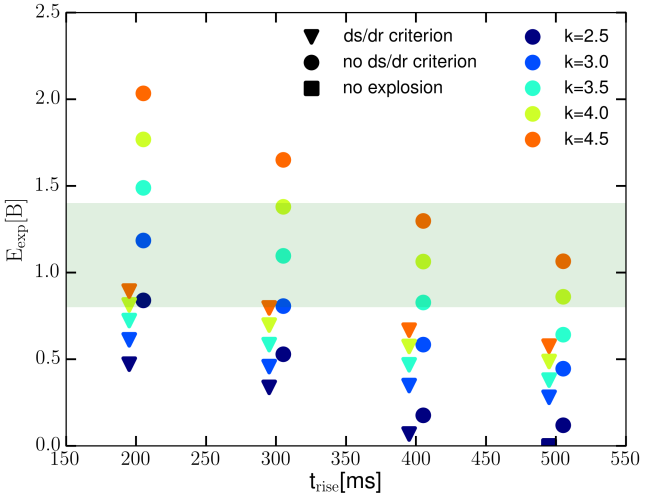

Fig. 5.5.: The explosion energies for the *s*18.8 progenitor are shown as a function of t_{rise} for different values of k_{PUSH}. The green band indicates the observational values of the energy of SN 1987A [21]. The figure illustrates the degeneracy of different parameter sets with respect to energy which represents a degree of freedom in the fitting procedure of PUSH. The markers are slightly offset (circles to the right and triangles to the left with respect to t_{rise}) to enhance the readability of the plot. Circles denote models that do not use the entropy-gradient criterion and triangles denote models that use it. This figure is taken from Ebinger et al. [88].

In figure 5.6 the dependence of the remnant mass and the explosion time on the variation of one of the free PUSH parameters is shown. We can tune the PUSH parameters in order to reproduce the expected order of magnitude of the explosion energy of a CCSN, e.g., SN 1987A ($\sim 10^{-51}$erg), and have the freedom to choose/set different possible explosion times and/or remnant masses.

In the new PUSH setup the presented freedom in the choice of parameters can be used for one further change of approach in comparison to the PUSH method presented in [87]. From the comparison of the explosion energies, remnant masses and explosion times for the *s*18.8 model with and without the entropy-gradient criterion we see that for simulations that reproduce the explosion energy constraints of SN 1987A the mass cut lies much deeper if they were done with the entropy-gradient criterion due to the relatively

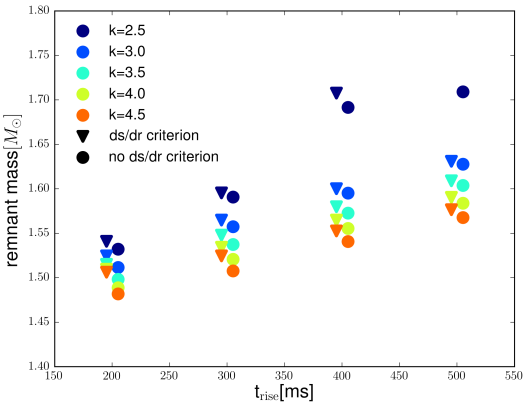

(a) Remnant mass as a function of the PUSH parameter $t_{\rm rise}$ for different $k_{\rm PUSH}$ values.

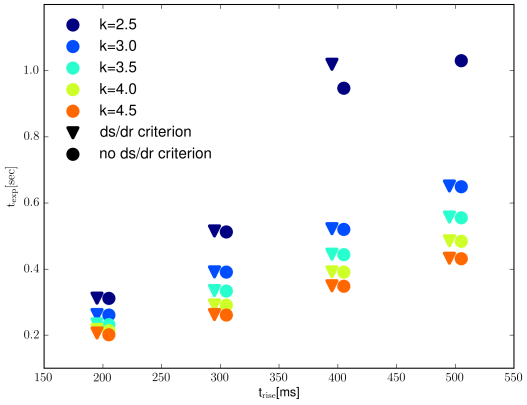

(b) Explosion time as a function of the PUSH parameter $t_{\rm rise}$ for different $k_{\rm PUSH}$ values.

Fig. 5.6.: The remnant mass and the explosion time of the $s18.8$ model are shown as function of $t_{\rm rise}$ for different values of $k_{\rm PUSH}$. Circles denote models with the entropy-gradient criterion and triangles denote models without the entropy criterion. Note that only exploding models are included in the plots.

early explosion times that are caused by the need for small $t_{\rm rise}$ values in order to reach explosion energies of the order of ~1 Bethe, limiting the possible mass accretion onto the PNS. We find that the larger $t_{\rm rise}$ values that are a possible choice for the runs without the entropy-gradient criterion also result in models with a sufficiently high explosion energy but a mass cut that is located further out due to a later explosion time. The explosion time affects the position of the mass cut and hence also the amount of ejected mass. Also determined by the location of the mass cut is the total amount of ejected nickel, and how much material with an electron fraction below 0.5 is ejected ($Y_{\rm e} < 0.5$) and can contribute to the nucleosynthesis yields, which has an influence on isotope ratios of, e.g., nickel, and therefore affects the relative amounts of ^{57}Ni and ^{58}Ni. Furthermore, the position of the mass cut is also important regarding the question if imposing an amount of

fallback might or might not be necessary to reproduce observational properties of CC-SNe, especially of SN 1987A. Where the former setup with the entropy-gradient criterion limited the choice of a fit for SN 1987A to relatively low t_{rise} values (~200 ms) if one wants to be in a reasonable explosion energy range, the new setup leaves the choice open and presents a situation where one can choose between early explosion times with the necessity to impose fallback or later explosion times without the need for additional fallback. We found that for the new setup we no longer need fallback to get reasonable and consistent results for the nucleosynthesis yields for all the observable values of yields of nuclei which we take into account in a calibration to SN 1987A (^{56}Ni, ^{57}Ni, ^{58}Ni, ^{44}Ti). Generally, fallback consists of an early component, which can only be determined in multi-dimensional simulations, and a late component, which requires simulation times far longer that what is feasible with the PUSH setup. The late fallback component, caused by shock reflections at density jumps of outer shell boundaries is not included in this study, as its effect is considered to be small (see, e.g., Sukhbold et al. [214])[1]. For the outcome of the simulations (successful explosion where a NS is formed or failed explosion where a BH is formed) fallback plays a minor role, since different mass cuts with and without the entropy-gradient criterion result in a similar ejecta mass after fallback is imposed to fit nucleosynthesis yields. However, it is not obvious how much fallback should be imposed for progenitor models that are outside of the mass range of possible SN 1987A progenitors. The new setup of PUSH (no entropy-gradient criterion) enables explosions that have explosion energies and nucleosynthesis yields that are consistent with SN 1987A without the necessity to impose fallback and allow for temporal evolutions of the shock radius, neutrino heating rates, and entropy profiles that are not limited to early explosions and show better agreement with multidimensional simulations by [137, 250] (see also chapter 6). From now on we use the new PUSH setup without entropy-gradient criterion. The first thing we do with the new PUSH setup is to perform the calibration of the method by reproducing observational properties of SN 1987A for a suitable progenitor model. In chapter 4 (which represents the paper PUSH I; Perego, Hempel, Fröhlich, Ebinger et al. [87]), we calibrated the PUSH method using models from the WHW02 with solar metallicity in the ZAMS mass range between 18 and 21 $M_\odot$ [40]. Two possible calibration candidates for SN 1987A were obtained (s18.0 and s19.4). Both models were able to reproduce the observed Ni yields when we imposed 0.1 $M_\odot$ of fallback by hand. We repeat the calibration procedure as described in chapter 4 using the progenitor models from the WHW02 set with ZAMS masses between 18.0 and 21.0 $M_\odot$ in order to find a suitable candidate able to reproduce the observational properties of SN 1987A. We find that for the parameters $k_{\mathrm{push}} = 4.3$ and $t_{\mathrm{rise}} = 400$ ms (which represent our calibration parameters for SN 1987A, see table 5.4) the s18.8 model is in good agreement with the observed

[1] The investigation of fallback remains an open point which can be investigated. An option would be an analytical approach guided by the works [192, 252] and references therein.

k_{push} [-]	t_{rise} [ms]	t_{on} [ms]	t_{off} [s]
4.3	400	80	1

Tab. 5.4.: Parameter values from the new calibration of the PUSH method to reproduce observed properties of SN 1987A for the model s18.8 (18.8$M_\odot$ ZAMS mass) from WHW02 [40].

Quantity	SN 1987A (observed)	PUSH (s18.8)
E_{expl} (10^{51} erg)	1.1 ± 0.3	1.2
M_{prog} ($M_\odot$)	18-21	18.8
^{56}Ni ($M_\odot$)	(0.071 ± 0.003)	0.069
^{57}Ni ($M_\odot$)	(0.0041 ± 0.0018)	0.0027
^{58}Ni ($M_\odot$)	0.006	0.0066
^{44}Ti ($M_\odot$)	$(1.5 \pm 0.3) \times 10^{-4}$	3.05×10^{-5}

Tab. 5.5.: The observed and calculated calibration properties of SN 1987A are presented. The s18.8 progenitor star (18.8$M_\odot$ ZAMS mass) was identified as the model which reproduces observational properties of SN 1987A for the parameters $k_{\mathrm{push}} = 4.3$ and $t_{\mathrm{rise}} = 400$ ms. The presented nucleosynthesis yields for SN 1987A are taken from [22] except for ^{58}Ni which is taken from [25] and ^{44}Ti which represents the value from [26]. The value for the explosion energy is adapted from [21]. This table is taken and adapted from Ebinger et al. [88].

explosion energy and yields of Ni and Ti with no need for any additional fallback. In table 5.5 the observational properties of SN 1987A and the corresponding values from our calibration model are summarized. With the exception of ^{44}Ti where we now use the newer results from [26] instead of [22], the presented observed properties of SN 1987A are the same as in the first calibration done in chapter 4.

5.3 Black Hole Formation and the Constant Parameter Calibration

In this section we want to get a first idea of what to expect from an application of the PUSH method to the whole progenitor range. We investigate the behavior of one-dimensional simulations of CCSNe with the PUSH setup for a subset across the available progenitor models without the application of the extra heating from PUSH, thus with the setting k_{PUSH} =0 and follow the initial idea to directly apply the PUSH method with constant parameters (in this section we use the constant test parameters $k_{\mathrm{PUSH}} = 4.0$ and $t_{\mathrm{rise}} = 400$ ms) to a broader range of progenitors without any dependence on their properties. The application of a constant parameter set across the ZAMS mass range is done to check if this represents a reasonable choice for usage of the PUSH method, and is similar to the analysis done for a limited ZAMS mass range between 18 and 21 $\mathrm{M}_{\odot}$ in Perego et al. (2015) [87]. These investigations are performed using the progenitor sets *s* and *w* with solar metallicity from WHW02 and WH07 [40, 41].

Self-consistent state of the art spherically symmetric simulations of CCSNe do not lead to explosions via the delayed neutrino-driven mechanism (see e.g. [56]). The reason being the lacking dimensionality that is the basis for many of the proposed explosion mechanisms (e.g. the convective neutrino-driven, the SASI, the acoustic, and the magneto-rotational mechanism, see also section 2.4), with the exception of the phase transition mechanism, which leads to successful SN explosions in one-dimensional models [60, 76]. The timescales on which the different models undergo collapse can depend on the structure of the progenitor and on the EOS that is used. The presented investigation of self-consistent one-dimensional models is done in order to disentangle aspects - other than the CCSN explosion mechanism - that have an influence on BH formation. Therefore, here we investigate the effect that different choices of the EOS and of the progenitor model can have in our one-dimensional simulations. We perform simulations for two EOS (SFHO and DD2, [95, 118, 253]). The two considered progenitor samples with solar metallicity provide us with different initial models for progenitors of several ZAMS masses and thus can also give an insight on the effects of uncertainties of progenitor models on the outcome of CCSN simulations. Figure 5.7 shows the temporal evolution of the central densities of two different progenitor models of a 40 $\mathrm{M}_{\odot}$ ZAMS mass star with solar metallicity (WH07 [41] in green and WHW02 [40] in blue) and two equations of state (HS(DD2) solid lines, SFHO dashed lines, [95, 118, 253]). The dependence of the BH formation time (BH formation starts to occur for central densities of $\sim 10^{15}\mathrm{g\,cm^{-3}}$) on the EOS (indicated by the colored areas) and the even stronger dependence on the pro-

genitor model for this progenitor ZAMS mass (difference between green and blue lines) is evident. Thus, both aspects can have an influence on the explodability of numerical models since they set an estimate for the upper limit of the timescale on which a delayed mechanism should revive the stalled shock with the collapse time to a BH. Besides the observation that uncertainties in progenitors can have a large impact (difference of green and blue region in figure 5.7) we see that models with the EOS SFHO collapse faster than the ones using HS(DD2). In figure 5.8 the BH formation times for a subset of different progenitor ZAMS masses are given. The differences of the BH formation times between the progenitors can be related to different accretion rates, which are correlated to compactness ξ_M (the compactness of the progenitors is shown e.g. in figure 5.1).

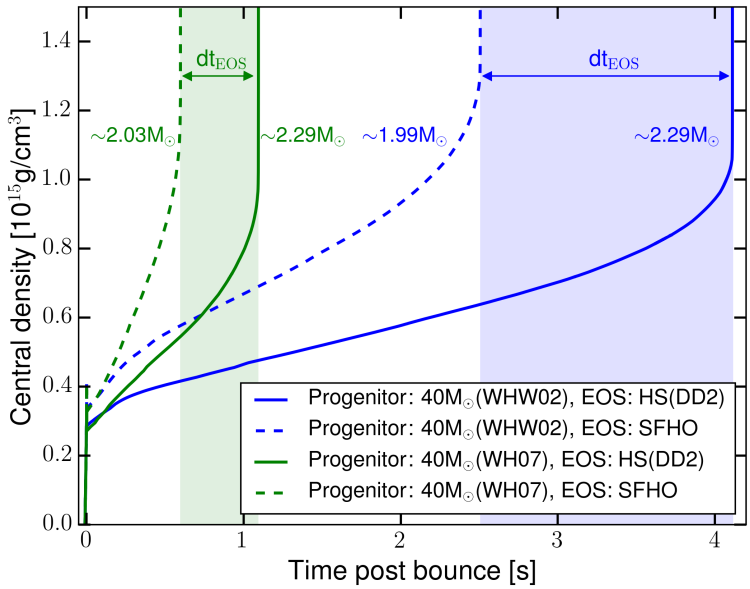

Fig. 5.7.: Temporal evolution of the central density of a 40 $M_\odot$ ZAMS mass star with solar metallicity for two progenitor models (WH07 [41] in green and WHW02 [40] in blue) and two equations of state (HS(DD2) solid lines, SFHO dashed lines, [95], [118]). The gravitational PNS masses at collapse are displayed next to the corresponding central density curves. This figure is taken from Ebinger et al. [88].

From the collapse timescales we obtain for the reduced sets of progenitor models (see figure 5.8) we can draw first conclusions on the explodability of the different progenitors. As expected, the progenitors with higher compactness have a shorter collapse time, namely the progenitor with 25 $M_\odot$ ZAMS mass and the progenitors with a ZAMS mass that is larger than 35 $M_\odot$. Also, the progenitor models of the WH07 set collapse to BHs on a shorter timescale overall. The relation between the collapse timescale and compactness, is also discussed in other works (see, e.g., [211]). The observed BH formation timescales of the self-consistent one-dimensional CCSN simulations in the PUSH setup interpreted as an upper boundary for the delayed neutrino-driven mechanism gives a first estimate

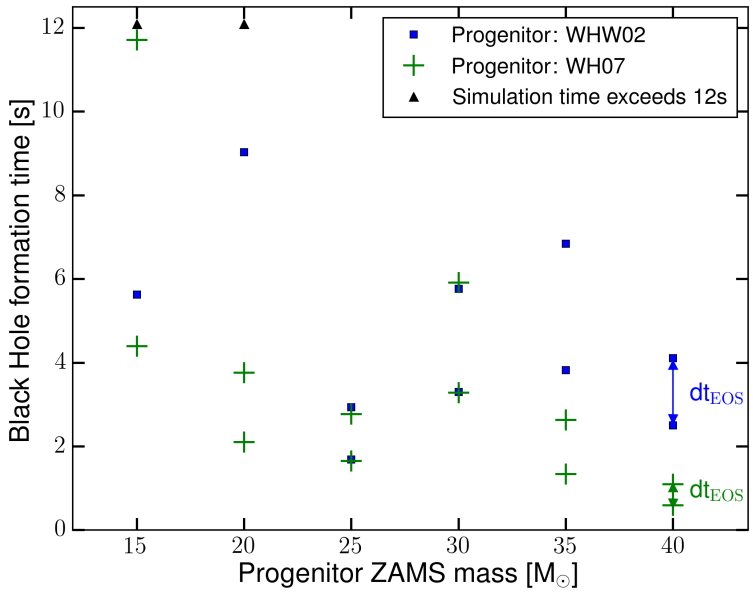

Fig. 5.8.: Black hole formation times for a sample of progenitor star ZAMS masses from two progenitor samples with solar metallicity (WH07 [41] in green and WHW02 [40] in blue) and two equations of state are shown (see also figure 5.7). Note that the shorter BH formation time for each progenitor corresponds to a model that is using the SFHO EOS. This figure is taken from Ebinger et al. [88].

of the range of progenitors that will not explode and eventually form BHs. In the simulations presented here, the candidates for BH formation are models with relatively high compactness $\xi_{2.0}$>0.5. From this, we expect that (at least some) progenitor models with a compactness value $\xi_{2.0}$>0.5 do not explode and end up as black holes. This will later be summarized as a constraint on the PUSH method when it is applied to a full sample of progenitor models.

In figure 5.9 we show the resulting explosion energies together with the compactness value $\xi_{2.0}$ of the constant application of PUSH parameters for the progenitors of the *s* and *w* sets. We quickly see that this does not lead to the expected outcome. Furthermore, we come to the conclusion that these results can not explain observations and are partially even opposite to the expected behavior with respect to explosion energy of neutrino-driven CCSNe (see also section 5.1 and , e.g., compare the figures 5.3 and 5.9). The induced explosion energy of PUSH shows a trend with compactness that needs to be taken into account in future calibrations. The presented constant calibration of PUSH reproduces observational values for stars with a ZAMS mass between 10 and 20$M_\odot$. Note that for lighter stars it results in explosion energies that are maybe slightly too high. For higher ZAMS masses, especially in the high compactness regions between 20 and 25$M_\odot$ and above 35$M_\odot$ the resulting explosion energies do not agree with the expected and ob-

served trends of the faint branch and are too low to fall into the HNe branch[1]. The fact that for a constant PUSH parameter set not a single BH was formed over the whole progenitor range is opposite to our expectations and the general trend in the literature (see e.g. [141, 170, 211]). We conclude that a different approach is needed.

In addition, figures 5.10 and 5.11 show the compactness together with the explosion energy (color coded) as a function of ZAMS mass and the explosion energy together with the CO-core mass (color coded) as a function of compactness. The constant PUSH calibration runs provide a good opportunity for a search of different dependencies. One interesting aspect that is noticeable is the degeneracy with respect to compactness of several models with different explosion energies. We identified the compactness as an important variable to determine the explosion properties. By looking at the differences between these degenerate models (besides explosion energy) we can identify further quantities that can have an effect on the explosion energy of the models. The different explosion energies observed for the models that are degenerate in compactness have different CO-core masses. A first observation is that a higher CO-core masses correlates with a lower explosion energy for models with similar compactness. This can be well seen in the figures 5.10 and 5.11, where a region of degeneracy in compactness is indicated by the green band to guide the eye. All models with the same compactness that lie on opposite sides of the high compactness peak around 24 $M_\odot$ show a similar difference in explosion energy even though the models have the same compactness. This gap in explosion energy between the two groups of CO-masses is also present in the standard calibration of the PUSH method.

[1] The explosion mechanism in the HNe branch is rare and likely not neutrino-driven.

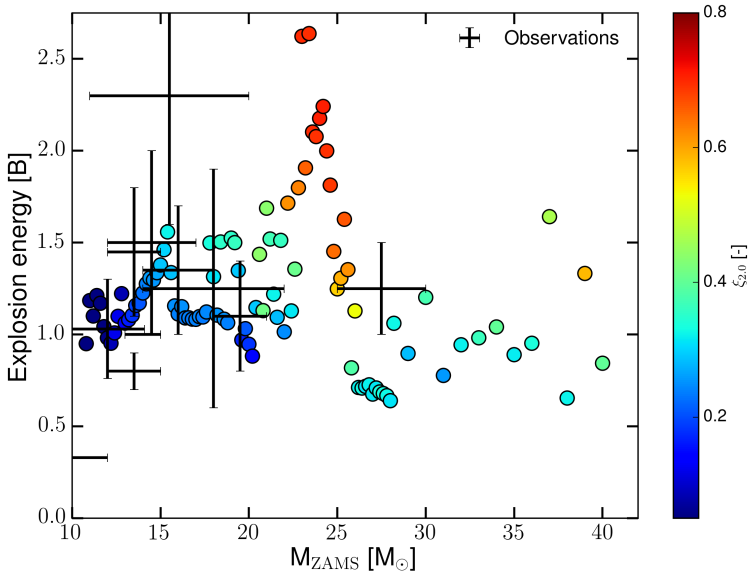

(a) Explosion energy for the progenitor set with solar metallicity from WHW02 [40] in the mass range between 10.8 $M_\odot$ and 40 $M_\odot$ for the application of constant PUSH parameters k_{push} and t_{rise}. The color bar describes the compactness corresponding to the progenitor.

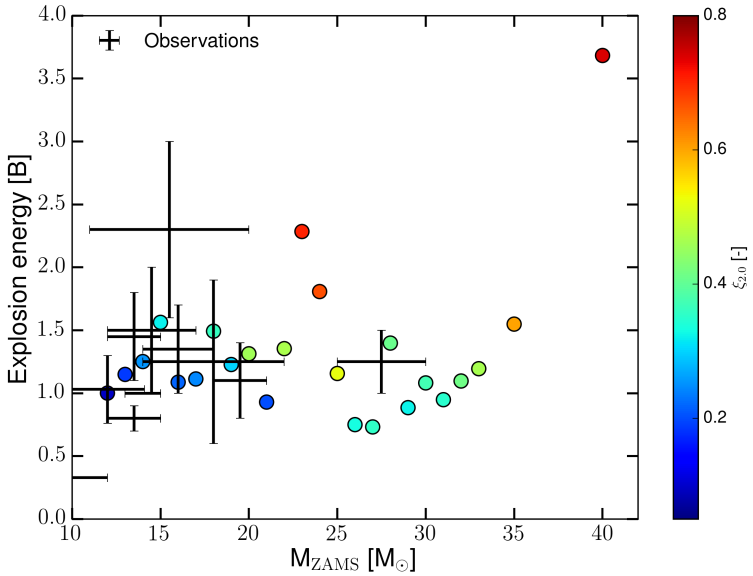

(b) Explosion energy for the progenitor set with solar metallicity from WH07 [41] in the mass range between 12 $M_\odot$ and 40 $M_\odot$ for the application of constant PUSH parameters k_{push} and t_{rise}. The color bar describes the compactness corresponding to the progenitor.

Fig. 5.9.: The presented values of the explosion energies in figures (a) and (b) show that the faint branch can not be reproduced with a constant application of PUSH parameters $k_{push} = 4.0$ and $t_{rise} = 400$ ms. The black error bars indicate observational values given in table 5.2.

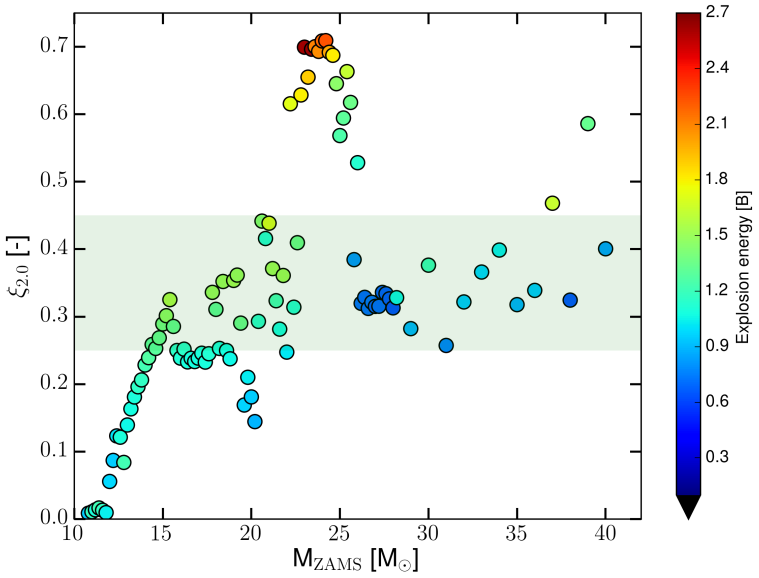

Fig. 5.10.: Compactness and explosion energy of the progenitor set *s* from WHW02 as a function of ZAMS mass for simulations with constant PUSH parameters k_{push} and t_{rise}. The green band indicates models with similar compactness values but different explosion energies.

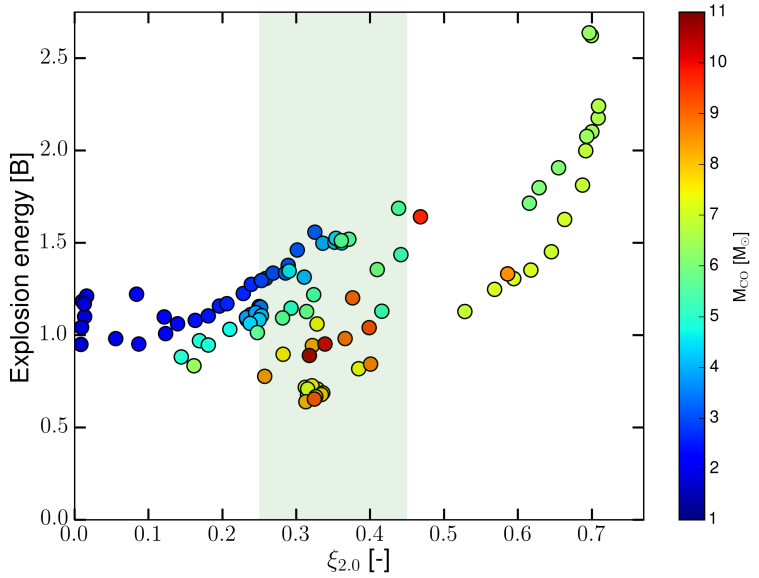

Fig. 5.11.: Explosion energy and CO-core masses of the progenitor set *s* from WHW02 as a function of compactness for simulations with constant PUSH parameters k_{push} and t_{rise}. The green band indicates models with degenerate compactness but different explosion energies.

5.4 The Calibration of the PUSH Method Across the Mass Range

The PUSH method is a parametrization of the neutrino-driven mechanism. The purpose of the method is to enable the investigation of CCSNe and their outcome in spherically symmetric simulations. In the last chapter we have seen that the application of a constant PUSH parameter to progenitors across the ZAMS mass range is not suited for an investigation of properties of neutrino-driven CCSNe. In this section we introduce requirements based on general features of CCSN observations that the PUSH method should fulfill when it is applied for large progenitor samples with a wide distribution in ZAMS masses. These requirements are formulated in the form of constraints on the parametrized framework of PUSH. By introducing a dependence in compactness we successfully calibrate the method and apply it to the solar metallicity progenitor models of WHW02 and WH07 in order to investigate the explodability, the progenitor-remnant connection and the nucleosynthesis yields of neutrino-driven CCSNe. For the calibration we use the compactness values at bounce that is shown together with the initial compactness of the used progenitor models in figure 5.12.

Let us introduce the constraints on the PUSH method that represent the main guidance in the calibration process. In addition to a possible fit to SN 1987A we also require that our calibration allows the possibility of formation of black holes and not only leads to robust explosions, as it is the case for a constant PUSH parameter set (see previous section). Furthermore, the PUSH calibration should also reproduce the lower explosion energies of observed CCSNe of less massive progenitors. Thus, in summary, applied across the ZAMS mass range of the investigated progenitor star models of CCSNe the PUSH method should:

(i) be able to reproduce the observational properties of SN 1987A for a suitable progenitor model,

(ii) allow for the possibility of black hole formation, and

(iii) result in lower explosion energies for stars with ZAMS masses of $\lesssim 13$ $M_\odot$ ("Crab-like SNe").

Our aim is to find a calibration for the whole progenitor range. A connection between the compactness and the resulting progenitor-explosion and progenitor-remnant con-

nection has been pointed out first by O'Connor and Ott (2011) and was later investigated and supported by Ugliano et al. (2012) and others [141, 170, 211, 212]. In the following, we introduce a dependence of the extra heating of PUSH on compactness in order to obtain a calibration that is suited to study explosion and remnant properties. It is obvious, that we can reproduce the observed properties of SN 1987A by requiring that the PUSH parameters are set to the calibrated values for the suited progenitor model. Our best fit model of SN 1987A is the model s18.8 (see previous section). When we consider the collapse timescales we obtained from our investigation of self-consistent one-dimensional SN simulations, we see that more compact progenitors have a shorter BH formation time. Interpreting the BH formation time of these simulations as an estimate of the upper limit of the time on which the neutrino-driven mechanism can revive the stalled shock and successfully launch an explosion, we relate higher compactness values with a trend towards weaker and failing explosions. Thus, by decreasing the parametrized extra heating above a critical compactness we allow for the possibility of BH formation and fulfill one of our constraints. In the previous section (see figure 5.2) we have seen that for a constant application of the PUSH parameters to all progenitor models we obtain explosion energies that are slightly too high for less massive stars. In figure 5.12 we see that progenitor models with lower ZAMS mass coincide with a lower compactness. Due to this correlation we can reduce the extra heating below a threshold compactness in order to fulfill the last requirement. Many tests and calibrations have been performed and large amount of data have been generated[1] in the course of the search for a possible calibration of the PUSH method. I will not list all attempts here in detail but rather give an overview and collect the main constraints that a calibration for the whole compactness range must fulfill in order to be in agreement with observations and some insights from multi-dimensional simulations. This as a result allows us to draw conclusions on the possible outcome of neutrino-driven CCSNe. If a certain aspect of the fitting process can be illuminated by certain tests they will be presented. In the calibration process we also made use of progenitors that now are obsolete. To still show the process of finding a calibration, we show the intermediate calibration steps and whenever a now obsolete old star model is used we will mention it. The final calibrations of PUSH that is using the calibration against SN 1987A for the s18.8 model with the best fit parameters given in table 5.4 can be found at the end of this section. We restrict the number of free parameters that can be tuned with compactness to one of the two free PUSH parameters: k_{PUSH}. Thus, the calibration of the PUSH method is represented by the function $k_{\mathrm{PUSH}}(\xi)$. The sheer amount of runs necessary to disentangle effects of the changes of two parameters with compactness did not seem promising with respect to the expected gain in physical insight from the parametrized method and goes beyond the scope of this work.This

[1] Even though a single run of a PUSH model in total only needs about 1GB of disk storage, the investigation of large parameter and progenitor sets quickly can lead to large amounts of data.

chapter represents the fitting of PUSH to observational values where mainly the explosion energies have been used since this quantity is readily available with the usage of the tracer tool and allows for a comparison to a larger data set. In addition, also post processing computations of nucleosynthesis yields have been made to verify that the resulting yields are in a reasonable range (for the best fit of SN 1987A this constraint was of course used an the same footing as the explosion energy). In chapter 6 we also compare the results of the PUSH method to multi-dimensional simulations performed with the ELEPHANT code.

Now we show how the requirements that the PUSH method should fulfill translate into constraints on the calibration of k_{PUSH} with compactness. Note, that we use the compactness at bounce since it marks the exact same point during the evolution, or rather the death, of the different stars and removes possible biases of the final states of the progenitor models. In figure 5.12 we show the compactness values at the onset of collapse and at bounce for the progenitor sets with solar metallicity from Woosley, Heger and Weaver (2002) and Woosley and Heger (2007) [40, 41]. With the usage of a constant parameter calibration ruled out, the investigated calibrations for k_{PUSH} consist of various kinds of linear decreasing calibrations and linear calibrations with plateau values towards smaller compactness values to stay in a reasonable explosion energy range for less compact stars.

Any calibration of PUSH has to include a best fit for SN 1987A, i.e., a model that reproduces the observed properties with a parameter k_{PUSH}, resulting in a calibration point at the compactness value of the best fit model. The constraints concerning the weaker explosion energy in the low compactness region and the BH formation for more compact stars result in fitting points similar to the fitting point given by the best fit of SN 1987A. The compactness values of progenitors for ZAMS masses below 21 $\mathrm{M}_{\odot}$, which represents also the upper limit of the mass range of the possible SN 1987A progenitors (that we assume to be the standard of neutrino-driven explosion forming models) are below a compactness of $\xi_{2.0} = 0.4 - 0.5$. In a first attempt to emulate a transition from the standard convective neutrino-driven mechanism to a regime of less efficiently convective neutrino-driven mechanism and eventually to BH formation we tuned the k_{PUSH} parameter linearly down above the compactness value of $\xi_{2.0} = 0.4 - 0.5$. This approach results in a satisfactory calibration to the observed explosion energies of CCSNe for the high compactness, BH forming region. From this calibration of PUSH we get the constraint that the parameter k_{PUSH} is set to zero at compactness values of $\xi_{2.0} = 0.7$ and beyond. We call the calibration of k_{PUSH} which consists of a plateau representing the fit parameter value of SN 1987A (see table 5.4) that is tuned down above a compactness $\xi_{2.0} = 0.4 - 0.5$ a *plateau calibration* from now on.

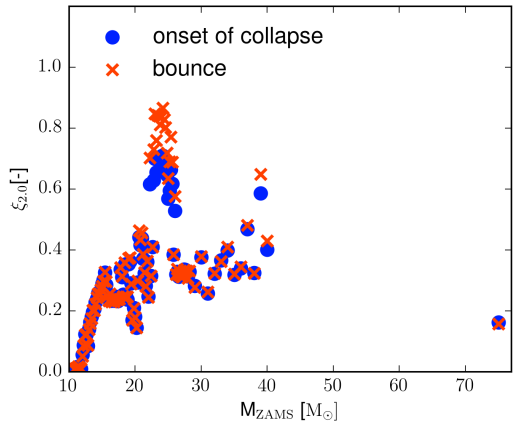

(a) Compactness $\xi_{2.0}$ of progenitors with solar metallicity from WHW02 [40] for all progenitors of the set.

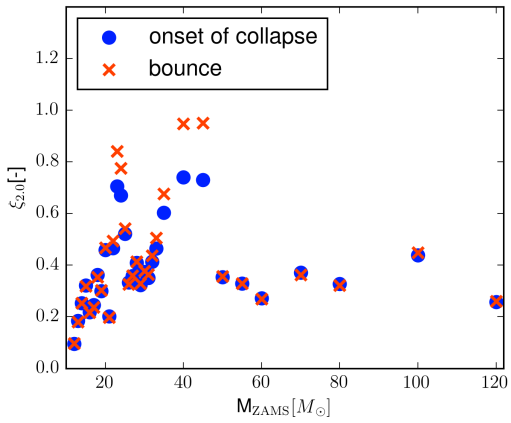

(b) Compactness $\xi_{2.0}$ of progenitors with solar metallicity from from WH07 [41] for all progenitors of the set.

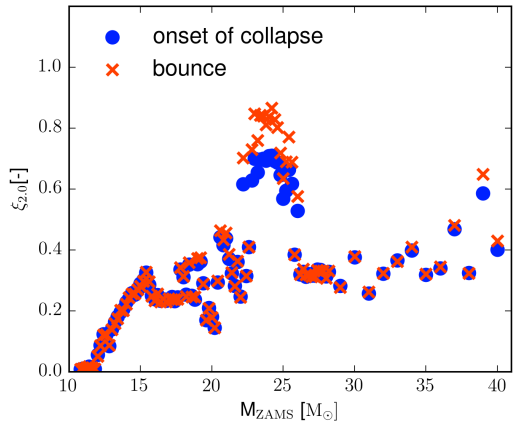

(c) Compactness $\xi_{2.0}$ of progenitors with solar metallicity from WHW02 [40] for a reduced range up to 40$M_\odot$.

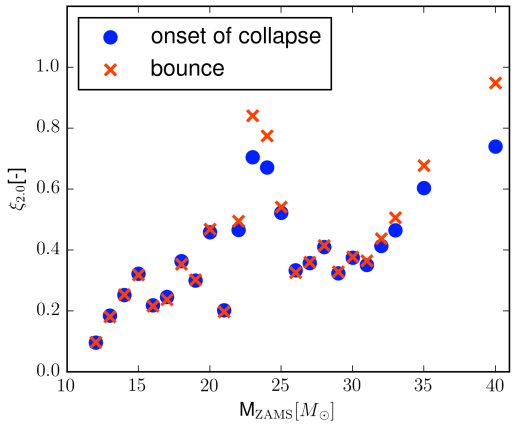

(d) Compactness $\xi_{2.0}$ of progenitors with solar metallicity from WH07 [41] for a reduced range up to 40$M_\odot$.

Fig. 5.12.: The compactness $\xi_{2.0}$ of the used progenitors from WHW02 and WH07 [40, 41] with solar metallicity is shown. In figures (a) and (b) all progenitors of the sets are shown. Figures (c) and (d) show a reduced set. Many of the progenitors do not show big differences between the compactness values at the onset of collapse and at bounce but for the most compact progenitors, there is a clearly visible increase of compactness at bounce.

Observations of the explosion energies of less massive progenitors also indicates reduced values towards lower compactness values. We tuned PUSH down from the k_{PUSH} fit parameter of SN 1987A towards lower compactness values in order to reproduce the lower observed values of explosion energies for the relatively low-mass CCSN progenitor models. Different initial values of the k_{PUSH} parameter towards zero compactness were tested

and eventually k_{PUSH} = 2.5 was chosen as the fitting point out of the simulation series sample. This additional decrease towards lower compactness values from the initially constant parameter value of k_{PUSH} leads to the calibration of the PUSH method that we will call *trapezoidal calibration* from now on. We summarize the two calibration points for lower and higher compactness values that result from the briefly described fitting processes in table 5.6.

$k_{\mathrm{PUSH}}(\xi_{2.0} = 0.0))$ [-]	$k_{\mathrm{PUSH}}(\xi_{2.0,BF}))$ [-]	$k_{\mathrm{PUSH}}(\xi_{2.0} = 0.7))$ [-]
2.5	4.3	0.0

Tab. 5.6.: Fitting points which are used as constraints for the final k_{PUSH} dependence on $\xi_{2.0}$ for low and high compactness values. Additional , we also need the constraint for $\xi_{2.0,BF} = 0.245$, which denotes the compactness of the best fit model for SN 1987A, s18.8 (see also table 5.4).

The calibration points from table 5.6 together with the fit parameters of SN 1987A result in three constraints on k_{PUSH}. Ultimately, assuming a polynomial dependence of k_{PUSH} on compactness and, given the three calibration points, we consider a paraboloidal dependence:

$$k_{\mathrm{PUSH}}(\xi) = a\xi^2 + b\xi + c. \tag{5.2}$$

As we mentioned above, we also tested other piece-wise linear dependences of k_{PUSH} on the compactness value. The results of these different calibrations are very similar, confirming that our results are not sensitive to the choice of the functional dependence of k_{PUSH}. In figure 5.13 we show the different possible choices for k_{PUSH}. To give an impression of the different possibilities and the resulting outcome of the fitting function for the different calibrations we present a comparison between the paraboloidal (2) and the trapezoidal calibration in figure 5.14. We know from section 5.3 that a constant PUSH calibration leads to too high explosion energies for low and high compactness values and does not form any BHs. Too high explosion energies for low compactness values rule out the the plateau calibration of PUSH. The paraboloidal and the trapezoidal calibration show very similar behavior and good agreement with observations. The paraboloidal calibration seems to be the most natural way to construct a parameter dependence on compactness from the three fitting points and has a smoother behavior than the other calibration possibilities. Thus, we choose a parabola as the function that describes the $k_{\mathrm{PUSH}}(\xi_{2.0})$ function which from here on represents our standard calibration. In figure 5.15 we show the compactness dependence of the k_{PUSH} parameter together with the three constraints of the standard calibration (in this calibration the model that reproduces SN 1987A is s18.8). Let us summarize the calibration values of the parabolic dependence of k_{PUSH}, that represents our standard calibration of the PUSH method which has

the form $k_{\mathrm{PUSH}}(\xi) = a\xi^2 + b\xi + c$. The calibration parameters which define the standard calibration of the PUSH method used from here on between the compactness values 0.0 and 0.7 with the best fit model of PUSH that reproduces SN 1987A s18.8 with k_{PUSH}=4.3 are

$$\begin{aligned} a &= -23.99 \\ b &= 13.22 \\ c &= 2.5. \end{aligned} \tag{5.3}$$

Note that the parameter t_{rise} is fixed to 400 ms.

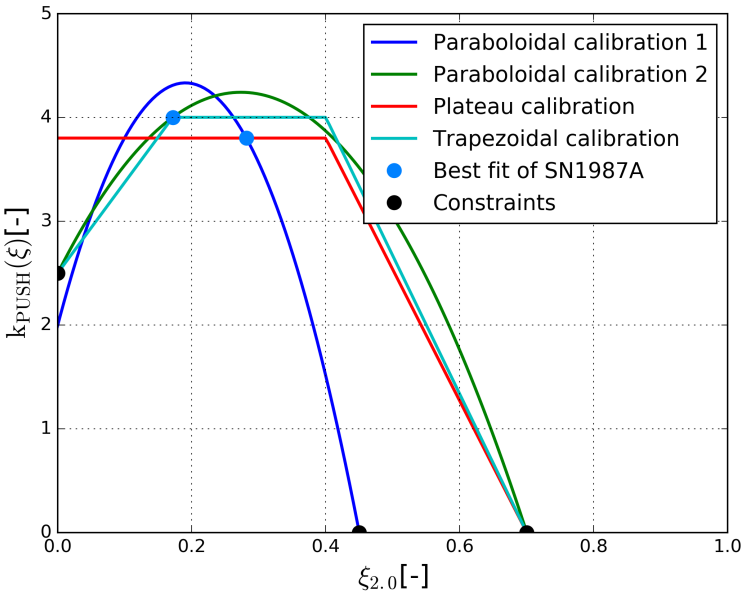

Fig. 5.13.: The different possible calibrations for the compactness dependence of the k_{PUSH} parameter are given. The blue dots denote the calibration points for two test fits to SN 1987A (for now obsolete progenitor models) and the black dots summarize the constraints for low and high compactness values that have been tested. This figure is intended to illustrate the different calibrations and how different versions overlap for certain compactness values. The paraboloidal (2) and the trapezoidal calibrations are compared to show the relative independence of the PUSH method on the specific choice of k_{PUSH} in figure 5.14.

Now, we apply the standard calibration to both series of progenitor models with solar metallicity. In figure 5.16, we show the resulting explosion energies and the amount of ejected ^{56}Ni as a function of ZAMS mass for the standard calibration. We also have a look at the amount of ejected ^{56}Ni against the explosion energies of all the progenitors in the *s* and *w* sets in figure 5.17. For both progenitor samples we see a rise from relatively low explosion energies for lighter stars that form "Crab like" SNe to robust explosions with energies between 0.8 and 1.6 Bethe between 15 and 21$M_\odot$ which is believed to be the

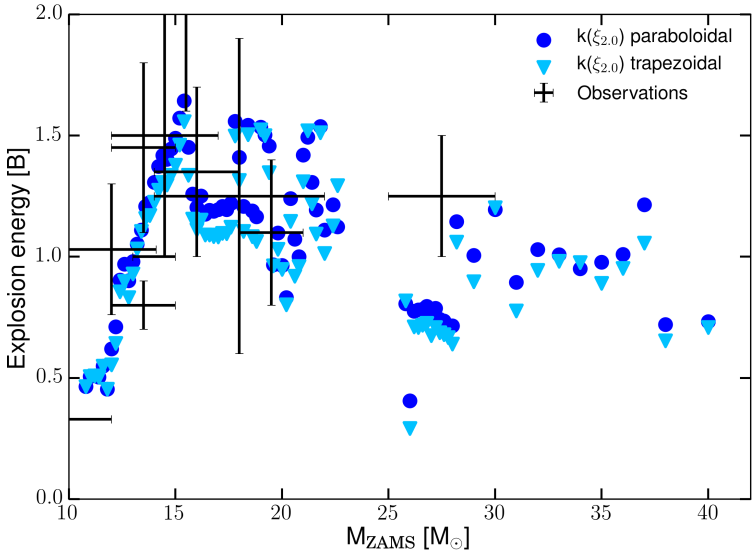

(a) Explosion energies of progenitors from [40] up to 40$M_\odot$ ZAMS mass.

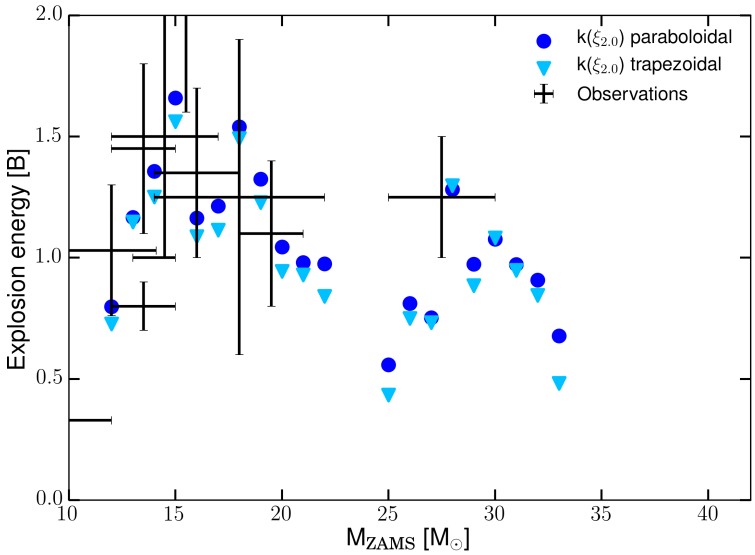

(b) Explosion energies of progenitors from [41] up to 40$M_\odot$ ZAMS mass.

Fig. 5.14.: The explosion energies for the trapezoidal and the paraboloidal calibration 2 of PUSH for progenitor samples with solar metallicity from [40, 41] are shown in figures (a) and (b). Note that only exploding models are shown.

range of the standard convective neutrino-driven mechanism. A region of BH formation lies in the high compactness ZAMS mass range between 22$M_\odot$ and 26$M_\odot$ (see also figure 5.12). These stars represents stellar models that have an increased carbon-oxygen core mass in comparison to lower ZAMS mass models and also have still major parts of their hydrogen and helium envelopes. This peak in compactness is followed by a patch of exploding models that have lost most of their hydrogen and helium envelopes with

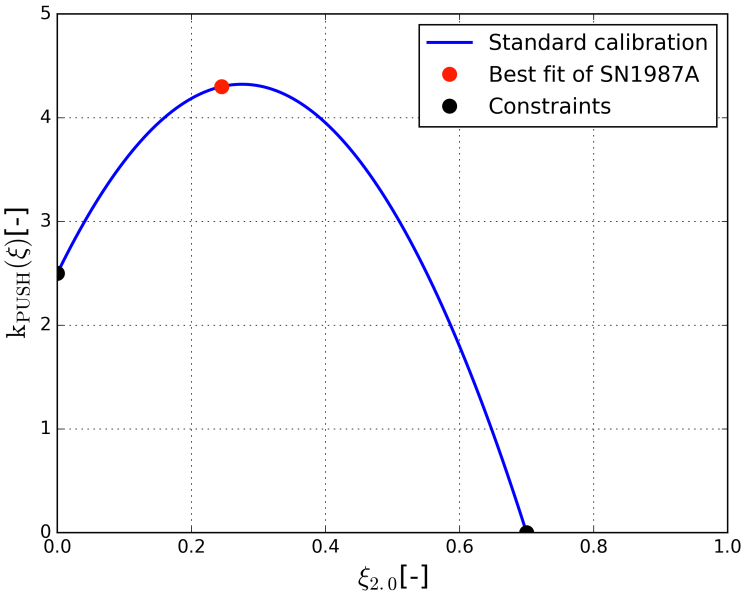

Fig. 5.15.: The compactness dependence of the k_{PUSH} parameter is shown together with the three constraints of the standard calibration of PUSH: (i) k_{PUSH} =2.5 at $\xi_{2.0} = 0.0$, the left black dot ("Crab-like SNe" for lower ZAMS masses), (ii) k_{PUSH} =4.3 at $\xi_{2.0} = 0.245$, the red dot (calibration model s18.8 for SN 1987A), (iii) k_{PUSH} =0.0 at $\xi_{2.0} \geqslant 0.7$, right black dot (BH formation). This figure is take from Ebinger et al. [88]

lower compactness. Above 30 $M_\odot$ the compactness of the progenitors increases again with higher CO-core and iron core masses. Progenitors beyond 35 $M_\odot$ can form BHs for the *w* progenitor set that has higher carbon-oxygen core and iron-core masses as well as higher hydrogen and helium envelope masses. The progenitors for stellar models with ZAMS masses above 50 $M_\odot$ of both sets explode (see figures 5.19 and 5.20). This explodability behavior is similar as in the works by O'Connor and Ott (2011) [211] (see also figure 2.1 that is from [40]). In section 5.7 we show the first preliminary results obtained for the explodability of the low metallicity progenitor sets *u* and *z* [40]. For the amount of ejected ^{56}Ni we see a good agreement with observations in the mass range between 10 and ~21 $M_\odot$ where a linear rising trend is emerging for stars between 10 and about 20 $M_\odot$ ZAMS mass. For the heavier progenitors of these sets we obtain explosions as well as ejected nickel masses. These stars explode and they eject similar amounts of ^{56}Ni. Due to the correlation of ejected mass of ^{56}Ni and the explosion energy, stars with different masses but with the same explosion energy eject similar amounts of ^{56}Ni. For the low-metallicity sets *u* and *z* the high-mass range does not explode (see section 5.7). Note that stars heavier than 40 $M_\odot$ are considerably less abundant than stars with ZAMS between 10 and 20 $M_\odot$ since the birth masses of stars follows the initial mass function (IMF) (see, e.g., [254–256][1]).The yields obtained by post-processing trajectories from the

[1] In the appendix we briefly describe the IMF (see A.3).

PUSH simulations (published in Curtis et al. [140]) can be used in calculations of the galactic chemical evolution.

We also investigate a different calibration of the PUSH method to the constraints by using the compactness value evaluated at a mass of $1.75 M_\odot$ that we call second calibration. The compactness value $\xi_{1.75}$ is more strongly depending on the iron core mass and shows a slightly different behavior than the compactness value $\xi_{2.0}$ used previously. In figure 5.18 we show k_{PUSH} of the second calibration and the resulting explosion energies compared to the observed values. The parameters of the second calibration of k_{PUSH} are $a = -25.05$, $b = -13.96$, and $c = 2.5$ (paraboloidal function in the compactness value evaluated at $1.75 M_\odot$). A summary of the outcomes of CCSN simulations obtained for the standard and the second calibration for both investigated progenitor samples with solar metallicity is shown in figure 5.19. We see that the second calibration results in a lower explodability overall and leads to a larger fraction of faint explosions and black holes. In this chapter we showed that with a calibration in compactness we obtain an effective model to investigate the properties of neutrino-driven CCSNe. The standard calibration is in good agreement with the constraints we formulated based on observational data and will be used to investigate the outcome of CCSN simulations for the full ZAMS mass range of available CCSN progenitor models.

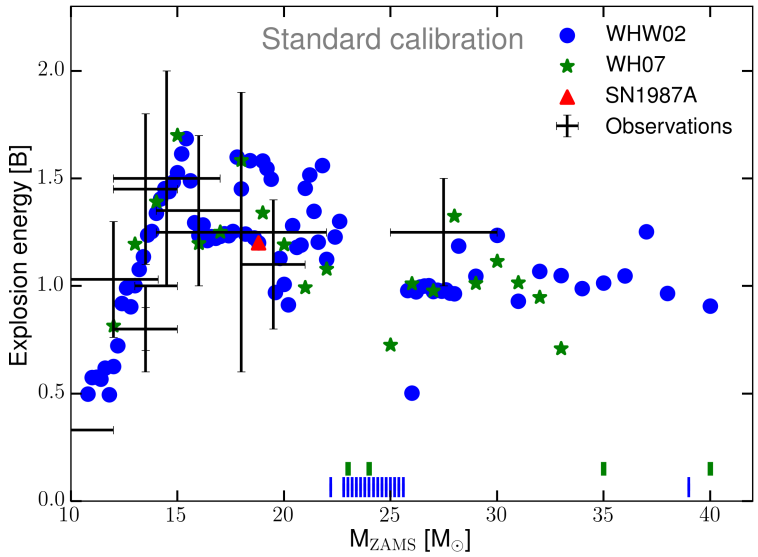

(a) Explosion energy for the progenitor sets with solar metallicity from [40, 41] in the mass range between 10.8 $M_\odot$ and 40 $M_\odot$. Vertical dashes at the bottom of the figure indicate ZAMS masses for which a BH was formed.

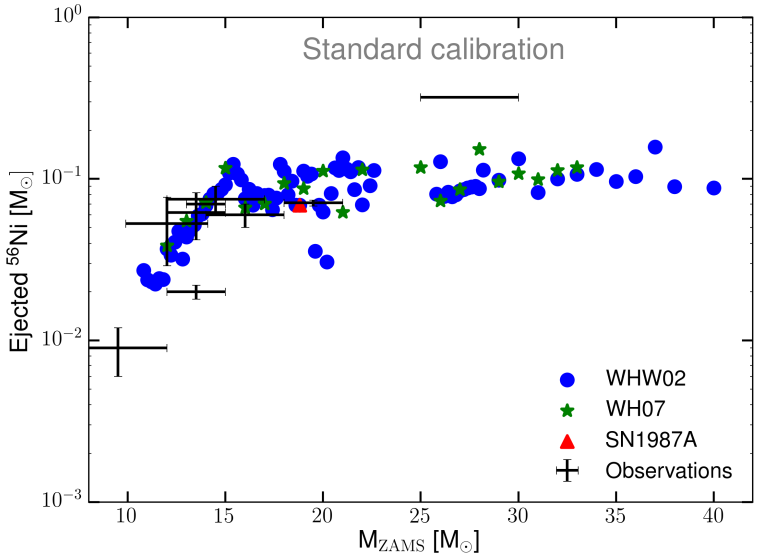

(b) Amount of ejected ^{56}Ni for the progenitors with solar metallicity from [40, 41] in the mass range between between 10.8 $M_\odot$ and 40 $M_\odot$.

Fig. 5.16.: The upper figure shows explosion energies as function of ZAMS mass for observed supernovae (black crosses with error bars), for progenitor models from WHW02 (blue circles) and WH07 (green stars) from the standard calibration of the PUSH method. The vertical dashes at the bottom of the figure indicate ZAMS masses for which a BH was formed. The lower figure shows ejected ^{56}Ni masses as function of ZAMS mass for the same models. In both figures, black crosses with error bars represent observational data and the red triangle indicates the calibration model for SN 1987A, s18.8. Note that the lower left black cross in the lower panel represents SN 2005cs with ZAMS mass of 9 $M_\odot$ which is below the mass range of our models. Figure (a) is taken from Ebinger et al. [88]. Figure (b) uses values from computations done in Ebinger et al. [88] and Curtis et al. [140].

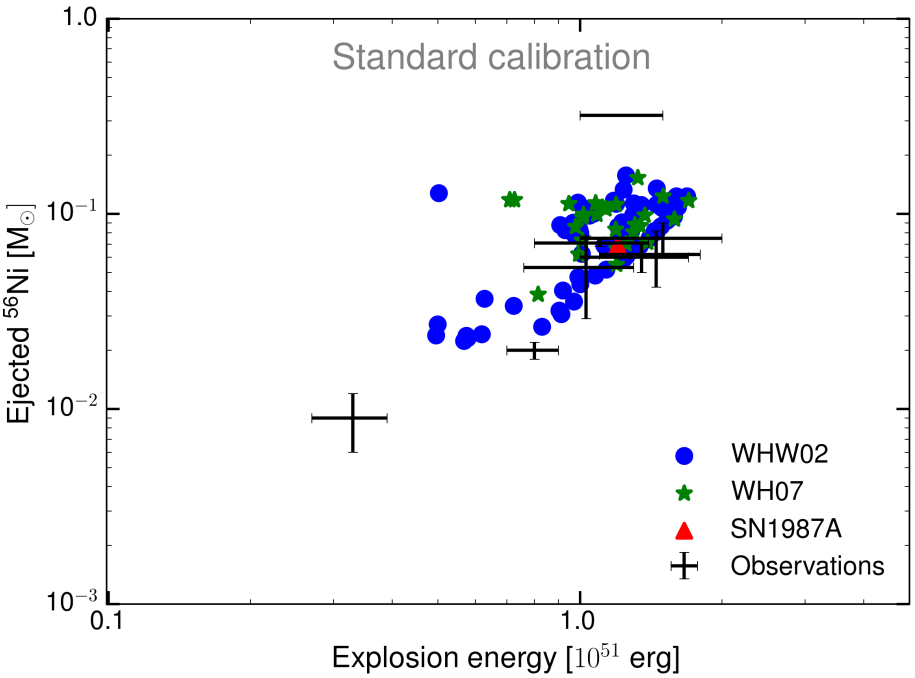

Fig. 5.17.: The figure shows ejected ^{56}Ni masses as function of explosion energy for the solar metallicity WHW02 progenitor sample (blue circles) and the WH07 progenitor sample (green stars) for the standard calibration of the PUSH method. Crosses with error bars represent observational data and the red triangle indicates the calibration model for SN 1987A, s18.8. Note that the lower left black cross in the lower panel represents SN 2005cs with ZAMS mass of 9 $M_\odot$ which is below the mass range of our models. This figure is taken from Ebinger et al. [88].

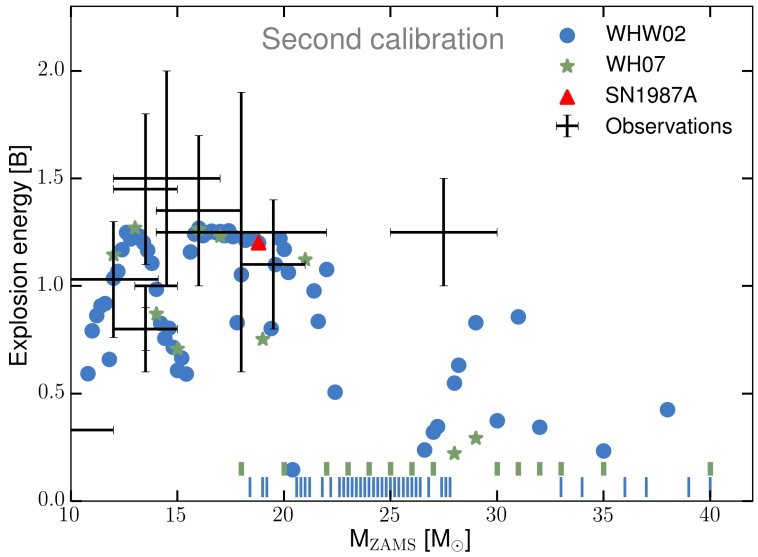

(a) Explosion energies for the progenitor sets with solar metallicity from [40, 41] in the mass range between 10.8 $M_\odot$ and 40 $M_\odot$. Vertical dashes at the bottom of the figure indicate ZAMS masses for which a BH was formed.

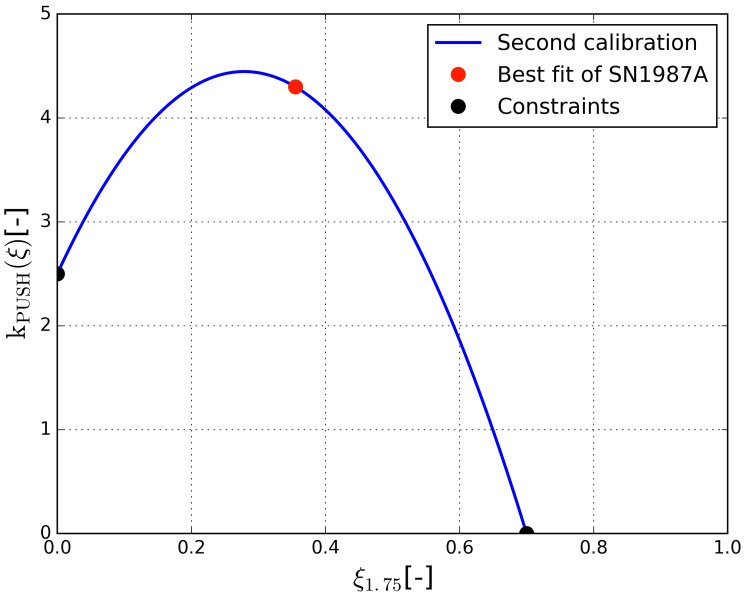

(b) Compactness dependence of k_{PUSH} for the second calibration.

Fig. 5.18.: The upper figure shows explosion energies as function of ZAMS mass for observed supernovae (black crosses with error bars), for progenitor models from WHW02 (blue circles) and WH07 (green stars) from the second calibration of the PUSH method, which results in lower explosion energies and is more prone to BH formation. The vertical dashes at the bottom of the figure indicate ZAMS masses for which a BH was formed. The lower figure shows the compactness dependence of the PUSH parameter k_{PUSH} for the second calibration together with the constraints: (i) k_{PUSH} =2.5 at $\xi_{1.75}$ = 0.0, the left black dot ("Crab-like SNe" for lower ZAMS masses), (ii) k_{PUSH} =4.3 at $\xi_{1.75}$ = 0.3551, the red dot (calibration model s18.8 for SN 1987A), (iii) k_{PUSH} =0.0 at $\xi_{1.75} \geqslant 0.7$, right black dot (BH formation). These figures are taken from Ebinger et al. [88].

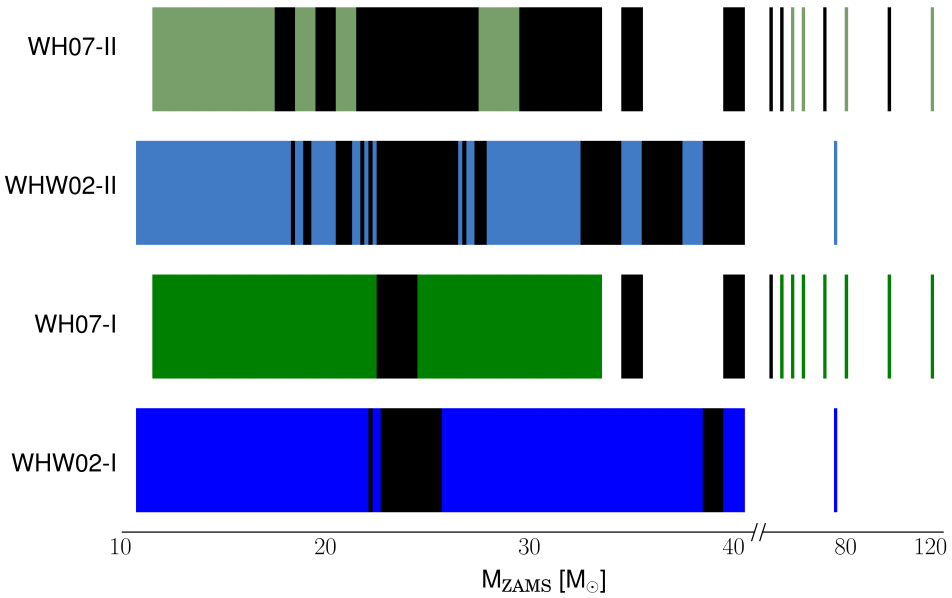

Fig. 5.19.: The explosion outcomes for the standard and the second calibration for the two progenitor sets are shown against ZAMS mass. Colored regions indicate exploding models that leave behind a NS as a remnant and black regions indicate BH formation. The lower two panels (darker colors) show the standard calibration and the upper two panels (lighter colors) show the second calibration. This figure is taken and adapted from Ebinger et al. [88].

5.5 Explosion Properties of Neutrino-driven CCSNe with PUSH

In this section we show, analyze, and discuss the explosion properties of the CCSN simulations done with the PUSH method for the entire WHW02 and WH07 samples with solar metallicity based on the standard calibration introduced in this chapter. The progenitor model samples include ZAMS masses between 10.8 and 120$M_\odot$. An overview of the predicted explosion and remnant properties for all considered progenitor models is given in figure 5.20. The figure shows, from top to bottom, the explosion energies, the explosion times, the ejected Ni masses, the total ejecta masses, and the remnant masses (baryonic mass) as a function of the ZAMS mass of the progenitor models for the WHW02 (in blue, left column) and the WH07 sample (in green, right column). Note that the two samples cover a different mass range and contain a different amount of models (see also table 5.3). In the following we summarize the features of the standard calibration of the PUSH method (see also figures 5.15 and 5.16). We see that the general features are similar for both samples. We obtain explosion energies from ~0.5 to ~1.7 Bethe, explosion times from ~0.26 to ~0.56 seconds, ejected nickel masses from ~0.02 to ~0.16$M_\odot$, totally ejected masses from ~4 to ~14.5$M_\odot$, and NS remnant masses (baryonic) from ~1.3 to ~2$M_\odot$ (see also the next section). We obtain the lowest explosion energies and Ni masses for the progenitors with the lowest ZAMS mass (around 11-12 $M_\odot$). The highest explosion energies and Ni masses result from progenitor models around 15 $M_\odot$, 18 $M_\odot$, and 21 $M_\odot$ ZAMS mass. For the most massive progenitor models (with ZAMS masses $\gtrsim$ 30 $M_\odot$), there is more variation between the two progenitor samples used in this work as well as in comparison with other works. The WH07 progenitor sample has lower explosion energies, is more prone to BH formation, and results in somewhat more massive NSs. Furthermore, the WH07 series has ejecta masses that are slightly larger for the same ZAMS mass when compared to the WHW02 series. The results presented here show a moderate trend of the explosion properties with ZAMS mass up to about 15 $M_\odot$ as expected from the calibration of PUSH. In the same mass range the compactness value exhibits an increasing trend with ZAMS mass (and the CO-core mass grows with increasing ZAMS mass, see figure 5.1). Beyond ~15 $M_\odot$, we see no obvious trend with ZAMS mass. In this ZAMS mass range, the relation between the mass and the compactness value is more complex, as discussed in [174]. In our results for the WHW02 and the WH07 series, we see a correlation between the explosion energy, the ejected Ni mass, and to a lesser degree the remnant mass. The total ejected mass is dominated by the mass of the pre-explosion model at collapse, hence we see a similar trend of the totally ejected mass with ZAMS mass as we see for the progenitor mass in figure 5.1.

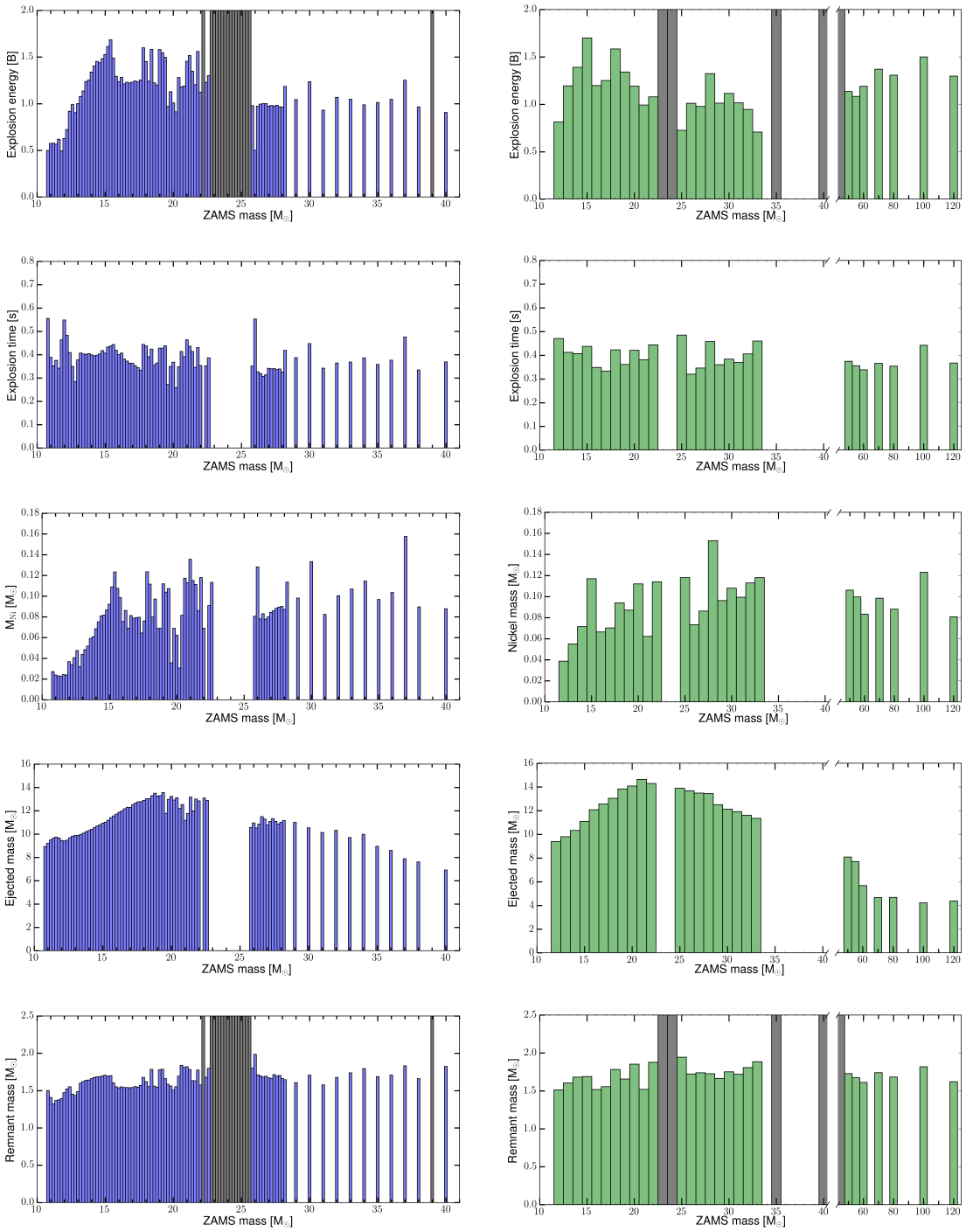

Fig. 5.20.: This figure shows from top to bottom: explosion energy, explosion time, ejected Ni mass, total ejecta mass, and remnant mass (baryonic mass) for the WHW02 sample (left column in blue) and WH07 sample (right column in green) as function of the ZAMS mass using the standard calibration of the PUSH method. The dark bars in the explosion energy and remnant mass panels indicate models that did not explode and formed black holes. These figures are taken from Ebinger et al. [88].

After this overview of the explosion properties of the progenitor sets as a function of ZAMS mass we now have a look at the dependencies of explosion energy, explosion times and the progenitor-remnant connection as a function of the compactness value $\xi_{2.0}$. The explosion energies, baryonic neutron star masses, and explosion times of the standard calibration as a function of compactness are shown in figure 5.21. For the remnant mass (only NSs) a linear correlation with compactness is visible. Models with a higher compactness value have a higher mass accretion rate and hence more matter is accreted onto the PNS before the explosion [87]. For a constant k_{PUSH} calibration we would get no BH formation and the linear trend of the baryonic mass of the nascent NSs is continued for high compactness values. Instead, with the standard calibration of the PUSH method, these high compactness models do not explode and eventually collapse to BHs which are not included in the figure. The explosion time shows a similar trend with compactness but with a broader distribution. For the lowest compactness values we see a scattered structure of the explosion time where it does not follow the general trend. We see that for intermediate compactness ($\xi_{2.0} \approx 0.3$), where the PUSH heating reaches maximum values, the explosion times are comparable to the value of t_{rise}. The explosion energy as a function of compactness shows two distinct features. The highest explosion energies for each series show a paraboloidal dependence on the compactness value, as expected from our k_{PUSH} calibration. Furthermore, a scatter (up to 0.5 B) in the explosion energies is present for compactness values between 02-0.45. In this region of intermediate compactness values the explosion energies and the explosion times can be categorized into two groups. We have seen that the compactness value of the progenitor models has a peak around a ZAMS mass of 24.2 $\mathrm{M}_{\odot}$ (WHW02) and 23.0 $\mathrm{M}_{\odot}$ (WH07) (see figure 5.1). To the left of the peak (i.e., with lower ZAMS mass) and to the right of the peak (i.e., with higher ZAMS mass) the progenitor models have similar compactness values of 0.2 to 0.45. However, we see that they are different in their behavior. Note that in figure 5.21 the models to the left of the peak value of compactness are indicated by open markers and the models to the right of the peak value of compactness are indicated by filled markers. Stars with lower ZAMS masses before the peak in compactness ultimately take longer to form explosions and have a higher explosion energy than their counterparts with the same compactness values but higher ZAMS and CO-core masses. This split into two groups is less pronounced in the case of the remnant mass. In the following, we want to compare our results with other works. Similar studies of CCSN properties obtained from simulations have been done in Ugliano et al. [141], Ertl et al. [170], Sukhbold et al. [214] based on P-HOTB. With a calibration of their spherically symmetric models to SN 1987A and, in the case of Ertl et al. [170], Sukhbold et al. [214], to lower explosion energies for less massive progenitors, the explosion properties and yields of CCSNe were investigated. Another recent study on the explodability of CCSNe that does not use hydrodynamic simulations has been presented in Müller et al. [257]. Müller et al. [257] use

physically motivated scaling laws and differential equations to describe crucial quantities of CCSNe like the shock propagation, the neutron star contraction and the heating conditions. Note that with the exception of Ugliano et al. [141] these other works use different progenitor star samples and ranges from 9 to 120 $M_\odot$, i.e. the smallest mass range is covered in Müller et al. [257], which investigates progenitor stars between 10 and 32.5 $M_\odot$ ZAMS mass. Our explosion energies are compatible with values found in observations and similar to other studies [141, 170, 214, 257, 258]. Exceptions are the relatively high explosion energies that Ugliano et al. [141] and Pejcha and Thompson [258] obtain for progenitor stars with lower ZAMS mass. In Sukhbold et al. [214], slightly lower explosion energies and nickel ejecta masses are obtained with a calibration for "Crab-like" SNe for ZAMS masses below 12 $M_\odot$. The results presented in Pejcha and Thompson [258] and Müller et al. [257] yield the largest range of explosion energies, spanning from 0.2 to 6 B, and from a few 0.01 B to above 2 B, respectively. A prominent feature is the region of non-explodability in the vicinity of 25 $M_\odot$ ZAMS mass. In our simulations we find BH forming models in similar mass regions to other works at 20 $M_\odot$, around 25 $M_\odot$ and between 30 and 100 $M_\odot$. Similar to Müller et al. [257], we do not find many BH forming models between 15 and 20 $M_\odot$. We want to stress, that in the other studies [170, 214, 257] different progenitor stars have been used and thus a perfect agreement is not expected.

In the last part of this section, we also have a look at trends of nucleosynthesis yields for the ejected material with compactness. We do this by showing the behavior of four key isotopes (^{56}Ni, ^{57}Ni, ^{58}Ni, and ^{44}Ti) with compactness in figure 5.22. We see that the amount of ejected ^{56}Ni and ^{44}Ti show a strong linear correlation with the compactness. These isotopes are symmetric, $N = Z$ isotopes. For these isotopes, ^{56}Ni in particular, the amount ejected depends on the explosion energy. For ^{57}Ni and ^{58}Ni the dependence on compactness is more complicated. The correlation broadens towards higher compactness values (for the highest compactness values a factor of three difference between the lowest and highest value of ejected ^{57}Ni can be seen). An even stronger broadening can be observed for ^{58}Ni. While the amount of ejected ^{56}Ni and ^{44}Ti show a linear correlation with explosion energy, the yields of ^{57}Ni and ^{58}Ni strongly depend on the local electron fraction and thus, whether regions with slightly lower Y_e are ejected or not. In general, for models with a similar compactness value, the models with a lower ZAMS mass (open symbols in figures 5.21 and 5.22) eject larger amounts of ^{57,58}Ni and ^{44}Ti. Note that an in depth study of the nucleosynthesis yields for the standard calibration of PUSH is published in [140].

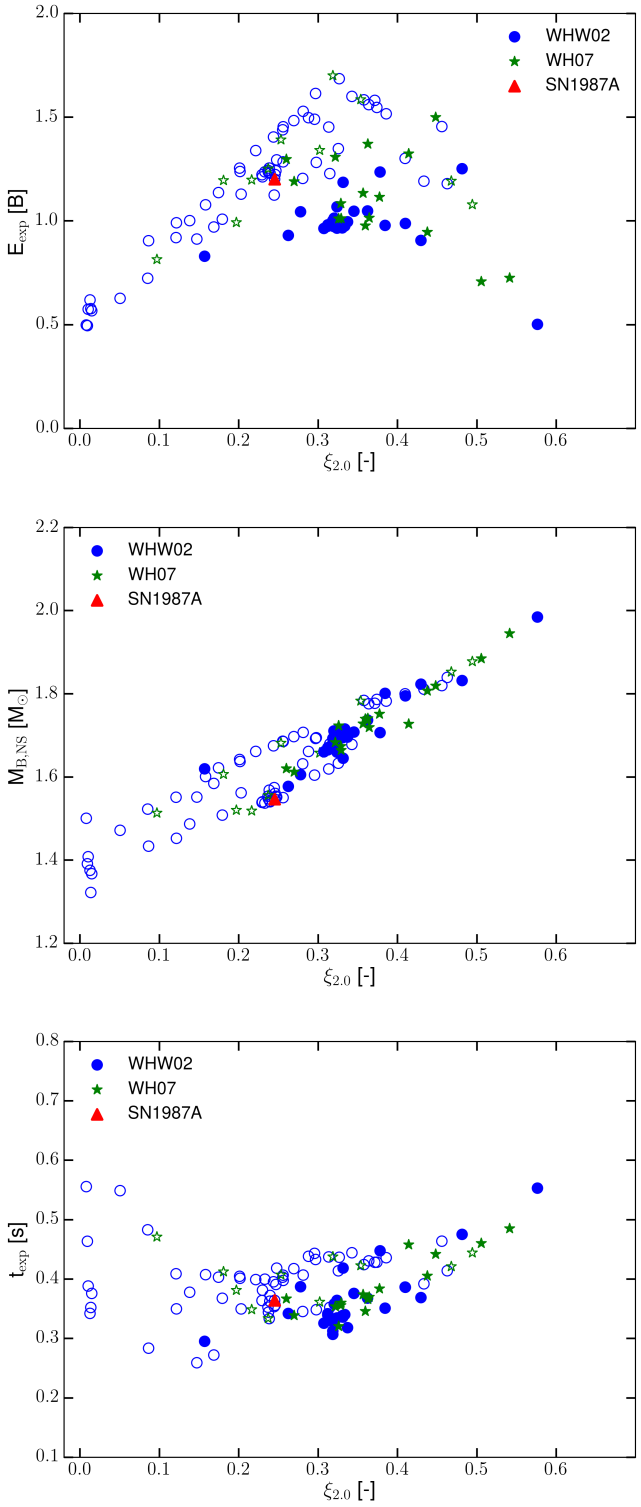

Fig. 5.21.: This figure shows (from top to bottom) the explosion energy, the remnant mass (baryonic mass), and the explosion time for models from the WHW02 series (denoted by the blue circles) and from the WH07 series (denoted by green stars) as function of the compactness value $\xi_{2.0}$. Note that only exploding models are shown. The red triangle indicates the calibration model (s18.8) of SN 1987A. Open symbols indicate models with a ZAMS mass to the left of the compactness peaks of the samples (see figure 5.12) and filled symbols indicate models to the right of the compactness peaks of the samples. These figures are taken from Ebinger et al. [88].

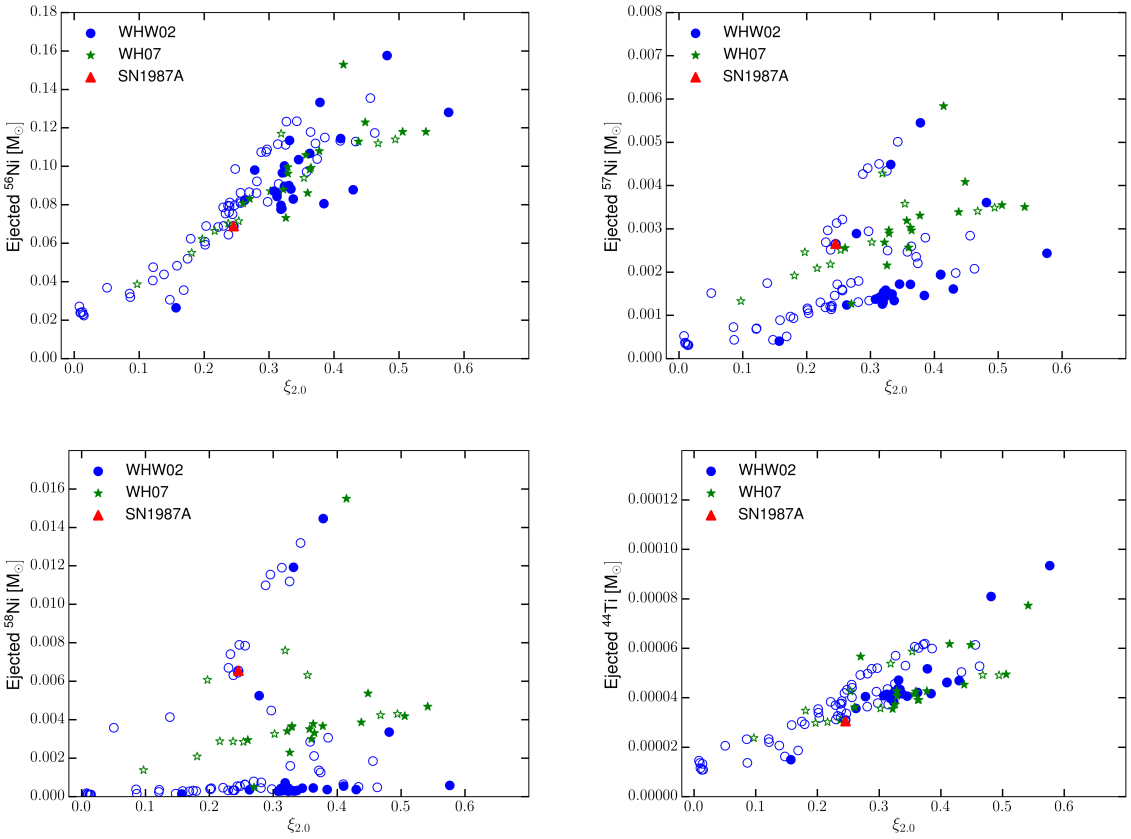

Fig. 5.22.: Ejected mass of ^{56}Ni (top left), ^{57}Ni (top right), ^{58}Ni (bottom left), and ^{44}Ti (bottom right) are shown as a function of the compactness value $\xi_{2.0}$ for the WHW02 and WH07 pre-explosion models. The markers describe the same models as in figure 5.21. These figures are taken from Ebinger et al. [88].

5.6 Remnant Properties of CCSNe

In this section we further cover an aspect of CCSNe that can be illuminated with the PUSH method, the progenitor-remnant connection. Besides the investigation and prediction of explodability, the explosion energies, and the nucleosynthesis we also gain a prediction of the NS and BH birth-mass distributions from our simulations. Here, we will present the resulting remnant masses of the standard calibration and the second calibration of PUSH obtained for the solar metallicity progenitor samples WHW02 and WH07 [40, 41] and show their mass probability distribution. Ultimately, we can compare our resulting masses of the compact remnants with observations. In our CCSN simulations performed with the PUSH setup (no excised inner PNS mass and a realistic nuclear EOS) we can follow the full evolution of the PNS and obtain the baryonic mass of the newly born hot NS (in the case of an explosion). The resulting gravitational masses of the corresponding cooled NSs (that may be observed) are smaller due to neutrino losses in the cooling phase. To compare with observations, we compute the zero-temperature gravitational mass of the initially hot neutron star formed in the CCSN explosion using the HS(DD2) nuclear EOS. We arrive at a distribution of gravitational birth-masses of NS by weighting the predicted cool NS masses as a function of ZAMS mass with the initial mass function (IMF). The IMF is an empirically found distribution function that describes the number densities of stars with different initial masses in a given population of stars [254–256]. It was first introduced by Salpeter [254] and was intended to give an easy way of parameterizing the relative numbers of stars as a function of their ZAMS masses. There are also different parameterizations (see e.g. [255, 259]) that refine the IMF, but for massive stars above 10 $M_\odot$ the IMF according to Salpeter [254] is sufficiently accurate[1]. With the Salpeter IMF we compute a predicted remnant mass probability distribution for the standard and the second calibration of PUSH applied to the *s* and *w* progenitor samples. First, we show the gravitational birth-mass distribution of cool neutron stars. From observations we know that the distribution of NS masses in slow pulsars and non-recycled high-mass eclipsing binaries has a mean of 1.28 $M_\odot$ (dispersion of 0.24 $M_\odot$), which is consistent with the formation in CCSNe [260]. In figure 5.23, we show the gravitational birth-mass distribution of NSs for the two progenitor sets that we obtain with the standard calibration. These two sets of progenitor stars include models with ZAMS masses between 10.8 and and 120 $M_\odot$. Note that the different colors in figure 5.23 indicate different ranges of ZAMS masses of the progenitor models. The predicted NS masses are between 1.2 and 1.8 $M_\odot$. We see that the lowest NS masses in the range between 1.2 and 1.4 $M_\odot$ are only noteworthily populated by the WHW02 sample. Furthermore, lower ZAMS mass stars contribute most of lower NS masses around 1.4 $M_\odot$ and the higher

[1] A short description of the IMF is given in section A.3 of the appendix.

ZAMS mass stars are the main contributors to the NS masses in the vicinity of 1.6 $M_\odot$. In figure 5.25 we see that the predicted NS birth mass distribution for the second (less energetic) calibration does not differ too much from our standard calibration. In comparison to the reported observed NS distribution, the mass ranges of our predicted distributions are somewhat shifted to higher masses. Due to a lack of progenitor models below a ZAMS mass of 10.8 $M_\odot$ in the used samples, remnants from lighter progenitors are not included in the study. These lighter progenitors, due to the applied Salpeter-IMF, would also considerably contribute to the lightest NS masses and would arguably reduce the lower mass limit of the predicted NS birth mass distribution. Note that for the WHW02 progenitor sample we did not include the outlier with 75 $M_\odot$ ZAMS mass in the computation of the mass distribution. We want to emphasize that the resulting mass distributions are valid for single non-rotating stars and do not consider the possible effects present in binary systems, such as mass accretion or loss due to a companion, which can lead to a very different evolution of the stars. A statistically significant comparison of our results with observed NS masses of double systems is beyond the scope of this study. Still, in the following we want to shortly compare our results with other works. Overall, our predicted NS masses are 0.1 to 0.2 $M_\odot$ higher than those given in Ugliano et al. [141] and Pejcha and Thompson [258], who used the same WHW02 progenitor star models. In general, our results are in agreement with Ertl et al. [170], who use different progenitor models below a ZAMS mass of 30 $M_\odot$. In Nakamura et al. [205] 2D axisymmetric simulations up to 1 s post bounce were performed for the same WHW02 progenitor sample. They find similar NS masses as we do, in the range of 1.2 to 2.1 $M_\odot$. As we have discussed, our simulations do not include fallback. In other studies it has been found that fallback does not have a major effect (see, e.g., [214]). Note that all our exploding models result in NSs. This is a consequence of our the numerical framework. In our spherically symmetric simulations it is not possible to have infalling and outgoing matter at the same time. This is the reason why we do not obtain any fallback for exploding models in our simulations, unlike in multi-dimensional simulations where it is possible to have simultaneous in- and outflow. A multi-dimensional simulation framework allows for substantial fallback in 2D and 3D simulations (e.g. [136, 261, 262]).

We now turn our attention to the birth mass distributions of BHs that are formed in failed CCSNe. In our numerical framework the CCSN simulations that run beyond the time on which PUSH is active and ultimately fail to explode, and simulations that directly form a BH contribute to the predicted birth mass distribution of BHs. Failed explosions that are obtained with the PUSH method for the (non-rotating) WHW02 and WH07 progenitor models correspond to BH masses from failed neutrino-driven CCSNe of non-rotating (or weakly rotating) stars. The amount of mass of the star that collapses to a BH depends on the amount of mass stripping and hence for the solar metallicity progenitor samples can

be as low as the CO-core mass. For the two progenitor samples considered here, the final masses of the stars at the onset of collapse do not exceed ~17 $M_\odot$ due to wind mass loss (see also figure 5.1).

In order to obtain the birth mass distributions of BHs, we weight the predicted BH masses with an IMF in the same way as we did it for the NS masses. In figure 5.24 we show the resulting BH birth mass distributions for our standard calibration of the PUSH method. To illustrate how mass loss may effect the final BH masses we show different shaded regions that correspond to different stellar cores that ultimately collapsed to a BH. For the WHW02 and WH07 progenitor star samples with solar metallicity we obtain BH formation as the outcome of our CCSN simulations for stars between 20 and 30 $M_\odot$, centered around ~25 $M_\odot$ ZAMS mass, resulting in BH masses centered around ~ 14 $M_\odot$. Stars with ZAMS masses above 30 $M_\odot$ that form BHs are mainly found in the WH07 progenitor sample, which consists of models that are more likely to collapse to BHs. Our second calibration of PUSH results in considerably more BHs that are formed. This shifts the resulting BH birth mass distribution to slightly lower masses for the second calibration (see figure 5.26). For this calibration we see that the gap between possible low and high BH masses is not as strongly present as for the standard calibration. We now can compute the fraction of stars that ultimately form BHs for both calibrations with the Salpeter IMF. We consider a ZAMS mass range from 8 to 150 $M_\odot$ for our estimate and assume that stars between 8 $M_\odot$ and the lowest ZAMS mass in each sample successfully explode and therefore leave behind a NS as a remnant. Also, we assume that the fate of the star with the highest ZAMS mass within each sample is continued up to 150 $M_\odot$. The estimates for the fraction of stars that end up as BHs for both calibrations and progenitor samples is given in table 5.7.

Progenitor series	Calibration	Black Hole fraction
WHW02	I	~5%
WHW02	II	~16%
WH07	I	~8%
WH07	II	~21%

Tab. 5.7.: Black hole fraction estimates for the standard calibration (indicated by I) and the second calibration (indicated by II) based on the results of the performed simulations with the PUSH method and the assumptions listed in the text. The different wind loss values for the solar metallicity progenitors has a comparably strong influence on the predicted progenitor remnant connection. The estimates are taken into account the neutrino-driven mechanism. Since there are also other mechanisms that enable CCSNe the given fractions can be seen as an upper limit.

Note that our results are broadly consistent with the observationally determined BH mass distribution ($7.8 \pm 1.2\ M_{\odot}$, given in Özel et al. [263]), when we assume that the part of the star that ultimately collapses to a BH is given by the helium core [264]. The BH masses that we obtain from our study of the two solar metallicity progenitor samples, WHW02 and WH07, are not high enough to explain the BH masses from the recent LIGO/VIRGO observations. BHs with such high masses can originate from low metallicity stars, which experience less or almost no mass loss during their evolution, if they collapse with almost their entire ZAMS mass.

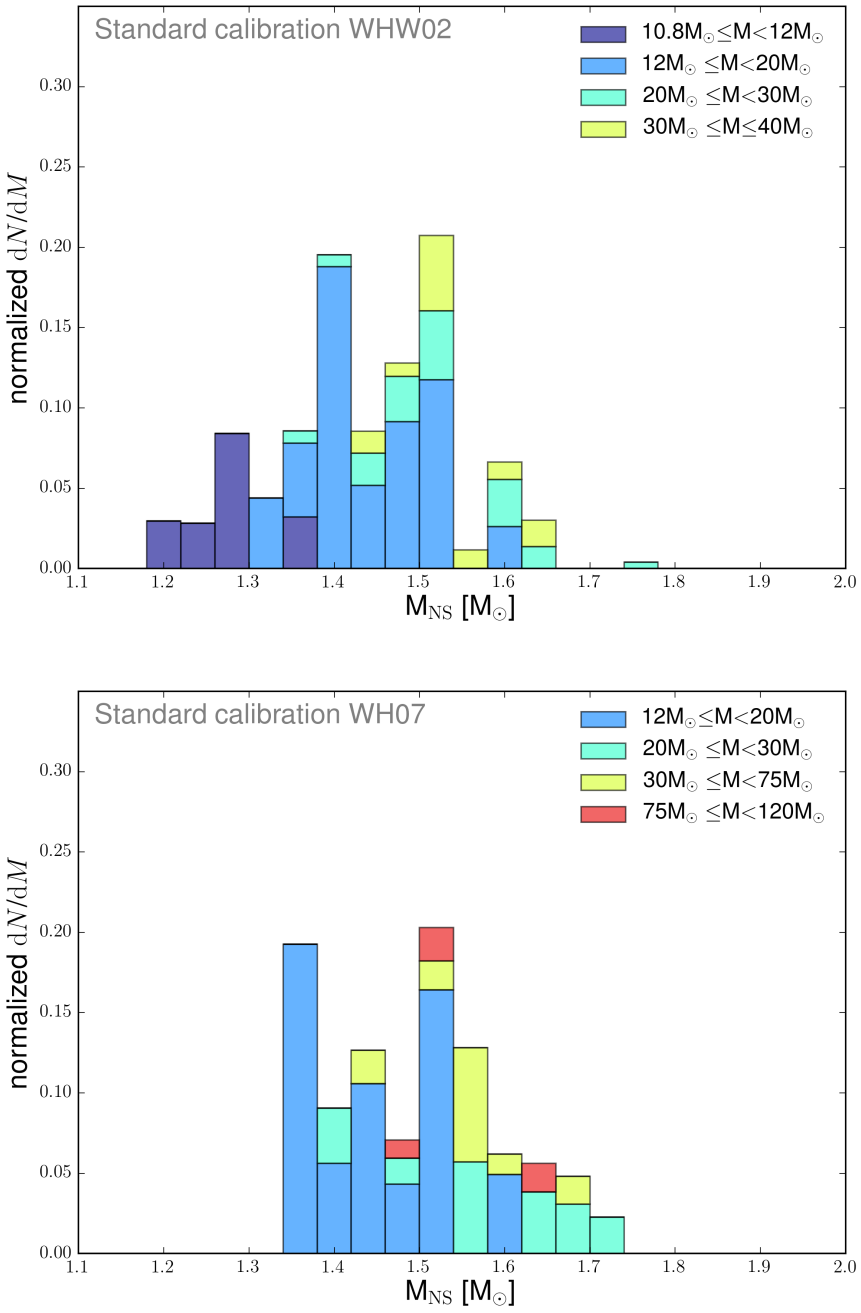

Fig. 5.23.: Gravitational birth mass distributions of cold neutron stars for WHW02 (top panel) and WH07 (bottom panel) for the standard calibration. These figures are taken from Ebinger et al. [88].

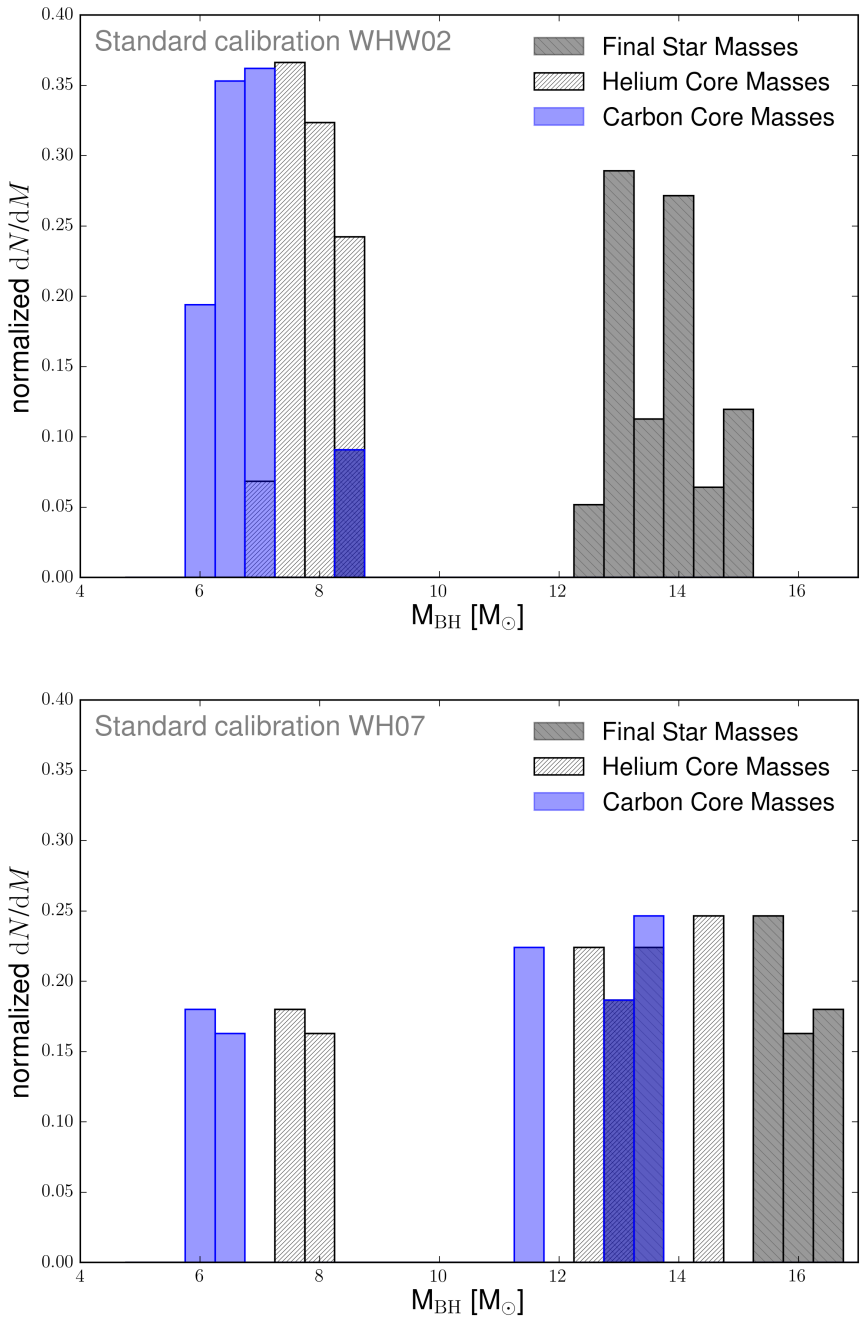

Fig. 5.24.: BH mass distribution with and without helium envelope and also for the final stellar masses for WHW02 (top panel) and WH07 (bottom panel) for the standard calibration. These figures are taken from Ebinger et al. [88].

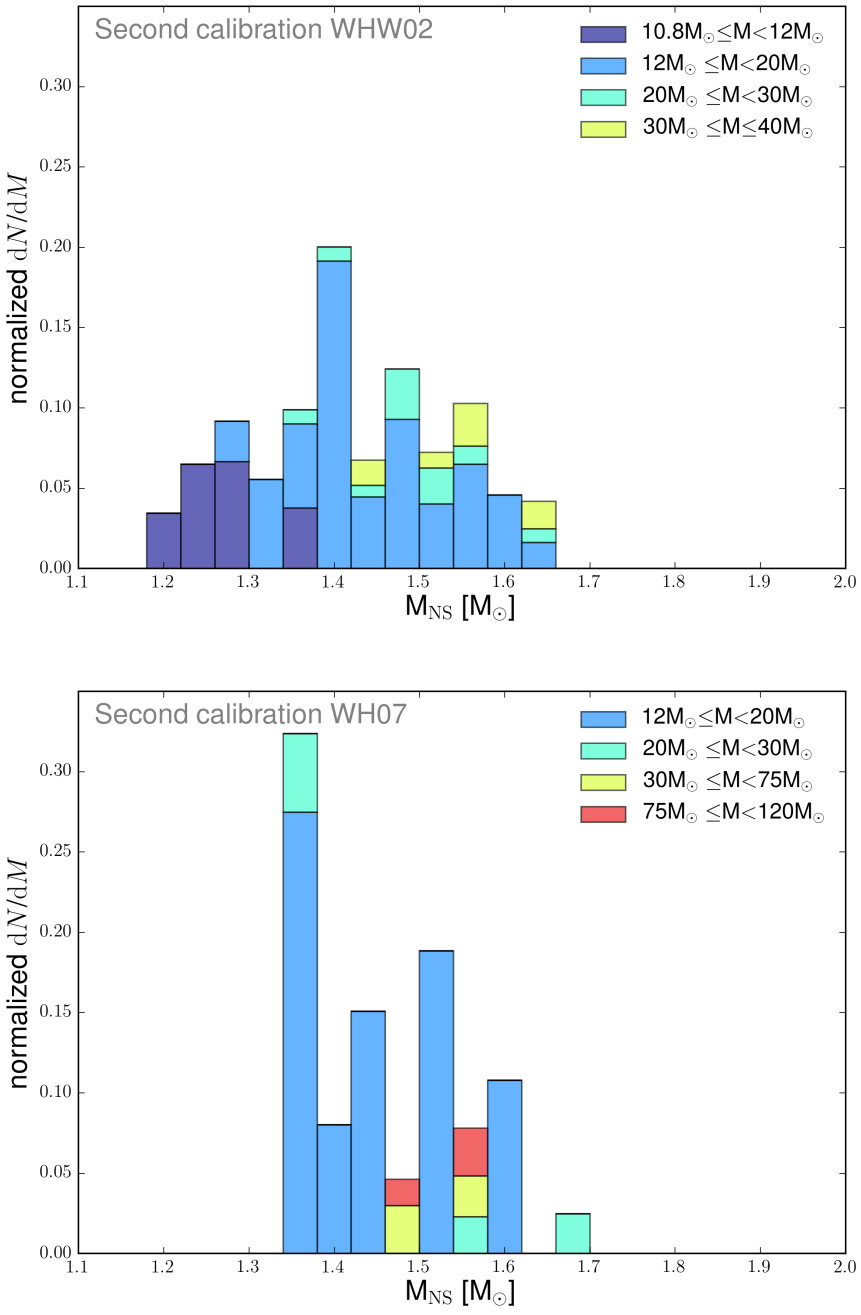

Fig. 5.25.: Gravitational birth mass distributions of cold neutron stars for WHW02 and WH07 for the second calibration. These figures are taken from Ebinger et al. [88].

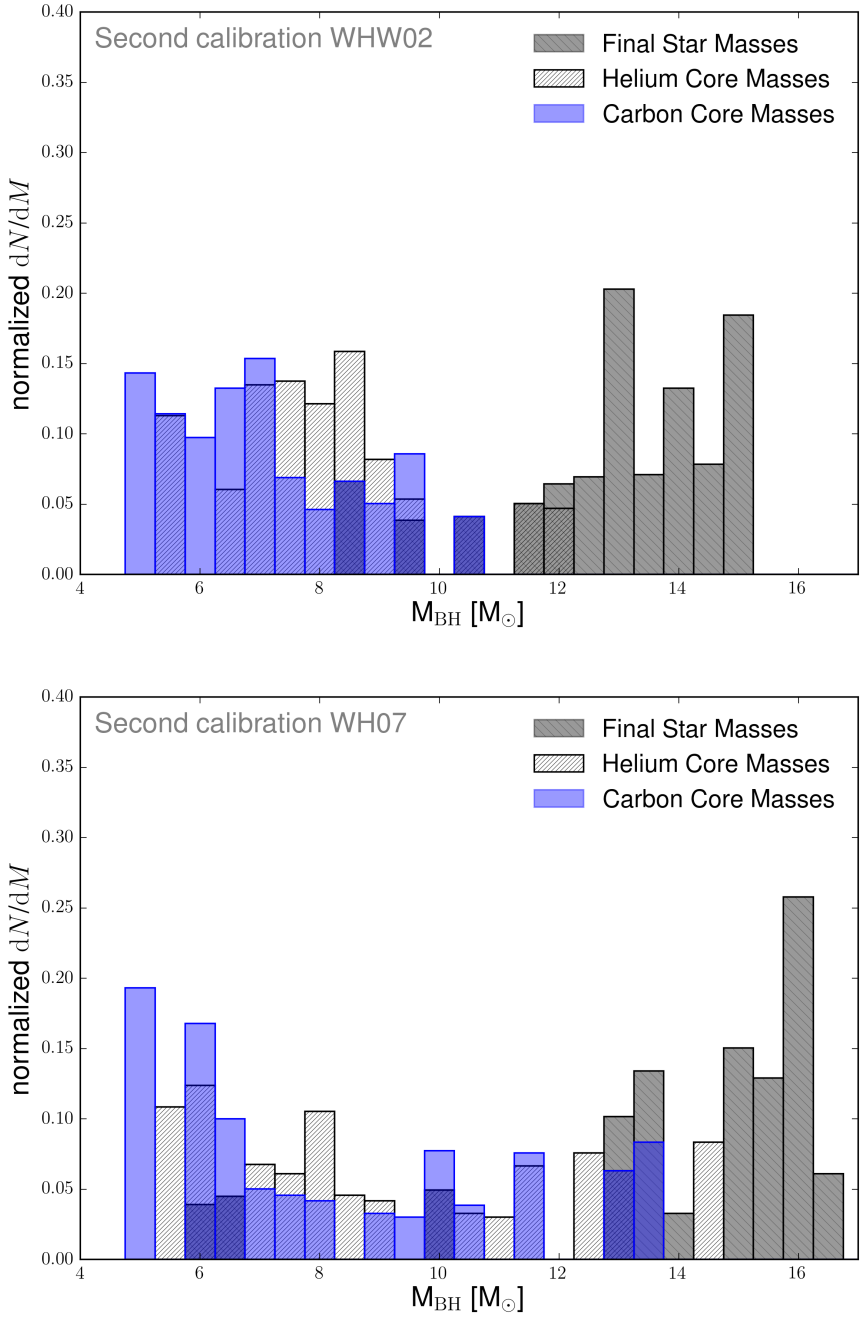

Fig. 5.26.: BH mass distribution with and without helium envelope and also for the final stellar masses for the second calibration. These figures are taken from Ebinger et al. [88].

5.7 Towards Different Metallicities

To give a more complete picture of the explodability of massive stars we also show preliminary studies that were performed for progenitors of [40] with metallicities $Z = Z_{\odot} \times 10^{-4}$ and $Z = 0$ (primordial), the progenitor sets *u* and *z*. The presented results (preliminary) are obtained for the parabola best fit discussed in the chapters above. The temporal constraints in the writing process of this thesis means that we can merely present the obtained explodability of a reduced subset of the available progenitors without nucleosynthesis yields yet. Still, we can see that simulations for the two low metallicity samples lead to a larger range of BH formation. A BH forming region in the vicinity of the compactness peak around 25 $M_{\odot}$ is present, as it was the case for the solar metallicity samples. For masses between ~25 $M_{\odot}$ and ~30 $M_{\odot}$ weaker explosions are obtained than for the solar metallicity progenitor samples. Above ~30 $M_{\odot}$ BHs are formed as expected due to the high compactness of the progenitor stars. With a future evaluation of the full sets we can present the full picture of the obtained explodability, neutron star mass distributions as well as nucleosynthesis yields. With a prediction of explodability and nucleosynthesis yields of different metallicities across the ZAMS mass range the metallicity dependent contribution of CCSNe to the galactic chemical evolution can be investigated. This might give valuable insight into chemical evolution as well as explodability via the evaluation of the GCE results.

Massive stars with low metallicity evolve into heavier CCSN progenitors because they experience less mass loss due to stellar winds. This leads to more compact progenitors as well as to the possibility of more massive BHs that are directly formed . In figure 5.27 we show the compactness and the progenitor mass of the progenitor sets *s*, *w*, *u*, and *z* as a function of ZAMS mass. With these results it is possible to estimate the percentage of BH formation for the investigated metallicities, as well as the influence of wind loss of the solar metallicity progenitors on the progenitor-remnant connection. We assume that the progenitors between 8 $M_{\odot}$ and the start of our progenitor samples successfully explode as CCSNe. Furthermore, based on our results we assume that both solar metallicity sets lead to CCSNe up to an upper limit of 150 $M_{\odot}$. Judging from our results for the *u* and *z* sets for higher masses we assume that they form BHs for the high mass progenitors up to 150 $M_{\odot}$. If we then weight the BH regions in our simulation samples with the IMF with the lower and upper limit of 8 and 150 $M_{\odot}$ we obtain the percentage of stars that form BHs. The results are summarized in table 5.8.

Progenitor set	Metallicity	Black Hole fraction
z (WHW02)	$Z = 0$	~ 18 %
u (WHW02)	$Z = Z_{\odot} \times 10^{-4}$	~ 21 %

Tab. 5.8.: Black hole fraction estimates based on the results of the performed PUSH simulations and the assumptions listed in the text (the calibration used is outdated but corresponds to a version of the standard calibration). We see that the lower metallicity progenitors result in a higher BH fraction than the solar metallicity progenitor samples used in this work (see also table 5.7).

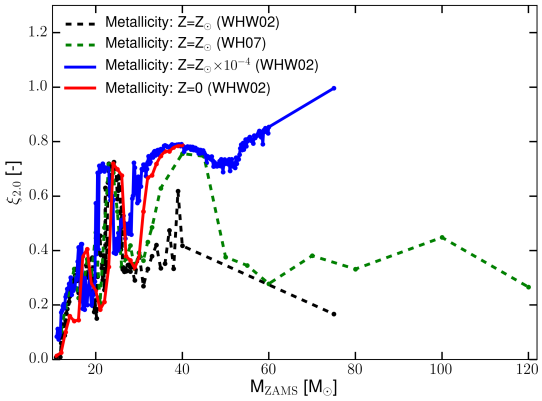

(a) Compactness of different progenitor sets from [40, 41] for the whole mass range

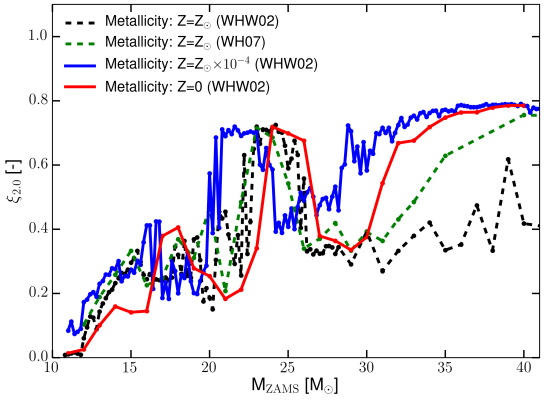

(b) Compactness of different progenitor sets from [40, 41] for the mass range between 10 and 45 $M_{\odot}$

Fig. 5.27.: Progenitor compactness of the progenitors from [40, 41].

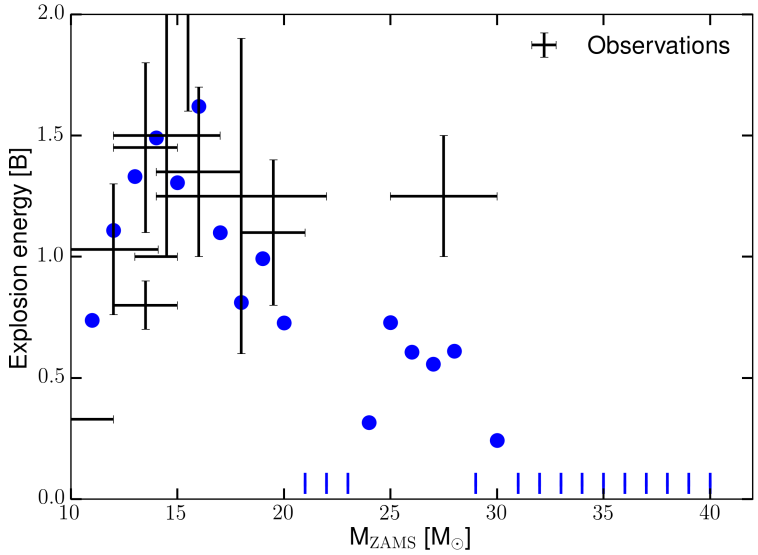

(a) Explosion energies of the parabola fit of PUSH for the progenitors of the *u* set.

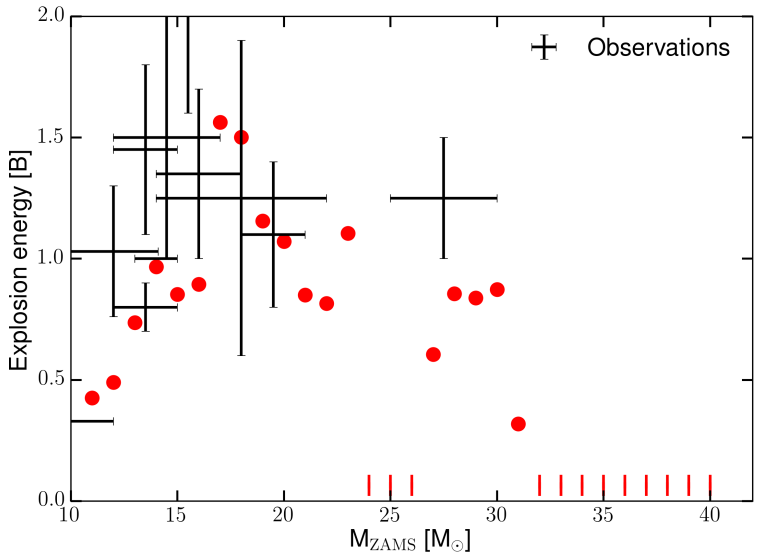

(b) Explosion energies of the parabola fit of PUSH for the progenitors of the *z* set.

Fig. 5.28.: Explodability landscape of the solar as well as the low metallicity sets [40, 41]. We see that the high mass progenitors of low metallicity stars collapse to BHs and do not form explosions. Thus, these progenitors are able to reproduce the faint SN branch.

5.8 Summary and Conclusions

The investigation of the CCSN mechanism remains an intriguing problem. The solution will likely require multi-dimensional hydrodynamical simulations, including general relativity, a nuclear equation of state, sophisticated neutrino transport, magnetic fields and rotation, and also take into account the asphericity of the progenitor structure. The high computational cost of such multi-dimensional simulations still limits the number of models that can be investigated and still motivates the usage of effective spherically symmetric models for extended progenitor and outcome studies.

In this chapter, we have improved the PUSH method from [87], which is used to artificially trigger parametrized core-collapse supernova explosions in spherical symmetry. The PUSH method provides a computationally affordable framework to study aspects of CCSNe that require the modeling of many different progenitors for several seconds after the onset of the explosion. Here, we focused on applying it to two sets of non-rotating, solar metallicity progenitor models between 10.8 $M_\odot$ and 120 $M_\odot$ to obtain explosions and predict compact remnant properties.

The PUSH method has two free parameters (k_{PUSH} and t_{rise}) that need to be determined from external constraints. We have used three general constraints from observational properties of CCSNe to set the parameters for any progenitor model. We required that the PUSH method (i) reproduces the observed properties of SN 1987A for a suitable progenitor model, (ii) allows for the formation of black holes, and (iii) results in lower explosion energies for the lowest-mass progenitors ("Crab-like SNe"). These requirements led to a compactness dependent function for k_{PUSH} (and a fixed value for t_{rise}).

Using this setup, we have simulated the death of the SN-progenitor models in the two samples as either successful neutrino-driven explosion or as failed explosion or direct collapse to a black hole. This investigation has led to several interesting predictions and conclusions:

As a whole, the resulting explosion energies from the PUSH method are in good agreement with the explosion energies of observed CCSNe. In addition, the same models also match observations simultaneously for ^{56}Ni ejecta and explosion energy.

We have shown and discussed that it is possible to infer several interesting trends of explosion properties with compactness (and CO-core mass). The compactness is a better indicator for the expected outcome than the ZAMS mass, however it does not tell the en-

tire story. For example, we found that for models of similar compactness a degeneracy exists that can be partially broken with the CO-core mass. This is consistent with the finding in recent multi-dimensional simulations, where the outcome of the CCSN simulation is related to the binding energy of the outer envelope exterior of a given mass, which has a strong correlation with compactness [213].

We found linear trends of ejected ^{56}Ni and ^{44}Ti yields with compactness (and explosion energy). The yields of ^{57,58}Ni do not follow the same simple correlation. Instead, the local electron fraction has a strong impact on the final yields of these isotopes.

The predicted outcome (NS or BH) is in agreement with predictions from other works that employ a comparable parametrized approach based on the neutrino-driven CCSN mechanism. In particular, we also find a region of BH formation around ~ 25 M$_\odot$ ZAMS mass. Note that some of these studies use different progenitor sets below 30 M$_\odot$ ZAMS mass.

We predict NS mass and BH mass distributions that are broadly consistent with observations. However, we do not find any BHs with $m_{\mathrm{BH}} \gtrsim 18$ M$_\odot$ since non of the progenitor models has a final mass at collapse above this due to mass loss. We saw in preliminary results that low metallicity progenitor models (which experience less mass loss) result in more massive BHs.

6 Additional Results: Three-Dimensional CCSN Simulations with ELEPHANT

This chapter represents the part of this thesis that has been done with the ELEPHANT code (ELegant and Efficient Parallel Hydrodynamics with Approximate Neutrino Transport) [93, 106, 251, 265]. It represents a different and independent part of the thesis that was done to investigate aspects of multi-dimensional CCSN simulations. Of course it was also intended to use the ELEPHANT code to compare results of the one-dimensional PUSH simulations with multi-dimensional results. In the following, an overview of the numerical implementation of the three-dimensional hydrodynamics code, aspects that have been improved and tools that have been developed to analyze and compare the ELEPHANT models to other three-dimensional simulations (e.g. Flash, Sphynx and fGR1, [251]) ,or to one-dimensional simulations done with PUSH, is given. This can help to understand and improve various aspects of the involved codes. In the future, this could be used to gain further insight in the differences between one and three-dimensional simulations and with this improve the PUSH method. For a more detailed discussion of ELEPHANT I refer to [93, 106, 251, 265–267].

6.1 Numerical Implementation of ELEPHANT

The code ELEPHANT is based on the three-dimensional magnetohydrodynamics code FISH and an implementation of the IDSA neutrino transport for the electron neutrinos and anti-neutrinos [93, 251, 265]. The energy loss caused by μ- and τ-neutrinos is computed with a neutrino leakage scheme during the whole simulation [268]. It has been shown, that neutrino electron-scattering plays a significant role in the collapse phase, but becomes rather insignificant in the post-bounce phase (e.g. [250, 269]). Thus, we

make use of the parametrized deleptonization scheme of Liebendörfer et al. (2005) [106] to take the neutrino-electron scattering into account in an efficient way during the collapse. In the post-bounce phase we neglect electron-neutrino scattering in IDSA. Furthermore, the version of ELEPHANT that is used in the framework of this thesis uses an implementation of HS(DD2) EOS [95, 96], the same EOS that was used for the presented PUSH simulations that has been incorporated recently into the ELEPHANT code by M. Hempel, O. Heinimann and myself. This means that the setup of the performed three-dimensional simulations presented in this chapter is the same as the one used for the PUSH simulations (except for the non-NSE treatment in PUSH). This is a good foundation for a first comparison of PUSH with three-dimensional models. ELEPHANT models the innermost part of a massive star during the collapse and the post-bounce evolution inside a three dimensional domain (usually cubic). This 3D domain uses the AGILE-IDSA code [91–93] (see also chapter 3) of a larger computational domain inside of which the 3D cube is embedded as boundary conditions. The main strength of the ELEPHANT code is its computational efficiency and simplicity. The simplicity expresses itself in the form of an equidistant mesh which limits the size of the three-dimensional computational domain to the innermost hundreds of km of the star, with typical resolutions between 0.5 to 2 km. Each doubling of the included domain or of the resolution increases the computational cost by a factor of $\sim 2^3 = 8$. Thus, for the most part we use a cubic domain with an edge length of 300 to 600 km and a resolution of 1 or 2 km. This amounts to a maximum of $600^3 = 216'000'000$ individual cubic simulation zones of the domain. The global computational domain is split into subdomains to make use of MPI parallelization and enables the distribution of the task onto several nodes (further, OpenMP parallelization can be used). Furthermore, ELEPHANT uses an implementation of Open ACC to make use of GPU parallelization to compute the neutrino transport (IDSA), which uses about $\sim 60-80\%$ of the total simulation time and thus represents the major part of the computational cost. This implementation of IDSA into ELEPHANT and FLASH has been the aim of a recent proposal of the Basel group. The magnetohydrodynamics part based on the FISH code is computed on the CPU of the used nodes. Typically, the global three-dimensional cubic domain is split into $4^3 = 64$ cubic subdomains that can be split up in as many MPI processes. These subdomains use the GPU parallelization to compute the neutrino transport. Always three planar sheets of the subdomain (one sheet is one individual zone wide) at a time are send to the GPU. In figure 6.1 we illustrate the setup of an ELEPHANT simulation, i.e. the innermost three-dimensional cube and the AGILE-IDSA domain that acts as a boundary and runs in the background (AGILE is also used to correct aspects that are not evolved in the best way in ELEPHANT due to a relatively low resolution, especially in the innermost part of the PNS, e.g., evolution of central entropy).

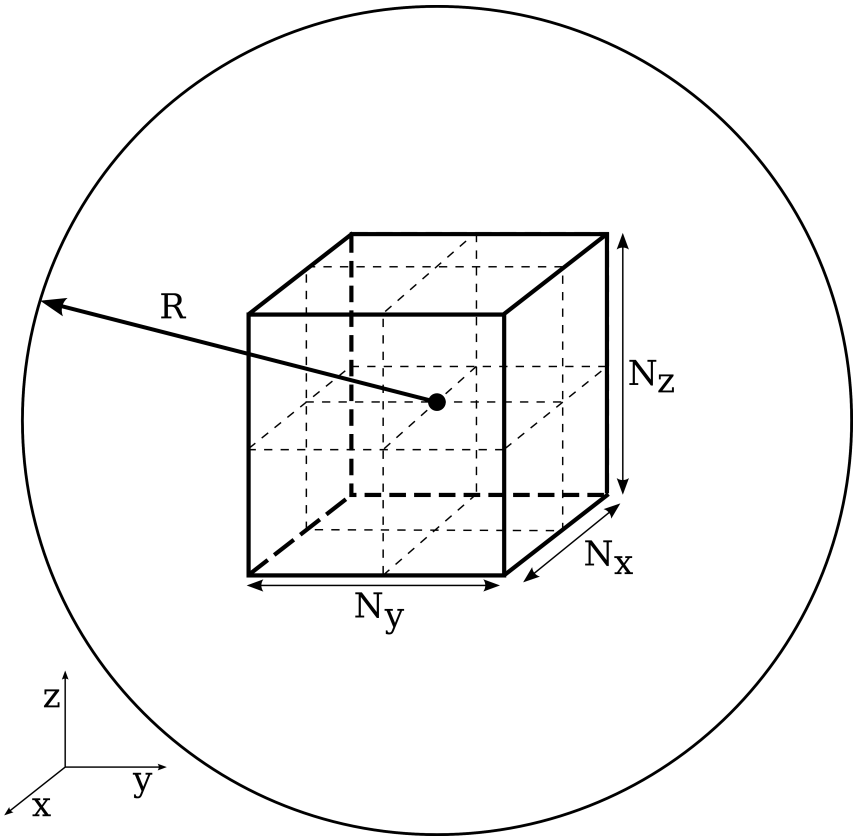

Fig. 6.1.: An illustration of the setup of ELEPHANT. The 3D cube has $N_x \times N_y \times N_z$ zones which usually have a size of about 1 km^3. This cube evolves the innermost ~ 600 km^3 of the collapse and post bounce phase in 3D. The AGILE-IDSA run that sets the boundaries for the 3D cube has a total extent of $R \sim 10^4$ km. The dashed lines indicate the xy-,xz-,yz-sheets which are stored in the hdf5-data segments for each time step with the full available resolution. We use these sheets to evaluate the ELEPHANT runs and find the shock position.

We now come to the equations that are solved by ELEPHANT in order to evolve the magneto-hydrodynamics (MHD) part. The equations of ideal MHD can be used to describe the temporal evolution of plasma and are used in ELEPHANT. Thus, the code solves the following set of three-dimensional conservation equations with gravitational source term (for the treatment of gravity, see section 6.2) [93, 251, 265–267, 270]

$$\frac{\partial \rho}{\partial t} + \nabla \cdot \left(\rho \boldsymbol{v}\right) = 0, \tag{6.1}$$

$$\frac{\partial \rho \boldsymbol{v}}{\partial t} + \nabla \cdot \left(\boldsymbol{v}\rho\boldsymbol{v} - \boldsymbol{b}\boldsymbol{b}\right) + \nabla P = -\rho \nabla \Phi, \tag{6.2}$$

$$\frac{\partial E}{\partial t} + \nabla \cdot \left[\left(E + P\right)\boldsymbol{v} - \boldsymbol{b}\left(\boldsymbol{v}\cdot\boldsymbol{b}\right)\right] = -\rho\boldsymbol{v}\nabla\Phi, \tag{6.3}$$

$$\frac{\partial \boldsymbol{b}}{\partial t} - \nabla \times \left(\boldsymbol{v}\times\boldsymbol{b}\right) = 0, \tag{6.4}$$

$$\frac{\partial}{\partial t}\left(\rho Y_e\right) + \nabla \cdot \left(\rho Y_e \boldsymbol{v}\right) = 0 \tag{6.5}$$

$$\frac{\partial}{\partial t}\left(\rho Y_\nu^t\right) + \nabla \cdot \left(\rho Y_\nu^t \boldsymbol{v}\right) = 0, \tag{6.6}$$

$$\frac{\partial}{\partial t}\left[\left(\rho Z_\nu^t\right)^{\frac{3}{4}}\right] + \nabla \cdot \left[\left(\rho Z_\nu^t\right)^{\frac{3}{4}}\boldsymbol{v}\right] = 0. \tag{6.7}$$

Equations (6.1)-(6.4) express the conservation of mass, momentum, energy, and magnetic flux. The variables in the equations above denote the baryonic mass density ρ, the velocity $\boldsymbol{v}$, the magnetic field $\boldsymbol{B} = \sqrt{4\pi}\boldsymbol{b}$, the total energy density $E = \rho e + (\rho/2)\,v^2 + b^2/2$ (e is the specific internal energy given by the EOS HS(DD2), and the total pressure $P = p + b^2/2$ (sum of the matter pressure p given by the EOS HS(DD2), and the magnetic pressure). The variable Y_e denotes the electron fraction.The equations used in ELEPHANT also include the advection of the trapped electron neutrino (and antineutrino) fractions Y_ν^t (the trapped neutrino spectrum can be approximated by a thermal spectrum) and a multiple of the neutrino entropies $\left(\rho Z_\nu^t\right)^{3/4}$, where Z_ν denotes the mean specific energy of the neutrinos [93, 251]. The gravitational potential (included in the equations above to take the effect of gravitational force into account) is given by Φ and fulfills the Poisson equation (see section 6.2)

$$\nabla^2\Phi = 4\pi G\rho. \tag{6.8}$$

With the assumption that magnetic monopoles do not exist the magnetic field has to fulfill the constraint

$$\nabla \cdot \boldsymbol{b} = 0. \tag{6.9}$$

For a more detailed description of such an approach we refer to [265–267, 271]. The computation of a time step in ELEPHANT is done with operator splitting technique as it is described in [265–267] for the FISH code. The numerical solution algorithm of ELE-

PHANT to the MHD equations is explicit. This means that the time step is restricted by the Courant, Friedrich, and Lewy (CFL) condition [272]

$$\Delta t = k \cdot \min_{i,j,k} \left(\frac{\Delta x}{c^x_{i,j,k}}, \frac{\Delta y}{c^y_{i,j,k}}, \frac{\Delta z}{c^z_{i,j,k}} \right). \tag{6.10}$$

In the above equation the variable $c^d_{i,j,k}$ which denotes the maximum speed at which information can travel in the whole computational domain in each direction ($d = x, y, z$) is given by

$$c^d_{i,j,k} = max\left(v^n_{d,i,j,k} + c^n_{F,i,j,k} \right). \tag{6.11}$$

This quantity represents the sum of the velocity component in d and the speed of the fast magnetosonic waves c_F. Typically, the CFL number k is set to 0.75 in our simulations.

6.2 Gravitation

In the ELEPHANT code an effective general relativistic potential is implemented to efficiently describe the effects of general relativity. The following section describes how the gravitational potential that is used in our 3D CCSN simulations is computed. The Poisson equation is a non-homogeneous, elliptic partial differential equation [104, 273]

$$\nabla^2 u = f, \tag{6.12}$$

where ∇^2 denotes the Laplace operator and the source term f is given. If the source term is equal to zero, equation (6.12) corresponds to the Laplace equation. Partial differential equations that do not involve a time derivative only have boundary conditions (BCs), and no initial conditions (ICs). This is the reason why these problems are called boundary value problems (BVPs). In comparison to the locally solved hyperbolic fluid equations where the propagation of information is limited by the fastest speed in the system, the Poisson equation is a BVP and thus has no restriction by any signal speed limit. To solve the Poisson equation the density distribution of the whole computational domain needs to be accessible. The compactness of the mass distribution involved in CCSNe makes it necessary to take general relativistic effects into account. A general relativistic treatment leads to stronger gravitational forces than a Newtonian description. Thus, the Newtonian treatment would lead to slower infall velocities and a reduced compactness of the PNS. Below it is shown how GR effects can be taken into account in 3D CCSN simulations with ELEPHANT by using an effective GR potential. The presented method is an effective general relativistic approximation to the full GR solution following case

"A" in Marek et al. (2006) [274]. We use the HYPRE[1] library that we implemented into ELEPHANT to efficiently solve the Poisson equation, specifically the V-cycle multigrid solver denoted PFMG (for historical reasons; parallel semicoarsening multigrid solver) included in HYPRE with a structured grid (see [275, 276] and references therein[2]). Thorough theoretical descriptions of multigrid methods can be found in, e.g. [277, 278].

Effective General Relativistic Gravitational Potential

In the Newtonian case the gravitational field inside a star is described by a gravitational potential Φ, which represents a solution of the Poisson equation. In spherical symmetry the Poisson equation reduces to

$$\frac{1}{r^2}\frac{\partial}{\partial r}\left(r^2\frac{\partial \Phi}{\partial r}\right) = 4\pi G\rho. \tag{6.13}$$

The vector of gravitational acceleration $\boldsymbol{g} = -\boldsymbol{\nabla}\Phi$ points towards the center of the star. In spherical symmetry only the radial component is non-vanishing $g_r = -\partial\Phi/\partial r$. From equation 6.13 one gets (integration over r)

$$\frac{\partial \Phi}{\partial r} = \frac{Gm}{r^2}, \tag{6.14}$$

where m is given by

$$m(r) = 4\pi\int_0^r \mathrm{d}r' r'^2\rho. \tag{6.15}$$

A purely Newtonian treatment of gravity is too simple and neglects the general relativistic effects that become relevant in CCSN simulations. In the case of ELEPHANT we approximate the radial effects of general relativistic gravity in a Newtonian hydrodynamics code by using an effective relativistic gravitational potential Φ_{eff}, which mimics the deeper gravitational well of the relativistic case, following [274]. To ensure that the effective potential approximates effects of general relativistic gravity, one demands that the potential reproduces the solution of hydrostatic equilibrium according to the Tolman-Oppenheimer-Volkoff equation [279, 280][3]. The effective gravitational potential that replaces the Newtonian potential in ELEPHANT is given by

$$\Phi_{\mathrm{eff}}(r) = -G\int_r^\infty \frac{\mathrm{d}r'}{r'^2}\left(m_{\mathrm{eff}} + \frac{4\pi r'^3}{c^2}[p + p_\nu]\right)\frac{1}{\Gamma^2}\left(\frac{\rho c^2 + e + p}{\rho c^2}\right), \tag{6.16}$$

[1] available online: http://computation.llnl.gov/projects/hypre-scalable-linear-solvers-multigrid-methods.

[2] See also the HYPRE user manual available on the afore mentioned webpage.

[3] The classical condition for hydrostatic equilibrium is given by $\frac{\partial p}{\partial r} = -\rho\frac{\partial \Phi}{\partial r}$.

and the effective mass is given by (using case A of [274])

$$m_{\mathrm{eff}}(r) = 4\pi \int_0^r \mathrm{d}r' r'^2 \Gamma \left(\rho + \frac{\rho e}{c^2} + \frac{E}{c^2} \right), \tag{6.17}$$

where p is the gas pressure, p_ν is the neutrino pressure, ρ is the rest-mass density, e is the internal energy density, and E is the neutrino energy density. The metric function Γ is given by

$$\Gamma = \sqrt{1 + \left(\frac{v}{c}\right)^2 - \frac{2Gm_{\mathrm{eff}}}{rc^2}}. \tag{6.18}$$

Note that v refers to the radial component of the velocity of the fluid.

The effective relativistic gravitational potential for multi-dimensional flows is calculated by replacing the "spherical contribution" $\bar{\Phi}(r)$ to the multi-dimensional Newtonian gravitational potential $\Phi(x, y, z)$ with the effective potential $\bar{\Phi}_{\mathrm{eff}}(r)$. For three-dimensional Cartesian coordinates we get

$$\Phi_{\mathrm{eff}}(x, y, z) = \Phi(x, y, z) - \bar{\Phi}(r) + \bar{\Phi}_{\mathrm{eff}}(r), \tag{6.19}$$

where the expressions $\bar{\Phi}(r)$ and $\bar{\Phi}_{\mathrm{eff}}(r)$ represent spherically averaged potentials where the effective potential is calculated according to equation (6.16). Thereby, the quantities ρ, e, v, p, p_ν, and E are replaced by their corresponding spherically averaged values.

6.3 Shock Capturing for Comparison with Other Simulations

A way to compare simulations with each other is the temporal evolution of their shock and of course, in the case of PUSH an interesting aspect, to compare neutrino heating rates and entropy profiles. This analysis can be done with a shock capturing Python tool for ELEPHANT that was created during this work. We outline this tool here and then use it to present initial comparisons with PUSH simulations. The tool was not only created to compare ELEPHANT with PUSH, but to compare ELEPHANT with other three-dimensional CCSN codes in the framework of [251]. In figure 6.1 the computational domain of ELEPHANT is shown. The three hdf5 data-segments that correspond to fully resolved sub-sheets in the xy-, xz-, and the yz-layers were indicated in this figure. Now, we use these data sheets due to their full resolution for all write-out times. With them it is possible to capture the shock evolution of a simulation done with ELEPHANT and

compare it to other runs.For each of the sheets we read in 8 rays by choosing a separation angle of 45 degrees. Thus, we follow the coordinate axes as well as the diagonals and read in the data along these rays. To capture the shock, we use the entropy as the critical indicator. Figure 6.2 shows the xy-segment sheet and the corresponding 8 rays as an example. A good way to find the shock efficiently is to follow the rays from outside to inside. We define the shock position as the radius where the entropy exceeds a critical value for the first time (for each ray). This value has been set to 6 k_B per baryon in the here presented studies. In the figures 6.2 and 6.3 the entropy per baryon and how the shock position is evaluated is shown for an ELEPHANT simulation of a 15 $M_\odot$ progenitor [41] with the EOS HS(DD2) at a time of 500 ms post bounce. The different rays are labeled A, B, C, D, E, F, G, H and we see how different the entropy curves can be for different directions in multi-dimensional simulations. The minimum and maximum position of the shock are indicated as well. The shock positions that are gathered for each time step result in a temporal evolution of the shock radius that can be compared to other simulations, e.g. PUSH. This comparison of different shock radius evolutions for various PUSH parameter combinations for the same progenitor, the same EOS, and the same neutrino transport is shown in the figures 6.4, and 6.5. We see that low $t_{\rm rise}$ (corresponding to the old calibration presented in chapter 4) do not compare well with the ELEPHANT simulations. The fit for SN 1987A with $t_{\rm rise}$ =400 ms is in better agreement with the ELEPHANT run. We also show runs with $t_{\rm rise}$ =500 ms and $t_{\rm rise}$ =600 ms. Based on this comparison (more should be performed in the future) we conclude that the temporal evolution of the shock radius for the larger $t_{\rm rise}$ is in better agreement with the ELEPHANT simulation performed with the same setup. We adapted a larger $t_{\rm rise}$ value earlier in chapter 5 to achieve a better agreement of PUSH with observational properties and with multi-dimensional simulations. Thus, it seems that the two comparisons of PUSH with multi-dimensional results lead to similar conclusions. For further investigations and comparisons of PUSH and ELEPHANT I suggest to also compare the neutrino heating profiles and use the comparison to possibly find refined criteria for the parametrized heating in PUSH. I outline such a process here by comparing the model of PUSH that was in comparably good agreement with the shock radius obtained in ELEPHANT (with $k_{\rm PUSH}$ =4.0 and $t_{\rm rise}$ =500 ms). In figure 6.6 the temporal neutrino heating profiles of PUSH for the run with $k_{\rm PUSH}$ =4.0 and $t_{\rm rise}$ =500 ms are shown. Figure 6.8 shows the neutrino heating profiles for the different rays at different times as well as the spherical average of the three-dimensional ELEPHANT simulation (dashed line). For this very preliminary investigation we just roughly compare the two simulations. At 150 ms post bounce the heating profiles seem to be similar in position and shape. The same holds for later times, i.e. at 450 ms post bounce up to the end of the ELEPHANT simulation (~500 ms post bounce). In between the heating profiles differ. While the PUSH heating temporarily recedes and intensives, the heating profiles for ELEPHANT gradually evolve outward. With increased time post bounce the

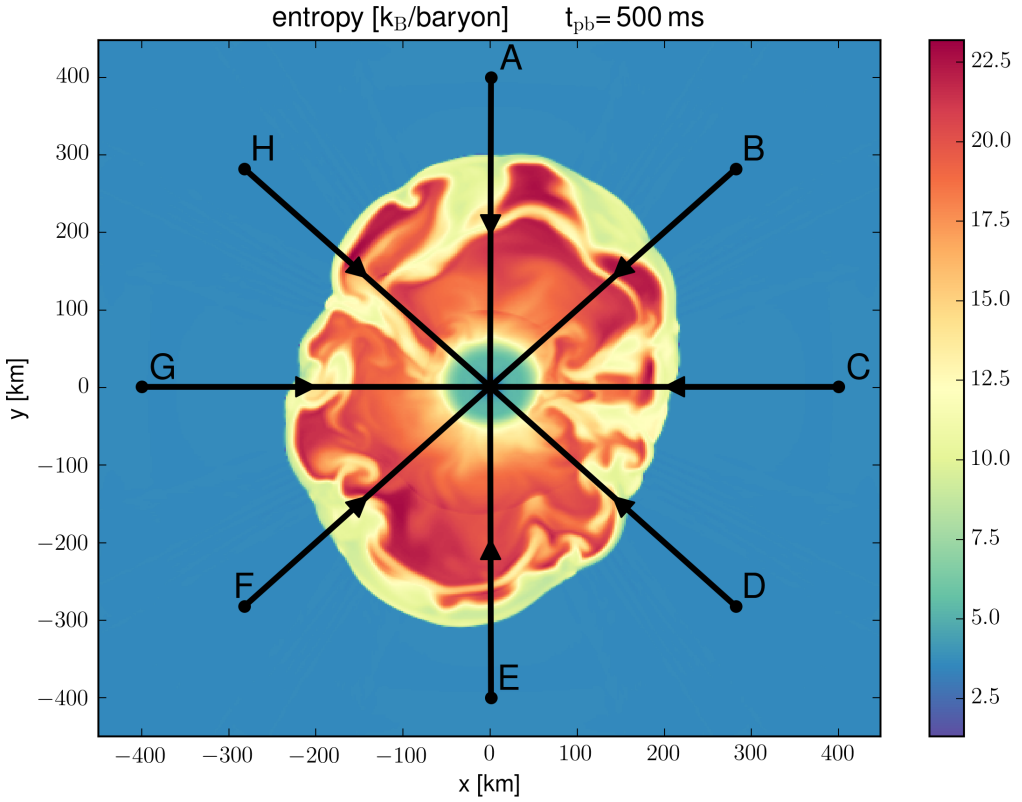

Fig. 6.2.: The different rays which are used to find the minimum and maximum radius of the shock are shown in equatorial plane as an example. They are are denoted by the letters A to H and go along the coordinate axes and the diagonal directions of the elephant simulation sheet. Here we see the xy-plane for a simulation for the w15 progenitor [41] with the EOS HS(DD2) [95] at a time of 500 ms post bounce. The simulation was performed on the Piz Daint supercomputer of the CSCS in Lugano with a resolution of 2 km and 450 zones per axis which are split up into subdomains with 150^3 zones resulting in $3^3 = 27$ MPI processes.

8 rays evaluated in the ELEPHANT run differ more and more, indicating developing aspherical properties of the star. This is meant as an illustration of the differences between, and the possibilities for future comparisons of 1D and 3D simulations. In figure 6.7 we show the xy-sheet of the neutrino heating at 500 ms post bounce that corresponds to the entropy sheet shown in figure 6.2.

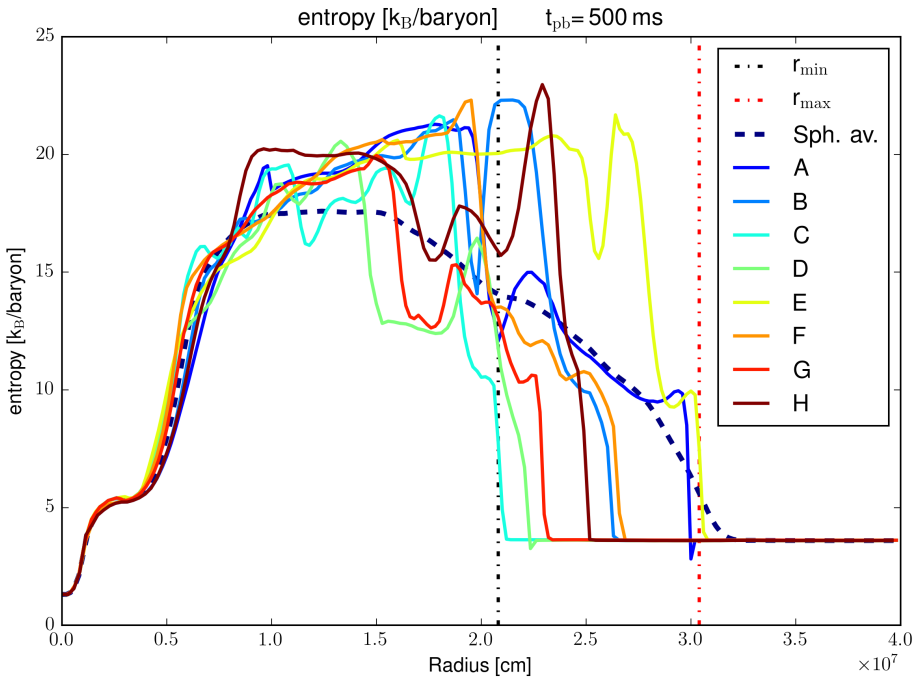

Fig. 6.3.: The evaluation of the different rays in the xy-plane are shown together with the spherically averaged (Sph. av., dashed line) value of the whole simulation. The minimum and maximum values of the radius for the shock front are given by r_{min} and r_{max}. The values of the shock position are defined by the point were the entropy rises the first time above a value of 6 k_B per baryon. The minimum, maximum and average values are collected for all three sheets through the center (xy-, xz-, yz-plane) over time and are used to compare the shock evolution of the ELEPHANT simulation to others.

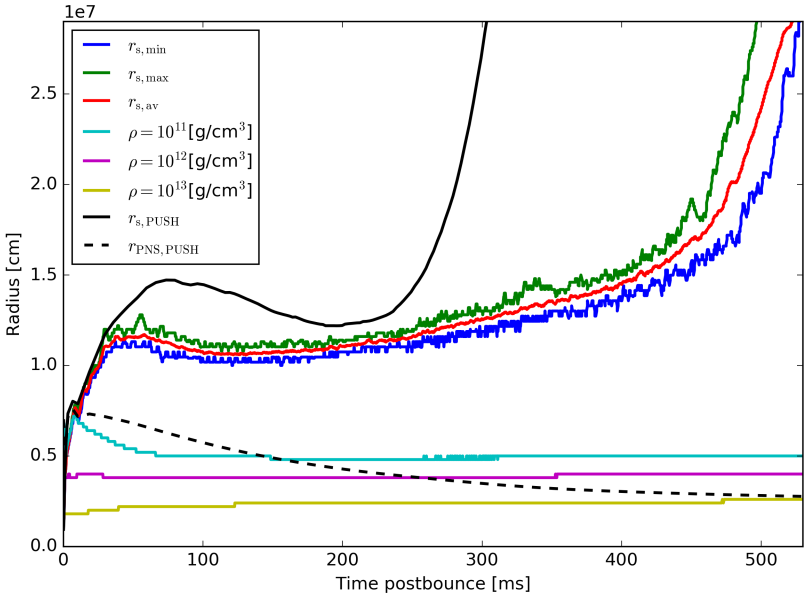

(a) Comparison of an ELEPHANT run with a calibration for PUSH presented in chapter 4.

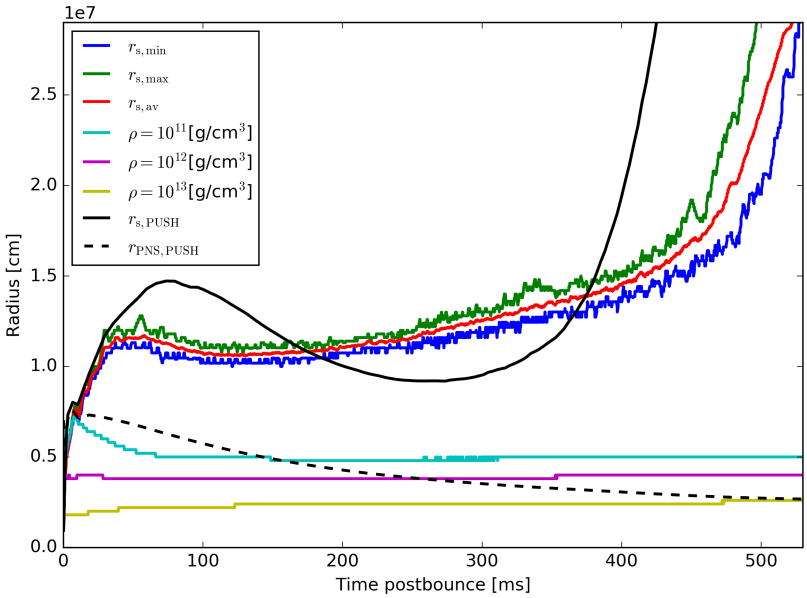

(b) Comparison of an ELEPHANT run with a calibration for PUSH presented in chapter 5.

Fig. 6.4.: We show the shock radii and PNS radii of PUSH runs in comparison with ELEPHANT run results. In figure (a) the best fit of chapter 4 with k_{PUSH} =3.5 and t_{rise} =200 ms is shown. Figure (b) shows the calibration of PUSH obtained in chapter 5 for k_{PUSH} =4.0 and t_{rise} =400 ms. All the runs use the same EOS and neutrino transport.

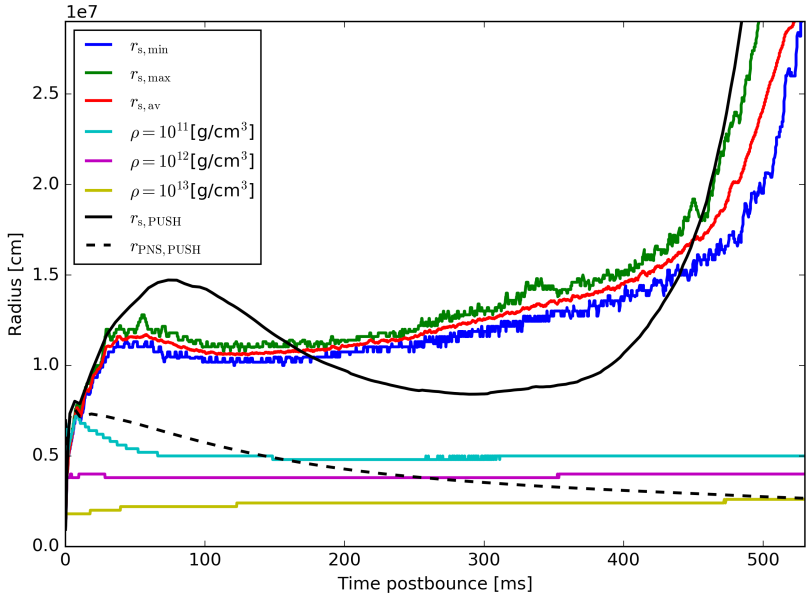

(a) Comparison of PUSH with ELEPHANT for t_{rise} =500 ms.

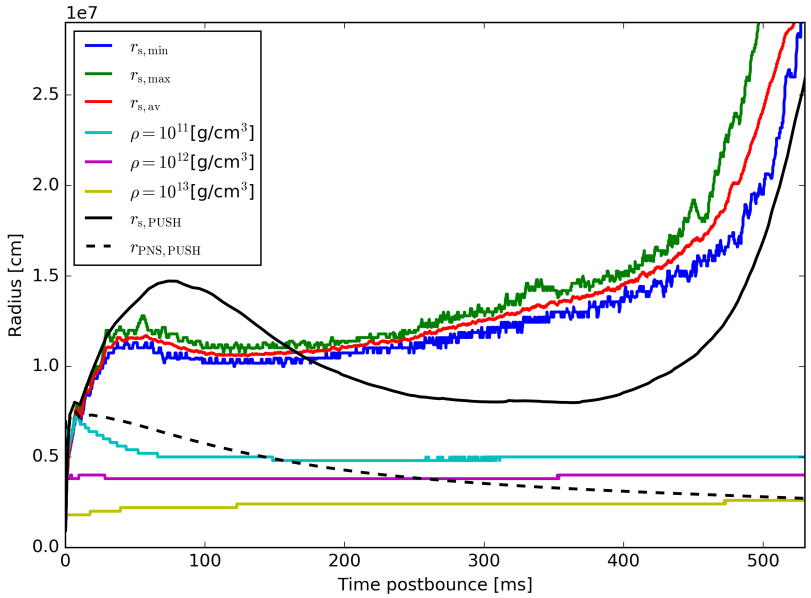

(b) Comparison of PUSH with ELEPHANT for t_{rise} =600 ms.

Fig. 6.5.: We show the shock radii and PNS radii of PUSH runs in comparison with ELEPHANT run results. Figures (a) and (b) are comparisons of ELEPHANT with PUSH runs with k_{PUSH} =4.0, and t_{rise} =500 ms and t_{rise} =600 ms, respectively. All the runs use the same EOS and neutrino transport.

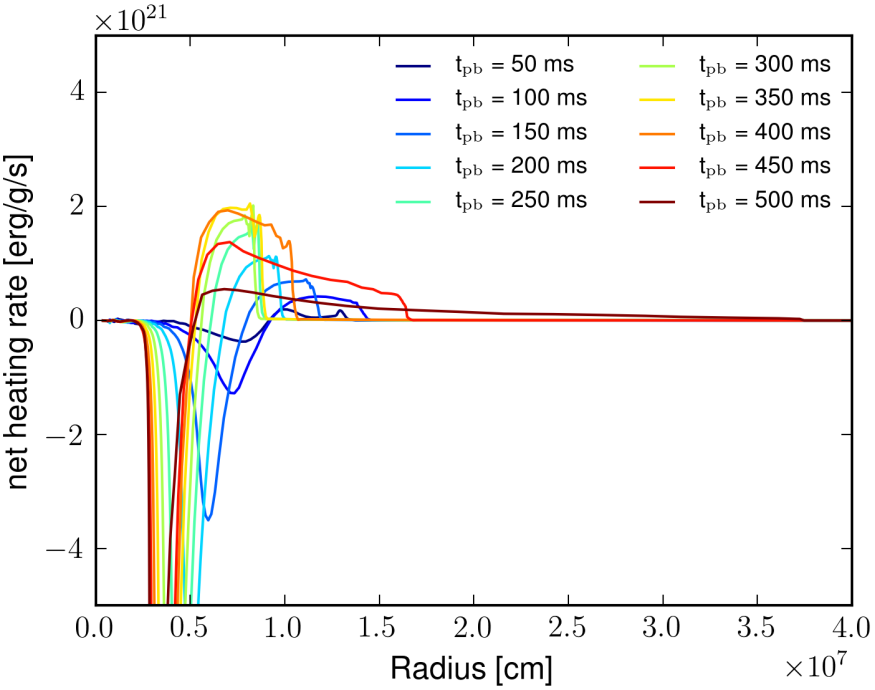

Fig. 6.6.: The neutrino heating profiles of electron neutrinos together with the PUSH extra heating for a PUSH simulation with the parameters k_{PUSH} =4.0 and t_{rise} =500 ms for a 15 $M_{\odot}$ progenitor [41] is shown for several time steps post bounce.

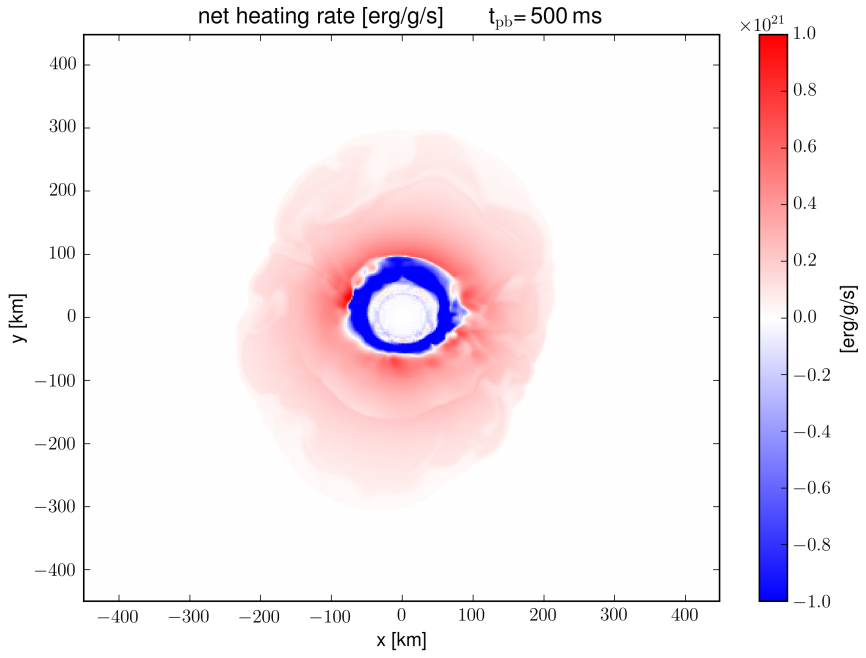

Fig. 6.7.: Neutrino heating at 500 ms post bounce for an ELEPHANT run performed with the EOS HS(DD2), IDSA, and a $\mu-$ and $\tau-$ neutrino leakage scheme. The model shown is the same as in figure 6.2.

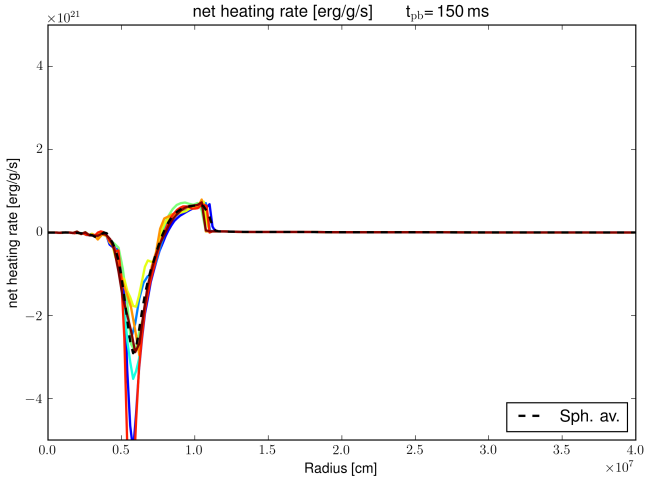

(a) ELEPHANT neutrino heating profile at 150 ms post bounce.

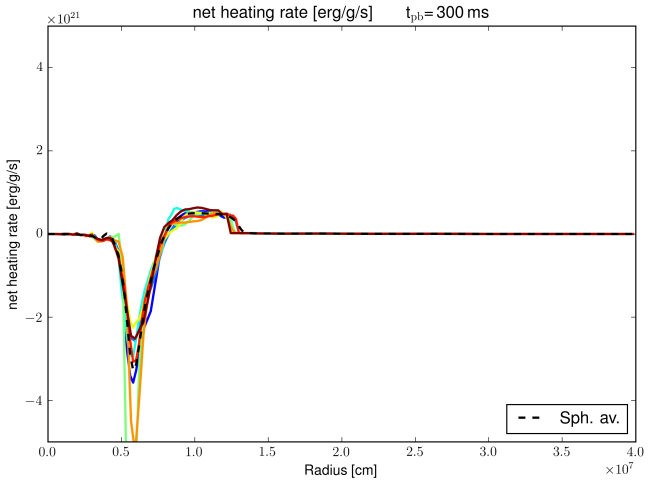

(b) ELEPHANT neutrino heating profile at 300 ms post bounce.

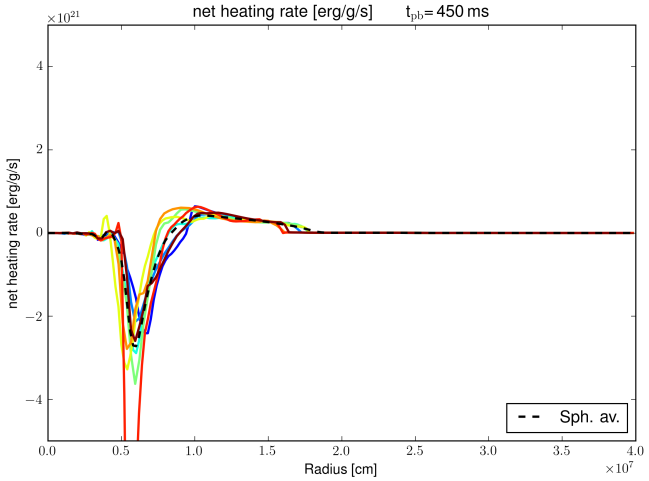

(c) ELEPHANT neutrino heating profile at 450 ms post bounce.

Fig. 6.8.: Neutrino heating profiles for the 8 rays defined above together with the spherical average (dashed line) of an ELEPHANT run for different times post bounce.

6.4 Outlook

This is a very short section. It contains findings from the last weeks of this PhD thesis. We only want to show some initial observations of interesting aspects in the ELEPHANT runs that can be investigated in the future. Further investigations need to be done do distinguish whether the observed features are physical or simply represent numerical features. Because the observed features are interesting we present them here. These features were observed during a more detailed investigation of the ELEPHANT runs which were used for the demonstrated comparisons with PUSH. For the simulation of a progenitor with 15 $M_{\odot}$, solar metallicity [41], the usage of the EOS HS(DD2) [95], and with a resolution of 2 km an oscillation of the PNS was observed that induced shock waves behind the stalled shock. In figure 6.9 we show entropy sheets for successive time steps to make the induced waves of the PNS oscillation visible. For the same progenitor (w15.0) but with an increased resolution of 1 km zones, a spiral motion was found. This is clearly visible in the density sheets, see figure 6.10. In figure 6.11 we show the entropy for the same time steps as the density profiles. These features look promising and should be investigated but one has to be careful since both aspects could be numerical features.

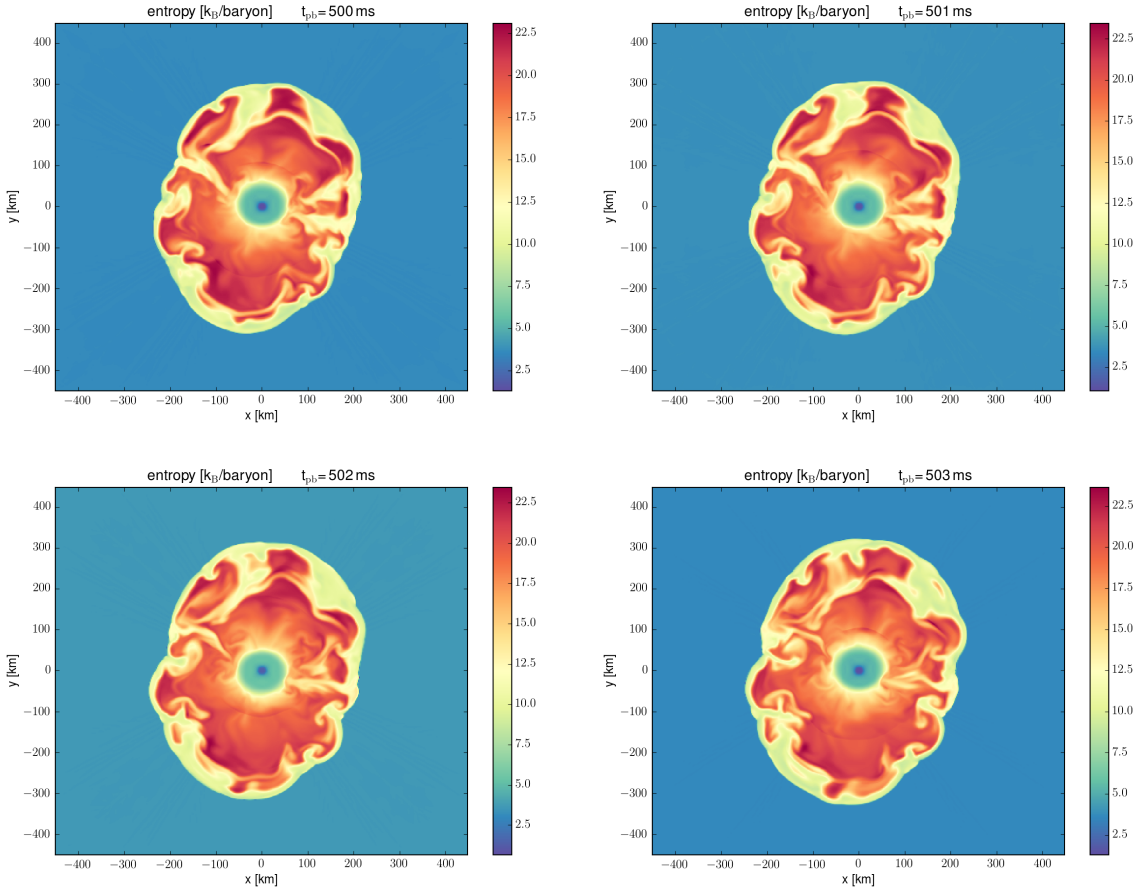

Fig. 6.9.: Entropy sheets (x and y axes in units of km and entropy in units of k_B/baryon) for consecutive time steps. Behind the main shock front motions are induced by the oscillating PNS. The times shown (from top left to bottom right) are 500 ms, 501 ms, 502 ms, and 503 ms post bounce.

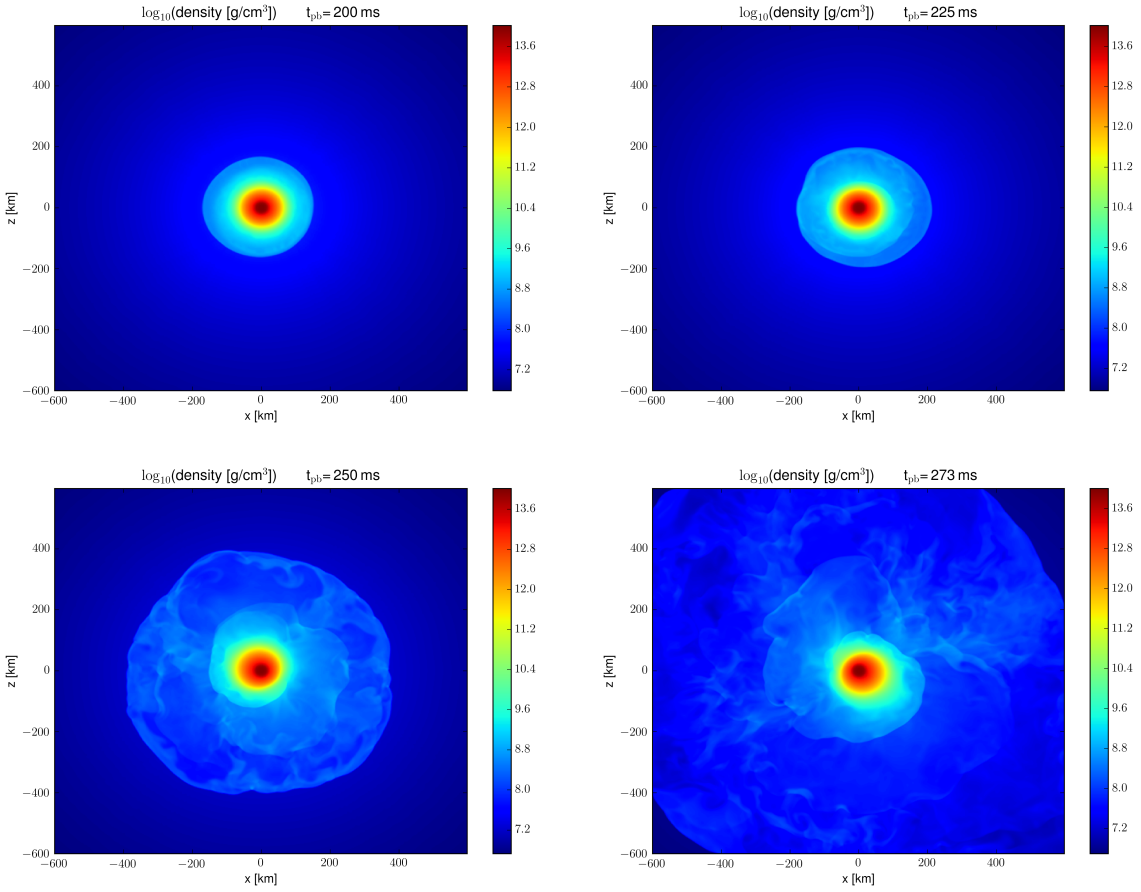

Fig. 6.10.: Density sheets (x and z axes in units of km and density in units of g/cm^3) for the time steps (from top left to bottom right) 200 ms, 225 ms, 250 ms, and 273 ms post bounce. At first the stalled shock is spherical and later develops a spiral structure.

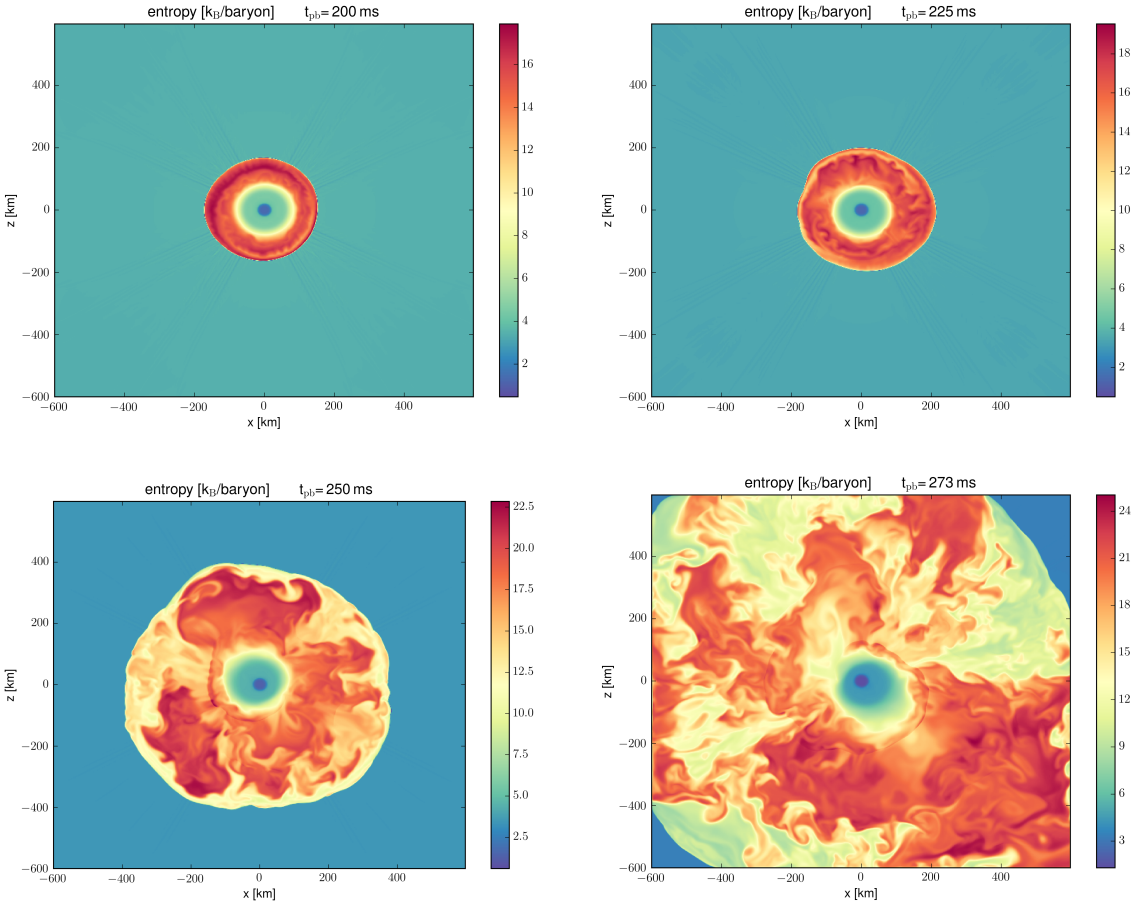

Fig. 6.11.: Entropy sheets (x and z axes in units of km and entropy in units of g/cm^3) for the time steps (from top left to bottom right) 200 ms, 225 ms, 250 ms, and 273 ms post bounce. The same times are shown as for the density.

7 Summary and Outlook

> *What we call the beginning is often the end.*
> *And to make and end is to make a beginning.*
> *The end is where we start from.*
>
> **— T.S. Eliot**
> Little Gidding

We have investigated the properties of neutrino-driven CCSNe with the PUSH method in spherically symmetric and ELEPHANT in three-dimensional simulations. CCSNe and the underlying explosion mechanism(s) are complex subjects that have been investigated for many years. To this day, they are not completely understood. In this thesis we use efficient spherically symmetric simulations to study global properties of neutrino-driven CCSNe. We are interested in the explodability as well as the explosion properties of these extremely energetic explosions for a variety of pre-explosion models across a wide range of ZAMS mass and identify trends of the explosion properties with progenitor properties.

We fitted PUSH to reproduce SN 1987A and calibrated the method with a dependence on compactness to observational data of other CCSNe for a broader range of ZAMS mass. Tracers created from the PUSH models were post-processed with the networks WINNET and CFNET. The calibrated PUSH method was applied to the solar metallicity progenitor samples of [40, 41] which in total include pre-explosion models with ZAMS masses between 10.8 and 120 $M_\odot$. This resulted in predictions of explosion energies, remnant masses, nucleosynthesis yields and the progenitor-remnant connection in general. The ELEPHANT code that formed a different part of this thesis has been used to compare the one-dimensional simulations with multi-dimensional results to get clues for possible choices of the PUSH parameters.

The calibration of the PUSH method and the subsequent investigation of the outcome of neutrino-driven CCSNe in numerical simulations has led to interesting results. We have seen that the resulting explosion energies and ^{56}Ni ejecta are in good agreement with observational data of CCSNe and obtain a progenitor-remnant connection which indicates which progenitors successfully explode and form a NS and which progenitors end their life as a BH. We find that the compactness is a better indicator of the expected outcome (explodability) than the ZAMS mass of the progenitor models. For ZAMS masses in the vicinity of ~25 $M_\odot$, we find a region of BH formation (non-exploding models) for our standard calibration and our second (more pessimistic) calibration. Above ~30 $M_\odot$ we find that fewer black holes are formed for our standard calibration (overall more for the progenitor sample of [41] than for the sample of [40]) than for the second calibration. For the second calibration we also obtain BH forming models below 20 $M_\odot$. The standard calibration is in good agreement with observational properties and was used to investigate the explosion properties and nucleosynthesis yields of neutrino-driven CCSNe across the ZAMS mass range.

The explosion energy, the remnant mass and the explosion time are presented as functions of compactness. We have found that models with similar compactness can have different explosion properties (which is visible in explosion energy in particular). For some models this degeneracy in compactness can be broken with the carbon-oxygen core mass of the progenitor star. We obtained linear trends with compactness for the amount of ejected ^{44}Ti and ^{56}Ni (symmetric $N = Z$ isotopes). The amount of ejected ^{57}Ni and ^{58}Ni do not show such a simple correlation with compactness. The abundances of these isotopes depend on the electron fraction of the ejected material.

We find that our predicted NS and BH birth mass distributions are broadly consistent with observations. The investigated solar metallicity samples do not contain progenitors with masses that exceed ~17 $M_\odot$ at collapse. Thus, we do not find BHs with masses that exceed this limit for solar metallicity. In preliminary results for lower metallicity progenitor star samples, we find that progenitors above ~30 $M_\odot$ ZAMS mass form BHs. These progenitors experience less mass loss and therefore these samples result in more massive BHs than the solar metallicity progenitor samples.

In the future, the PUSH method can be further refined by taking into account other dependencies besides compactness, e.g., carbon-oxygen core mass and mass accretion at the shock front. Also, by extending the initial comparison with multi-dimensional simulations one could try to mimic the neutrino heating rates of these simulations more accurate by other spatial and temporal dependencies of the extra heating provided by PUSH and compare the shock radii and temporal evolution of the simulations in further inves-

tigations. Furthermore, the used approximate network can be extended or a more elaborate network can be implemented in the setup of the simulations. This would simplify the non-NSE treatment immensely. As has been outlined in chapter 5, the simulations performed with the PUSH method can be extended to other progenitor sets in the future, e.g., to different metallicities to investigate the properties and outcomes of CCSNe for these models as well. We have already presented first preliminary results. Another possibility would be the study of solar metallicity progenitor samples of different groups to investigate the effects of the uncertainties in the progenitor models for the same metallicity and together with observational data possibly find constraints for the progenitor models. A straightforward next step after the finding of the results for nucleosynthesis yields with PUSH would be the application in simulations of the galactic chemical evolution. The prediction of explodability and ejected nucleosynthesis yields can be used in these computations to check the validity of the models as well as to gain deeper understanding of the contribution of CCSNe to this process. With complete predictions of different metallicity progenitors the corresponding metallicity dependent GCE can be investigated. This can be used as a testing case for the PUSH method as well as the galactic chemical evolution simulations. It would also be possible to investigate the effects of different equations of state on the explodability and the resulting remnant-masses. The results of such studies can be compared with observations. There are many possibilities, but in my opinion a fruitful and logical first step would be to investigate different progenitor samples with the PUSH method, especially with different metallicities to get a dependence of nucleosynthesis yields and explodability on metallicity to investigate their implications on the galactic chemical enrichment.

Appendix A

> *Wo sich berühren Raum und Zeit,*
> *Am Kreuzpunkt der Unendlichkeit –*
> *Wie Windeswehen in gemalten Bäumen*
> *Umrauscht uns diese Welt, die wir nur träumen.*
>
> — **Maša Kaléko**

A.1 Typical Neutrino Cross-Section

Two opacity contributions for neutrinos (mentioned in section 2.2) are

(1) Free nucleon scattering: $\nu + n \to \nu + n, \quad \nu + p \to \nu + p$

(2) Coherent scattering by heavy nuclei: $\nu + (Z, A) \to \nu + (Z, A)$,

which are mediated by the Z boson. The total cross section (measured in the matter rest frame) of free neutron scattering (with $E_\nu \ll m_n c^2$) is given by [43]

$$\sigma_n \approx \frac{1}{4}\sigma_0 \left(\frac{E_\nu}{m_e c^2}\right)^2, \tag{A.1}$$

and the total cross section for coherent scattering by heavy nuclei is given by [43] (see also [14])

$$\sigma_{A,\mathrm{coh}} \approx \frac{1}{16}\sigma_0 \left(\frac{E_\nu}{m_e c^2}\right)^2 A^2 \left[1 - \frac{Z}{A} + (4\sin^2\theta_w - 1)\frac{Z}{A}\right], \tag{A.2}$$

with $E_\nu \ll 300 A^{-1/3}\mathrm{MeV}$, where θ_w is the Weinberg angle. Both cross sections are proportional to the quantity σ_o (typical neutrino cross-section) given by [43]

$$\sigma_0 \equiv \frac{4}{\pi}\left(\frac{\hbar}{m_e c}\right)^{-4}\left(\frac{G_F}{m_e c^2}\right)^2 \approx 1.76 \times 10^{-44}\mathrm{cm}^2. \tag{A.3}$$

A.2 A Criterion for Convection

In the following, we briefly introduce a criterion for convection according to [281]. A fluid is in mechanical equilibrium (in a gravitational field with potential ϕ) when the equation $\partial p/\partial r$=-$\rho\partial\phi/\partial r$ holds. This condition for mechanical equilibrium can be fulfilled without the temperature being constant in the fluid. In such a situation the equilibrium is not guaranteed be stable. If the equilibrium is unstable fluid movements (convection) appear and lead to mixing that equalizes the temperature in the fluid. For a mechanical equilibrium is to be stable the condition for the absence of convection needs to be satisfied. The condition for the absence of convection is given below.

A fluid element is at position r with the specific volume $V(p,s)$, where p and s are the equilibrium values for pressure and entropy at this location. When this fluid element is displaced upwards adiabatically by a distance h, its specific volume becomes $V(p\prime,s)$, with $p\prime$ being the pressure at position $r+h$. For the system to be stable the emerging force on the fluid element has to be in the direction of the original position. Thus, the fluid element has to be heavier than the fluid element which it displaces in the new position. The specific volume of the fluid element that is displaced is $V(p\prime,s\prime)$, where $s\prime$ denotes the equilibrium entropy at the position $r+h$. We therefore have the criterion of stability given by

$$V(p\prime,s\prime)-V(p\prime,s)>0. \tag{A.4}$$

We expand this expression in powers of $\mathrm{d}s=s\prime-s=(\mathrm{d}s/\mathrm{d}r)h$ and arrive at

$$\left(\frac{\partial V}{\partial s}\right)_p\frac{\mathrm{d}s}{\mathrm{d}r}>0. \tag{A.5}$$

By using the thermodynamical relation

$$\left(\frac{\partial V}{\partial s}\right)=\frac{T}{c_p}\left(\frac{\partial V}{\partial T}\right)_p, \tag{A.6}$$

where c_p denotes the specific heat capacity at constant pressure (which is always non-negative, as is the temperature). Thus, we get the relation

$$\left(\frac{\partial V}{\partial T}\right)_p\frac{\mathrm{d}s}{\mathrm{d}r}>0. \tag{A.7}$$

Since most materials expand when heated we use

$$\left(\frac{\partial V}{\partial T}\right)_p>0, \tag{A.8}$$

and get the criterion for stability (no convection)

$$\frac{\mathrm{d}s}{\mathrm{d}r} > 0. \tag{A.9}$$

This means that entropy has to increase with height for layers of the fluid to be stable against convection. Without derivation, we also list the Ledoux criterion for convective stability. Negative entropy gradients $\mathrm{d}s/\mathrm{d}r$ are unstable according to the Ledoux criterion [44, 279]

$$\left(\frac{\partial\rho}{\partial s}\right)_{Y_e,p} \frac{\mathrm{d}s}{\mathrm{d}r} + \left(\frac{\partial\rho}{\partial Y_e}\right)_{s,p} \frac{\mathrm{d}Y_e}{\mathrm{d}r} > 0, \tag{A.10}$$

which defines growth conditions for convection and Rayleigh-Taylor structures.

A.3 The Initial Mass Function

The initial mass function is an empirically found distribution function that describes the number densities of stars with different initial masses in a given population of stars [254–256]. It is not easy to find an exact description of the IMF that is connected to the complex process of stellar formation and the parameterizations of the function vary for different population types (e.g. galaxies, dwarf galaxies, globular clusters etc.) [255]. In general, inside a given stellar population, the abundance of low-mass stars is greater than the abundance of high-mass stars since they are formed in larger numbers and have a longer lifetime on the main sequence. The IMF was first introduced by E. Salpeter [254] and was intended to give an easy way of parameterizing the relative numbers of stars as a function of their ZAMS masses. There are also different parameterizations (see e.g. [255, 259]) that refine the IMF, but for massive stars above 10 $\mathrm{M}_\odot$ the parametrization of the IMF $\xi(m)$ given by [254] is sufficient. We briefly introduce the IMF according to [7] after [254].

For the mass interval relevant for the presented neutron star mass distribution analysis (and available to us in the form of progenitors) the lower limit is given by the mass M_{min}=10.8$\mathrm{M}_\odot$ or M_{min}=12.0$\mathrm{M}_\odot$, which represents the lightest progenitors in the used samples. Of course, some lighter progenitors of CCSN and electron capture SNe would complete the picture, since they can also contribute to the neutron star population and can be added in a future study. The considered massive stars have roughly a lifetime of the order of $\sim 10^6 - 10^7$ years, which is much smaller than the age of the Milky Way (which is of the order of $\sim 10^9 - 10^{10}$). Thus, we assume that for the presented study we can neglect temporal effects (constant star formation rate) and in a first approximation

directly apply the IMF to the remnant mass distribution. The IMF enables estimations of the numbers of stars within a mass range,

$$\frac{\mathrm{d}N}{\mathrm{d}m} = \frac{\xi(m)}{m} \propto m^{-(\alpha+1)}, \tag{A.11}$$

where $m = \mathrm{M}/\mathrm{M}_\odot$ (stellar mass in the units of solar masses)[1]. The total mass bound inside stars with initial masses between m_1 and m_2 is given by

$$M(m_1, m_2) = \int_{m_1}^{m_2} \xi(m)\mathrm{d}m \tag{A.12}$$

and the total number of stars in this range is

$$N(m_1, m_2) = \int_{m_1}^{m_2} \frac{\xi(m)}{m}\mathrm{d}m. \tag{A.13}$$

Using $\xi(m) = \xi_0 m^{-\alpha}$, these equations yield the following results

$$M(m_1, m_2) = \frac{\xi_0(m_1^{-\alpha+1} - m_2^{-\alpha+1})}{\alpha - 1}, \tag{A.14}$$

$$N(m_1, m_2) = \frac{\xi_0(m_1^{-\alpha} - m_2^{-\alpha})}{\alpha}. \tag{A.15}$$

The normalized probability that a star in a given population between the masses m_a and m_b is in the mass interval $[m_i, m_{i+1}]$, with $m_a \leq m_i < m_{i+1} \leq m_b$, is given by

$$P(m_i, m_{i+1}) = \frac{N(m_i, m_{i+1})}{N(m_a, m_b)}. \tag{A.16}$$

In this form all the constant prefactors of the $\xi(M)$ function cancel and for a given value of the parameter α for each mass interval a simple expression of $P(m_i, m_{i+1})$ is found:

$$P(m_i, m_{i+1}) = \frac{m_i^{-\alpha} - m_{i+1}^{-\alpha}}{m_a^{-\alpha} - m_b^{-\alpha}}. \tag{A.17}$$

We use the canonical Salpeter slope $\alpha = 1.35$ to describe the IMF above $M \sim 10\mathrm{M}_\odot$ [254, 255, 259].

[1] In the literature the IMF is often found in a power-law of the form (Salpeter [254] introduced the IMF in this form) $\phi(\log_{10}(m)) = \dfrac{\mathrm{d}N}{\mathrm{d}(\log_{10}(m))} \propto m^{-\alpha}$ [254, 255].

Bibliography

[1] H. A. Bethe. Supernova mechanisms. *Reviews of Modern Physics*, 62:801–866, October 1990. doi: 10.1103/RevModPhys.62.801.

[2] D. Arnett. *Supernovae and nucleosynthesis: an investigation of the history of matter, from the big bang to the present*. Princeton University Press, Princeton, New Jersey.

[3] C. Iliadis. *Nuclear Physics of Stars*. Wiley-VCH Verlag, 2007.

[4] P. Podsiadlowski. The progenitor of SN 1987 A. *Publications of the Astronomical Society of the Pacific*, 104:717–729, September 1992. doi: 10.1086/133043.

[5] R. M. Bionta, G. Blewitt, C. B. Bratton, D. Casper, and A. Ciocio. Observation of a neutrino burst in coincidence with supernova 1987A in the Large Magellanic Cloud. *Physical Review Letters*, 58:1494–1496, April 1987. doi: 10.1103/PhysRevLett.58.1494.

[6] K. Hirata, T. Kajita, M. Koshiba, M. Nakahata, and Y. Oyama. Observation of a neutrino burst from the supernova SN1987A. *Physical Review Letters*, 58:1490–1493, April 1987. doi: 10.1103/PhysRevLett.58.1490.

[7] W. D. Arnett, J. N. Bahcall, R. P. Kirshner, and S. E. Woosley. Supernova 1987A. ARA&A, 27:629–700, 1989. doi: 10.1146/annurev.aa.27.090189.003213.

[8] A. Burrows. Supernova explosions in the Universe. *Nature*, 403:727–733, February 2000. doi: 10.1038/35001501.

[9] W. Baade and F. Zwicky. On Super-novae. *Proceedings of the National Academy of Science*, 20:254–259, May 1934. doi: 10.1073/pnas.20.5.254.

[10] W. Baade and F. Zwicky. Cosmic Rays from Super-Novae. *Proceedings of the National Academy of Science*, 20:259–263, may 1934.

[11] J. Chadwick. Possible Existence of a Neutron. *Nature*, 129:312, February 1932. doi: 10.1038/129312a0.

[12] J. Chadwick. The Existence of a Neutron. *Proceedings of the Royal Society of London Series A*, 136:692–708, June 1932. doi: 10.1098/rspa.1932.0112.

[13] C. Giunti and W. K. Chung. *Fundamentals of Neutrino Physics and Astrophysics*. Oxford University Press, 2007.

[14] T. Padmanabhan. *Theoretical Astrophysics, Volume 2: Stars and Stellar Systems*. April 2001.

[15] D. Branch and G. A. Tammann. Type IA supernovae as standard candles. *Ann. Rev. Astron. Astrophys.*, 30:359–389, 1992. doi: 10.1146/annurev.aa.30.090192.002043.

[16] A. G. Riess, A. V. Filippenko, P. Challis, A. Clocchiatti, A. Diercks, P. M. Garnavich, R. L. Gilliland, C. J. Hogan, S. Jha, R. P. Kirshner, B. Leibundgut, M. M. Phillips, D. Reiss, B. P. Schmidt, R. A. Schommer, R. C. Smith, J. Spyromilio, C. Stubbs, N. B. Suntzeff, and J. Tonry. Observational Evidence from Supernovae for an Accelerating Universe and a Cosmological Constant. *Astron. J.*, 116:1009–1038, September 1998. doi: 10.1086/300499.

[17] S. Perlmutter, G. Aldering, G. Goldhaber, R. A. Knop, P. Nugent, P. G. Castro, S. Deustua, S. Fabbro, A. Goobar, D. E. Groom, I. M. Hook, A. G. Kim, M. Y. Kim, J. C. Lee, N. J. Nunes, R. Pain, C. R. Pennypacker, R. Quimby, C. Lidman, R. S. Ellis, M. Irwin, R. G. McMahon, P. Ruiz-Lapuente, N. Walton, B. Schaefer, B. J. Boyle, A. V. Filippenko, T. Matheson, A. S. Fruchter, N. Panagia, H. J. M. Newberg, W. J. Couch, and T. S. C. Project. Measurements of Ω and Λ from 42 High-Redshift Supernovae. *Astrophys. J.*, 517:565–586, June 1999. doi: 10.1086/307221.

[18] A. Heger, C. L. Fryer, S. E. Woosley, N. Langer, and D. H. Hartmann. How Massive Single Stars End Their Life. ApJ, 591:288–300, July 2003. doi: 10.1086/375341.

[19] Bruno Leibundgut and Nicholas B. Suntzeff. Optical light curves of supernovae. *Lect. Notes Phys.*, 598:77, 2003. doi: 10.1007/3-540-45863-8_6.

[20] R. G. Eastman, B. P. Schmidt, and R. Kirshner. The Atmospheres of Type II Supernovae and the Expanding Photosphere Method. ApJ, 466:911, August 1996. doi: 10.1086/177563.

[21] S. Blinnikov, P. Lundqvist, O. Bartunov, K. Nomoto, and K. Iwamoto. Radiation Hydrodynamics of SN 1987A. I. Global Analysis of the Light Curve for the First 4 Months. ApJ, 532:1132–1149, April 2000. doi: 10.1086/308588.

[22] I. R. Seitenzahl, F. X. Timmes, and G. Magkotsios. The Light Curve of SN 1987A Revisited: Constraining Production Masses of Radioactive Nuclides. ApJ, 792:10, September 2014. doi: 10.1088/0004-637X/792/1/10.

[23] T. Shigeyama and K. Nomoto. Theoretical light curve of SN 1987A and mixing of hydrogen and nickel in the ejecta. ApJ, 360:242–256, September 1990. doi: 10.1086/169114.

[24] S. E. Woosley. SN 1987A - After the peak. ApJ, 330:218–253, July 1988. doi: 10.1086/166468.

[25] C. Fransson and C. Kozma. Radioactivities and nucleosynthesis in SN 1987A. New A Rev., 46:487–492, July 2002. doi: 10.1016/S1387-6473(02)00188-4.

[26] S. E. Boggs, F. A. Harrison, H. Miyasaka, B. W. Grefenstette, A. Zoglauer, C. L. Fryer, S. P. Reynolds, D. M. Alexander, H. An, D. Barret, F. E. Christensen, W. W. Craig, K. Forster, P. Giommi, C. J. Hailey, A. Hornstrup, T. Kitaguchi, J. E. Koglin, K. K. Madsen, P. H. Mao, K. Mori, M. Perri, M. J. Pivovaroff, S. Puccetti, V. Rana, D. Stern, N. J. Westergaard, and W. W. Zhang. ^{44}Ti gamma-ray emission lines from SN1987A reveal an asymmetric explosion. *Science*, 348:670–671, May 2015. doi: 10.1126/science.aaa2259.

[27] F. Mannucci, M. Della Valle, N. Panagia, E. Cappellaro, G. Cresci, R. Maiolino, A. Petrosian, and M. Turatto. The supernova rate per unit mass. A&A, 433:807–814, April 2005. doi: 10.1051/0004-6361:20041411.

[28] G. Bruno, W. Fulgione, A. Molinario, and C. Vigorito and. The core collapse supernova rate from 24 years of data of the large volume detector. *Journal of Physics: Conference Series*, 888:012256, sep 2017. doi: 10.1088/1742-6596/888/1/012256. URL https://doi.org/10.1088%2F1742-6596%2F888%2F1%2F012256.

[29] Martin J. Rees Ray J. Stoneham (eds.) Robert P. Kirshner (auth.). *Supernovae: A Survey of Current Research: Proceedings of the NATO Advanced Study Institute held at Cambridge, U.K., June 29–July 10, 1981*. NATO Advanced Study Institutes Series 90. Springer Netherlands, 1 edition, 1982. ISBN 978-94-009-7878-2,978-94-009-7876-8. URL `http://gen.lib.rus.ec/book/index.php?md5=C73F5390277834771C77E767D7DECA25`.

[30] K. U. Ratnatunga and S. van den Bergh. The rate of stellar collapses in the galaxy. ApJ, 343:713–717, August 1989. doi: 10.1086/167743.

[31] R. A. Muller, H. J. M. Newberg, C. R. Pennypacker, S. Perlmutter, T. P. Sasseen, and C. K. Smith. High rate for Type IC supernovae. ApJ, 384:L9–L13, January 1992. doi: 10.1086/186251.

[32] E. Cappellaro, M. Turatto, S. Benetti, D. Y. Tsvetkov, O. S. Bartunov, and I. N. Makarova. The Rate of Supernovae - Part Two - the Selection Effects and the Frequencies Per Unit Blue Luminosity. A&A, 273:383, June 1993.

[33] G. A. Tammann, W. Loeffler, and A. Schroeder. The Galactic supernova rate. ApJS, 92:487–493, June 1994. doi: 10.1086/192002.

[34] R. G. Strom. 'Guest stars', sample completeness and the local supernova rate. A&A, 288:L1–L4, August 1994.

[35] E. Cappellaro, M. Turatto, D. Y. Tsvetkov, O. S. Bartunov, C. Pollas, R. Evans, and M. Hamuy. The rate of supernovae from the combined sample of five searches. A&A, 322:431–441, June 1997.

[36] F. X. Timmes, R. Diehl, and D. H. Hartmann. Constraints from ^{26}Al Measurements on the Galaxy's Recent Global Star Formation Rate and Core-Collapse Supernovae Rate. ApJ, 479:760–763, April 1997.

[37] P. M. Dragicevich, D. G. Blair, and R. R. Burman. Why are supernovae in our Galaxy so frequent? MNRAS, 302:693–699, February 1999. doi: 10.1046/j.1365-8711.1999.02145.x.

[38] Enrico Cappellaro and Massimo Turatto. Supernova types and rates. *Astrophys. Space Sci. Libr.*, 264:199, 2001. doi: 10.1007/978-94-015-9723-4_16.

[39] B. C. Reed. New Estimates of the Solar-Neighborhood Massive Star Birthrate and the Galactic Supernova Rate. AJ, 130:1652–1657, October 2005. doi: 10.1086/444474.

[40] S. E. Woosley, A. Heger, and T. A. Weaver. The evolution and explosion of massive stars. *Reviews of Modern Physics*, 74:1015–1071, November 2002. doi: 10.1103/RevModPhys.74.1015.

[41] S. E. Woosley and A. Heger. Nucleosynthesis and remnants in massive stars of solar metallicity. Phys. Rep., 442:269–283, April 2007. doi: 10.1016/j.physrep.2007.02.009.

[42] E. M. Burbidge, G. R. Burbidge, W. A. Fowler, and F. Hoyle. Synthesis of the Elements in Stars. *Reviews of Modern Physics*, 29:547–650, 1957. doi: 10.1103/RevModPhys.29.547.

[43] S. L. Shapiro and S. A. Teukolsky. *Black holes, white dwarfs, and neutron stars: The physics of compact objects*. 1983.

[44] H.-T. Janka. Explosion Mechanisms of Core-Collapse Supernovae. *Annual Review of Nuclear and Particle Science*, 62:407–451, November 2012. doi: 10.1146/annurev-nucl-102711-094901.

[45] H.-T. Janka, T. Melson, and A. Summa. Physics of Core-Collapse Supernovae in Three Dimensions: A Sneak Preview. *Annual Review of Nuclear and Particle Science*, 66:341–375, October 2016. doi: 10.1146/annurev-nucl-102115-044747.

[46] K. Nomoto, C. Kobayashi, and N. Tominaga. Nucleosynthesis in Stars and the Chemical Enrichment of Galaxies. ARA&A, 51:457–509, August 2013. doi: 10.1146/annurev-astro-082812-140956.

[47] F.-K Thielemann, J. J. Cowan, and Truran J. W. *Nuclear Evolution of the Universe*. The University of Chicago Press. In preparation.

[48] G. Audi, A. H. Wapstra, and C. Thibault. The AME2003 atomic mass evaluation (I). *Nuclear Physics*, A729, 129, 2003.

[49] G. Audi, A. H. Wapstra, and C. Thibault. AME2003 atomic mass evaluation (II). *Nuclear Physics*, A729, 337, 2003.

[50] M. Limongi, O. Straniero, and A. Chieffi. Massive Stars in the Range 13-25 M_{solar}: Evolution and Nucleosynthesis. II. The Solar Metallicity Models. ApJS, 129:625–664, August 2000. doi: 10.1086/313424.

[51] W. R. Hix and F.-K. Thielemann. Computational methods for nucleosynthesis and nuclear energy generation. *Journal of Computational and Applied Mathematics*, 109:321–351, September 1999.

[52] S. Chandrasekhar. *An introduction to the study of stellar structure*. 1939.

[53] A. H. Wapstra and K. Bos. 1975 Mass Predictions: A 1975 Midstream Atomic Mass Evaluation. *Atomic Data and Nuclear Data Tables*, 17:474, 1976. doi: 10.1016/0092-640X(76)90039-5.

[54] P. Goldreich and S. V. Weber. Homologously collapsing stellar cores. ApJ, 238:991–997, June 1980. doi: 10.1086/158065.

[55] H.-T. Janka, K. Langanke, A. Marek, G. Martínez-Pinedo, and B. Müller. Theory of core-collapse supernovae. *Phys. Rept.*, 442:38–74, April 2007. doi: 10.1016/j.physrep.2007.02.002.

[56] M. Liebendörfer, O. E. B. Messer, A. Mezzacappa, S. W. Bruenn, C. Y. Cardall, and F.-K. Thielemann. A Finite Difference Representation of Neutrino Radiation Hydrodynamics in Spherically Symmetric General Relativistic Spacetime. ApJS, 150:263–316, January 2004. doi: 10.1086/380191.

[57] S. A. Colgate and R. H. White. The Hydrodynamic Behavior of Supernovae Explosions. *ApJ*, 143:626, March 1966. doi: 10.1086/148549.

[58] H. A. Bethe and J. R. Wilson. Revival of a stalled supernova shock by neutrino heating. *ApJ*, 295:14–23, August 1985. doi: 10.1086/163343.

[59] N. A. Gentile, M. B. Aufderheide, G. J. Mathews, F. D. Swesty, and G. M. Fuller. The QCD phase transition and supernova core collapse. *ApJ*, 414:701–711, September 1993. doi: 10.1086/173116.

[60] I. Sagert, T. Fischer, M. Hempel, G. Pagliara, J. Schaffner-Bielich, A. Mezzacappa, F.-K. Thielemann, and M. Liebendörfer. Signals of the QCD Phase Transition in Core-Collapse Supernovae. *Physical Review Letters*, 102(8):081101, February 2009. doi: 10.1103/PhysRevLett.102.081101.

[61] C. Winteler, R. Käppeli, A. Perego, A. Arcones, N. Vasset, N. Nishimura, M. Liebendörfer, and F.-K. Thielemann. Magnetorotationally Driven Supernovae as the Origin of Early Galaxy r-process Elements? ApJ, 750:L22, May 2012. doi: 10.1088/2041-8205/750/1/L22.

[62] D. L. Meier, R. I. Epstein, W. D. Arnett, and D. N. Schramm. Magnetohydrodynamic phenomena in collapsing stellar cores. *ApJ*, 204:869–878, March 1976. doi: 10.1086/154235.

[63] Adam Burrows, Eli Livne, Luc Dessart, Christian Ott, and Jeremiah Murphy. A new mechanism for core-collapse supernova explosions. *Astrophys. J.*, 640:878–890, 2006. doi: 10.1086/500174.

[64] Adam Burrows, E. Livne, L. Dessart, C. D. Ott, and J. Murphy. Features of the Acoustic Mechanism of Core-Collapse Supernova Explosions. *Astrophys. J.*, 655:416–433, 2007. doi: 10.1086/509773.

[65] M. Shibata. Numerical Realtivity: 100 years of general relativity Vol. 1. 2016.

[66] H.-T. Janka. Conditions for shock revival by neutrino heating in core-collapse supernovae. *Astron. Astrophys.*, 368:527–560, March 2001. doi: 10.1051/0004-6361:20010012.

[67] H. A. Bethe. SN 1987A - an empirical and analytic approach. ApJ, 412:192–202, July 1993. doi: 10.1086/172911.

[68] H. A. Bethe. Supernova Shock. VIII. ApJ, 490:765–771, December 1997. doi: 10.1086/304901.

[69] J. M. LeBlanc and J. R. Wilson. A Numerical Example of the Collapse of a Rotating Magnetized Star. ApJ, 161:541, August 1970. doi: 10.1086/150558.

[70] A. Burrows, L. Dessart, E. Livne, C. D. Ott, and J. Murphy. Simulations of Magnetically Driven Supernova and Hypernova Explosions in the Context of Rapid Rotation. ApJ, 664:416–434, July 2007. doi: 10.1086/519161.

[71] P. Mösta, S. Richers, C. D. Ott, R. Haas, A. L. Piro, K. Boydstun, E. Abdikamalov, C. Reisswig, and E. Schnetter. Magnetorotational Core-collapse Supernovae in Three Dimensions. ApJ, 785:L29, April 2014. doi: 10.1088/2041-8205/785/2/L29.

[72] B. Wehmeyer, M. Pignatari, and F.-K. Thielemann. Galactic evolution of rapid neutron capture process abundances: the inhomogeneous approach. MNRAS, 452: 1970–1981, September 2015. doi: 10.1093/mnras/stv1352.

[73] A. Burrows, E. Livne, L. Dessart, C. D. Ott, and J. Murphy. A New Mechanism for Core-Collapse Supernova Explosions. ApJ, 640:878–890, April 2006. doi: 10.1086/500174.

[74] A. Burrows, E. Livne, L. Dessart, C. D. Ott, and J. Murphy. Features of the Acoustic Mechanism of Core-Collapse Supernova Explosions. ApJ, 655:416–433, January 2007. doi: 10.1086/509773.

[75] N. N. Weinberg and E. Quataert. Non-linear saturation of g-modes in proto-neutron stars: quieting the acoustic engine. MNRAS, 387:L64–L68, June 2008. doi: 10.1111/j.1745-3933.2008.00486.x.

[76] T. Fischer, I. Sagert, G. Pagliara, M. Hempel, J. Schaffner-Bielich, T. Rauscher, F.-K. Thielemann, R. Käppeli, G. Martínez-Pinedo, and M. Liebendörfer. Core-collapse Supernova Explosions Triggered by a Quark-Hadron Phase Transition During the Early Post-bounce Phase. ApJS, 194:39, June 2011. doi: 10.1088/0067-0049/194/2/39.

[77] John M. Blondin and Anthony Mezzacappa. Pulsar spins from an instability in the accretion shock of supernovae. *Nature*, 445:58, 2007. doi: 10.1038/nature05428.

[78] F. Hanke, B. Müller, A. Wongwathanarat, A. Marek, and H.-T. Janka. SASI Activity in Three-dimensional Neutrino-hydrodynamics Simulations of Supernova Cores. ApJ, 770:66, June 2013. doi: 10.1088/0004-637X/770/1/66.

[79] I. Tamborra, F. Hanke, H.-T. Janka, B. Müller, G. G. Raffelt, and A. Marek. Self-sustained Asymmetry of Lepton-number Emission: A New Phenomenon during the Supernova Shock-accretion Phase in Three Dimensions. ApJ, 792:96, September 2014. doi: 10.1088/0004-637X/792/2/96.

[80] M. Asplund, N. Grevesse, and A. J. Sauval. The Solar Chemical Composition. In III T. G. Barnes and F. N. Bash, editors, *Cosmic Abundances as Records of Stellar Evolution and Nucleosynthesis*, volume 336 of *Astronomical Society of the Pacific Conference Series*, page 25, September 2005.

[81] C. Winteler. *Light Element Production in the Big Bang and the Synthesis of Heavy Elements in 3D MHD Jets from Core-Collapse Supernovae.* PhD thesis, 2013.

[82] A. G. W. Cameron. Nuclear Reactions in Stars and Nucleogenesis. PASP, 69:201, June 1957. doi: 10.1086/127051.

[83] A. G. W. Cameron. Stellar Evolution, Nuclear Astrophysics, and Nucleogenesis. Report CRL-41, Chalk River, 1957.

[84] W. A. Fowler, G. R. Caughlan, and B. A. Zimmerman. Thermonuclear Reaction Rates. *Ann. Rev. Astron. Astrophys.*, 5:525, 1967. doi: 10.1146/annurev.aa.05.090167.002521.

[85] W. A. Fowler, G. R. Caughlan, and B. A. Zimmerman. Thermonuclear Reaction Rates, II. *Ann. Rev. Astron. Astrophys.*, 13:69, 1975. doi: 10.1146/annurev.aa.13.090175.000441.

[86] J. M. Blatt and V. F. Weisskopf. *Theoretical Nuclear Physics.* Wiley, New York, 1952.

[87] A. Perego, M. Hempel, C. Fröhlich, K. Ebinger, M. Eichler, J. Casanova, M. Liebendörfer, and F.-K. Thielemann. PUSHing Core-collapse Supernovae to Explosions in Spherical Symmetry I: the Model and the Case of SN 1987A. ApJ, 806:275, June 2015. doi: 10.1088/0004-637X/806/2/275.

[88] Kevin Ebinger, Sanjana Curtis, Carla Fröhlich, Matthias Hempel, Albino Perego, Matthias Liebendörfer, and Friedrich-Karl Thielemann. PUSHing core-collapse supernovae to explosions in spherical symmetry. II. explodability and remnant

properties. *The Astrophysical Journal*, 870(1):1, dec 2018. doi: 10.3847/1538-4357/aae7c9. URL https://doi.org/10.3847%2F1538-4357%2Faae7c9.

[89] T. Fischer, S. C. Whitehouse, A. Mezzacappa, F.-K. Thielemann, and M. Liebendörfer. Protoneutron star evolution and the neutrino-driven wind in general relativistic neutrino radiation hydrodynamics simulations. A&A, 517:A80, July 2010. doi: 10.1051/0004-6361/200913106.

[90] L. Hüdepohl, B. Müller, H.-T. Janka, A. Marek, and G. G. Raffelt. Neutrino Signal of Electron-Capture Supernovae from Core Collapse to Cooling. *Physical Review Letters*, 104(25):251101, June 2010. doi: 10.1103/PhysRevLett.104.251101.

[91] M. Liebendörfer, A. Mezzacappa, and F.-K. Thielemann. Conservative general relativistic radiation hydrodynamics in spherical symmetry and comoving coordinates. *Phys. Rev. D*, 63(10):104003, May 2001. doi: 10.1103/PhysRevD.63.104003.

[92] M. Liebendörfer, S. Rosswog, and F.-K. Thielemann. An Adaptive Grid, Implicit Code for Spherically Symmetric, General Relativistic Hydrodynamics in Comoving Coordinates. *ApJs*, 141:229–246, July 2002. doi: 10.1086/339872.

[93] M. Liebendörfer, S. C. Whitehouse, and T. Fischer. The Isotropic Diffusion Source Approximation for Supernova Neutrino Transport. ApJ, 698:1174–1190, June 2009. doi: 10.1088/0004-637X/698/2/1174.

[94] A. Perego, R. M. Cabezón, and R. Käppeli. An Advanced Leakage Scheme for Neutrino Treatment in Astrophysical Simulations. ApJS, 223:22, April 2016. doi: 10.3847/0067-0049/223/2/22.

[95] M. Hempel and J. Schaffner-Bielich. A statistical model for a complete supernova equation of state. *Nuclear Physics A*, 837:210–254, June 2010. doi: 10.1016/j.nuclphysa.2010.02.010.

[96] S. Typel, G. Röpke, T. Klähn, D. Blaschke, and H. H. Wolter. Composition and thermodynamics of nuclear matter with light clusters. Phys. Rev. C, 81(1):015803, January 2010. doi: 10.1103/PhysRevC.81.015803.

[97] R. A. D'Inverno. *Introducing Einstein's relativity*. 1992.

[98] C. W. Misner, K. S. Thorne, and J. A. Wheeler. *Gravitation*. 1973.

[99] U.E. Schröder. *Gravitation: Einführung in die Allgemeine Relativitätstheorie*. Verlag Harri Deutsch, 5. edition edition, 2011.

[100] Charles W. Misner and David H. Sharp. Relativistic Equations for Adiabatic, Spherically Symmetric Gravitational Collapse. *Phys. Rev.*, 136:B571–B576, Oct 1964. doi: 10.1103/PhysRev.136.B571. URL http://link.aps.org/doi/10.1103/PhysRev.136.B571.

[101] L. Smarr and Jr. J. W. York. Kinematical conditions in the construction of spacetime. *Phys. Rev. D*, 17:2529–2551, May 1978. doi: 10.1103/PhysRevD.17.2529.

[102] M. M. May and R. H. White. *Hydrodynamic Calculations of General Relativistic Collapse*, page 96. 1967.

[103] J. V. Romero, J. M. A. Ibanez, J. M. A. Marti, and J. A. Miralles. A New Spherically Symmetric General Relativistic Hydrodynamical Code. *ApJ*, 462:839, May 1996. doi: 10.1086/177198.

[104] W. H. Press, S. A. Teukolsky, W. T. Vetterling, and B. P. Flannery. *Numerical recipes in FORTRAN. The art of scientific computing*. 1992.

[105] A. Perego, S. Rosswog, R. M. Cabezón, O. Korobkin, R. Käppeli, A. Arcones, and M. Liebendörfer. Neutrino-driven winds from neutron star merger remnants. MNRAS, 443:3134–3156, October 2014. doi: 10.1093/mnras/stu1352.

[106] M. Liebendörfer. A Simple Parameterization of the Consequences of Deleptonization for Simulations of Stellar Core Collapse. ApJ, 633:1042–1051, November 2005. doi: 10.1086/466517.

[107] A. Mezzacappa and S. W. Bruenn. Stellar core collapse, A Boltzmann treatment of neutrino-electron scattering. *ApJ*, 410:740–760, June 1993. doi: 10.1086/172791.

[108] A. Mezzacappa and S. W. Bruenn. Type II supernovae and Boltzmann neutrino transport - The infall phase. *ApJ*, 405:637–668, March 1993. doi: 10.1086/172394.

[109] S. Hannestad and G. Raffelt. Supernova Neutrino Opacity from Nucleon-Nucleon Bremsstrahlung and Related Processes. ApJ, 507:339–352, November 1998. doi: 10.1086/306303.

[110] A. Bartl, C. J. Pethick, and A. Schwenk. Supernova Matter at Subnuclear Densities as a Resonant Fermi Gas: Enhancement of Neutrino Rates. *Physical Review Letters*, 113(8):081101, August 2014. doi: 10.1103/PhysRevLett.113.081101.

[111] S. W. Bruenn. Stellar core collapse, Numerical model and infall epoch. *ApJs*, 58: 771–841, August 1985. doi: 10.1086/191056.

[112] A. Mezzacappa and S. W. Bruenn. A numerical method for solving the neutrino Boltzmann equation coupled to spherically symmetric stellar core collapse. *ApJ*, 405:669–684, March 1993. doi: 10.1086/172395.

[113] S. Reddy, M. Prakash, and J. M. Lattimer. Neutrino interactions in hot and dense matter. Phys. Rev. D, 58(1):013009, July 1998. doi: 10.1103/PhysRevD.58.013009.

[114] L. F. Roberts, S. Reddy, and G. Shen. Medium modification of the charged-current neutrino opacity and its implications. Phys. Rev. C, 86(6):065803, December 2012. doi: 10.1103/PhysRevC.86.065803.

[115] G. Martínez-Pinedo, T. Fischer, A. Lohs, and L. Huther. Charged-Current Weak Interaction Processes in Hot and Dense Matter and its Impact on the Spectra of Neutrinos Emitted from Protoneutron Star Cooling. *Physical Review Letters*, 109 (25):251104, December 2012. doi: 10.1103/PhysRevLett.109.251104.

[116] Matthias Hempel. Nucleon self-energies for supernova equations of state. *Phys. Rev.*, C91:055807, 2015. doi: 10.1103/PhysRevC.91.055807.

[117] P. Möller, J. R. Nix, W. D. Myers, and W. J. Swiatecki. Nuclear Ground-State Masses and Deformations. *Atomic Data and Nuclear Data Tables*, 59:185, 1995. doi: 10.1006/adnd.1995.1002.

[118] T. Fischer, M. Hempel, I. Sagert, Y. Suwa, and J. Schaffner-Bielich. Symmetry energy impact in simulations of core-collapse supernovae. *European Physical Journal A*, 50:46, February 2014. doi: 10.1140/epja/i2014-14046-5.

[119] J. M. Lattimer and F. Douglas Swesty. A generalized equation of state for hot, dense matter. *Nuclear Physics A*, 535:331–376, December 1991. doi: 10.1016/0375-9474(91)90452-C.

[120] H. Shen, H. Toki, K. Oyamatsu, and K. Sumiyoshi. Relativistic Equation of State of Nuclear Matter for Supernova Explosion. *Progress of Theoretical Physics*, 100: 1013–1031, November 1998. doi: 10.1143/PTP.100.1013.

[121] P. B. Demorest, T. Pennucci, S. M. Ransom, M. S. E. Roberts, and J. W. T. Hessels. A two-solar-mass neutron star measured using Shapiro delay. Nature, 467:1081–1083, October 2010. doi: 10.1038/nature09466.

[122] John Antoniadis et al. A Massive Pulsar in a Compact Relativistic Binary. *Science*, 340:6131, 2013. doi: 10.1126/science.1233232.

[123] T. Plewa and E. Müller. The consistent multi-fluid advection method. A&A, 342: 179–191, February 1999.

[124] Rosemary A. Coldwell Horsfall and Alexei A. Maradudin. ZeroPoint Energy of an Electron Lattice. *Journal of Mathematical Physics*, 1(5):395–404, 1960. doi: 10.1063/1.1703670. URL `http://dx.doi.org/10.1063/1.1703670`.

[125] R. M. Cabezón, D. García-Senz, and E. Bravo. High-Temperature Combustion: Approaching Equilibrium Using Nuclear Networks. ApJS, 151:345–355, April 2004. doi: 10.1086/382352.

[126] H.-T. Janka and E. Mueller. Neutrino heating, convection, and the mechanism of Type-II supernova explosions. A&A, 306:167, February 1996.

[127] J. Nordhaus, A. Burrows, A. Almgren, and J. Bell. Dimension as a Key to the Neutrino Mechanism of Core-collapse Supernova Explosions. ApJ, 720:694–703, September 2010. doi: 10.1088/0004-637X/720/1/694.

[128] F. Hanke, A. Marek, B. Müller, and H.-T. Janka. Is Strong SASI Activity the Key to Successful Neutrino-driven Supernova Explosions? ApJ, 755:138, August 2012. doi: 10.1088/0004-637X/755/2/138.

[129] F. Hanke, B. Müller, A. Wongwathanarat, A. Marek, and H.-T. Janka. SASI Activity in Three-dimensional Neutrino-hydrodynamics Simulations of Supernova Cores. ApJ, 770:66, June 2013. doi: 10.1088/0004-637X/770/1/66.

[130] J. C. Dolence, A. Burrows, J. W. Murphy, and J. Nordhaus. Dimensional Dependence of the Hydrodynamics of Core-collapse Supernovae. ApJ, 765:110, March 2013. doi: 10.1088/0004-637X/765/2/110.

[131] S. M. Couch. On the Impact of Three Dimensions in Simulations of Neutrino-driven Core-collapse Supernova Explosions. ApJ, 775:35, September 2013. doi: 10.1088/0004-637X/775/1/35.

[132] T. Melson, H.-T. Janka, and A. Marek. Neutrino-driven Supernova of a Low-mass Iron-core Progenitor Boosted by Three-dimensional Turbulent Convection. ApJ, 801:L24, March 2015. doi: 10.1088/2041-8205/801/2/L24.

[133] J. W. Murphy and A. Burrows. Criteria for Core-Collapse Supernova Explosions by the Neutrino Mechanism. ApJ, 688:1159-1175, December 2008. doi: 10.1086/592214.

[134] T. Handy, T. Plewa, and A. Odrzywołek. Toward Connecting Core-collapse Supernova Theory with Observations. I. Shock Revival in a 15 M Blue Supergiant Progenitor with SN 1987A Energetics. ApJ, 783:125, March 2014. doi: 10.1088/0004-637X/783/2/125.

[135] L. Scheck, K. Kifonidis, H.-T. Janka, and E. Müller. Multidimensional supernova simulations with approximative neutrino transport. I. Neutron star kicks and the anisotropy of neutrino-driven explosions in two spatial dimensions. A&A, 457:963–986, October 2006. doi: 10.1051/0004-6361:20064855.

[136] A. Marek and H.-T. Janka. Delayed Neutrino-Driven Supernova Explosions Aided by the Standing Accretion-Shock Instability. ApJ, 694:664–696, March 2009. doi: 10.1088/0004-637X/694/1/664.

[137] Stephen W. Bruenn et al. The Development of Explosions in Axisymmetric AB INITIO Core-Collapse Supernova Simulations of 12-25 $M_\odot$ Stars. *Astrophys. J.*, 818(2): 123, 2016. doi: 10.3847/0004-637X/818/2/123.

[138] E. O'Connor and C. D. Ott. The Progenitor Dependence of the Pre-explosion Neutrino Emission in Core-collapse Supernovae. ApJ, 762:126, January 2013. doi: 10.1088/0004-637X/762/2/126.

[139] T. Foglizzo, L. Scheck, and H.-T. Janka. Neutrino-driven Convection versus Advection in Core-Collapse Supernovae. ApJ, 652:1436–1450, December 2006. doi: 10.1086/508443.

[140] Sanjana Curtis, Kevin Ebinger, Carla Fröhlich, Matthias Hempel, Albino Perego, Matthias Liebendörfer, and Friedrich-Karl Thielemann. PUSHing core-collapse supernovae to explosions in spherical symmetry. III. nucleosynthesis yields. *The Astrophysical Journal*, 870(1):2, dec 2018. doi: 10.3847/1538-4357/aae7d2. URL https://doi.org/10.3847%2F1538-4357%2Faae7d2.

[141] M. Ugliano, H.-T. Janka, A. Marek, and A. Arcones. Progenitor-explosion Connection and Remnant Birth Masses for Neutrino-driven Supernovae of Iron-core Progenitors. ApJ, 757:69, September 2012. doi: 10.1088/0004-637X/757/1/69.

[142] S. W. Bruenn, A. Mezzacappa, W. R. Hix, E. J. Lentz, O. E. B. Messer, E. J. Lingerfelt, J. M. Blondin, E. Endeve, P. Marronetti, and K. N. Yakunin. Axisymmetric Ab Initio Core-collapse Supernova Simulations of 12-25 M Stars. ApJ, 767:L6, April 2013. doi: 10.1088/2041-8205/767/1/L6.

[143] R. Buras, Hans-Thomas Janka, M. Rampp, and K. Kifonidis. Two-dimensional hydrodynamic core-collapse supernova simulations with spectral neutrino transport. 2. models for different progenitor stars. *Astron. Astrophys.*, 457:281, 2006. doi: 10.1051/0004-6361:20054654.

[144] Y. Suwa, K. Kotake, T. Takiwaki, S. C. Whitehouse, M. Liebendörfer, and K. Sato. Explosion Geometry of a Rotating 13M Star Driven by the SASI-Aided Neutrino-Heating Supernova Mechanism. PASJ, 62:L49–L53, December 2010. doi: 10.1093/pasj/62.6.L49.

[145] B. Müller, H.-T. Janka, and A. Marek. A New Multi-dimensional General Relativistic Neutrino Hydrodynamics Code for Core-collapse Supernovae. II. Relativistic Explosion Models of Core-collapse Supernovae. ApJ, 756:84, September 2012. doi: 10.1088/0004-637X/756/1/84.

[146] S. M. Couch and E. P. O'Connor. High-resolution Three-dimensional Simulations of Core-collapse Supernovae in Multiple Progenitors. ApJ, 785:123, April 2014. doi: 10.1088/0004-637X/785/2/123.

[147] T. Takiwaki, K. Kotake, and Y. Suwa. A Comparison of Two- and Three-dimensional Neutrino-hydrodynamics Simulations of Core-collapse Supernovae. ApJ, 786:83, May 2014. doi: 10.1088/0004-637X/786/2/83.

[148] T. Rauscher and F.-K. Thielemann. Astrophysical Reaction Rates From Statistical Model Calculations. *Atomic Data and Nuclear Data Tables*, 75:1–351, May 2000. doi: 10.1006/adnd.2000.0834.

[149] C. Fröhlich, G. Martínez-Pinedo, M. Liebendörfer, F.-K. Thielemann, E. Bravo, W. R. Hix, K. Langanke, and N. T. Zinner. Neutrino-Induced Nucleosynthesis of A>64 Nuclei: The νp Process. *Physical Review Letters*, 96(14):142502, April 2006. doi: 10.1103/PhysRevLett.96.142502.

[150] C. Weber, V.-V. Elomaa, R. Ferrer, C. Fröhlich, D. Ackermann, J. Äystö, G. Audi, L. Batist, K. Blaum, M. Block, A. Chaudhuri, M. Dworschak, S. Eliseev, T. Eronen, U. Hager, J. Hakala, F. Herfurth, F. P. Heßberger, S. Hofmann, A. Jokinen, A. Kankainen, H.-J. Kluge, K. Langanke, A. Martín, G. Martínez-Pinedo, M. Mazzocco, I. D. Moore, J. B. Neumayr, Y. N. Novikov, H. Penttilä, W. R. Plaß, A. V. Popov, S. Rahaman, T. Rauscher, C. Rauth, J. Rissanen, D. Rodríguez, A. Saastamoinen, C. Scheidenberger, L. Schweikhard, D. M. Seliverstov, T. Sonoda, F.-K. Thielemann, P. G. Thirolf, and G. K. Vorobjev. Mass measurements in the vicinity of the rp-process and the νp-process paths with the Penning trap facilities JYFLTRAP and SHIPTRAP. Phys. Rev. C, 78(5):054310, November 2008. doi: 10.1103/PhysRevC.78.054310.

[151] F. X. Timmes and F. D. Swesty. The Accuracy, Consistency, and Speed of an Electron-Positron Equation of State Based on Table Interpolation of the Helmholtz Free Energy. ApJS, 126:501–516, February 2000. doi: 10.1086/313304.

[152] S. E. Woosley and T. A. Weaver. The Evolution and Explosion of Massive Stars. II. Explosive Hydrodynamics and Nucleosynthesis. ApJS, 101:181, November 1995. doi: 10.1086/192237.

[153] M. Limongi and A. Chieffi. The Nucleosynthesis of ^{26}Al and ^{60}Fe in Solar Metallicity Stars Extending in Mass from 11 to 120 M_{solar}: The Hydrostatic and Explosive

Contributions. ApJ, 647:483–500, August 2006. doi: 10.1086/505164.

[154] A. Chieffi and M. Limongi. Pre-supernova Evolution of Rotating Solar Metallicity Stars in the Mass Range 13-120 M and their Explosive Yields. ApJ, 764:21, February 2013. doi: 10.1088/0004-637X/764/1/21.

[155] F.-K. Thielemann, K. Nomoto, and M.-A. Hashimoto. Core-Collapse Supernovae and Their Ejecta. ApJ, 460:408, March 1996. doi: 10.1086/176980.

[156] H. Umeda and K. Nomoto. How Much ^{56}Ni Can Be Produced in Core-Collapse Supernovae? Evolution and Explosions of 30-100 M Stars. ApJ, 673:1014-1022, February 2008. doi: 10.1086/524767.

[157] A. Burrows and J. Goshy. A Theory of Supernova Explosions. ApJ, 416:L75, October 1993. doi: 10.1086/187074.

[158] T. Yamasaki and S. Yamada. Effects of Rotation on the Revival of a Stalled Shock in Supernova Explosions. ApJ, 623:1000–1010, April 2005. doi: 10.1086/428496.

[159] W. Iwakami, K. Kotake, N. Ohnishi, S. Yamada, and K. Sawada. Three-Dimensional Simulations of Standing Accretion Shock Instability in Core-Collapse Supernovae. ApJ, 678:1207-1222, May 2008. doi: 10.1086/533582.

[160] W. Iwakami, K. Kotake, N. Ohnishi, S. Yamada, and K. Sawada. Effects of Rotation on Standing Accretion Shock Instability in Nonlinear Phase for Core-Collapse Supernovae. ApJ, 700:232–242, July 2009. doi: 10.1088/0004-637X/700/1/232.

[161] Y. Yamamoto, S.-i. Fujimoto, H. Nagakura, and S. Yamada. Post-shock-revival Evolution in the Neutrino-heating Mechanism of Core-collapse Supernovae. ApJ, 771: 27, July 2013. doi: 10.1088/0004-637X/771/1/27.

[162] M. Herant, W. Benz, W. R. Hix, C. L. Fryer, and S. A. Colgate. Inside the supernova: A powerful convective engine. ApJ, 435:339–361, November 1994. doi: 10.1086/174817.

[163] J. M. Blondin, A. Mezzacappa, and C. DeMarino. Stability of Standing Accretion Shocks, with an Eye toward Core-Collapse Supernovae. ApJ, 584:971–980, February 2003. doi: 10.1086/345812.

[164] J. M. Blondin and A. Mezzacappa. The Spherical Accretion Shock Instability in the Linear Regime. ApJ, 642:401–409, May 2006. doi: 10.1086/500817.

[165] L. Scheck, H.-T. Janka, T. Foglizzo, and K. Kifonidis. Multidimensional supernova simulations with approximative neutrino transport. II. Convection and the advective-acoustic cycle in the supernova core. A&A, 477:931–952, January 2008. doi: 10.1051/0004-6361:20077701.

[166] R. Fernández. The Spiral Modes of the Standing Accretion Shock Instability. ApJ, 725:1563–1580, December 2010. doi: 10.1088/0004-637X/725/2/1563.

[167] J. Guilet and T. Foglizzo. On the linear growth mechanism driving the standing accretion shock instability. MNRAS, 421:546–560, March 2012. doi: 10.1111/j.1365-2966.2012.20333.x.

[168] B. Müller, H.-T. Janka, and A. Heger. New Two-dimensional Models of Supernova Explosions by the Neutrino-heating Mechanism: Evidence for Different Instability Regimes in Collapsing Stellar Cores. ApJ, 761:72, December 2012. doi: 10.1088/0004-637X/761/1/72.

[169] C. Fröhlich, P. Hauser, M. Liebendörfer, G. Martínez-Pinedo, F.-K. Thielemann, E. Bravo, N. T. Zinner, W. R. Hix, K. Langanke, A. Mezzacappa, and K. Nomoto. Composition of the Innermost Core-Collapse Supernova Ejecta. ApJ, 637:415–426, January 2006. doi: 10.1086/498224.

[170] T. Ertl, H.-T. Janka, S. E. Woosley, T. Sukhbold, and M. Ugliano. A Two-parameter Criterion for Classifying the Explodability of Massive Stars by the Neutrino-driven Mechanism. ApJ, 818:124, February 2016. doi: 10.3847/0004-637X/818/2/124.

[171] E. O'Connor and C. D. Ott. A new open-source code for spherically symmetric stellar collapse to neutron stars and black holes. *Classical and Quantum Gravity*, 27(11):114103, June 2010. doi: 10.1088/0264-9381/27/11/114103.

[172] E. O'Connor and C. D. Ott. Black Hole Formation in Failing Core-Collapse Supernovae. ApJ, 730:70, April 2011. doi: 10.1088/0004-637X/730/2/70.

[173] P. Podsiadlowski, T. S. Morris, and N. Ivanova. The progenitor of SN 1987A. In S. Immler, K. Weiler, and R. McCray, editors, *Supernova 1987A: 20 Years After: Su-*

pernovae and Gamma-Ray Bursters, volume 937 of *American Institute of Physics Conference Series*, pages 125–133, October 2007. doi: 10.1063/1.3682893.

[174] T. Sukhbold and S. E. Woosley. The Compactness of Presupernova Stellar Cores. ApJ, 783:10, March 2014. doi: 10.1088/0004-637X/783/1/10.

[175] Yudai Suwa, Shoichi Yamada, Tomoya Takiwaki, and Kei Kotake. The criterion of supernova explosion revisited: the mass accretion history. *Astrophys. J.*, 816(1):43, 2016. doi: 10.3847/0004-637X/816/1/43.

[176] C. Kozma and C. Fransson. Late Spectral Evolution of SN 1987A. I. Temperature and Ionization. ApJ, 496:946–966, March 1998. doi: 10.1086/305409.

[177] C. Kozma and C. Fransson. Late Spectral Evolution of SN 1987A. II. Line Emission. ApJ, 497:431–457, April 1998. doi: 10.1086/305452.

[178] V. P. Utrobin and N. N. Chugai. Strong effects of time-dependent ionization in early SN 1987A. A&A, 441:271–281, October 2005. doi: 10.1051/0004-6361:20042599.

[179] T. Fischer, S. C. Whitehouse, A. Mezzacappa, F. K. Thielemann, and M. Liebendorfer. The neutrino signal from protoneutron star accretion and black hole formation. *Astron. Astrophys.*, 499:1, 2009. doi: 10.1051/0004-6361/200811055.

[180] F.-K. Thielemann, M.-A. Hashimoto, and K. Nomoto. Explosive nucleosynthesis in SN 1987A. II - Composition, radioactivities, and the neutron star mass. ApJ, 349: 222–240, January 1990. doi: 10.1086/168308.

[181] N. N. Chugai, R. A. Chevalier, R. P. Kirshner, and P. M. Challis. Hubble Space Telescope Spectrum of SN 1987A at an Age of 8 Years: Radioactive Luminescence of Cool Gas. ApJ, 483:925–940, July 1997.

[182] A. Jerkstrand, C. Fransson, and C. Kozma. The ^{44}Ti-powered spectrum of SN 1987A. A&A, 530:A45, June 2011. doi: 10.1051/0004-6361/201015937.

[183] J. Larsson, C. Fransson, G. Östlin, P. Gröningsson, A. Jerkstrand, C. Kozma, J. Sollerman, P. Challis, R. P. Kirshner, R. A. Chevalier, K. Heng, R. McCray, N. B. Suntzeff, P. Bouchet, A. Crotts, J. Danziger, E. Dwek, K. France, P. M. Garnavich, S. S. Lawrence, B. Leibundgut, P. Lundqvist, N. Panagia, C. S. J. Pun, N. Smith, G. Son-

neborn, L. Wang, and J. C. Wheeler. X-ray illumination of the ejecta of supernova 1987A. Nature, 474:484–486, June 2011. doi: 10.1038/nature10090.

[184] S. A. Grebenev, A. A. Lutovinov, S. S. Tsygankov, and C. Winkler. Hard-X-ray emission lines from the decay of ^{44}Ti in the remnant of supernova 1987A. Nature, 490: 373–375, October 2012. doi: 10.1038/nature11473.

[185] B. W. Grefenstette, F. A. Harrison, S. E. Boggs, S. P. Reynolds, C. L. Fryer, K. K. Madsen, D. R. Wik, A. Zoglauer, C. I. Ellinger, D. M. Alexander, H. An, D. Barret, F. E. Christensen, W. W. Craig, K. Forster, P. Giommi, C. J. Hailey, A. Hornstrup, V. M. Kaspi, T. Kitaguchi, J. E. Koglin, P. H. Mao, H. Miyasaka, K. Mori, M. Perri, M. J. Pivovaroff, S. Puccetti, V. Rana, D. Stern, N. J. Westergaard, and W. W. Zhang. Asymmetries in core-collapse supernovae from maps of radioactive ^{44}Ti in CassiopeiaA. Nature, 506:339–342, February 2014. doi: 10.1038/nature12997.

[186] T. Rauscher, A. Heger, R. D. Hoffman, and S. E. Woosley. Nucleosynthesis in Massive Stars with Improved Nuclear and Stellar Physics. ApJ, 576:323–348, September 2002. doi: 10.1086/341728.

[187] H. Umeda and K. Nomoto. Nucleosynthesis of Zinc and Iron Peak Elements in Population III Type II Supernovae: Comparison with Abundances of Very Metal Poor Halo Stars. ApJ, 565:385–404, January 2002. doi: 10.1086/323946.

[188] V. Margerin, A.St.J. Murphy, T. Davinson, R. Dressler, J. Fallis, A. Kankainen, A.M. Laird, G. Lotay, D.J. Mountford, C.D. Murphy, C. Seiffert, D. Schumann, T. Stowasser, T. Stora, C.H.-T. Wang, and P.J. Woods. Study of the reaction and implications for core collapse supernovae. *Physics Letters B*, 731:358–361, 2014. ISSN 0370-2693. doi: 10.1016/j.physletb.2014.03.003. URL `http://www.sciencedirect.com/science/article/pii/S0370269314001580`.

[189] K. Farouqi, K.-L. Kratz, B. Pfeiffer, T. Rauscher, F.-K. Thielemann, and J. W. Truran. Charged-particle and Neutron-capture Processes in the High-entropy Wind of Core-collapse Supernovae. ApJ, 712:1359–1377, April 2010. doi: 10.1088/0004-637X/712/2/1359.

[190] G Martínez-Pinedo, T Fischer, and L Huther. Supernova neutrinos and nucleosynthesis. *Journal of Physics G: Nuclear and Particle Physics*, 41(4):044008, 2014. URL `http://stacks.iop.org/0954-3899/41/i=4/a=044008`.

[191] T. Fischer, G. Martínez-Pinedo, M. Hempel, and M. Liebendörfer. Neutrino spectra evolution during protoneutron star deleptonization. Phys. Rev. D, 85(8):083003, April 2012. doi: 10.1103/PhysRevD.85.083003.

[192] R. A. Chevalier. Neutron star accretion in a supernova. ApJ, 346:847–859, November 1989. doi: 10.1086/168066.

[193] C. G. Bernal, D. Page, and W. H. Lee. Hypercritical Accretion onto a Newborn Neutron Star and Magnetic Field Submergence. ApJ, 770:106, June 2013. doi: 10.1088/0004-637X/770/2/106.

[194] N. Fraija, C. G. Bernal, and A. M. Hidalgo-Gaméz. Signatures of neutrino cooling in the SN1987A scenario. MNRAS, 442:239–250, July 2014. doi: 10.1093/mnras/stu872.

[195] M. Koshiba. Observational neutrino astrophysics. Phys. Rep., 220:229–381, November 1992. doi: 10.1016/0370-1573(92)90083-C.

[196] F. Vissani. Comparative analysis of SN1987A antineutrino fluence. *Journal of Physics G Nuclear Physics*, 42(1):013001, January 2015. doi: 10.1088/0954-3899/42/1/013001.

[197] K. Kifonidis, T. Plewa, L. Scheck, H.-T. Janka, and E. Müller. Non-spherical core collapse supernovae. II. The late-time evolution of globally anisotropic neutrino-driven explosions and their implications for SN 1987 A. A&A, 453:661–678, July 2006. doi: 10.1051/0004-6361:20054512.

[198] T. C. Chan, K. S. Cheng, T. Harko, H. K. Lau, L. M. Lin, W. M. Suen, and X. L. Tian. Could the Compact Remnant of SN 1987A BE a Quark Star? ApJ, 695:732–746, April 2009. doi: 10.1088/0004-637X/695/1/732.

[199] H. Ögelman and M. A. Alpar. Constraints on a Putative Pulsar in SN 1987A. ApJ, 603:L33–L35, March 2004. doi: 10.1086/383085.

[200] G. J. M. Graves, P. M. Challis, R. A. Chevalier, A. Crotts, A. V. Filippenko, C. Fransson, P. Garnavich, R. P. Kirshner, W. Li, P. Lundqvist, R. McCray, N. Panagia, M. M. Phillips, C. J. S. Pun, B. P. Schmidt, G. Sonneborn, N. B. Suntzeff, L. Wang, and J. C.

Wheeler. Limits from the Hubble Space Telescope on a Point Source in SN 1987A. ApJ, 629:944–959, August 2005. doi: 10.1086/431422.

[201] G. Zanardo, L. Staveley-Smith, C.-Y. Ng, B. M. Gaensler, T. M. Potter, R. N. Manchester, and A. K. Tzioumis. High-resolution Radio Observations of the Remnant of SN 1987A at High Frequencies. ApJ, 767:98, April 2013. doi: 10.1088/0004-637X/767/2/98.

[202] G. Zanardo, L. Staveley-Smith, R. Indebetouw, R. A. Chevalier, M. Matsuura, B. M. Gaensler, M. J. Barlow, C. Fransson, R. N. Manchester, M. Baes, J. R. Kamenetzky, M. Lakićević, P. Lundqvist, J. M. Marcaide, I. Martí-Vidal, M. Meixner, C.-Y. Ng, S. Park, G. Sonneborn, J. Spyromilio, and J. T. van Loon. Spectral and Morphological Analysis of the Remnant of Supernova 1987A with ALMA and ATCA. ApJ, 796:82, December 2014. doi: 10.1088/0004-637X/796/2/82.

[203] Y. Suwa, T. Takiwaki, K. Kotake, T. Fischer, M. Liebendörfer, and K. Sato. On the Importance of the Equation of State for the Neutrino-driven Supernova Explosion Mechanism. ApJ, 764:99, February 2013. doi: 10.1088/0004-637X/764/1/99.

[204] Adam Burrows. Colloquium: Perspectives on core-collapse supernova theory. *Rev. Mod. Phys.*, 85:245, 2013. doi: 10.1103/RevModPhys.85.245.

[205] Ko Nakamura, Tomoya Takiwaki, Takami Kuroda, and Kei Kotake. Systematic Features of Axisymmetric Neutrino-Driven Core-Collapse Supernova Models in Multiple Progenitors. *Publ. Astron. Soc. Jap.*, 67:107, 2015. doi: 10.1093/pasj/psv073.

[206] P. A. Young and C. L. Fryer. Uncertainties in Supernova Yields. I. One-dimensional Explosions. ApJ, 664:1033–1044, August 2007. doi: 10.1086/518081.

[207] S. M. Couch and C. D. Ott. Revival of the Stalled Core-collapse Supernova Shock Triggered by Precollapse Asphericity in the Progenitor Star. ApJ, 778:L7, November 2013. doi: 10.1088/2041-8205/778/1/L7.

[208] B. Müller and H.-T. Janka. Non-radial instabilities and progenitor asphericities in core-collapse supernovae. MNRAS, 448:2141–2174, April 2015. doi: 10.1093/mnras/stv101.

[209] S. M. Couch, E. Chatzopoulos, W. D. Arnett, and F. X. Timmes. The Three-dimensional Evolution to Core Collapse of a Massive Star. ApJ, 808:L21, July 2015. doi: 10.1088/2041-8205/808/1/L21.

[210] W. D. Arnett, C. Meakin, M. Viallet, S. W. Campbell, J. C. Lattanzio, and M. Mocák. Beyond Mixing-length Theory: A Step Toward 321D. ApJ, 809:30, August 2015. doi: 10.1088/0004-637X/809/1/30.

[211] E. O'Connor and C. D. Ott. Black Hole Formation in Failing Core-Collapse Supernovae. ApJ, 730:70, April 2011. doi: 10.1088/0004-637X/730/2/70.

[212] K. Nakamura, T. Takiwaki, T. Kuroda, and K. Kotake. Systematic features of axisymmetric neutrino-driven core-collapse supernova models in multiple progenitors. PASJ, 67:107, December 2015. doi: 10.1093/pasj/psv073.

[213] A. Burrows, D. Vartanyan, J. C. Dolence, M. A. Skinner, and D. Radice. Crucial Physical Dependencies of the Core-Collapse Supernova Mechanism. Space Sci. Rev., 214:33, February 2018. doi: 10.1007/s11214-017-0450-9.

[214] T. Sukhbold, T. Ertl, S. E. Woosley, J. M. Brown, and H.-T. Janka. Core-collapse Supernovae from 9 to 120 Solar Masses Based on Neutrino-powered Explosions. ApJ, 821:38, April 2016. doi: 10.3847/0004-637X/821/1/38.

[215] B. Müller, A. Heger, D. Liptai, and J. B. Cameron. A simple approach to the supernova progenitor-explosion connection. MNRAS, 460:742–764, July 2016. doi: 10.1093/mnras/stw1083.

[216] B. P. Abbott, R. Abbott, T. D. Abbott, M. R. Abernathy, F. Acernese, K. Ackley, C. Adams, T. Adams, P. Addesso, R. X. Adhikari, and et al. Observation of Gravitational Waves from a Binary Black Hole Merger. *Physical Review Letters*, 116(6): 061102, February 2016. doi: 10.1103/PhysRevLett.116.061102.

[217] S. E. Woosley and J. S. Bloom. The Supernova Gamma-Ray Burst Connection. ARA&A, 44:507–556, September 2006. doi: 10.1146/annurev.astro.43.072103.150558.

[218] B. Paczyński. Are Gamma-Ray Bursts in Star-Forming Regions? ApJ, 494:L45–L48, February 1998. doi: 10.1086/311148.

[219] K. Nomoto, K. Maeda, P. A. Mazzali, H. Umeda, J. Deng, and K. Iwamoto. Hypernovae and Other Black-Hole-Forming Supernovae. In C. L. Fryer, editor, *Astrophysics and Space Science Library*, volume 302 of *Astrophysics and Space Science Library*, pages 277–325, April 2004. doi: 10.1007/978-0-306-48599-2_10.

[220] K. Nomoto, N. Tominaga, H. Umeda, C. Kobayashi, and K. Maeda. Nucleosynthesis yields of core-collapse supernovae and hypernovae, and galactic chemical evolution. *Nuclear Physics A*, 777:424–458, October 2006. doi: 10.1016/j.nuclphysa.2006.05.008.

[221] K. Nomoto, H. Yamaoka, O. R. Pols, E. P. J. van den Heuvel, K. Iwamoto, S. Kumagai, and T. Shigeyama. A carbon-oxygen star as progenitor of the type Ic supernova 1994I. Nature, 371:227–229, September 1994. doi: 10.1038/371227a0.

[222] T. Shigeyama, T. Suzuki, S. Kumagai, K. Nomoto, H. Saio, and H. Yamaoka. Theoretical light curves of Type IIb supernova 1993J. ApJ, 420:341–347, January 1994. doi: 10.1086/173564.

[223] S. E. Woosley, R. G. Eastman, T. A. Weaver, and P. A. Pinto. SN 1993J: A Type IIb supernova. ApJ, 429:300–318, July 1994. doi: 10.1086/174319.

[224] T. R. Young, E. Baron, and D. Branch. Light Curve Studies of SN 1993J and SN 1994I. ApJ, 449:L51, August 1995. doi: 10.1086/309618.

[225] O. S. Bartunov, S. I. Blinnikov, N. N. Pavlyuk, and D. Y. Tsvetkov. A model for Supernova 1993J. A&A, 281:L53–L55, January 1994.

[226] W. L. Freedman, S. M. Hughes, B. F. Madore, J. R. Mould, M. G. Lee, P. Stetson, R. C. Kennicutt, A. Turner, L. Ferrarese, H. Ford, J. A. Graham, R. Hill, J. G. Hoessel, J. Huchra, and G. D. Illingworth. The Hubble Space Telescope Extragalactic Distance Scale Key Project. 1: The discovery of Cepheids and a new distance to M81. ApJ, 427:628–655, June 1994. doi: 10.1086/174172.

[227] D. Poznanski. An emerging coherent picture of red supergiant supernova explosions. MNRAS, 436:3224–3230, December 2013. doi: 10.1093/mnras/stt1800.

[228] L. Dessart, E. Livne, and R. Waldman. Determining the main-sequence mass of Type II supernova progenitors. MNRAS, 408:827–840, October 2010. doi: 10.1111/

j.1365-2966.2010.17190.x.

[229] M. A. Hendry, S. J. Smartt, R. M. Crockett, J. R. Maund, A. Gal-Yam, D.-S. Moon, S. B. Cenko, D. W. Fox, R. P. Kudritzki, C. R. Benn, and R. Østensen. SN 2004A: another Type II-P supernova with a red supergiant progenitor. MNRAS, 369:1303–1320, July 2006. doi: 10.1111/j.1365-2966.2006.10374.x.

[230] J. R. Maund, E. Reilly, and S. Mattila. A late-time view of the progenitors of five Type IIP supernovae. MNRAS, 438:938–958, February 2014. doi: 10.1093/mnras/stt2131.

[231] N. N. Chugai, S. N. Fabrika, O. N. Sholukhova, V. P. Goranskij, P. K. Abolmasov, and V. V. Vlasyuk. Optical Observations of Type-IIP Supernova 2004dj: Evidence for Asymmetry of the 56Ni Ejecta. *Astronomy Letters*, 31:792–805, December 2005. doi: 10.1134/1.2138766.

[232] T. Zhang, X. Wang, W. Li, X. Zhou, J. Ma, Z. Jiang, and J. Chen. Optical Photometry of the Type II-P Supernova 2004dj in NGC 2403. AJ, 131:2245–2255, April 2006. doi: 10.1086/500972.

[233] J. Maíz-Apellániz, H. E. Bond, M. H. Siegel, Y. Lipkin, D. Maoz, E. O. Ofek, and D. Poznanski. The Progenitor of the Type II-P SN 2004dj in NGC 2403. ApJ, 615:L113–L116, November 2004. doi: 10.1086/426120.

[234] X. Wang, Y. Yang, T. Zhang, J. Ma, X. Zhou, W. Li, Y.-Q. Lou, and Z. Li. The Progenitor of SN 2004dj in a Star Cluster. ApJ, 626:L89–L92, June 2005. doi: 10.1086/431903.

[235] J. Vinkó, K. Sárneczky, Z. Balog, S. Immler, B. E. K. Sugerman, P. J. Brown, K. Misselt, G. M. Szabó, S. Csizmadia, M. Kun, P. Klagyivik, R. J. Foley, A. V. Filippenko, B. Csák, and L. L. Kiss. The Young, Massive, Star Cluster Sandage-96 After the Explosion of Supernova 2004dj in NGC 2403. ApJ, 695:619–635, April 2009. doi: 10.1088/0004-637X/695/1/619.

[236] A. Jerkstrand, C. Fransson, K. Maguire, S. Smartt, M. Ergon, and J. Spyromilio. The progenitor mass of the Type IIP supernova SN 2004et from late-time spectral modeling. A&A, 546:A28, October 2012. doi: 10.1051/0004-6361/201219528.

[237] D. K. Sahu, G. C. Anupama, S. Srividya, and S. Muneer. Photometric and spectroscopic evolution of the Type IIP supernova SN 2004et. MNRAS, 372:1315–1324, November 2006. doi: 10.1111/j.1365-2966.2006.10937.x.

[238] V. P. Utrobin and N. N. Chugai. High mass of the type IIP supernova 2004et inferred from hydrodynamic modeling. A&A, 506:829–834, November 2009. doi: 10.1051/0004-6361/200912273.

[239] R. M. Crockett, S. J. Smartt, A. Pastorello, J. J. Eldridge, A. W. Stephens, J. R. Maund, and S. Mattila. On the nature of the progenitors of three Type II-P supernovae: 2004et, 2006my and 2006ov. MNRAS, 410:2767–2786, February 2011. doi: 10.1111/j.1365-2966.2010.17652.x.

[240] J. R. Maund, S. J. Smartt, and I. J. Danziger. The progenitor of SN 2005cs in the Whirlpool Galaxy. MNRAS, 364:L33–L37, November 2005. doi: 10.1111/j.1745-3933.2005.00100.x.

[241] K. Takáts and J. Vinkó. Distance estimate and progenitor characteristics of SN 2005cs in M51. MNRAS, 372:1735–1740, November 2006. doi: 10.1111/j.1365-2966.2006.10974.x.

[242] V. P. Utrobin and N. N. Chugai. Progenitor mass of the type IIP supernova 2005cs. A&A, 491:507–513, November 2008. doi: 10.1051/0004-6361:200810272.

[243] M. Fraser, K. Takáts, A. Pastorello, S. J. Smartt, S. Mattila, M.-T. Botticella, S. Valenti, M. Ergon, J. Sollerman, I. Arcavi, S. Benetti, F. Bufano, R. M. Crockett, I. J. Danziger, A. Gal-Yam, J. R. Maund, S. Taubenberger, and M. Turatto. On the Progenitor and Early Evolution of the Type II Supernova 2009kr. ApJ, 714:L280–L284, May 2010. doi: 10.1088/2041-8205/714/2/L280.

[244] A. Jerkstrand, S. J. Smartt, M. Fraser, C. Fransson, J. Sollerman, F. Taddia, and R. Kotak. The nebular spectra of SN 2012aw and constraints on stellar nucleosynthesis from oxygen emission lines. MNRAS, 439:3694–3703, April 2014. doi: 10.1093/mnras/stu221.

[245] S. Bose, B. Kumar, F. Sutaria, B. Kumar, R. Roy, V. K. Bhatt, S. B. Pandey, H. C. Chandola, R. Sagar, K. Misra, and S. Chakraborti. Supernova 2012aw - a high-energy

clone of archetypal Type IIP SN 1999em. MNRAS, 433:1871–1891, August 2013. doi: 10.1093/mnras/stt864.

[246] M. Dall'Ora, M. T. Botticella, M. L. Pumo, L. Zampieri, L. Tomasella, G. Pignata, A. J. Bayless, T. A. Pritchard, S. Taubenberger, R. Kotak, C. Inserra, M. Della Valle, E. Cappellaro, S. Benetti, S. Benitez, F. Bufano, N. Elias-Rosa, M. Fraser, J. B. Haislip, A. Harutyunyan, D. A. Howell, E. Y. Hsiao, T. Iijima, E. Kankare, P. Kuin, J. R. Maund, A. Morales-Garoffolo, N. Morrell, U. Munari, P. Ochner, A. Pastorello, F. Patat, M. M. Phillips, D. Reichart, P. W. A. Roming, A. Siviero, S. J. Smartt, J. Sollerman, F. Taddia, S. Valenti, and D. Wright. The Type IIP Supernova 2012aw in M95: Hydrodynamical Modeling of the Photospheric Phase from Accurate Spectrophotometric Monitoring. ApJ, 787:139, June 2014. doi: 10.1088/0004-637X/787/2/139.

[247] J. R. Maund, M. Fraser, S. J. Smartt, M. T. Botticella, C. Barbarino, M. Childress, A. Gal-Yam, C. Inserra, G. Pignata, D. Reichart, B. Schmidt, J. Sollerman, F. Taddia, L. Tomasella, S. Valenti, and O. Yaron. Supernova 2012ec: identification of the progenitor and early monitoring with PESSTO. MNRAS, 431:L102–L106, April 2013. doi: 10.1093/mnrasl/slt017.

[248] N. Tominaga, M. Tanaka, K. Nomoto, P. A. Mazzali, J. Deng, K. Maeda, H. Umeda, M. Modjaz, M. Hicken, P. Challis, R. P. Kirshner, W. M. Wood-Vasey, C. H. Blake, J. S. Bloom, M. F. Skrutskie, A. Szentgyorgyi, E. E. Falco, N. Inada, T. Minezaki, Y. Yoshii, K. Kawabata, M. Iye, G. C. Anupama, D. K. Sahu, and T. P. Prabhu. The Unique Type Ib Supernova 2005bf: A WN Star Explosion Model for Peculiar Light Curves and Spectra. ApJ, 633:L97–L100, November 2005. doi: 10.1086/498570.

[249] G. Folatelli, C. Contreras, M. M. Phillips, S. E. Woosley, S. Blinnikov, N. Morrell, N. B. Suntzeff, B. L. Lee, M. Hamuy, S. González, W. Krzeminski, M. Roth, W. Li, A. V. Filippenko, R. J. Foley, W. L. Freedman, B. F. Madore, S. E. Persson, D. Murphy, S. Boissier, G. Galaz, L. González, P. J. McCarthy, A. McWilliam, and W. Pych. SN 2005bf: A Possible Transition Event between Type Ib/c Supernovae and Gamma-Ray Bursts. ApJ, 641:1039–1050, April 2006. doi: 10.1086/500531.

[250] K.-C. Pan, M. Liebendörfer, M. Hempel, and F.-K. Thielemann. Two-dimensional Core-collapse Supernova Simulations with the Isotropic Diffusion Source Approximation for Neutrino Transport. ApJ, 817:72, January 2016. doi: 10.3847/0004-637X/817/1/72.

[251] R. M. Cabezón, K.-C. Pan, M. Liebendörfer, T. Kuroda, K. Ebinger, O. Heinimann, A. Perego, and F.-K. Thielemann. Core-collapse supernovae in the hall of mirrors. A three-dimensional code-comparison project. A&A, 619:A118, November 2018. doi: 10.1051/0004-6361/201833705.

[252] F. C. Michel. Neutron star disk formation from supernova fall-back and possible observational consequences. Nature, 333:644, June 1988. doi: 10.1038/333644a0.

[253] A. W. Steiner, M. Hempel, and T. Fischer. Core-collapse Supernova Equations of State Based on Neutron Star Observations. ApJ, 774:17, September 2013. doi: 10.1088/0004-637X/774/1/17.

[254] E. E. Salpeter. The Luminosity Function and Stellar Evolution. ApJ, 121:161, January 1955. doi: 10.1086/145971.

[255] N. Bastian, K. R. Covey, and M. R. Meyer. A Universal Stellar Initial Mass Function? A Critical Look at Variations. ARA&A, 48:339–389, September 2010. doi: 10.1146/annurev-astro-082708-101642.

[256] G. E. Miller and J. M. Scalo. The initial mass function and stellar birthrate in the solar neighborhood. ApJS, 41:513–547, November 1979. doi: 10.1086/190629.

[257] B. Müller, A. Heger, D. Liptai, and J. B. Cameron. A simple approach to the supernova progenitor-explosion connection. MNRAS, 460:742–764, July 2016. doi: 10.1093/mnras/stw1083.

[258] O. Pejcha and T. A. Thompson. The Landscape of the Neutrino Mechanism of Core-collapse Supernovae: Neutron Star and Black Hole Mass Functions, Explosion Energies, and Nickel Yields. ApJ, 801:90, March 2015. doi: 10.1088/0004-637X/801/2/90.

[259] P. Kroupa. On the variation of the initial mass function. MNRAS, 322:231–246, April 2001. doi: 10.1046/j.1365-8711.2001.04022.x.

[260] F. Özel, D. Psaltis, R. Narayan, and A. Santos Villarreal. On the Mass Distribution and Birth Masses of Neutron Stars. ApJ, 757:55, September 2012. doi: 10.1088/0004-637X/757/1/55.

[261] C. D. Ott, L. F. Roberts, A. da Silva Schneider, J. M. Fedrow, R. Haas, and E. Schnetter. The Progenitor Dependence of Core-collapse Supernovae from Three-dimensional Simulations with Progenitor Models of 12-40 M . ApJ, 855:L3, March 2018. doi: 10.3847/2041-8213/aaa967.

[262] C. Chan, B. Müller, A. Heger, R. Pakmor, and V. Springel. Black Hole Formation and Fallback during the Supernova Explosion of a 40 M Star. ApJ, 852:L19, January 2018. doi: 10.3847/2041-8213/aaa28c.

[263] F. Özel, D. Psaltis, R. Narayan, and J. E. McClintock. The Black Hole Mass Distribution in the Galaxy. ApJ, 725:1918–1927, December 2010. doi: 10.1088/0004-637X/725/2/1918.

[264] C. S. Kochanek. Failed Supernovae Explain the Compact Remnant Mass Function. ApJ, 785:28, April 2014. doi: 10.1088/0004-637X/785/1/28.

[265] R. Käppeli, S. C. Whitehouse, S. Scheidegger, U.-L. Pen, and M. Liebendörfer. FISH: A Three-dimensional Parallel Magnetohydrodynamics Code for Astrophysical Applications. ApJS, 195:20, August 2011. doi: 10.1088/0067-0049/195/2/20.

[266] S. Scheidegger. *Gravitational Waves from 3D MHD Core-Collapse Supernova Simulations with Neutrino Transport.* PhD thesis, 2011.

[267] R. Käppeli. *Numerical Methods for 3D Magneto-Rotational Core-Collapse Supernova Simulation with Jet Formation.* PhD thesis, 2013.

[268] A. Perego, S. Rosswog, R. M. Cabezón, O. Korobkin, R. Käppeli, A. Arcones, and M. Liebendörfer. Neutrino-driven winds from neutron star merger remnants. MNRAS, 443:3134–3156, October 2014. doi: 10.1093/mnras/stu1352.

[269] S. W. Bruenn. The prompt-shock supernova mechanism. II - Supranuclear EOS behavior and the precollapse model. ApJ, 341:385–400, June 1989. doi: 10.1086/167502.

[270] R. M. Kulsrud. *Plasma Physics for Astrophysics.* Princeton University Press, 2005.

[271] E.F. Toro. *Riemann Solvers and Numerical Methods for Fluid Dynamics, A Practical Introduction.* Springer-Verlag Berlin Heidelberg, 1999.

[272] R. Courant, K. Friedrichs, and H. Lewy. Über die partiellen Differenzengleichungen der mathematischen Physik. *Mathematische Annalen*, 100(1):32–74, 1928. ISSN 1432-1807. doi: 10.1007/BF01448839. URL http://dx.doi.org/10.1007/BF01448839.

[273] S. J. Farlow. *Partial Differential Equations for Scientists and Engineers*. Dover Publications, 1993.

[274] A. Marek, H. Dimmelmeier, H.-T. Janka, E. Müller, and R. Buras. Exploring the relativistic regime with Newtonian hydrodynamics: an improved effective gravitational potential for supernova simulations. A&A, 445:273–289, January 2006. doi: 10.1051/0004-6361:20052840.

[275] S. Ashby and R. D. Falgout. A parallel multigrid preconditioned conjugate gradient algorithm for groundwater flow simulations. *Nuclear Science and Engineering*, 124 (1):145–159, 1996.

[276] Robert D. Falgout, Jim E. Jones, and Ulrike Meier Yang. *The Design and Implementation of hypre, a Library of Parallel High Performance Preconditioners*, pages 267–294. Springer Berlin Heidelberg, Berlin, Heidelberg, 2006. ISBN 978-3-540-31619-0. doi: 10.1007/3-540-31619-1_8. URL http://dx.doi.org/10.1007/3-540-31619-1_8.

[277] W. L Briggs, V. E. Henson, and S. F. McCormick. *A Multigrid Tutorial*. SIAM, Society for Industrial and Applied Mathematics, 2nd edition edition, 2000.

[278] Y. Saad. *Iterative methods for sparse linear systems*. SIAM, Society for Industrial and Applied Mathematics, 2nd edition edition, 2003.

[279] R. Kippenhahn and A. Weigert. *Stellar Structure and Evolution*. Springer-Verlag Berlin Heidelberg, corrected 2nd printing edition, 1991.

[280] M. Rampp and H.-T. Janka. Radiation hydrodynamics with neutrinos. Variable Eddington factor method for core-collapse supernova simulations. A&A, 396:361–392, December 2002. doi: 10.1051/0004-6361:20021398.

[281] L. D. Landau and E. M. Lifshitz. *Fluid mechanics*. 1959.